ACID-SALT-SURFACTANT LYOTROPIC LIQUID CRYSTALLINE MESOPHASES: SYNTHESIS, CHARACTERIZATION, AND ELECTROCHEMICAL PROPERTIES OF MESOPOROUS $M_2P_2O_7$ AND $M_{2-x}M'_xP_2O_7$ (M AND M'= MN(II), CO(II) AND NI(II)) POWDERS AND FILMS

A DISSERTATION SUBMITTED TO

THE GRADUATE SCHOOL OF ENGINEERING AND SCIENCE

OF BILKENT UNIVERSITY

IN PARTIAL FULFILLMENT OF THE REQUIREMENTS FOR

THE DEGREE OF

DOCTOR OF PHILOSOPHY

IN

CHEMISTRY

By

Işıl Ulu

October 2023

ACID-SALT-SURFACTANT LYOTROPIC LIQUID CRYSTALLINE MESOPHASES: SYNTHESIS, CHARACTERIZATION, AND ELECTROCHEMICAL PROPERTIES OF MESOPOROUS $M_2P_2O_7$ AND $M_{2-x}M'_xP_2O_7$ (M AND M'= MN(II), CO(II) AND NI(II)) POWDERS AND FILMS

By Işıl Ulu

October, 2023

We certify that we have read this dissertation and that, in our opinion, it is fully adequate, in scope and in quality, as a dissertation for the degree of Doctor of Philosophy.

_____
Ömer Dağ (Advisor)

_____
Ayşen Yılmaz

_____
Emren Nalbant

_____
Burak Ülgüt

_____
Halil İbrahim Okur

Approved for the Graduate School of Engineering and Science:

_____
Orhan Arıkan
Director of the Graduate School

ABSTRACT

ACID-SALT-SURFACTANT LYOTROPIC LIQUID CRYSTALLINE MESOPHASES: SYNTHESIS, CHARACTERIZATION, AND ELECTROCHEMICAL PROPERTIES OF MESOPOROUS $M_2P_2O_7$ AND $M_{2-x}M'_xP_2O_7$ (M AND M'= MN(II), CO(II) AND NI(II)) POWDERS AND FILMS

Işıl Ulu

Ph.D. in Chemistry

Advisor: Ömer Dağ

October 2023

The mesoporous metal pyrophosphates ($M_2P_2O_7$) are considered to be important as energy storage materials. This thesis proposes that a surfactant-assisted approach for the synthesis of the mesoporous $M_2P_2O_7$ would be a good solution since the high surface area is crucial for energy storage materials. A novel synthesis method for the synthesis of mesoporous metal pyrophosphates ($Ni_2P_2O_7$, $Co_2P_2O_7$, $Mn_2P_2O_7$, and binary metal pyrophosphates) is investigated by using a modified MASA (Molten Salt Assisted Self-Assembly) method using related acid; phosphoric acid (PA, H_3PO_4) or pyrophosphoric acid (PPA, $H_4P_2O_7$), salts ($[Mn(H_2O)_4](NO_3)_2$, $[Co(H_2O)_6](NO_3)_2$, $[Ni(H_2O)_6](NO_3)_2$) and surfactant (pluronic P123 ($EO_{20}PO_{70}EO_{20}$, where EO is ethylene oxide and PO is propylene oxide)). Firstly, homogeneous solutions using a broad range of inorganic ingredients are prepared. These solutions are then coated (spin-coating, drop-cast coating, or dip-coating) over a substrate to form lyotropic liquid crystalline (LLC) mesophases that can be calcined at various temperatures to synthesize the mesoporous metal pyrophosphates.

The mesophases are characterized using small-angle XRD, ATR-FTIR, POM, and gravimetric measurements during the water evaporation from the solution phases. Aging the mesophases at room temperature forms an ordered (display diffraction(s) at small angles) mesostructured semi-solid (exhibit some cracks under POM with particle-like morphology) $M_2H_xP_2O_7(NO_3)_x{\cdot}nH_2O$ materials as a result of a polymerization reaction (followed by ATR-FTIR) between transition metal species

and PPA. This process initiates in the solution phase and continues within the mesophase by releasing water and nitrate species and becomes stable in 24 h under ambient conditions.

The mesostructured semi-solid $M_2H_xP_2O_7(NO_3)_x \cdot nH_2O$ materials are calcined at 300 ^oC to produce mesoporous spherical $M_2P_2O_7$ with surface areas of 60, 111, and 41 m^2/g for Ni(II), Co(II), and Mn(II) pyrophosphates, respectively. These mesoporous $M_2P_2O_7$ materials, calcined at 300 ^oC and higher temperatures, are further characterized using wide-angle XRD, ATR-FTIR, XPS, SEM-EDX, TEM, N_2 adsorption-desorption, and electrochemical characterization techniques. Both $Co_2P_2O_7$ and $Mn_2P_2O_7$ are amorphous up to 600 ^oC, then crystallizing at around 600 ^oC to their alpha and beta phases, respectively. In contrast, the crystallization temperature of $Ni_2P_2O_7$ is around 700 ^oC, and it has mainly alpha and minimal delta phases. Mesoporous $NiCoP_2O_7$ and $MnCoP_2O_7$ with surface areas of 68 and 70 m^2/g, respectively, become crystalline at 600 ^oC to α-$NiCoP_2O_7$ and β-$MnCoP_2O_7$ phases, and they form solid-solutions when the mole ratio of the metal species is varied.

The clear solutions are spin-coated onto an FTO surface and then calcined to produce FTO-coated electrodes; however, those electrodes are not stable during the electrochemical measurements. Therefore, the diluted solutions from the mother liquor are dip-coated over a pure graphite rod (GR) and subsequently calcined to fabricate electrodes of mesoporous metal pyrophosphates. The GR-electrodes, which remain stable during the measurements, are tested using cyclic voltammetry (CV) and galvanostatic charge-discharge measurements with a 3-electrode system in a 3M KOH electrolyte. It is important to note that the metal pyrophosphates transform to their corresponding hydroxides in an alkaline solution during the electrochemical measurements. As a result, the collected data from the electrochemical measurements originate from the $M(OH)_2$ species rather than $M_2P_2O_7$. The mesoporous spherical $Ni_2P_2O_7$ material is converted into a very thin needle-like β-$Ni(OH)_2$ (1.5 nm thick and 7 nm wide) in alkaline media, maintaining its spherical morphology. In contrast, the mesoporous spherical $Co_2P_2O_7$ and $Mn_2P_2O_7$ particles transform into much thicker plate-like β-$Co(OH)_2$ and β-$Mn(OH)_2$ particles. The transformation time differs depending on the type of metal; the $Co_2P_2O_7$ and $Mn_2P_2O_7$ materials transform rapidly (about 30 sec), whereas the complete transformation of $Ni_2P_2O_7$ to its hydroxide takes

around 1 hour. The transformation time determines the particle size and morphology, consequently influencing the capacitance values. The β-$Ni(OH)_2$ exhibits a high charge capacity and specific capacitance (102 mA·s and 368 mF/cm^2 at a current density of 1 mA/cm^2). However, these values are nearly 10 times smaller in the β-$Mn(OH)_2$ and β-$Co(OH)_2$ electrodes. The addition of nickel ions to the cobalt system in the preparation of binary metal pyrophosphates enhances the capacity and specific capacitance values, with the sample having β-$Ni_{0.67}Co_{0.33}(OH)_2$ composition displaying the highest capacity value in alkali media (170 mA·s at a current density of 1 mA/cm^2). Nevertheless, other binary systems ($Mn_{1-x}Co_x(OH)_2$ and $Ni_{1-x}Mn_x(OH)_2$) display almost similar capacity behavior to pure cobalt and manganese systems.

Keywords: Mesoporous metal pyrophosphates, lyotropic liquid crystalline (LLC) mesophases, molten-salt assisted self-assembly, mesostructured semi-solid materials, metal hydroxides, specific capacitance.

ÖZET

ASİT-TUZ-YÜZEY AKTİF MADDE LİYOTROPİK SIVI KRİSTAL ARAFAZLAR: MEZOGÖZENEKLİ $M_2P_2O_7$ VE $M_{2-x}M'_xP_2O_7$ (M VE M'= MN(II), CO(II) VE NI(II)) TOZLARININ VE FİLMLERİNİN SENTEZİ, KARAKTERİZASYONU VE ELEKTROKİMYASAL DAVRANIŞLARI

Işıl Ulu

Kimya, Doktora

Tez Danışmanı: Ömer Dağ

Ekim, 2023

Mezogözenekli metal pirofosfatlar ($M_2P_2O_7$) enerji depolama malzemeleri olarak büyük öneme sahiptir. Bu tez, yüksek yüzey alana sahip enerji depolama malzemelerinin önemi dikkate alınarak, yüzey aktif madde destekli bir sentez yaklaşımı ile mezogözenekli $M_2P_2O_7$ malzemelerinin sentezinde iyi bir çözüm olacağını göstermeyi hedeflemiştir. Mezogözenekli metal pirofosfatların ($Ni_2P_2O_7$, $Co_2P_2O_7$, $Mn_2P_2O_7$, ve ikili metal pirofosfatlar) genel sentezi, ilgili asit olan fosforik asit (FA, H_3PO_4) veya pirofosforik asit (PFA, $H_4P_2O_7$), tuzlar ($[Mn(H_2O)_4](NO_3)_2$, $[Co(H_2O)_6](NO_3)_2$, $[Ni(H_2O)_6](NO_3)_2$) ve yüzey aktif madde (pluronik P123, ($EO_{20}PO_{70}EO_{20}$, EO etilen oksit ve PO propilen oksit)) kullanılarak modifiye edilmiş EYKO (eriyik tuz yardımlı kendiliğinden oluşma) yöntemi kullanılarak çalışılmıştır. Çok geniş bir inorganik bileşen yelpazesi kullanılarak hazırlanan homojen çözeltiler bir alttaş üzerine (döndürerek kaplama, damlatıp-yayarak kaplama veya daldırma-çekme kaplama yöntemleri ile) kaplanarak liyotropik sıvı kristal (LSK) arafazlar oluşturdu ve daha sonra çeşitli sıcaklıklarda kalsine edilerek mezogözenekli metal pirofosfatlara dönüştürüldü.

Arafazlar, çözelti fazından başlayarak suyun buharlaşması sırasında küçük-açı XRD, ATR-FTIR, POM ve gravimetrik ölçümler ile karakterize edildi. Arafazların oda sıcaklığında yaşlandırılması, çözelti fazında başlayan ve arafazda devam eden bir polimerizasyon reaksiyonu sonucunda düzenli (küçük açılarda kırınım gösteren) ve mezoyapılı yarı-katı (POM altında bazı çatlaklar ve parçacık gibi oluşumlar

sergileyen) $M_2H_xP_2O_7(NO_3)_x \cdot nH_2O$ malzemelerini oluşturur. Bu dönüşüm sulu çözelti fazında başlar, jel fazında devam eder ve 24 saat içinde kararlı bir yapıya ortamdan su ve nitrat bileşikleri atarak ulaşır.

Mezoyapılı yarı-katı $M_2H_xP_2O_7(NO_3)_x \cdot nH_2O$ malzemelerinin 300 ^oC'de yakılması sonucu, yüzey alanları sırası ile 60, 111 ve 41 m^2/g olan mezogözenekli küremsi Ni(II), Co(II) ve Mn(II) pirofosfatlar üretildi. 300 ^oC ve daha yüksek sıcaklıklarda yakılmış mezogözenekli $M_2P_2O_7$'lar XRD, ATR-FTIR, XPS, SEM-EDX, TEM, N_2 adsorpsiyon-desorpsiyon ve elektrokimyasal teknikleri kullanılarak karakterize edildi. $Co_2P_2O_7$ ve $Mn_2P_2O_7$'lar 600 ^oC'ye kadar amorf yapıdadır ve bu sıcaklıkta sırasıyla kendilerinin alfa ve beta fazlarına kristallenirler. Fakat, kristallenme sıcaklığı 700 ^oC olan $Ni_2P_2O_7$ az miktarda delta fazı içermesine karşın alfa fazındadır. Yüzey alanları sırası ile 68 ve 70 m^2/g olan mezogözenekli $NiCoP_2O_7$ ve $MnCoP_2O_7$'lar 600 ^oC'de α-$NiCoP_2O_7$ ve β-$MnCoP_2O_7$ fazlarına kristallenir ve metallerin mol oranlarına bağlı olarak katı-çözeltiler oluştururlar.

Berrak çözeltiler, döngülü-kaplama yöntemi ile FTO alttaş yüzeyine kaplandı ve kalsine edilerek elektrotları üretildi; fakat bu elektrotlar elektrokimyasal ölçümler sırasında kararlı değildir. Bu nedenle, ana çözeltilerden seyreltilmiş çözeltiler kullanılarak daldırma-çekme kaplama yöntemi ile saf grafit çubuklar (GÇ) üzerine kaplandı ve kalsine edilerek mezogözenekli metal pirofosfat elektrotlarına dönüştürüldü. Ölçümler esnasında kararlı olan GÇ-elektrotlar, döngüsel voltametre (DV) ve galvanostatik şarj-deşarj ölçümleri, 3M KOH elektrolit içinde bir 3-elektrot sistemi kullanılarak yapıldı. Metal pirofosfatlar, elektrokimyasal ölçümler sırasında, alkali bir çözelti içerisinde kendilerinin hidroksitlerine dönüştüğü ilk defa bu çalışma ile gösterildi. Bu nedenle, elektrokimyasal ölçümlerden toplanan verilerin $M_2P_2O_7$ yerine $M(OH)_2$ malzemelerinden kaynaklandığı belirlendi. Mezogözenekli küresel $Ni_2P_2O_7$ malzemesi alkali bir ortamda, küresel morfolojisini koruyarak çok ince (1,5 nm kalınlığında ve 7 nm genişliğinde) nano-yaprak benzeri β-$Ni(OH)_2$ malzemesine dönüşür. Buna karşı, mezogözenekli küresel $Co_2P_2O_7$ ve $Mn_2P_2O_7$ malzemeleri çok daha kalın plaka benzeri β-$Co(OH)_2$ ve β-$Mn(OH)_2$ parçacıklarına dönüştüğü belirlendi. Dönüşüm süresi, metalin türüne bağlı olarak değişkenlik gösterir; $Co_2P_2O_7$ ve $Mn_2P_2O_7$ malzemeleri çok hızlı (yaklaşık 30 saniye içinde) bir şekilde dönüşürken, $Ni_2P_2O_7$'ın komple değişimi yaklaşık 1 saat sürer. Dönüşüm süresi parçacık boyutunu

ve morfolojisini belirler ve doğrudan kapasite değerlerini etkiler. β-$Ni(OH)_2$ yüksek bir şarj kapasitesine ve spesifik kapasitansa sahiptir (1 mA/cm^2 akı yoğunluğunda 102 mA.s kapasite ve 368 mF/cm^2 spesifik kapasitans). Fakat bu değerler β-$Mn(OH)_2$ ve β-$Co(OH)_2$ elektrotları için yaklaşık 10 kat daha küçüktür. İkili metal pirofosfatların hazırlanması sırasında kobalt sistemine nikel iyonlarının eklenmesi, kapasite ve spesifik kapasitans değerlerini iyileştirir ve β-$Ni_{0.67}Co_{0.33}(OH)_2$ bileşimine sahip olan malzeme alkali ortamda en yüksek kapasite değerini sergiler (1 mA/cm^2 akı yoğunluğunda 170 mA.s). Ancak, diğer ikili sistemler ($Mn_{1-x}Co_x(OH)_2$ ve $Ni_{1-x}Mn_x(OH)_2$), saf kobalt ve mangan sistemlerine benzer kapasite davranışı gösterirler.

Anahtar Kelimeler: Mezogözenekli metal pirofosfatlar, liyotropik sıvı kristal (LSK) arafazlar, eriyik tuz yardımlı kendiliğinden oluşma yöntemi, mezoyapılı yarı-katı malzemeler, metal hidroksitler, spesifik kapasitans.

Acknowledgment

First and foremost, I am profoundly thankful to my supervisor, Prof. Ömer Dağ, for his invaluable mentorship, exceptional insights, and unwavering support. From my early years as an undergraduate, he has shared his excellent perspectives on science with me. His guidance has shaped the direction of this research and my overall development in academic life. I will never forget his enormous contribution to my life.

I would also like to thank TÜBİTAK for financial support during my graduate studies, provided under project numbers 119Z877 and 222Z040.

I want to extend my sincere appreciation to the members of my examining committee, Prof. Ayşen Yılmaz and Assoc. Prof. Burak Ülgüt, for their insightful feedback, constructive criticism, and significant contributions to enhancing the quality of this thesis.

I am also deeply thankful to my best friend, my sister, Irmak Karakaya, for her incredible support during my entire university journey. I cannot imagine a life without her unwavering presence. Additionally, I want to express my profound gratitude to my other best friend, Assel Amirzhanova, for her invaluable patience and for being around whenever I needed her support. Also, I want to thank all Dağ Group members, especially Hamid Ali Raza, Najeeb Ullah, Gözde Ceran, Arda Altan, Pamir Göksu, and Muratcan Ös, for their precious companionship, support and for creating a great environment that led to unforgettable moments.

I am indebted to my family, mom, İkbal Uzunok, dad, Rafet Uzunok, and brother Rıfatcan Uzunok, for their boundless love and support throughout this endeavor. Their belief in my educational pursuits has been a major source of my motivation. I cannot pass over the support of my parents-in-law, Hülya Ulu, Sinan Ulu, and Bora Ulu, whose sacrifices have contributed significantly to my success in this field.

Last but certainly not least, I would like to be grateful to my beloved husband, Burak Ulu, who deserves a worthy thank for his incredible patience, everlasting support, and love.

To my family…

Contents

List of Figures

List of Tables

List of Abbreviations

LC	: Liquid Crystal
LLC	: Lyotropic Liquid Crystal
TLC	: Thermotropic Liquid Crystals
CMC	: Critical Micelle Concentration
DRH	: Deliquescence Relative Humidity
EISA	: Evaporation-Induced Self-Assembly
MASA	: Molten Salt-Assisted Self-Assembly
PEO	: Poly Ethylene Oxide
PPO	: Poly Propylene Oxide
CTAB	: Cetyl Trimethyl Ammonium Bromide
SDS	: Sodium Dodecyl Sulfate
MPP	: Metal Pyrophosphates
PA	: Phosphoric Acid
PPA	: Pyrophosphoric Acid
XRD	: X-Ray Diffraction
POM	: Polarized Optical Microscopy
SEM	: Scanning Electron Microscopy
TEM	: Transmission Electron Microscopy
EDX	: Energy Dispersive X-Ray Spectroscopy
XPS	: X-Ray Photoelectron Spectroscopy
ATR-FTIR	: Attenuated Total Reflection Fourier-Transform Infrared
BET	: Brunauer, Emmett, and Teller

BJH	: Barrett, Joyner, and Halenda
IUPAC	: International Union of Pure and Applied Chemistry
RT	: Room Temperature
ND	: Number of Dilution
FWHM	: Full Width at Half Maximum
ICDD	: International Centre for Diffraction Data
WOR	: Water Oxidation Reaction
OER	: Oxygen Evolution Reaction
FTO	: Fluorine doped Tin Oxide
GR	: Graphite Rod
NHE	: Normal Hydrogen Electrode
CV	: Cyclic Voltammetry
GCD	: Galvanostatic Charge-Discharge
SC	: Supercapacitors
PC	: Pseudocapacitors
EDLC	: Electrochemical Double-Layer Capacitor

Chapter 1

1. Introduction

1.1. Mesoporous Materials

Mesoporous materials have been defined by IUPAC as those with pores ranging in size from 2 to 50 nm. [1] As its name implies, the pore size of mesoporous materials is in between microporous (smaller than 2 nm pores) and macroporous (higher than 50 nm) materials. Mesoporous materials have a high surface area and pore volume, providing a high interfacial surface and improved ionic and electronic conductivity for some materials. Compared to their bulk materials, these features have essential roles for many applications in energy generation, storage, conversion, and catalysis. [2], [3]

The mesoporous materials have been synthesized and characterized over 30 years. The first examples of mesoporous materials were synthesized in 1990 by Yanagisawa and his co-workers, resulting in a single-layered polysilicate kanemite ($NaHSi_2O_5.3H_2O$) with a pore diameter ranging from 2 to 4 nm and a surface area of 900 m^2/g.[4] However, the fundamental developments in this field started with Kresge and his team (Mobil Corporation scientists), focusing on synthesizing mesoporous silica by liquid-crystal templating mechanism. [5], [6] The main motivation behind the work was to increase the pores in the zeolites and create better catalytic structures for the larger molecules. It has been started by the addition of a long chain, like $C_{16}H_{33}^-$,

as an R group of ammonium salt ($(NR_4)Br$), which is used as a template in zeolite synthesis. The aim was to enlarge the pores by introducing larger templates into the sol-gel environment. Specifically, the $C_{16}H_{33}N(CH_3)_3Br$ salt was utilized for this purpose, also known as CTAB (cetyl trimethyl ammonium bromide). CTAB is a charged surfactant that can form a micelle structure in a solution when a critical concentration is reached. In the pioneering work of Kresge and his co-workers, CTAB was added to a basic aqueous solution of a silica source. The silica is polymerized in the basic medium and covers the micelle structure, forming a lyotropic liquid crystal phase. Subsequently, the organic materials are removed by a thermal process to produce a stable and ordered mesoporous molecular sieve. This work has attracted other researchers worldwide, leading to intensive studies that significantly contributed to the literature on this topic. [7]–[10] In 1996, Pinnavaia and his colleagues synthesized the first example of mesoporous silica materials using a neutral surfactant. [11] In the same year, Attard and his group announced the synthesis of mesostructured silica using lyotropic liquid crystalline phase from aqueous silica ingredients and non-ionic surfactants in their Nature article. [12] In 1996, the first examples of mesoporous silica film were introduced by Yang and his co-workers. [13] They demonstrated that the mesoporous film could grow at the interface between air and water by surfactant templating, even in the absence of a solid surface. Later studies have primarily concentrated on the control of the pore size and morphology of the powder silicates. Several methods have been explored extensively to control the morphology and structure of mesoporous silicates. [14] A similar effort has been devoted to the synthesis of silicates using different silica sources and surfactants. In addition to silica-based mesoporous materials, numerous unique methods have been developed for the synthesis of organosilicates[15] and titania-based mesoporous materials. [16] Furthermore, extensive studies have been conducted on the synthesis of metal oxides[15], [17]–[19], metal sulfides[20], and metal phosphates[21]–[23] using preexisting and novel methods. The synthesis of these materials with a well-controlled structure and morphology may open up new areas since they are crucial for energy production and storage applications. Understanding the mechanism that controls the structures of mesoporous materials requires many more investigations. Investigations on mesoporous metals[24], metal oxides[17], [25], metal phosphates[22], pyrophosphates[26], metal sulfides[27], [28] and metal selenates[28] synthesis

methods are still undergoing towards effective materials for the energy production and storage technologies. Unfortunately, only a few successful methods exist to synthesize the above mesoporous materials. Although the first example of mesoporous metal sulfides and selenides was demonstrated in 1995, there have been no significant developments in the synthesis of large-scale mesoporous metal sulfides and selenides in various forms. The same challenges have been encountered in the synthesis of mesoporous metal phosphates and metal polyphosphates. Control of the formation kinetics of these materials during the self-assembly process and the preservation of the mesostructures during high-temperature processes are still unclear. Therefore, there is an essential need to develop facile and cost-effective methods for the synthesis of these materials. Metal phosphates and polyphosphates are expected to be in high demand for battery and supercapacitor technologies in the upcoming years, and synthesizing their porous forms will contribute significantly to the literature on the advancement of these technologies. Various attempts have been made to overcome problems in producing mesoporous non-silicates during the last 20 years. These attempts have included both hard- and soft-templating methods.

1.1.1. Hard-Templating Method

The hard-templating method is a practical and straightforward approach to synthesize a mesoporous material. [29]–[34] This method uses robust and porous pre-synthesized materials (for example, silica or carbon) as a template. In the initial step of this method, the pores of the template are filled with a desired material and then calcined to fabricate the mesoporous material, simulating the porous structure of the template. After calcination, the template is removed by dissolving it in either an acidic (mostly HF) or a basic solution, depending on the template, to obtain the target mesoporous material. The schematic representation of the steps of the hard-templating method is shown in Figure 1.1.

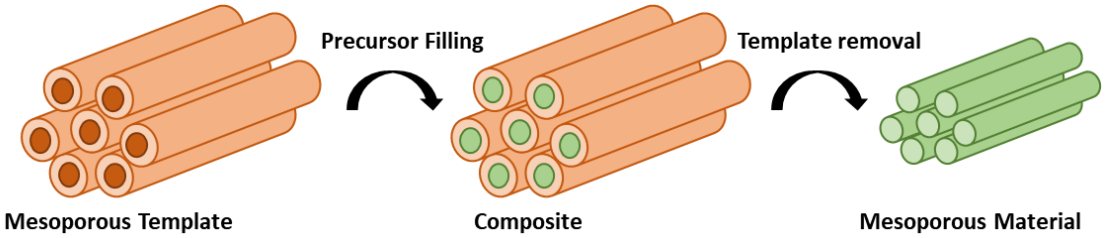

Figure 1.1: Schematic representation of the hard-templating method.

This method was first employed by Martin in 1994 for the synthesis of nanomaterials, using a porous alumina membrane as a template. [35] However, mesoporous silica or carbon are ideal hard templates for the synthesis of materials with more uniform pores and highly ordered structures. Ryoo and his co-workers synthesized highly ordered mesoporous carbon for the first time using mesoporous silica as a template. [29] They converted the sucrose to carbon inside the pores of mesoporous silica by carbonization using sulfuric acid. They obtained the mesoporous carbon with a BET surface area of 1380 m^2/g and a pore size diameter of 3 nm. After that invention, mesoporous carbon, due to its ease of removal, became the preferred choice for synthesizing mesoporous metal oxides as a template compared to silica, which can be removed by etching in either acidic (HF) or basic (NaOH) solutions. [36]–[38] Zhu et al. synthesized the metal oxide (Cr_2O_3) for the first time by using silica as a template. They reported a surface area of 58 m^2/g with a pore volume of 0.143 cm^3/g and a pore size of 3.4 nm. [39] Silica was introduced as a template for the hard-templating method by Stucky for the first time. [40] In the following years, mesoporous silica has been utilized as a hard template for the synthesis of titania[34], tin oxide[33], some other transition metal oxides[41], and also some lithiated metal oxides[42]. However, due to the multi-step nature of the hard-templating method, its practicality for the synthesis of many mesoporous materials is limited. Moreover, it is almost impossible to synthesize the target materials as a thin film. Therefore, there is an ongoing demand for new, practical, and cheap methods.

1.1.2. Soft-Templating Method

The soft-templating method, as the name implies, is based on the use of molecular/block-copolymer surfactants. [43] This method has been utilized for many mesoporous materials, including the first examples. In the first step of this method, a

surfactant is mixed with a proper solvent to obtain a micellar structure that forms when the surfactant concentration reaches a critical value, known as critical micelle concentration (CMC). Further increasing the surfactant concentration in the media leads to the formation of a lyotropic liquid crystalline (LLC) mesophase (see later). The inorganic species are mixed in the LLC phase to obtain mesostructured material. The template (surfactant) is then removed through either calcination[44] or solvent extraction[45] to get mesoporous material. Figure 1.2 illustrates the schematic representation of the steps of this method.

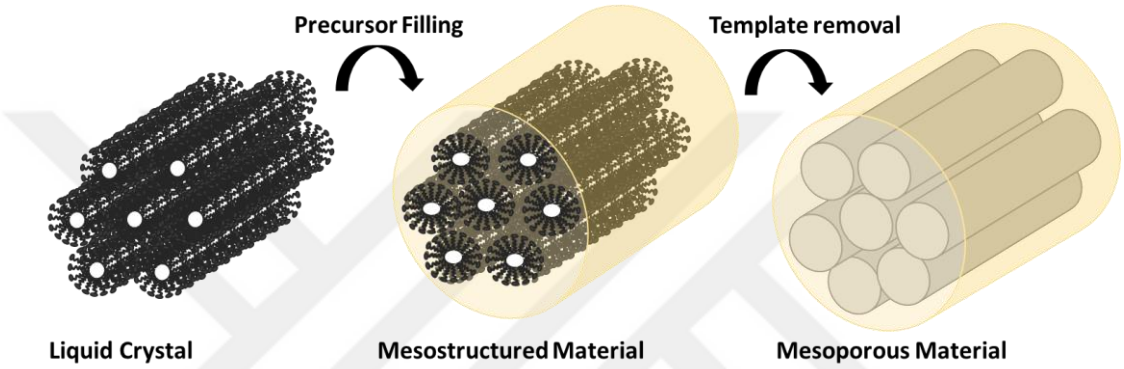

Figure 1.2: Schematic representation of the soft-templating method.

The first example of mesoporous silica was synthesized by Kresge in 1992 using surfactants (quaternary ammonium surfactants, like CTAB) that are considered to be a soft template. [5] The first examples of ordered mesoporous metal oxides were synthesized using both cationic and anionic surfactants as a soft template in 1994 by Huo et al. [9] This method was also utilized to produce ordered mesoporous titania[16], Nb_2O_5[46], ZrO_2[47], and VO_x. [48]

In 1999, Brinker and co-workers published one type of soft templating method that enables the rapid fabrication of ordered mesoporous films or powders. [49] They utilized CTAB as a template and demonstrated the formation of ordered mesostructure through the evaporation of a water/ethanol mixture as a solvent. As the evaporation of the solvent, the concentration of surfactant and other polymerizing ingredients in the media increase, leading to the formation of an LLC phase or mesostructured semi-solid. This method is named as evaporation induced self-assembly (EISA). Typically, dip-coating is employed as a coating method after the inorganic species are mixed with the surfactant and solvent. The use of a non-aqueous or water/alcohol mixture as a

solvent provides a control for the hydrolysis, condensation reaction, and processing to coat over a flat surface. This method is highly advantageous to fabricate ordered mesoporous monoliths and thin films. [50], [51] Like in all soft-templating methods, in the last step of the EISA process, the surfactant templates are removed by chemical or heat treatments.

When comparing hard- and soft-templating methods, both have their respective advantages and disadvantages. The hard templating method allows the synthesizing a mesoporous material with a high surface area in powder form. However, it is a costly method, and there can be some problems during the removal of the template that requires an acidic (HF) or a basic (NaOH) solution. [52] On the contrary, the soft templating method allows control at the macroscopic level. Still, it can also lead to some problems during the removal of the template (undesired residues or collapsing the pores). [53]

The EISA process comes with its own set of disadvantages; evaporation time can lead to extended waiting periods. Otherwise, if a fast removal is applied, it can end with a solidification of precursors or a disordered mesostructure. Additionally, this method is limited to certain metal precursors (specifically the metal alkoxides). Therefore, it is necessary to design new synthetic approaches for the fabrication of desired materials with practical applications.

1.1.3. Molten Salt-Assisted Self-Assembly (MASA) Method

There are always some challenges in producing mesoporous materials using well-known methods. Many transition metal salts remain stable in their solution form, and it is hard to make them undergo a hydrolysis/condensation reaction and assemble them in the mesostructure form. A new method, known as the molten salt-assisted self-assembly (MASA) method, was discovered in 2011 by Dag *et al.* to fabricate mesoporous materials with an ordered structure and high surface area. [54] In this approach, the salt species used act as a secondary solvent, meaning they remain in the molten phase between the micellar structures formed by surfactant species. Typically, two surfactants are used in this process: one non-ionic ($C_{12}EO_{10}$ (10-lauryl ether) or pluronics (P65, P85, P103, or P123)) and one charged (CTAB) surfactant. The reason for the usage of charged surfactant is to provide stabilization in the mesophase. The

charged part of the surfactant can balance the charge balance in the interface of salt-surfactant in the mesophase so that it can accommodate very high salt concentrations. In the first example of mesoporous material fabricated by the MASA approach, it was demonstrated that an extensive amount (53-mole percent) of transition metal salts (cadmium and zinc nitrate salts) could be confined between the silica walls and the surfactants domains (10-lauryl ether and CTAB) in a molten phase (secondary solvent). This mesostructured phase was converted to mesoporous CdO/SiO_2 and ZnO/SiO_2 thin films (about 1.6 nm thick layers of metal oxides over the silica pore-walls) through a calcination process. [54] Later, the same method was extended to synthesize many mesoporous metal titanate[55]–[57] (including $CdTiO_3$, Zn_2TiO_4, $CoTiO_3$, $MnTiO_3$, and $Li_4Ti_5O_{12}$), metal sulfide and selenide[57], metal oxide (NiO)[25], lithiated metal oxide ($LiCoO_2$, $LiMnO_2$, $LiMn_{2-x}Co_xO_4$)[58], [59], and metal cobaltite ($MnCo_2O_4$, $NiCo_2O_4$ and, $ZnCo_2O_4$)[18] thin films.

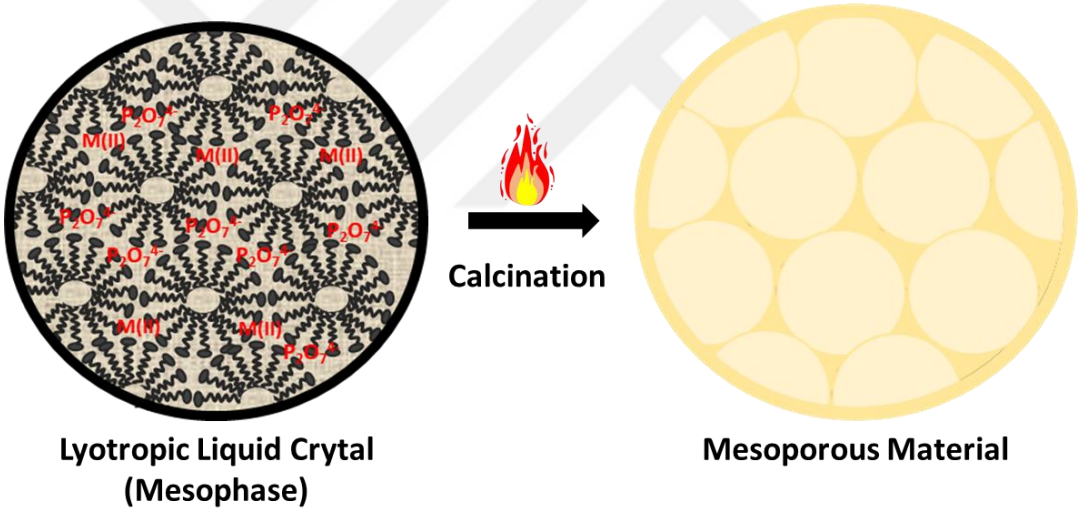

Figure 1.3: Schematic representation of the MASA method.

The most important feature of the MASA approach is that the species form a molten phase among the micelle domains and act as a secondary solvent, where the primary solvent can be either water, ethanol, or a mixture of both. Initially, a solution of the ingredients is coated over a substrate to generate the ordered LLC mesophase. Subsequently, the surfactants are removed by a thermal treatment (burned out, leaving the pores behind), resulting in the fabrication of mesoporous materials, see Figure 1.3. The MASA process distinguishes itself from the EISA method due to the uniqueness

of the LLC mesophase with a relatively high concentration of salt/surfactant. Furthermore, in the EISA process, mesostructured solid forms immediately during the evaporation step, which limits the metal alkoxides since they can undergo hydrolysis and condensation reactions. However, MASA yields a highly stable LLC mesophase with the aging of the gel phase. Further heating steps are required to obtain mesostructured or mesoporous materials. Unlike the EISA approach, there are no limitations in the metal precursors for this process; it is more applicable for those precursors that can undergo hydrolysis and condensation reactions in the EISA process. Note also that the MASA method gives an opportunity to control the thickness of the films by adjusting the concentration of an original solution of ingredients. It can be applied with various coating techniques, including spin-coating, drop-cast coating, dip-coating, and spray coating.

1.2. Lyotropic Liquid Crystalline Mesophases

The liquid crystal (LC) phase is considered the fourth phase of matter, which has behaviors between liquid and solid phases. Since the LC phase has some degree of ordered structure like solid and fluidity like liquid phases, it is called mesophase, as depicted in Figure 1.4. [60] The mesophases exhibit a higher degree of order and orientation compared to liquids, and they maintain greater mobility than solid phases.

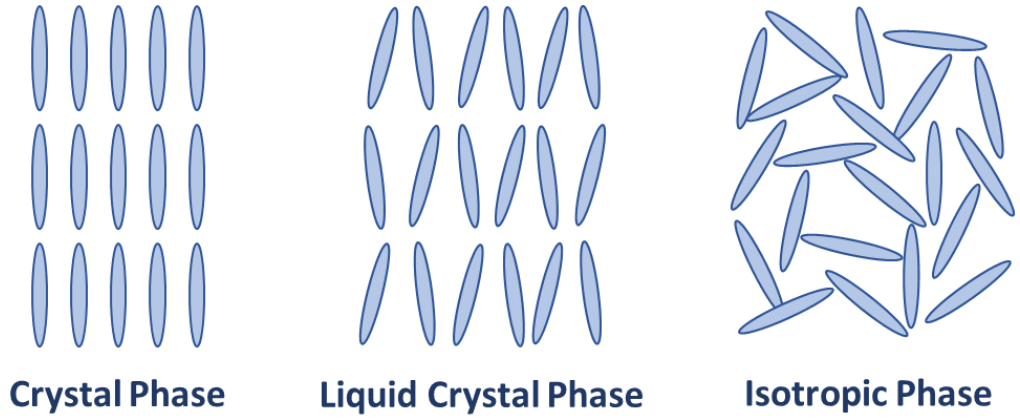

Figure 1.4: Schematic representation of (left) crystal, (middle) liquid crystal, and (right) isotropic phases.

Two significant LC mesophases exist: thermotropic liquid crystals (TLC) and lyotropic liquid crystals (LLC). TLC undergoes phase transformation as the temperature changes in an exact temperature range. [61] This phase transition is independent of the concentration gradient. On the other hand, the LLCs are formed by dissolving surfactants in a solvent within a particular concentration and temperature range. [62] This thesis will primarily focus on analyzing lyotropic liquid crystalline (LLC) mesophases of surfactant (P123) with an acid ($H_4P_2O_7$) and transition metal salts. Surfactants consist of a long hydrophobic tail group and a polar hydrophilic head group called amphiphilic molecules. The hydrophilic head can be either neutral (like pluronics or 10-lauryl ether) or charged (cationic like CTAB or anionic like sodium dodecyl sulfate (SDS)) molecules. [63], [64] With the help of the attractive and repulsive forces between those tail and head groups, the micellar structure is formed by the aggregation of the surfactant molecules with a hydrophilic shell and hydrophobic core. The specific structure formed depends on the type of solvent. There is an optimum surfactant-to-solvent ratio at which micellar structure form, namely CMC. Below this concentration, the surfactant molecules are solvated and exist as individual molecules. Evaporation of the excess solvent facilitates the assembly of the micelles into an ordered LLC phase. Depending on the type and concentration of the surfactant, the structure of the mesophase can be hexagonal, cubic, and lamellar, which are the most common phases. Figure 1.5 provides the schematic representations of a micelle and structures of the common mesophases. Lamellar mesophase results from the bilayer structure of surfactants, where the hydrophobic tails are aligned head-to-head, and the hydrophilic heads are pointed out where the solvent molecules reside. It is possible to analyze this phase under a polarized optic microscope (POM) since it has a distinct texture (often referred to as an oily streak). [65] The hexagonal mesophase is formed by the packing of micellar structures in the hexagonal arrangement. This phase exhibits anisotropy, similar to the lamellar structure, and is birefringent (meaning that the structure has two different refractive indices). As a result, it displays a characteristic ‘fan texture’ when observed under POM. [65] Unfortunately, the cubic mesophase cannot be analyzed using POM because it is an isotropic phase, meaning it has the same optical properties in every direction where the micelles align in the cubic lattice. [66] Another effective method to figure out the LLC mesophases is through small-angle XRD (x-ray diffraction) measurements. Since

the LLC mesophases are formed by micelles consisting of extremely larger building blocks than any molecular crystalline structure, they diffract at small angles (between 1 and 5°, 2θ) with large d-spacing values. The d-spacing values can be calculated by using Bragg's law:

$$n\lambda = 2d \sin\theta \qquad \text{eq. 1.1}$$

Where θ is the incident angle (°), d is the spacing of crystal planes (Å), λ is the x-ray wavelength (1.5406 Å for Cu K_α x-ray source), and n is the order and 1 in regular diffractometers. [67] With known d-spacing values, the diffracted planes can be indexed according to the structure of mesophase.

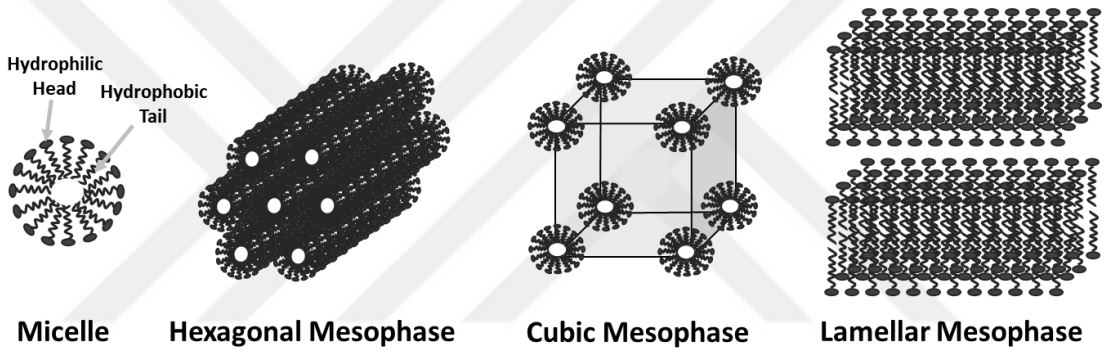

Figure 1.5: Schematic representation of micelle and different LLC phases.

The liquid crystalline phase was discovered accidentally by Friedrich Reinitzer in 1888 while studying natural organic compounds based on their melting behaviors. [68] Kresge et al. used the structural concepts of the LCs and proposed the liquid crystal templating method using quaternary ammonium surfactants to synthesize ordered mesoporous silicates in 1992. [6] In 1995, Attard et al. investigated the usage of liquid crystalline phases of non-ionic surfactants ($C_{12}EO_8$ and $C_{16}EO_8$) for the synthesis of mesoporous silica monoliths and thin films. [12] Alexandridis and co-workers also studied the LLC mesophases of pluronic P84 with water and oil as a solvent, and they showed nine different phases of LLC mesophases (for cubic, hexagonal, and lamellar) in their system. [69]

A new LLC mesophase was discovered by Dag et al. in 2001 by using salts as the second component of the mesophase. They used a non-ionic surfactant (10-lauryl

ether) with transition metal complex salts to obtain cubic and hexagonal LLC mesophases and showed the structural behavior of the new mesophases by changing the surfactant and salt mole ratios and temperature. [70] They also worked on the effects of anions of transition metals on the LLC mesophases. [71] In the later works, they searched the effects of different types of non-ionic surfactants. [72] The role of adding charged surfactant (for example, CTAB) as a second surfactant to the LLC system was also demonstrated with improved stability on the LLC at higher salt concentrations. [73] Usually, the salt/surfactant mole ratio can be as high as 20 for the stable LLC formed by P123. However, they showed that it could be improved by 2-5 times through the addition of a second surfactant, specifically a charged surfactant. [73] Moreover, it has been studied not only the small surfactants but also larger surfactants, like pluronic (tri-block co-polymers). [74]–[77] The same group has revealed essential fundamental knowledge in this field since 2001. [70] In these studies, one of the most valuable findings is the discovery of the secondary solvent of the salts, which helps to assemble the surfactant molecules in a liquid crystal phase. The salts are trapped in very small hydrophilic domains (a few nanometers), introducing a concept of the 'confinement effect'. The confinement effect helps to decrease the melting points of some salts in a small confined space. This phenomenon was published in 2011, and they showed that the melting point of zinc nitrate salt ($[Zn(H_2O)_6](NO_3)_2$) can be reduced to -52 ^oC within the LLC mesophase. [74] Another important milestone was enhancing the solubility of some salts using the confinement effect using lithium salts as a second component in the presence of some water. [75] In this investigation, the stable mesophases that keep the water/salt mole ratio at around 3 were illustrated for the first time without experiencing any phase separation. Since the conductivity of those LLC mesophases is relatively high, they are excellent candidates for use as a gel electrolyte in electrochemical applications. These two important features were combined with the concept of percent deliquescence relative humidity (DRH, at which the salt starts to capture moisture and dissolves completely). It is shown that this concept is the determining parameter in the formation of stable mesophases. [76] The mesophases formed by the salts having the lowest % DRH values (for example, Li(I), Ca(II), and Mg(II) salts) exhibited higher stability, whereas the salts with high % DRH values were found to be insoluble or leached out rapidly after the solution of the ingredients was coated. For the salts with intermediate % DRH

value (such as KSCN, NaI, and $NaClO_4$), the mesophases are stable only at very low salt concentrations or high water amounts that evaporate quickly, leading to the mesophase undergo phase separation. However, it was shown that the mesophase stability could be improved by increasing the alkyl chain length of the surfactant. [76] The LLC mesophases of the phosphoric and sulfuric acids, which have a high vapor pressure, were also demonstrated later using the concept of % DRH. [77], [78] It was discovered that the phosphoric acid and non-ionic surfactant molecules self-assembled into LLC mesophases and exhibited high proton conductivity, which can be used as proton-conducting gel electrolytes in energy applications. [78] Similarly, a strong acid (H_2SO_4) and non-ionic surfactant formed ordered LLC mesophases with various structures (cubic or 2D-hexagonal) having a high proton conductivity. Moreover, with the help of the acidity of sulfuric acid, carbon quantum dots were produced by carbonization in the LLC mesophase. [77] With the discovery of the MASA approach, many ordered LLC mesophases were synthesized, and with further calcination methods, they were converted to mesoporous materials, as mentioned in the MASA process section.

1.3. Metal Phosphates and Pyrophosphates

Metal phosphates[79]–[86] and metal pyrophosphates[87]–[97] have been extensively studied by numerous research groups over the years due to their importance in energy production and storage applications (such as battery and supercapacitor materials). The phosphates have a high diversity in their chemistry. Since synthesizing those materials is a complex process, one should give importance to achieving the appropriate synthesis conditions and preventing impure or mixed phases during the synthesis. Although the first mesoporous silica was synthesized in 1992, and thousands of studies have been carried out for this material, there is still work on synthesizing mesoporous silica. A similar effort needs to be given to the phosphates in terms of the synthesis conditions and control over the properties of the chemistry behind them to have promising advancements in their applications.

1.3.1. Metal Phosphates

In 1997, Padhi and his co-workers investigated materials that were cost-effective and environmentally friendly candidates for the rechargeable lithium batteries as the cathode. [79] They showed the intercalation/decalation process of Li^+ ion in $LiFePO_4$ material at 3.5 V vs. lithium at 0.05 mA/cm^2. [79] They also mentioned that the introduction of Mn(II) into the lithium iron phosphate system created an additional reaction and displayed lithium intercalation/deintercalation at 3.4 V and 4.1 V vs. lithium for the Fe^{3+}/Fe^{2+} and Mn^{3+}/Mn^{2+} couples, respectively. Since the charge capacity of those materials ($LiMnPO_4$) was around 170 mAh/g, they attracted many researchers to develop new synthesis methods. [84], [98], [99] The appeal of the olivine structure (with space group Pnma, where the oxygen atoms are hexagonal-close-packed stacking order, phosphorus atoms occupy tetrahedral sites, transition metals, and lithium atoms located at octahedral position) of lithium metal phosphates, where the metal can be Fe, Mn, Co, and Ni, stems from their unique features as high-potential cathode materials for rechargeable Li-ion batteries. [22], [100]

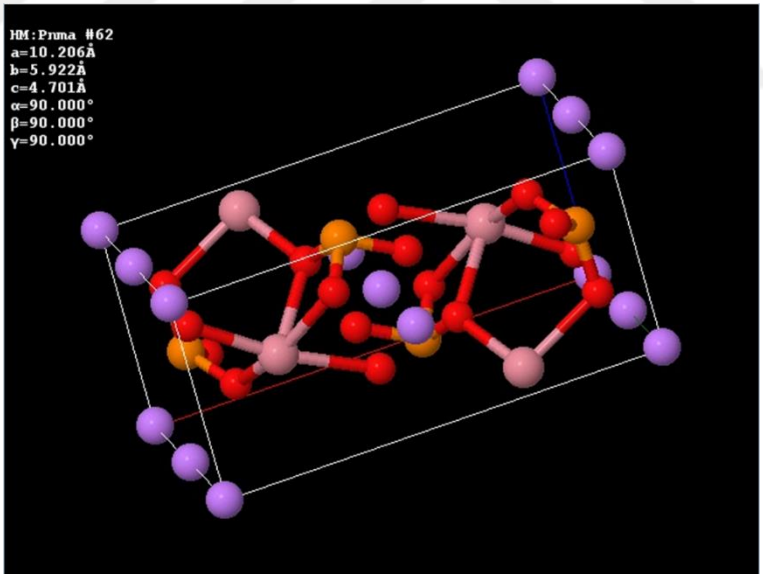

Figure 1.6: Unit cell of olivine phase (orthorhombic) of $LiCoPO_4$.

Making these materials mesoporous brings lots of new advantages: 1) The intercalation/decalation process of lithium-ion becomes more prominent since the transformation of the material takes place in smaller channels; 2) the diffusion of the Li-ion will be easier, resulting in the intercalation/decalation process more efficient

and rapid with the help of the porous morphology; 3) the connection between electrode and electrolyte will be increased due to the high surface area enhancing in the Li-ion flux through an interface. [22], [81], [82], [85], [101]–[104]

The methods that were used for the synthesis of mesoporous silica may not always be applicable for the metal phosphates or pyrophosphates due to the fast reaction between the metal ion and phosphate ion that results in the precipitation of large particles instead of self-assembling into an ordered mesostructure. To control the kinetics of this reaction, phosphoric acid or pyrophosphoric acid as a phosphate precursor could be the solution to this problem. [22], [78], [103] In 2018, mesoporous vanadium phosphate nanosheets, which is a supercapacitor material, were reported for the first time with a liquid crystal templating method using P123 as a surfactant and phosphoric acid as a phosphate precursor. The mesoporous vanadium phosphate displayed a less-ordered mesostructure after calcination with an 18 m^2/g surface area but exhibited 767 F/g specific capacitance at 0.5 A/g. [103] In 2019, Uzunok et al. published the first examples of synthesizing mesoporous lithium transition metal (Mn, Fe, Co, and Ni) phosphates using an LLC templating method, again using phosphoric acid to have kinetic control over the formation. [22] The mixture of nitrate salts of lithium and transition metals, phosphoric acid, and surfactant (P123) is spin-coated or drop-cast coated over a substrate to form ordered LLC mesophases, then further calcined to synthesize the first examples of mesoporous lithium metal phosphates, which are in the olivine structures having a surface area as high as 79 m^2/g.

1.3.2. Metal Pyrophosphates

Having a limited number of synthesis methods is also valid for the mesoporous metal pyrophosphates. However, in recent years, metal pyrophosphates, especially $Ni_2P_2O_7$, $Co_2P_2O_7$, and $Mn_2P_2O_7$, have been the materials of interest in the field of catalysts and energy storage applications due to their low cost, electroactivity, extensive working potential range, reversibility, conductivity, and superior properties for energy storage. In terms of chemical stability and offering much space for the travel of ions in the medium, they are better candidates for application in those fields than their phosphates. [87]–[97]

In 2012, Pang et al. synthesized $NH_4MnPO_4 \cdot H_2O$ micro-nanostructures without using any template and converted them into porous micro-nanostructured manganous pyrophosphate ($Mn_2P_2O_7$) by thermal decomposition. [97] They showed that those materials could be used as an electrochemical capacitor, but they reported relatively low specific capacitance values for the $NH_4MnPO_4 \cdot H_2O$ and $Mn_2P_2O_7$ materials (31 and 35 F/g, respectively). Later, in 2013, the same group synthesized the cobalt pyrophosphate by the same method (thermal decomposition of $NH_4CoPO_4 \cdot H_2O$) and demonstrated that the electrode of $Co_2P_2O_7$ exhibited a much higher specific capacitance (367 F/g at 0.625 A/g current density in 3.0 M KOH solution) and also kept the 96.2% of capacitance even after 3000 charge-discharge cycles. [96] This value was improved to 525 F/g at 0.625 A/g by changing the electrolytes by Wang et al. [105] In 2015, Pang and co-workers continued to synthesize metal pyrophosphates using $NH_4NiPO_4 \cdot H_2O$ precursor and obtained an amorphous nickel pyrophosphate. [106] They tested the nickel pyrophosphate as a flexible solid-state electrochemical energy storage device with KOH-polyvinyl alcohol as a solid-state electrolyte. The specific capacitance was also measured in 3.0M KOH solution as 1050 F/g at a 0.5 A/g current density. In the same year, the porous sodium-doped $Ni_2P_2O_7$ tablets with a hexagonal shape having a surface area of 190 m^2/g with a pore size of 2-4 nm were fabricated by simple hydrothermal method and examined the behavior as a flexible solid-sate hybrid supercapacitor in a 3-electrode system using 3.0M NaOH as an electrolyte and displayed 557.7 F/g at a current density of 1.2 A/g. [95] They proved that the porous structures make accessing the ions in the electrodes easy, which is a suitable property for those working on redox reactions. The preparation of $Ni_2P_2O_7$ material in the form of grain-like particles using a different technique (coprecipitation) was suggested by Senthilkumar et al., who explored the usage of this material as a cathode material for hybrid supercapacitors, where the anode material was highly porous graphitic carbon (with a surface area 1254 m^2/g) with a maximum 1893 F/g at a current density of 2 A/g in a sodium-based electrolyte. [90] The electrodes, both anode, and cathode, were prepared by mixing the active material with super P carbon black, PVDF (polyvinylidene difluoride) with the percentages of 75:20:5, respectively, in an organic solvent (N-methyl-pyrrolidone) to obtain a slurry in order to coat it on carbon paper prior to the measurements. In 2016, Chen and his group invented the incorporation of two transition metals in the pyrophosphate system,

which offered a unique and impressive method to develop the electrochemical performance of those materials in supercapacitor applications. [88] By adjusting both ratios of Co-Ni species and calcination temperature, the amorphous phase Co-Ni pyrophosphate electrodes were fabricated using a similar slurry method and used in the electrochemical measurements. They found out that the material that had a 1:4 ratio of Co:Ni ($Co_{0.4}Ni_{1.6}P_2O_7$) upon calcination at 400 ^oC displayed the highest specific capacitance (1259 F/g at 1.5 A/g), which is higher than their pure phases (790 and 510 F/g at 1.5 A/g for $Ni_2P_2O_7$[106] and $Co_2P_2O_7$[105], respectively). However, it was still lower than the study of Senthilkumar et al. (1893 F/g at 2 A/g). This difference has been devoted to different crystal sizes and synthetic methods. Further, in 2018, Sankar et al. reported for the first time the synthesis of structurally robust binder-free nickel pyrophosphate nanorods grown on Ni foam by the hydrothermal method. It was as a cathode material for novel hybrid supercapacitors consisting of capacitive type n-doped reduced graphene oxide as an anode material in an aqueous redox-added electrolyte ($K_3[Fe(CN)_6]$ was added to 1 M KOH solution) which provided a better electrolyte diffusion at a reasonable rate. [92] The one-dimensional (1D) nanorods had a hexagonal shape with a diameter of 60–135 nm and a length of 22–28 μm with smooth surfaces. 1D nanorods of $Ni_2P_2O_7$ displayed a maximum specific capacitance of 8120 mF/cm^2 at 5 mV/s. Based on the CV (cyclic voltammetry) measurements, they also mentioned that the 1D nanorods of $Ni_2P_2O_7$ stored almost all charges based on a diffusion-controlled battery-type process instead of a capacitive one. They calculated the b values in the equation of $i_p=av^b$ (see the details later) at around 0.5, corresponding to a diffusion-controlled process, depending on the amount of redox-additive. The same idea (redox-additive) by Khan et al. was also applied for the improvement of capacitive behaviors (the specific capacitance value was enhanced from 286 F/g to 580 F/g with the additive) of the $Co_2P_2O_7$ nanosheets. [89] Zhang and his colleagues showed the growth of $Ni_2P_2O_7$ nanoarrays on a conductive substrate, Ni foam, to enhance conductivity during the electrochemical applications. The nanoarrays were decorated with C_3N_4 (carbon nitride), which has unique properties like good chemical and thermal stability, to increase the stability of the nickel pyrophosphate during long charge-discharge cycles. [107] The capacitance values were measured as 862 mF/cm^2 at 2 mA/cm^2 with retaining 91% stability after 1000 charge-discharge cycles when an asymmetric supercapacitor (ASC) was constructed using active carbon as negative and

$Ni_2P_2O_7$ nanoarrays decorated by C_3N_4 as positive electrodes Zhou *et al.* (in 2019) prepared porous nickel pyrophosphates nanowires by applying a chemical bath and solvothermal processes to the precursor of $NH_4NiPO_4 \cdot H_2O$, followed by a calcination process. [87] The BET surface area of the nanowires was reported to be 41 m^2/g with a 2.8 nm pore size, which belongs to the mesoporous category. The specific capacitance became much higher due to the porous structure of nanowires, which can lead to effective diffusion through the pores for the ions in the electrolyte. The ASC was constructed using porous $Ni_2P_2O_7$ nanowires as a positive electrode and carbon nanotubes as a negative electrode in a PVA/PAAS/KOH (polyvinyl alcohol/sodium polyacrylate/potassium hydroxide) gel electrolyte and a high specific capacitance of 772.5 F/g at 1 A/g was achieved. The incorporation of two transition metals for the synthesis of metal pyrophosphates was also tried by Wei et al. in 2019. [91] They formed porous sodium-doped $Ni_2P_2O_7$-$Co_2P_2O_7$ (with a surface area of 45 m^2/g) with a uniform bowknot structure by a hydrothermal route with a guiding reagent of sodium tartarate. The porosity and the synergistic effect between the two metals improved the electrochemical performances. They reached a capacity value of 295.2 C/g (equal to 738 F/g since the potential window was 0.4 V) at a 2.0 A/g current density. Moreover, they built an ASC device using activated carbon as an anode material. Matheswaran et al. in 2020 synthesized binder-free 1D nanograsses of $Ni_2P_2O_7/Co_2P_2O_7$ nanocomposites grown on a conductive substrate, nickel foam, through a hydrothermal method without any surfactant at various processing temperatures (100, 140, 180, and 220 ◦C). [93] They compared the temperature effect on the cycling ability. They concluded that the $Ni_2P_2O_7/Co_2P_2O_7$ nanograsses prepared at 140 ◦C exhibited enhanced performance in the cycling while preserving the morphology in compassion with other samples. In the same year, the rose-shape cobalt pyrophosphates were illustrated by Zhang et al. [94] The solvothermal method was used for the fabrication of the material by controlling the calcination temperature (above 600 ◦C) of a series of poly-porous structures. Since the calcination temperature of the material was very high, the rose-shape cobalt pyrophosphates were obtained as a highly crystalline alpha phase of $Co_2P_2O_7$. Very recently (in 2021), Padhy and co-workers claimed that they reported the highest capacitance values of cobalt pyrophosphate (a composite with partially graphitized carbon) from open-framework cobalt phosphite as of a 900 F/g capacitance. [108] Priyadharshini *et al.*, in 2022, synthesized the nickel

pyrophosphates with surfactant-dependent self-organization (soft-templating method). [109] They tested the effect of non-ionic and ionic surfactants on the structure, morphology, and, most importantly, electrochemical properties. They achieved better capacitive performance with the CTAB-assisted (since the electrostatic stabilization from CTAB lasts longer than the others) $Ni_2P_2O_7$ with 250 F/g at the current density of 2 A/g.

Since this thesis will primarily focus on the $Ni_2P_2O_7$, $Co_2P_2O_7$, $Mn_2P_2O_7$, and binary metal pyrophosphate, most examples are on those transition metals. Among them, $Ni_2P_2O_7$ is the most attractive to many researchers in this field due to its higher capacitance than $Co_2P_2O_7$ and $Mn_2P_2O_7$, even though it is isostructural with them. [110] Besides them, $Fe_2P_2O_7$ [111]–[113] (due to high chemical stability), $Cu_2P_2O_7$ [114], [115] (due to good reversibility), TiP_2O_7 [116], [117] (due to redox-active behavior), $Zn_2P_2O_7$ [118] (due to high electrical and thermal conductivity) have also been studied widely in this field.

The structures can be variable depending on the synthesis method and calcination temperature of metal pyrophosphates. Generally, the materials prepared at low temperatures exist as their alpha phases, where the space groups can be B21/c or P21/c. High temperatures can lead to phase transition from alpha to beta phase having C2/m or A2/m space group. Figure 1.7 shows some phases of metal pyrophosphates for Ni, Co, and Mn metals.

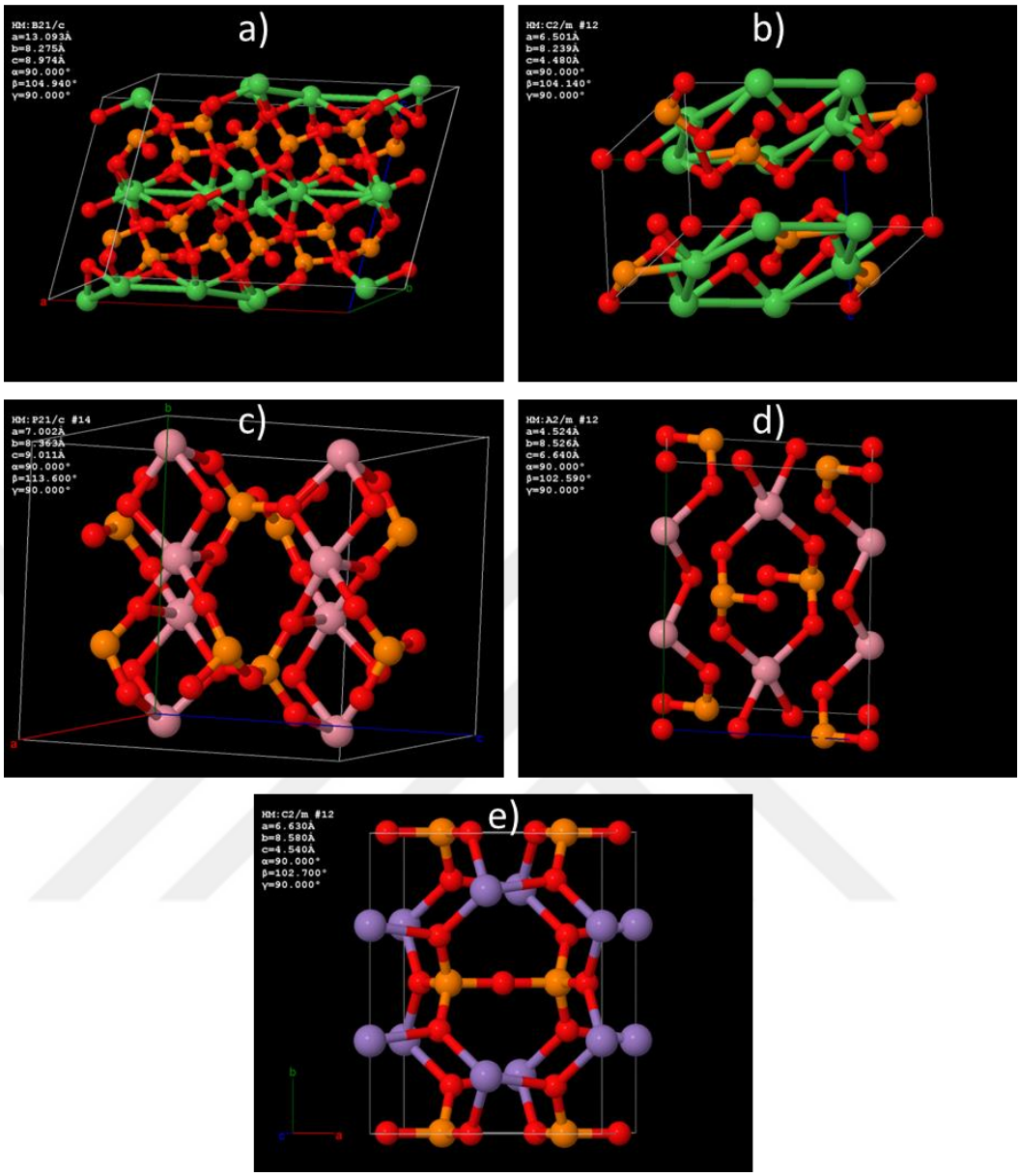

Figure 1.7: Crystal structures of a) α-$Ni_2P_2O_7$, b) β-$Ni_2P_2O_7$, c) α-$Co_2P_2O_7$, d) β-$Co_2P_2O_7$, and e) β-$Mn_2P_2O_7$.

In general, the pyrophosphate-based electrodes were reported that during the electrochemical measurements, the $M_2P_2O_7$ material oxidized to the $M_2P_2O_7(OH)_2$ compound where M^{2+} goes to M^{3+} in the first oxidation step and further oxidized to $M_2P_2O_7(O)_2$ (M^{4+}). However, this mechanism is completely wrong and misleading (see later from our findings in the results and discussion section). Since the analysis after electrochemical measurements is not easy for many researchers due to mixing the electroactive materials with many additives, they missed a critical point. The electrodes of pyrophosphate are extremely unstable in the alkaline medium, and they

are converted to their hydroxides. Almost all electrochemical measurements in the literature were performed in very basic solutions (generally 3 M KOH or NaOH), which is more than enough to convert the pyrophosphates to their hydroxide species. This thesis will be the first example of this transformation and introduce a new method to synthesize metal hydroxides.

1.4. Metal Hydroxides

Due to their fast and reversible redox reactions, transition metal hydroxides have been widely investigated as electrode materials for supercapacitors. In this field, nickel and cobalt hydroxides are the most attractive materials since they display very high specific capacitance due to their layered structures with large interlayer spacing. [119], [120] The metal hydroxides have two different phases: alpha and beta (see Figure 1.8). The alpha and beta phases are differentiated by their interlayer spacings where the α-$Ni(OH)_2$ has a d-spacing of 8.0 Å corresponding to the (001) plane and β-$Ni(OH)_2$ with a 4.6 Å layer-layer separation. This difference is almost identical for the alpha and beta hydroxides (alpha is >7 Å, dependent on intercalated anions, and beta is 4.6 Å). [121], [122] Since the layer-layer separation is high in the alpha phase, it crystallizes with additional water molecules between the layers. The material has a formula of α-$M(OH)_2 \cdot xH_2O$ (M is cobalt or nickel) where x is the degree of hydration varied in a range of $0.41 \leq x \leq 0.7$, but generally, it is not preferred to use the formula of intrinsically hydrated material like this; instead it is denoted as only α-$M(OH)_2$. [123]

Both alpha and beta phases are favorable materials for electrochemical applications, but the alpha phases of nickel and cobalt hydroxides display higher specific capacitance with the help of accessibility of the structure for redox reactions, and they are promising materials as oxygen evolution catalysts. [124], [125] However, the alpha phase is not stable under alkali media and transforms into the beta phase. Since the preparation methods and the morphology of the end product affect the supercapacitive performances, chemical, hydrothermal, and electrodeposition methods have been employed to synthesize different morphologies like mesoporous nanowires, flowerlike shapes, nanocone arrays, coral-like shapes, and nanoflakes. [120], [124], [126]–[132]

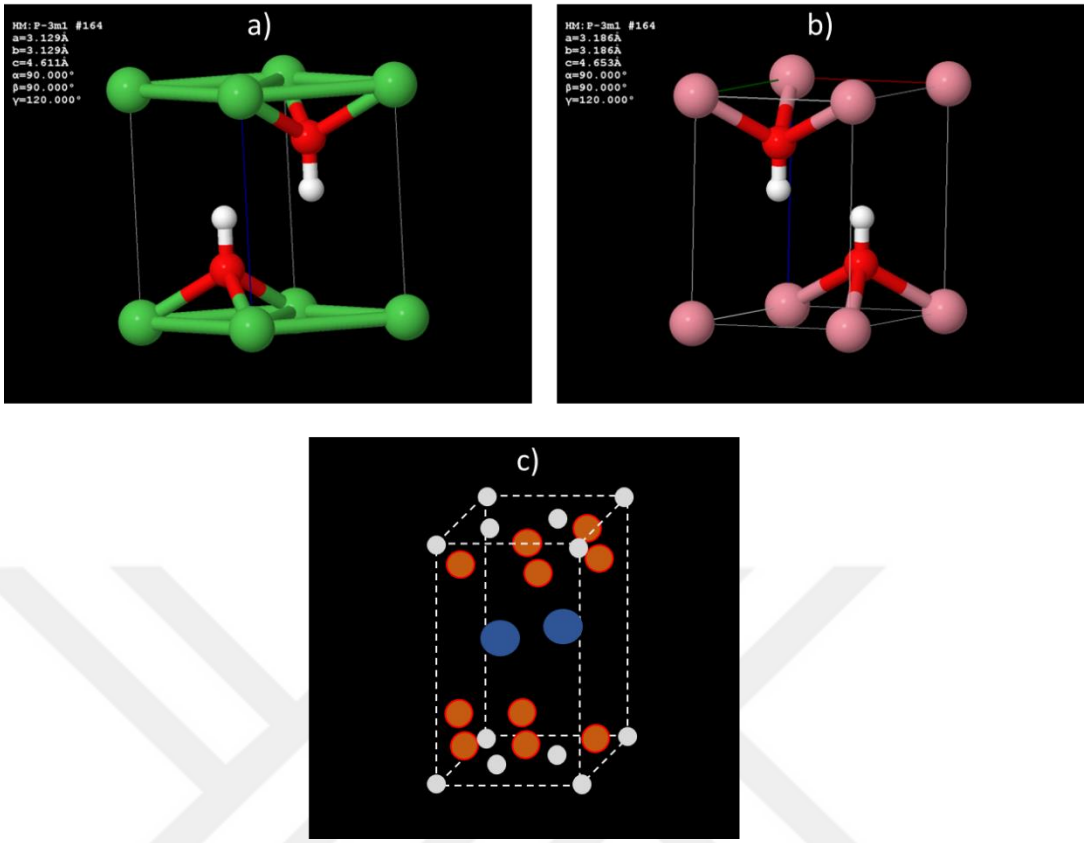

Figure 1.8: Crystal structures of a) β-$Ni(OH)_2$ (green-Ni, red-O, and white H), b) β-$Co(OH)_2$ (pink-Co, red-O, and white H), and c) α-$M(OH)_2$ (orange-M, white-O, and blue-H_2O).

1.5. Electrochemical Background

There are some techniques to analyze the electrochemical performance of the materials. Cyclic voltammetry and galvanostatic charge-discharge (GCD) measurements are the most popular ones to characterize the materials having battery or capacitive behaviors, which were used to analyze the synthesized materials in this thesis.

1.5.1. Cyclic Voltammetry

Cyclic voltammetry (CV) is one of the powerful and popular electrochemical techniques used to investigate materials in various electrochemical applications. It provides valuable insights into the redox features, adsorption processes, and electron transfer reactions. The CV curve is generated by linearly sweeping the potential over time at a desired scan rate while recording the current. Either single or multiple CV curves can be collected depending on the analysis requirements. Generally (according

to IUPAC guidelines), the potential sweep typically starts from a negative voltage and progresses to a positive voltage to identify firstly the oxidation peak (oxidation of species) in the positive current side (anodic current), then the reduction peak in the negative current side (cathodic current) is obtained by reversing the potential sweep towards negative voltage by reducing the oxidized species in the cyclic voltammograms, see Figure 1.9 for an example of CV curve. CV is generally employed to determine the potential ranges of various redox processes and evaluate the efficiency of water oxidation reaction (WOR) (or oxygen evolution reaction (OER)). Furthermore, it is a convenient technique to determine the surface concentration and capacitance property and perform Tafel slope analysis for the electroactive materials. [133]–[135]

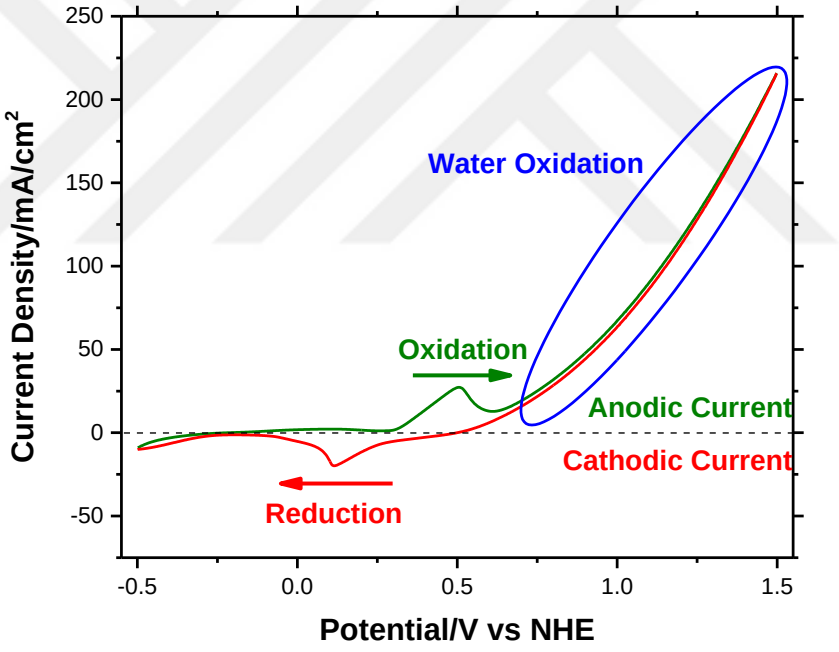

Figure 1.9: An example of cyclic voltammogram of $Ni_2P_2O_7$ electrode, recorded in 3M KOH solution using a 3-electrode system (Pt wire, counter electrode, Ag/AgCl, reference electrode, and graphite rod coated $Ni_2P_2O_7$, working electrode) at a scan rate of 50 mV/s.

The surface concentration of a working electrode, coated by redox-active species, can be evaluated using CV curves. During the oxidation-reduction processes, the electrolyte species can be adsorbed onto the active sites of the electrode surface. The current response of electrode-adsorbed species directly depends on the scan rate,

which controls the speed at which the applied potential window, see Figure 1.10. The surface coverage can be calculated based on this dependence using an equation derived from Nernst's equation, see eq. 1.2;

$$i_p = \frac{n^2F^2}{4RT}\nu A\Gamma \qquad \textbf{eq. 1.2}$$

Where i_p is the current at peak maxima (oxidation or reduction) (in A), n is the number of electrons transferred, F is the Faraday constant (96485 C/mol), R is the gas constant (8.3148 J/K·mol), T is the temperature (in K), ν is the scan rate (in V/s), A is the electrode area (in cm^2), Γ is the surface coverage (in mol/cm^2).

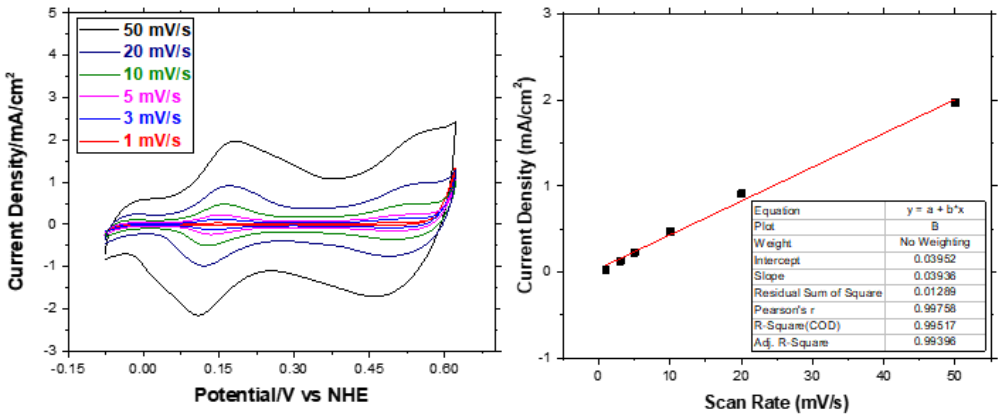

Figure 1.10: (Left) An example of scan rate-dependent CV curves of the $Co_2P_2O_7$ sample, which has a surface-adsorbed process, and (right) plot of oxidation current density of peak maxima at 0.15 V versus scan rate.

Since the current is linearly dependent on the scan rate, the equation above can be rewritten as in eq. 1.3. [136] The surface coverage of active species on the electrode surface can be quantitively calculated by linear fitting of the current versus scan rate data.

$$slope = \frac{n^2F^2A\Gamma}{4RT} \qquad \textbf{eq. 1.3}$$

From the scan rate-dependent analysis, it is also possible to determine how fast the applied potential should be scanned. Under a faster scan rate, a higher current

density is observed. This is due to a decrease in the size of the diffusion layer with a faster scan rate. Freely diffusing redox species involved in the electrochemically reversible electron transfer process can be expressed by the Randles-Sevcik equation, see eq.1.3. [134] This equation describes how the peak current increases with the square root of the scan rate.

$$i_p = 0.446nFAC^0\left(\frac{nF\nu D_o}{RT}\right)^{1/2} \qquad \textbf{eq. 1.4}$$

Where i_p is the current at peak maxima (oxidation or reduction) (in A), n is the number of electrons transferred, F is the Faraday constant (96485 C/mol), R is the gas constant (8.3148 J/K·mol), T is the temperature (in K), ν is the scan rate (in V/s), A is the electrode area (in cm^2), D_o (in cm^2/s) is the diffusion coefficient of the oxidized/reduced analyte, and C^0 (in mol/cm^3) is the bulk concentration of the analyte.

This equation can indicate that the mechanism of the redox reaction is a diffusion-limited process. The deviations from the linearity of i_p versus $\nu^{1/2}$ show either electrochemical quasi-reversibility or the process has both electron transfer of surface-adsorbed species and diffusion-limited process.

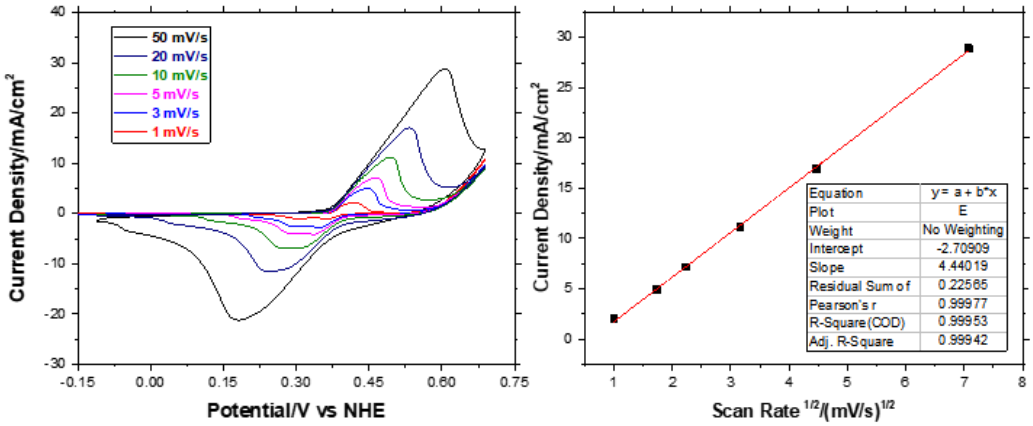

Figure 1.11: (Left) An example of scan rate-dependent CV curves of a $Ni_2P_2O_7$ sample, which has a diffusion-limited process, and (right) a plot of oxidation current density of peak maxima versus scan rate.

1.5.2. Capacitance

When a potential is applied to a metal plate or any other conductor, the charge is accumulated on the conductor. [137] Capacitance is the ratio of the total charge on the conductor to the potential difference, and the capacitance unit is Farad (F). Charge is the number of electrons passing in a circuit and expressed in the units of coulombs (C) (1 C equals 6.24×10^{18} electrons). Current is the rate of electron flow in a second, and the current unit is ampere (A), which is equivalent to C/s. Therefore, the charge can be expressed as a product of current and time. The specific capacitance is calculated by dividing the capacitance value by the amount of active material in the electrode. The equation is shown in eq. 1.5; [133]

$$C_s = \frac{It}{m\ \Delta V} \qquad \textbf{eq. 1.5}$$

Where C_s is the specific capacitance (in F/g), I is the constant discharge current (in A), t is the discharge time (in s), m is the amount of active material (in g), ΔV ($V_f - V_i$) is the potential range.

The capacitance or specific capacitance can be measured by performing galvanostatic charge-discharge (GCD) experiments using an electrochemistry setup. After determining the proper potential range for each particular sample, it is cycled with a known current density to investigate the charge-discharge ability and the capacity and capacitance values. Depending on the type of material, the shape of the GCD graph is varied. If the material has only capacitive behavior without any redox reaction, it is a triangle in shape. If there is a redox reaction in addition to the capacitive behavior, the triangle shape is distorted with some plateau regions originating from the redox couple, see Figure 1.12.

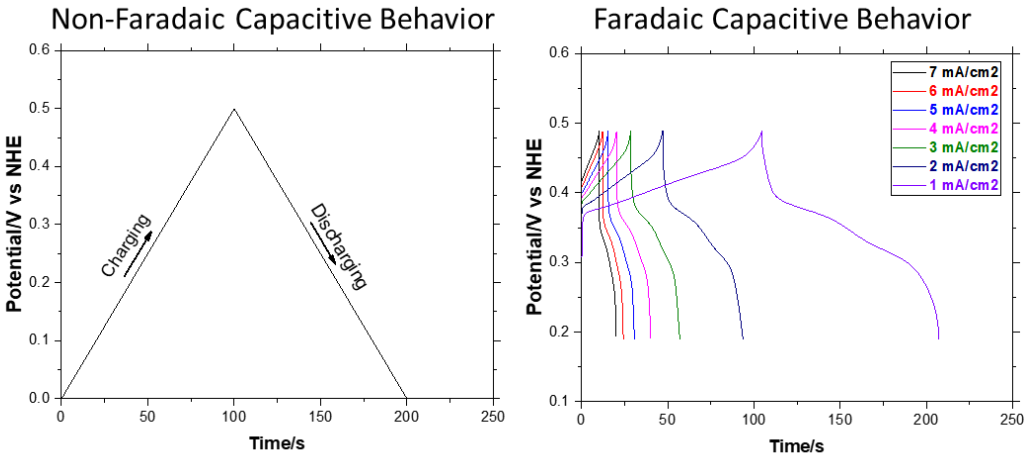

Figure 1.12: Examples of GCD graphs of (left) non-faradaic and (right) faradaic capacitive behavior.

CV curve is also helpful in determining the capacitance or specific capacitance values of the materials. Since the charge is equivalent to the current times time, this information can also be obtained from the CV curve. Since the capacitance is the quotient of the charge induced on the electrodes due to the potential difference between two electrodes and the difference in potential, it is possible to find the quantitative value using the area ($\int i \cdot dV$) of the CV curve, see Figure 1.13. [137] The specific capacitance of a material is the capacitance value over the catalytic load of that sample. The specific capacitance values can be evaluated from CV curves; [138]–[140]

$$C_s = \frac{1}{2\,m\,\nu\,\Delta V} \int i \cdot dV \qquad \textbf{eq. 1.6}$$

Where C_s is the specific capacitance (in F/g), m is the amount of active material (in g), ν is the scan rate (in V/s), ΔV ($V_f - V_i$) is the potential range of the CV curve (in V), $\int i \cdot dV$ is the polygon area of CV curve (in A·V).

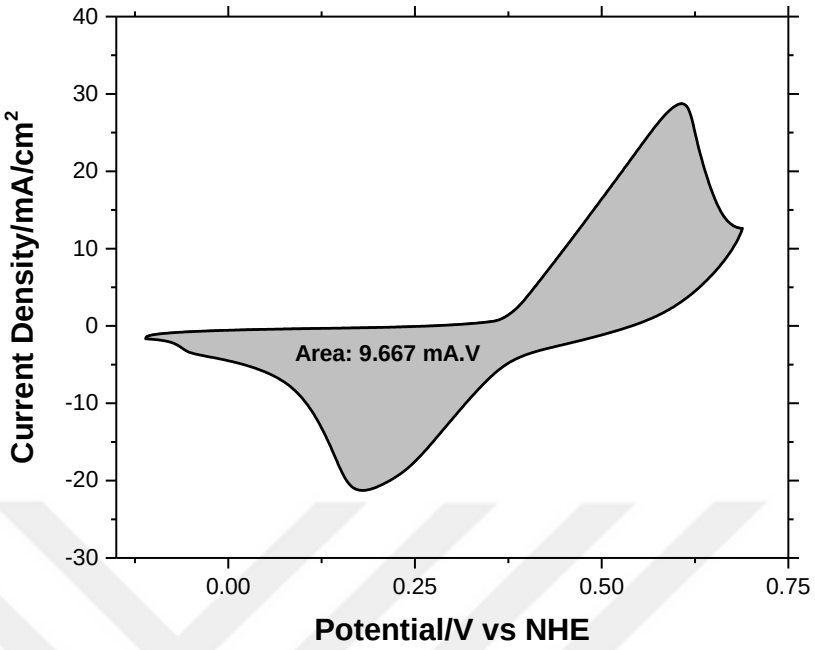

Figure 1.13: CV curve of $Ni_2P_2O_7$ sample at a scan rate of 50 mV/s with the calculated area.

1.5.3. Supercapacitor

Environmental and energy crises have become increasingly severe worldwide. Substantial research efforts have been devoted to designing energy storage materials by many researchers. [141], [142] Supercapacitors (SC) have been noticed as one of the most promising energy storage devices for fast and highly reversible storage and release of electrical energy.[143] SCs are novel energy storage devices that exhibit a higher specific capacitance and energy rather than traditional capacitors. [144] Moreover, in favor of better power efficiency and faster charge-discharge ability, SCs are more promising energy materials than batteries. For having the energy efficiency and displaying long term usage, the batteries are still promising materials. [32]–[37]

SCs can be classified into two sub-groups as pseudocapacitors (PCs) and electrochemical double-layer capacitors (EDLCs). They can be differentiated by charge storage mechanisms. The EDLCs are mainly obtained from carbon-based material without having electrochemical activity. There is no electrochemical reaction on the electrode while charging; instead, there are only physical charges at the interface between the electrode and electrolyte. [151], [152] Meanwhile, the PCs have

electrochemically active electrode materials. Since the PCs store charges based on redox reactions in the electrochemically active electrodes, they have higher specific capacitance than the carbon-based EDLCs. One efficient method is to obtain porous electrode materials to improve the capacitance, which requires materials with a larger surface area, higher conductivity, and controlled pore size. For this purpose, some porous active carbon material as a negative electrode and some electrochemically active electrode material as a positive electrode have been used for the asymmetric SCs.[153]

Compared to EDLCs, the materials which are electrochemically active have received more attention, like transition metal oxides (such as cobalt oxide, ruthenium oxide, and nickel oxide).[154], [155] Although ruthenium oxide has high capacitance, its high cost hinders expanded research in that field. Cobalt oxide and nickel oxides are ideal in terms of earth abundance. [153], [154]

A surfactant-assisted approach for the synthesis of mesoporous $M_2P_2O_7$ and $M_{2-x}M'_xP_2O_7$ would be a good solution as a high surface area is essential for energy storage materials. In this thesis, we are aiming to synthesize mesoporous $M_2P_2O_7$ and $M_{2-x}M'_xP_2O_7$ particles via a modified MASA method (since there is acid instead of charged surfactant) using related acid (phosphoric acid (H_3PO_4) or pyro-phosphoric acid ($H_4P_2O_7$)), salts ($[Mn(H_2O)_4](NO_3)_2$, $[Co(H_2O)_6](NO_3)_2$, $[Ni(H_2O)_6](NO_3)_2$) and surfactant (pluronic P123 (EO_{20}-PO_{70}-EO_{20})), and to show the characterization at each stage of the process.

Chapter 2

2. Experimental Section

2.1. Materials

Phosphoric acid (PA, 85-88% w/w), pyrophosphoric acid (PPA, ≥94%), manganese (II) nitrate tetrahydrate ($[Mn(H_2O)_4](NO_3)_2$, 97%), cobalt (II) nitrate hexahydrate ($[Co(H_2O)_6](NO_3)_2$, 98%), nickel (II) nitrate hexahydrate ($[Ni(H_2O)_6](NO_3)_2$, 99.9%), Poly(ethylene glycol)-block-poly(propylene glycol)-block-poly(ethylene glycol (PEO-PPO-PEO, Pluronic P-123, Mw~5800g/mol, 99.9%) were purchased from the Sigma-Aldrich.

All chemicals were used without further purification. Deionized water was obtained using a Millipore water purification system (18.2 MΩ·cm) to prepare aqueous solutions.

2.2. Preparation of M(II):Acid:P123 Solutions

Clear solutions of $[M(OH_2)_6](NO_3)_2$ (where M is Mn(II), Co(II), and Ni(II)): H_3PO_4 (PA) or $H_4P_2O_7$ (PPA): surfactant (P123) were first prepared in 10 ml of deionized water. The mole ratio of salts and acid was kept stoichiometric for $M_2P_2O_7$ (MPP) (with 1:X:Y mole ratios, where X and Y refer to the salts and acid to P123 mole ratio, respectively). The salt/P123 mole ratio has been varied from 10 to 100, by an

increment of 10 for the Ni(II):PPA:P123 solutions, whereas, in the rest of the metal salts, it is ranged from 30 to 90-mole ratio by an increment of 30, see Table 2.1.

For the binary metal systems, the total metal mole ratio is kept at 60, and two metals are changed by increment 10, see Table 2.2 for the compositions.

Table 2.1: Amounts of ingredients used for given molar ratios of the NiPP, MnPP, and CoPP solutions.

$Ni_2P_2O_7$;

Mole ratio /ingredients	P123	$[Ni(H_2O)_6](NO_3)_2$	H_3PO_4
1:30:30	1.000 g	1.517 g	0.600 g
1:60:60	1.000 g	3.034 g	1.201 g
1:90:90	1.000 g	4.552 g	1.804 g

Mole ratio/ingredients	P123	$[Ni(H_2O)_6](NO_3)_2$	$H_4P_2O_7$
1:10:5	1.000 g	0.506 g	0.155 g
1:20:10	1.000 g	1.011 g	0.310 g
1:30:15	1.000 g	1.517 g	0.465 g
1:40:20	1.000 g	2.022 g	0.619 g
1:50:25	1.000 g	2.528 g	0.774 g
1:60:30	1.000 g	3.034 g	0.929 g
1:70:35	1.000 g	3.540 g	1.084 g
1:80:40	1.000 g	4.045 g	1.239 g
1:90:45	1.000 g	4.552 g	1.394 g
1:100:50	1.000 g	5.067 g	1.548 g

$Mn_2P_2O_7$;

Mole ratio /ingredients	P123	$[Mn(H_2O)_4](NO_3)_2$	H_3PO_4
1:30:30	1.000 g	1.309 g	0.600 g
1:60:60	1.000 g	2.619 g	1.201 g
1:90:90	1.000 g	3.929 g	1.804 g

Mole ratio/ingredients	P123	$[Mn(H_2O)_4](NO_3)_2$	$H_4P_2O_7$
1:30:15	1.000 g	1.309 g	0.465 g
1:60:30	1.000 g	2.619 g	0.929 g
1:90:45	1.000 g	3.929 g	1.394 g

$Co_2P_2O_7$;

Mole ratio /ingredients	P123	$[Co(H_2O)_6](NO_3)_2$	H_3PO_4
1:30:30	1.000 g	1.518 g	0.600 g
1:60:60	1.000 g	3.037 g	1.201 g
1:90:90	1.000 g	4.555 g	1.804 g

Mole ratio/ingredients	P123	$[Co(H_2O)_6](NO_3)_2$	$H_4P_2O_7$
1:30:15	1.000 g	1.518 g	0.465 g
1:60:30	1.000 g	3.037 g	0.929 g
1:90:45	1.000 g	4.555 g	1.394 g

Table 2.2: Amounts of ingredients used for given molar ratios of the MnCoPP, NiCoPP, and NiMnPP solutions.

$Mn_{2-x}Co_xP_2O_7$;

Mole ratio/ingredients	P123	$H_4P_2O_7$	$[Mn(H_2O)_4](NO_3)_2$	$[Co(H_2O)_6](NO_3)_2$
1:50:10:30	1.000 g	0.929 g	2.183 g	0.506 g
1:40:20:30	1.000 g	0.929 g	1.746 g	1.012 g
1:30:30:30	1.000 g	0.929 g	1.310 g	1.519 g
1:20:40:30	1.000 g	0.929 g	0.873 g	2.025 g
1:10:50:30	1.000 g	0.929 g	0.437 g	2.531 g

$Ni_{2-x}Co_xP_2O_7$;

Mole ratio/ingredients	P123	$H_4P_2O_7$	$[Ni(H_2O)_6](NO_3)_2$	$[Co(H_2O)_6](NO_3)_2$
1:50:10:30	1.000 g	0.929 g	2.528 g	0.506 g
1:40:20:30	1.000 g	0.929 g	2.023 g	1.012 g
1:30:30:30	1.000 g	0.929 g	1.517 g	1.519 g
1:20:40:30	1.000 g	0.929 g	1.011 g	2.025 g
1:10:50:30	1.000 g	0.929 g	0.506 g	2.531 g

$Ni_{2-x}Mn_xP_2O_7$;

Mole ratio/ingredients	P123	$H_4P_2O_7$	$[Ni(H_2O)_6](NO_3)_2$	$[Mn(H_2O)_4](NO_3)_2$
1:50:10:30	1.000 g	0.929 g	2.528 g	0.437 g
1:40:20:30	1.000 g	0.929 g	2.023 g	0.873 g
1:30:30:30	1.000 g	0.929 g	1.517 g	1.310 g
1:20:40:30	1.000 g	0.929 g	1.011 g	1.746 g
1:10:50:30	1.000 g	0.929 g	0.506 g	2.183 g

Firstly, the metal salts are dissolved in a 3 ml of deionized water in a 20 ml vial. Then, melted surfactant (at 80 ^oC) and acid are mixed in a 7 ml deionized water in another vial until a clear homogeneous solution is obtained. This ensures the minimization of the highly concentrated acid effect on the metal salts. Dissolving all the ingredients takes about 3-4 hours. Then, both vials are combined and stirred for one more day to homogenize the mixtures, see Figure 2.1.

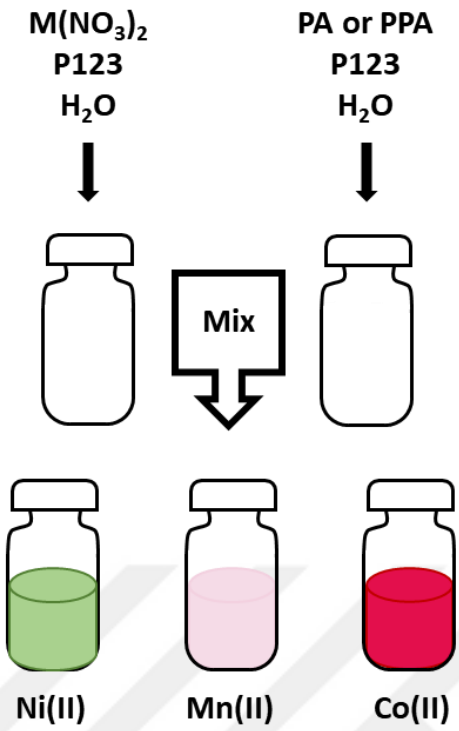

Figure 2.1: Schematic representation of solution preparation.

2.3. Preparation of M(II):Acid:P123 Mesophases

Above clear solutions are coated over glass substrates via either spin-coating (typically 2000 rpm for 10 sec for thin films) or drop-cast coating (for powders) methods to obtain LLC films or thicker gels, respectively. The spin-coated glass slides are directly used for the characterization or calcination process without aging the mesophases even for a while. In contrast, the drop-cast coating samples need a further process to evaporate the excess solvent in the samples on the glass substrate. After dropping a few droplets from the solution into the glass substrate, the excess solution is poured back into its vial, and the gel-like thin solution is spread over and fully covers the glass slide. Then, it is aged for some time (around 1-2 min) in a vertical position on the bench on a paper towel to obtain homogeneous thick films, see Figure 2.2. Then, the films are used for further treatments.

2.4. Synthesis of Mesoporous Metal Pyrophosphates (m-MPP)

Above gel-like films are directly calcined at 300 °C in a preheated oven for 1 h to produce mesoporous metal pyrophosphates (denoted as m-MPP) and annealed at higher temperatures (400, 500, 600, and 700 °C, denoted as m-MPP-X, where X is the annealing temperature in Celsius) in a ceramic cuvette for various purposes. The annealing time is 1 h for each calcination temperature. Then, the calcined samples are collected by scraping as a powder form for further analysis.

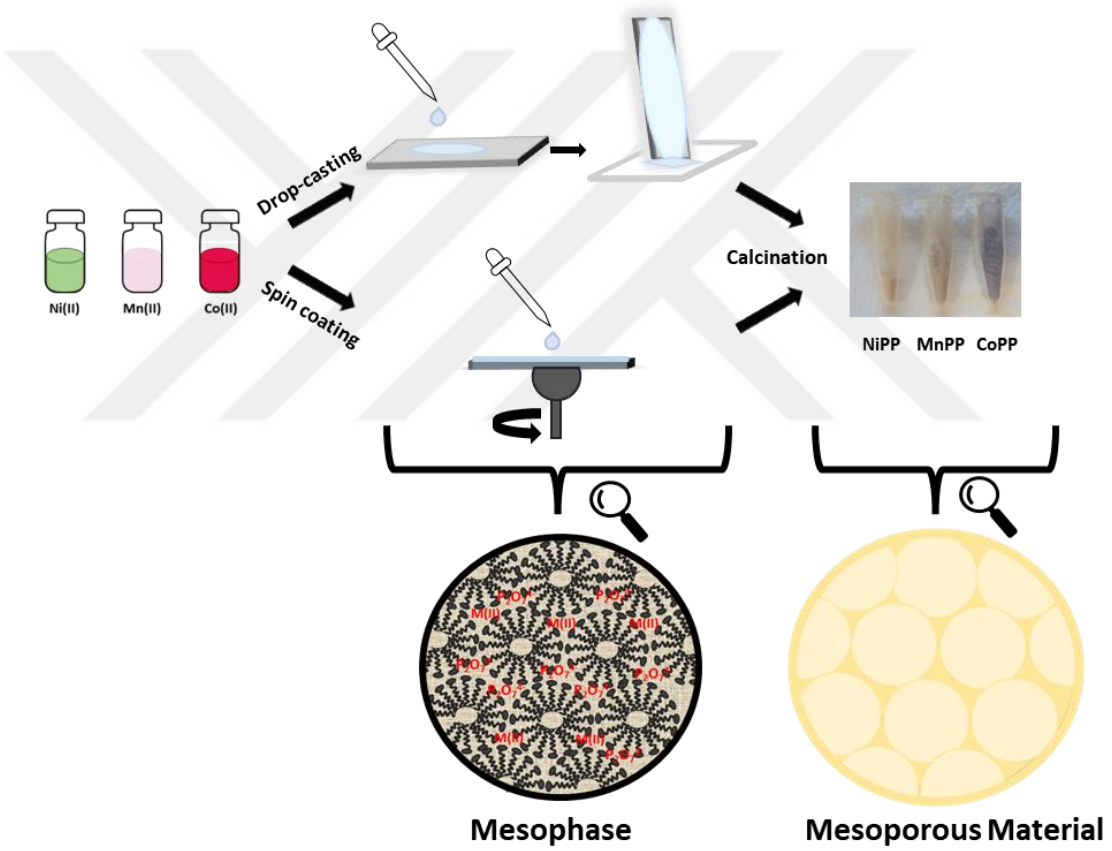

Figure 2.2: Schematic representation of the preparation of LLC mesophases and mesoporous materials.

2.5. Preparation of m-MPP Coated Electrodes

The electrodes for electrochemical measurements are fabricated by using two different substrates: spin-coated over fluorine-doped tin oxide (FTO) glasses to obtain a 1 cm^2 area of coating or dip-coating the clear diluted solutions of M(II):Acid:P123 over a pure graphite rod with a 3 mm diameter for a 1 cm^2 area with a pulling-speed of 1.45 mm/s. For spin coating, half of the 2x1 cm FTO is covered by tape to coat only a 1 cm^2 area. The tape is removed after coating for further calcination process, see Figure 2.3a. The pure graphite rod, which is 15 cm, is first cut into 3 cm long pieces. The cut parts are smoothed by figure-eight motion on clean paper.[156] A circular motion should not be applied because the surface becomes slanted in this motion. Next, the smoothed 3 cm graphite rods must be cleaned with deionized water and ethanol. After drying, the GR should be covered by parafilm to obtain only a 1 cm^2 area for coating before dipping, see Figure 2.3. Since the dip-coating method gives thicker films over the substrate, diluted solutions (5-, 10-, and 15 times using original 30, 60, and 90-mole ratio solutions, respectively, with deionized water) are used that keep the original mole ratios of the ingredients in the coated graphite rod (GR) surface. The dip-coated electrodes are aged for a few minutes under laboratory conditions to evaporate the excess solvent after removing the parafilm and then calcined directly in a preheated oven at the desired temperature (300, 400, 500, 600, and 700 °C) for 1 h.

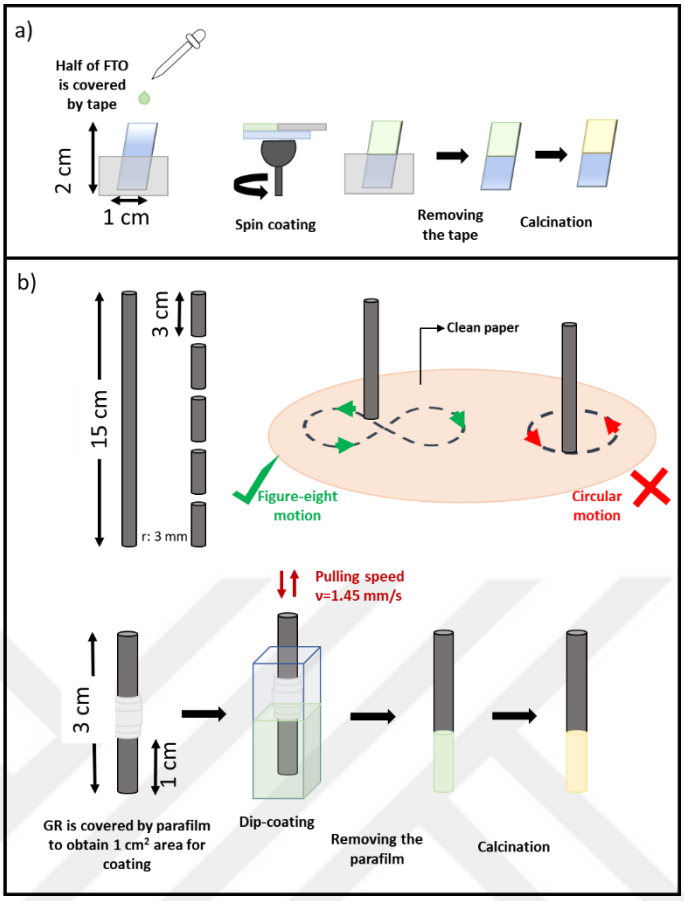

Figure 2.3: Schematic representation of the preparation of fabrication of a) FTO and b) GR electrodes.

2.6. Instrumentation

2.6.1. Polarized optical microscope (POM)

POM images of the gel-like films are recorded using a ZEISS Axio Scope A1 polarizing optical microscope with different optic lenses (5X, 10X, 20X, and 50X) between crossed polarizers to observe the mesophases on the microscope slides, prepared by drop-cast coating or spin coating methods.

2.6.2. X-Ray Diffraction (XRD) Patterns

Small-angle (1-5°, 2θ) XRD measurements of the gel-like films, prepared over glass slides, were performed by using a Rigaku Miniflex diffractometer equipped with a CuK$_\alpha$ (λ=1.5405Å) x-rays source, operating at 30 kV/15mA and a Scintillator NaI (T1) detector with a Be window. The patterns were collected by directly inserting the microscope slides, coated with mesophases, into the sample holder position. For the

wide-angle XRD (10-80°, 2θ) measurements, a PANalytical Multipurpose X-ray diffractometer equipped with a CuK_α (λ=1.5405Å) x-rays source, operating at 45 kV/40mA was used from the calcined powder that is packed uniformly on a sample holder.

2.6.3. Attenuated Total Reflection Fourier-Transform Infrared (ATR-FTIR) Spectroscopy

To collect the ATR-FTIR spectra, a Bruker Alpha Platinum ATR-FTIR spectrometer with a Digi Tect TM DLATGS detector was used with a resolution of 4 cm^{-1} and 64 scans in the 400-4000 cm^{-1} range. The spectra were collected by putting a few drops of solutions for the gel phase analysis or a pinch of powder for the calcined samples on the diamond ATR crystal.

2.6.4. Fourier-Transform Infrared (FTIR) Spectroscopy

To collect FTIR spectra in transmittance mode, a Bruker Tensor 27 model FTIR spectrometer with a Digi Tect TM DLATGS detector was used with a resolution of 4 cm^{-1} and 64 scans in the 400-4000 cm^{-1} range. The spectra were collected from pallets, prepared by mixing 0.190 g of KBr and around 0.01 g of the desired powder sample and pressing under 5 tons.

2.6.5. Scanning Electron Microscope (SEM)

SEM images were collected using an FEI Quanta 200 FEG at an operating voltage of 15 kV and spot size of 3 nm under a high vacuum (about 10^{-6} Torr). The samples are scraped from the glass substrate and put on carbon tape attached to the aluminum sample holder. Furthermore, EDAX data of the samples were also collected using x-ray detectors of the microscope.

2.6.6. Transmittance Electron Microscope (TEM)

TEM images were collected using an FEI Technai G2 F30 at an operating voltage of 200 kV. To collect high-quality images, the samples should be prepared using the spin-coating method. Then the thin films were scrapped, after calcination, from the microscope slide, grinded well in a mortar using absolute ethanol, and

dispersed using a sonicator for 30 min. Finally, a few drops of the dispersed solution were put on a TEM grid (holey carbon film on a 200-mesh copper grid) and heated under a powerful light for drying.

2.6.7. N_2-Adsorption-Desorption Measurements

The N_2-adsorption-desorption (77.4 K) isotherms are collected using a Micromeritics Tristar 3000 automated gas adsorption analyzer in a relative pressure range, P/P_0 from 0.01 to 0.99 over 5-minute intervals. The powder samples calcined at various temperatures were dehydrated under vacuum until they reached a 35-40 mTorr for 2 h at 200 ^oC before the measurements. The tubes for the analysis were cleaned well by washing them with aqua-regia, water, and ethanol before the measurements. After dying, the sample tubes were also evacuated using the same vacuuming system so that the weight of the sample was accurately determined. The sample tubes with the dehydrated samples were placed on the instrument with an isothermal jacket to keep the temperature stable since the measurement was carried out in liquid nitrogen.

2.6.8. X-Ray Photoelectron Spectrometer (XPS)

A Thermo Scientific K_α X-ray photoelectron spectrometer operating with an Al Kα micro-focused monochromatic source (1486.68 eV and 400 μm spot size) and a flood gun for charge neutralization were used to collect the XPS spectra. The scraped powder samples from the glass substrate were put on copper tape for the XPS analysis. The XPS spectra of the coated graphite electrodes were also recorded by directly inserting the coated part of the graphite rods into the spectrometer. The copper tape was again used for contacting the electrode surface to the spectrometer holder. The raw data were always calibrated using the C 1s peak at 285 eV in the spectrum.

2.6.9. Electrochemical Characterization

All electrochemical studies were carried out using a three-electrode cell, represented in Figure 2.4; a Pt wire as a counter electrode, Ag/AgCl (3.5 M KCl) electrode as a reference electrode, and a graphite rod coated with the m-MPP as a working electrode in a polypropylene cell with 3.0M KOH solution. The measurements were performed using a Gamry instrument (potentiostat-IFC5000-

07565). The measured potentials are corrected and reported as the normal hydrogen electrode (NHE). The cyclic voltammetry (CV) and galvanostatic charge/discharge (GCD) tests were subsequently recorded for each electrode on the same electrochemical workstation. The CV curves of the m-MPP electrodes were recorded in the potential range of -0.5 to 1.5 V (vs. Ag/AgCl) with a scan rate of 50 mV/s. The scan rate-dependent CV curves were also collected by changing the scan rate from 50 mV/s up to 1 mV/s (to 0.1 mV/s for some cases). The potential window for the GCD measurements was determined from the CV curves at slow scan rates (e.g., 1 mV/s). The GCD curves were recorded using different current densities depending on the samples. To observe the stability of the coated electrodes, 100 cycles of the GCD were recorded at each current density. According to the galvanostatic discharge curves, the corresponding specific capacitance has been evaluated using the following equation (eq. 2.1) :[133]

$$C_{SC} = \frac{I\Delta t}{A\Delta V} \qquad \textbf{eq. 2.1}$$

Where C_{sc} is the specific capacitance, I (A) is the discharge current, Δt (s) is the discharge time, A (cm^{-2}) is the area of coated material, and ΔV (V) is the potential window.

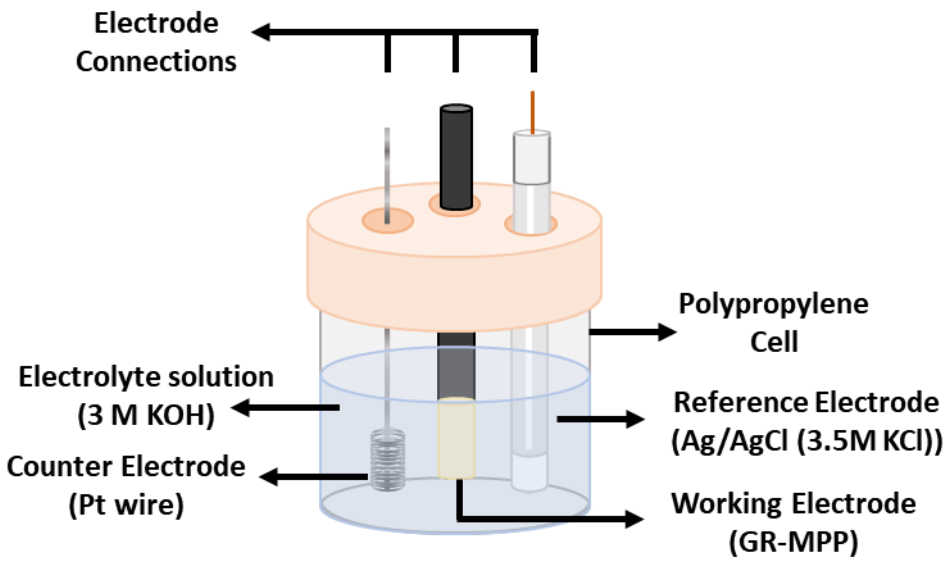

Figure 2.4: Schematic representation of electrochemical setup for the 3-electrode system.

Chapter 3

3. Results and Discussions

The solutions of M(II):Acid:P123 (M= Mn(II), Co(II), and Ni(II)) are prepared by using two separate vials to minimize the effect of high acid concentration on direct acid and salt mixing. The mesophases, obtained from homogenous solutions of M(II):Acid:P123, are prepared using both phosphoric acid (PA) and pyrophosphoric acid (PPA) precursors, see Table 2.1 and characterized by small-angle XRD, ATR-FTIR, and POM imaging techniques for each transition metal salt system. After calcination, the mesoporous metal pyrophosphates (m-MPP) are produced and characterized using various techniques such as wide-angle XRD, ATR-FTIR, SEM, TEM, XPS, N_2-adsorption-desorption, and electrochemical methods. Each transition metal system will be analyzed in separate parts.

3.1. Synthesis and Characterization of m-$Ni_2P_2O_7$ Samples

3.1.1. Preparation and Characterization of Ni(II):Acid:P123 Mesophases

The homogeneous aqueous solutions of Ni(II):Acid:P123 are prepared using PA or PPA, as mentioned in the experimental section, with compositions in Table 2.1. The ratios of other ingredients are calculated to be stoichiometric to the acid precursor (for example, PA/P123 is added the same as the salt/P123 ratio, whereas the PPA is added half of the salt/P123 mole ratio). The mole ratio of salt/P123 was changed from 10 to 100 for the PPA solutions to investigate the mesophase formation and stability.

Homogenous solutions of Ni(II):Acid:P123 are first drop-cast coated on a microscope slide to form a mesophase by evaporating the excess water under ambient laboratory conditions. Then, the obtained mesophases are characterized by small-angle XRD, ranging from 1 to 5º, 2θ, to analyze their stability while aging at room temperature (RT). Figure 3.1 shows the XRD patterns of all ratios of Ni(II):Acid:P123 mesophases aged at RT. Note that aging and evaporation of excess water are used for the same intention. Simply, in this process, excess water evaporates under ambient conditions to form a gel phase. The gel phase and mesophase are used to describe the sample after water evaporation. The diffraction lines at small angles show that the mesophases have an ordered structure, and almost all compositions are stable for up to 1 day. Minor changes in the diffraction lines during gelation indicate that the water evaporation rate while forming gel-like films differs. Because the concentration of the solutions of Ni(II):Acid:P123 is different. The diffraction lines are not as intense as expected. The plane with the highest d-spacing must be below 1º, 2θ, which could not be measured using our XRD set-up. The observed diffraction lines must result from the order planes of the mesophase with higher hkl values and smaller d-spacings.

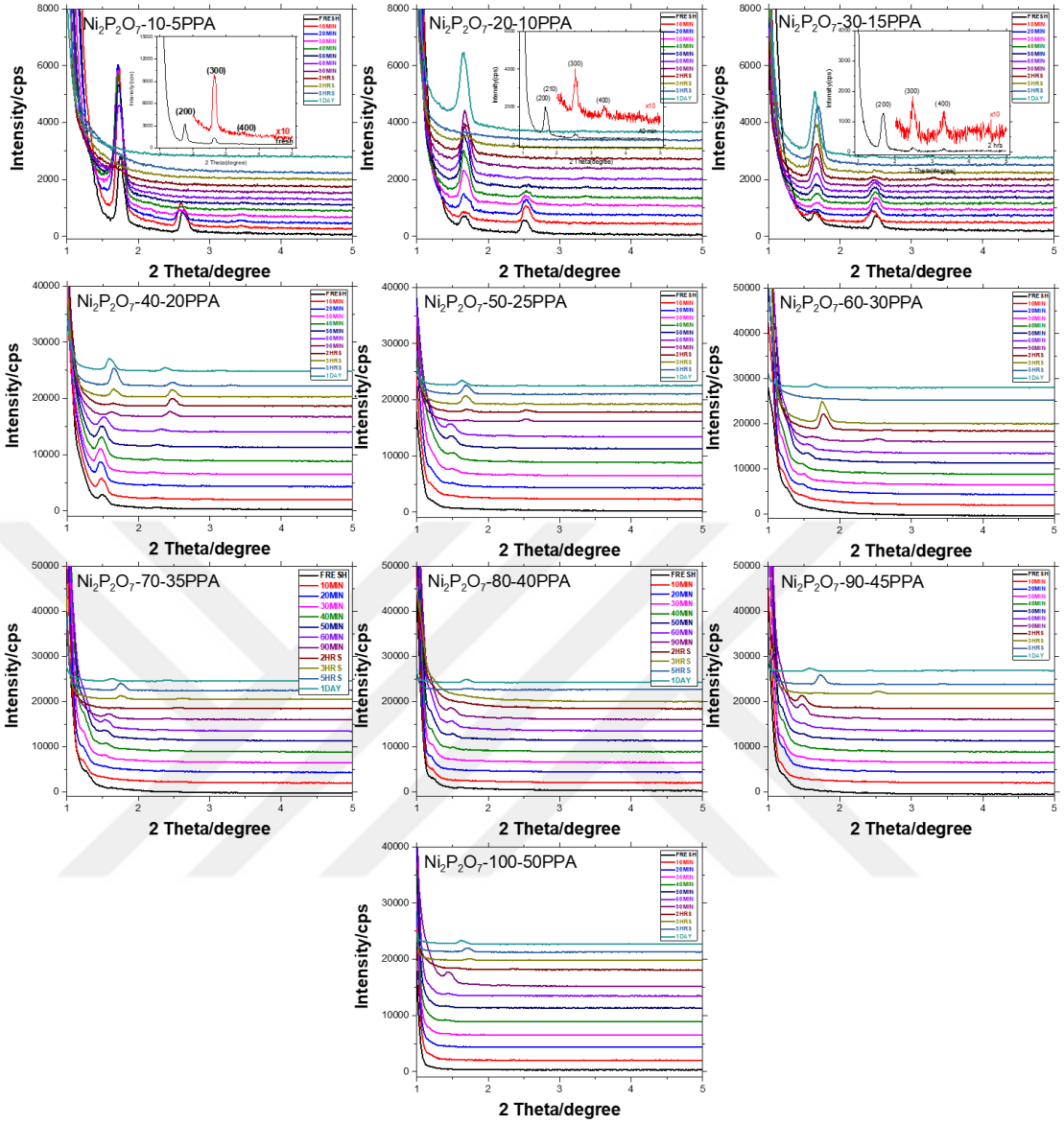

Figure 3.1: Small-angle XRD patterns of Ni(II):Acid:P123 with salt mole ratios of 10-100 prepared using PPA.

The patterns in the insets are multiplied by 10 to make this region visible (insets of Figure 3.1). The diffraction lines of the NiPP-10 and the NiPP-30 samples (NiPP-n, n indicating the mole ratio of salt/P123) can be indexed to (200), (300), and (400) planes and observed at 1.75, 2.65, and 3.46º, 2θ, with d-spacings of 50.44, 33.31, and 25.52 Å, and at 1.66, 2.52, and 3.33º, 2θ, with d-spacings of 53.18, 35.03, and 26.51Å, respectively. The pattern of the NiPP-20 has an extra broad line at around 1.70º, 2θ, indexed to (210) plane with a d-spacing of 51.93 Å. The diffraction lines are almost at the same position in the NiPP-40 to NiPP-100 compositions with a small shift to lower

angles. Notice that the inorganic ingredient is increased by 10 times, but the response in the XRD patterns is negligibly small. Therefore, it is reasonable to suggest that the aggregation number (the number of surfactant molecules in the micelle domains) decreases by increasing the concentration of the inorganic ingredient in the LLC mesophases.

The mesophases of NiPP were also investigated using the small-angle XRD techniques by changing the acid precursor (phosphoric acid (PA) or pyrophosphoric acid (PPA)), see Figure 3.2. There are slight differences between the patterns of the PA and PPA samples. A diffraction line for the Ni(II):PA:P123 mesophase appears at 1.4^{o} and shifts to 1.8^{o}, 2θ, indicating the unit cell shrinkage during the first 60 min of aging. Then, the same line continues to shift but to a lower angle (1.65^{o}, 2θ) after 60 min till 2 days of aging. Two diffraction lines are observed from the mesophases, aged around 80-90 min, which are at 1.75 and 2.66^{o}, 2θ, and can be indexed to (200) and (300) planes, respectively.

The Ni(II):PPA:P123 mesophase diffracts a broad diffraction line at 1.2^{o}, 2θ, with another diffraction line below 1^{o}, 2θ. The diffraction line at around 1.5^{o}, 2θ, shifts to 1.75^{o}, 2θ, showing the shrink of the unit cell after 3 h aging. Similar to the PA mesophase, the 3 h aged PPA mesophases diffract multiple diffraction lines at 1.75, 2.65, and 3.47^{o}, 2θ, and can be indexed to (200), (300), and (400) planes, respectively. The interaction between acid and metal ions differs in the gelation process since the acidity of PPA (pK_a = 0.91) is slightly higher than PA (pK_a = 2.16).[157]

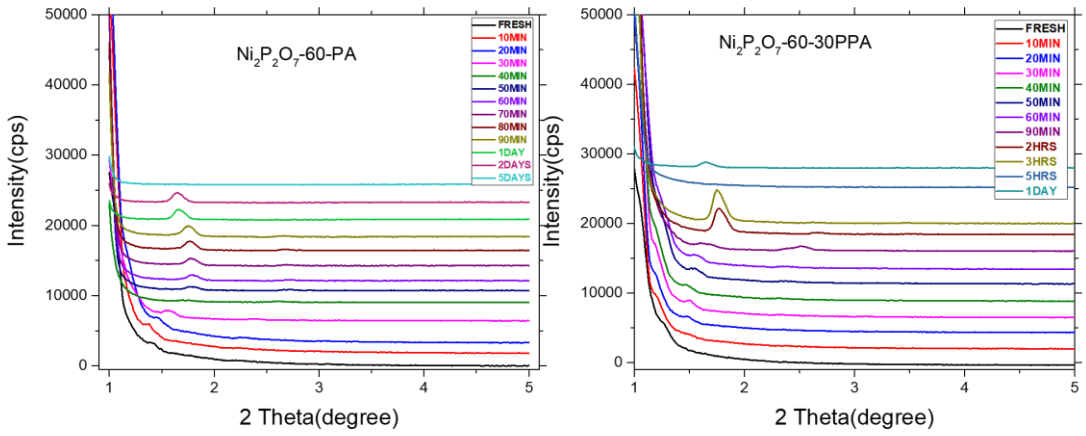

Figure 3.2: Small-angle XRD patterns of the 60-Ni(II):Acid:P123 gel phases, prepared using PA and PPA.

The Ni(II):PPA:P123 mesophases were also analyzed using POM using the samples, which were obtained by drop-casting the aqueous solutions on microscope slides and then aging them under ambient conditions. Figure 3.3 shows the POM images of all compositions after 15 min and 1 day of aging. The texture in the images displays small domains in 15 min aged samples; however, after 1 day, those small domains enhance and cover the slides with some cracks, indicating the formation of solid-like particles. The particles have a composition of $Ni_2H_xP_2O_7(NO_3)_x{\cdot}nH_2O$ (see eq. 3.1). Even though the formation of solid-like particles enhanced during aging, the mesostructure is still preserved and provides X-ray diffractions at small angles. Also, note that there is no crystallization of salt species during water evaporation in 5 days, see Figure 3.4.

$$2Ni(NO_3)_2(aq) + H_4P_2O_7(aq) + nH_2O \leftrightarrow Ni_2H_xP_2O_7(NO_3)_x.nH_2O(s) + (4-x)HNO_3(g) \quad \textbf{eq. 3.1}$$

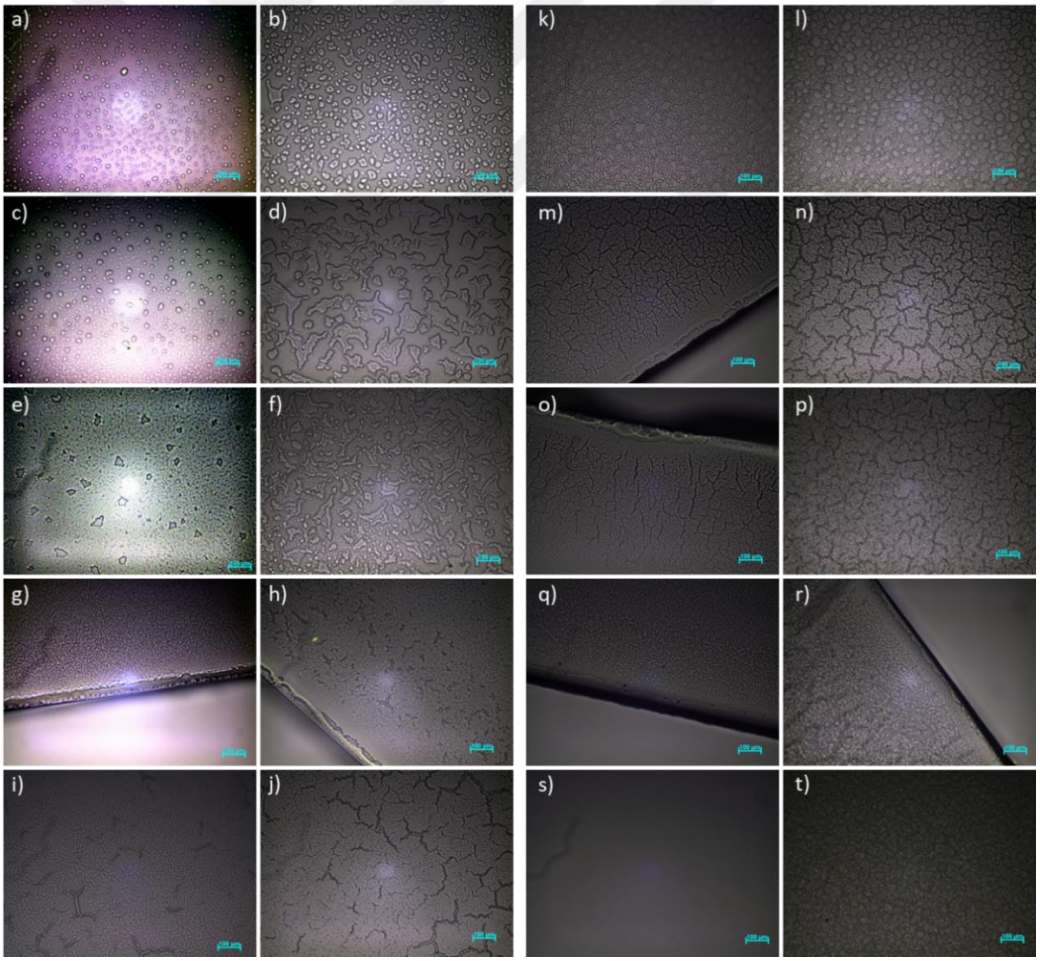

Figure 3.3: POM images of a) and b) NiPP-10, c) and d) NiPP-20, e) and f) NiPP-30, g) and h) NiPP-40, i) and j) NiPP-50, k) and l) NiPP-60 m) and n) NiPP-70, o) and p) NiPP-80, q) and r) NiPP-90 and s) and t) NiPP-100 for 15 min and 1 day aged drop-cast coated samples, respectively (The scale bars are 100 μm).

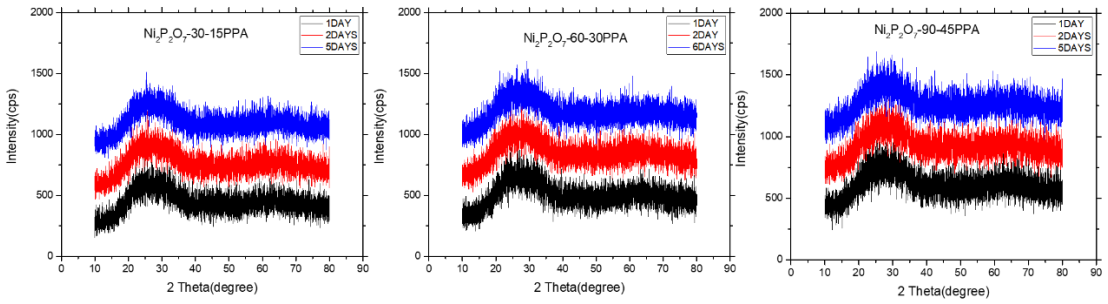

Figure 3.4: Wide-angle XRD patterns of 1, 2, and 5 days aged mesophases of (left) 30-Ni(II):Acid:P123, (middle) 60-Ni(II):Acid:P123, and (right) 90-Ni(II):Acid:P123 samples at RT.

The NiPP mesophases are also characterized by ATR-FTIR spectroscopy to investigate the gelation mechanism. The spectra were collected by adding one drop of solutions of NiPP-n (n is 30, 60, and 90) for low, intermediate, and high mole ratios, respectively, on the ATR diamond, starting from the time of dropping (0 min) till 48 hours. Figure 3.5 shows the time-dependent, baseline-corrected ATR-FTIR spectra of NiPP solutions. The intensities of peaks, at around 3600-3000 and 1640 cm^{-1}, originate from the stretching and bending modes of water species and at about 1470-1290 cm^{-1} due to the nitrate species decrease during aging, whereas the intensity of peaks at around 1200-800 cm^{-1} due to the phosphate species increase. This is the indication of the evaporation of water, as well as the decomposition of the nitrate species from the media, likely as nitric acid or its decomposition products, see eq. 3.1. The evaporation results in an increase in both concentrations of the ingredients in the media and the refractive index of the dropped sample on the ATR diamond, causing an intensity increase (see later for the details of the technique).

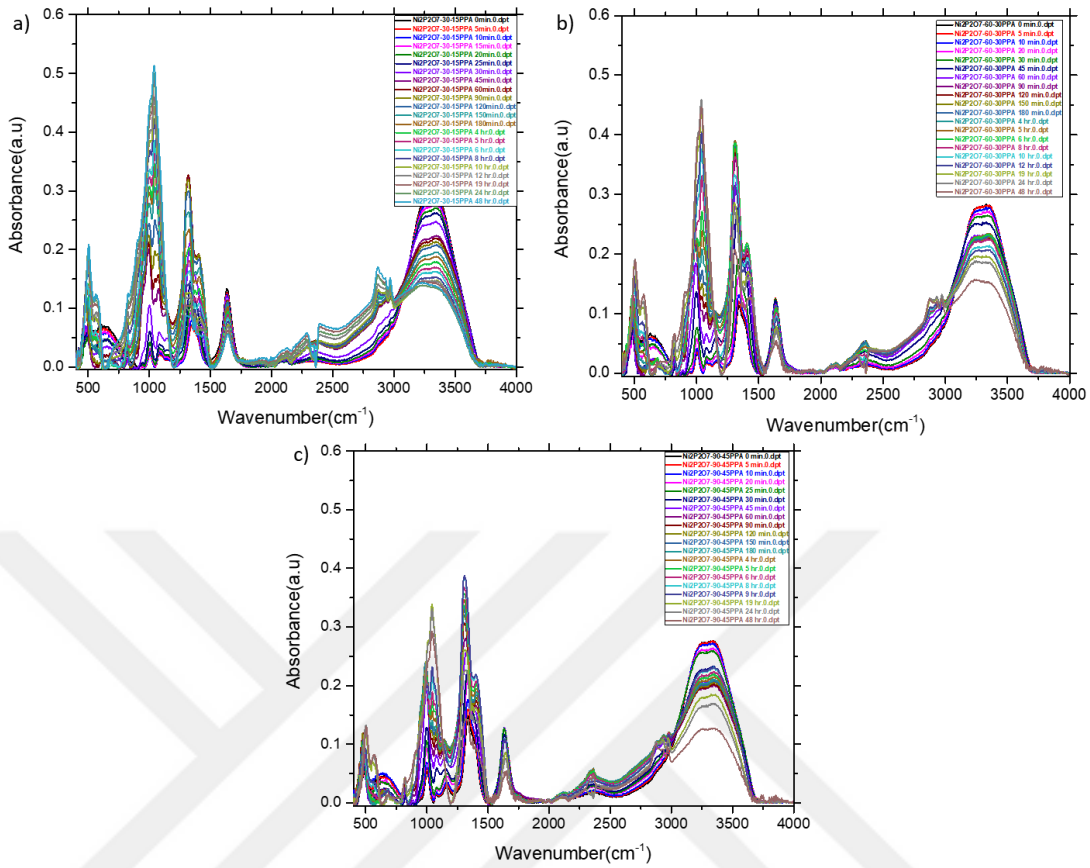

Figure 3.5: Time-dependent baseline corrected ATR-FTIR spectra of a) NiPP-30, b)-60, and c)-90 prepared using PP.

Since the concentration and refractive index of the samples are changing, it is necessary to analyze the ATR-FTIR spectra after normalizing using an ingredient peak that does not change during evaporation, for instance, a surfactant or phosphate peak. The working principle of ATR-FTIR spectroscopy relies on a total internal reflection process. The internal infrared beam coming to the ATR crystal at a certain angle generates evanescent waves, see Figure 3.6. These waves extend into the sample over the ATR crystal and get absorbed and attenuated by the sample. The attenuated beam returns to the ATR crystal and exits from the opposite end of the crystal. The reflected beam is detected by the infrared detector, and it is recorded as an interferogram signal that can be utilized to transform into an infrared spectrum. The sample thickness on the crystal does not matter in favor of thick samples, different from the transmittance FTIR spectroscopy. The measured thickness depends on the refractive index of the sample and the wavelength of IR radiation; however, the software of the spectrometer

handles the wavelength dependence. Therefore, one must be careful while comparing the spectra collected from these two spectrometers, ATR-FTIR and regular FTIR. The penetration depth (d_p), which is a measure of how far the evanescent waves extend into the sample, can be calculated by the following equation:

$$d_p = \frac{\lambda}{2\pi n_c \sqrt{sin^2\theta - (\frac{n_s}{n_c})^2}} \qquad \textbf{eq. 3.2}$$

Where n_c and n_s are refractive indexes of the ATR crystal and the measured sample, respectively, λ is the wavelength of the IR beam, and θ is the angle of the incident beam. Note also that the absorbance and thickness of the sample are directly proportional to each other and obey Beer's law: A = εbc, where ε is the extinction coefficient, b is thickness, and c is the sample concentration. Also, notice the sample's concentration and refractive index (refractive index changes between 1.33 and 1.50 for pure water and gel phase, respectively)[158], see Figure 3.6 for the relationships in eq. 3.2. Therefore, the thickness of the measured sample changes during the water evaporation.

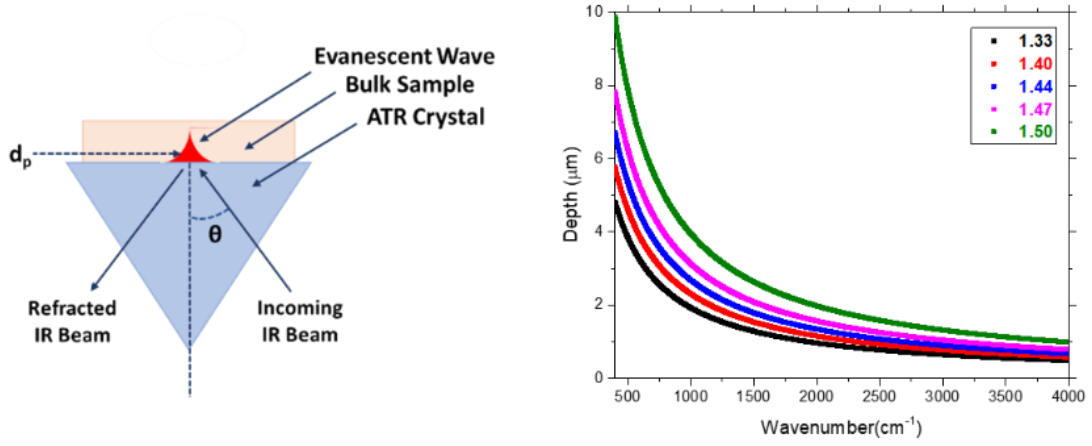

Figure 3.6: Schematic representation of evanescent wave of ATR cell, the depth vs. wavenumber plots for different refractive indexes.

These changes need to be compensated to compare the spectra with each other by normalizing the spectra. Figure 3.7 shows the normalized spectra of NiPP-30, -60, and -90 samples starting from fresh (0 min) to 48 h, extending the absorbance axes to

observe the spectral changes. Moreover, the normalized spectra help to investigate the quantitative results of gelation and polymerization processes. The first spectra of those 3 compositions were assumed to be the initial composition of the solution, and they were calculated as 82, 41, and 27.3 for water-to-nickel mole ratios in the NiPP-30, NiPP-60, and NiPP-90 solutions, respectively. The nitrate to nickel mole ratio is assumed to be 2 in the NiPP-30 sample. Then, the ratios of nitrate to nickel for the other two compositions can be calculated accordingly, and their normalized spectra as 1.58 and 1.10 for 60 and 90-mole ratios, respectively. Figure 3.8 shows the relationship between the mole ratios of water/nickel and nitrate/nickel versus time for all those 3 compositions. NiPP-30 sample has the most water content initially, but it loses its water very quickly (in 25 min), and at the same point, the nitrate/nickel ratio drops to 0.8. The NiPP-60 and NiPP-90 samples also follow a similar trend with the NiPP-30 sample. The decay of the nitrate species follows the water decay. This means that the nitrate decomposition depends on the water content of the solution. Moreover, the spectral data also prove that the nitrate decomposition starts in the solution phase. The first sharp decrease (in the first 30 min) corresponds to a gelation process. In contrast, after this point, the decline is low, meaning that the polymerization of pyrophosphate with the nickel ions takes place, named to be a solidification process. When the breakpoints are deeply analyzed, it is found that this point corresponds to 6 H_2O/Ni(II). The nitrate/Ni(II) and water/Ni(II) mole ratios drop to 0.35 and 1.85 in the NiPP-30 sample, to 0.3 and 0.75 in the NiPP-60 sample, and to 0.15 and 0.7 in the NiPP-30 sample after 48 h of aging. The compositions become $Ni_2H_{0.7}P_2O_7(NO_3)_{0.7}\cdot 3.7H_2O$, $Ni_2H_{0.6}P_2O_7(NO_3)_{0.6}\cdot 1.5H_2O$, and $Ni_2H_{0.3}P_2O_7(NO_3)_{0.3}\cdot 1.4H_2O$ from the NiPP-30, NiPP-60, and NiPP-90 samples, respectively. The majority of the nitrates are removed by the reaction in eq. 3.1 as nitric acid or its decomposition products.

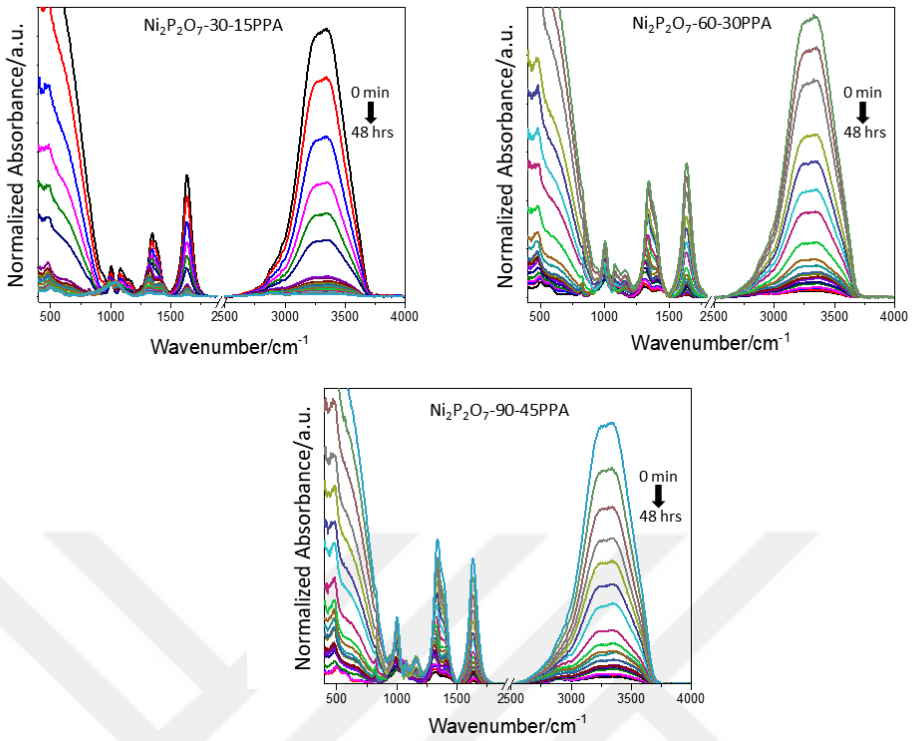

Figure 3.7: Time-dependent normalized ATR-FTIR spectra of NiPP-30, -60, and 90 prepared using PPA.

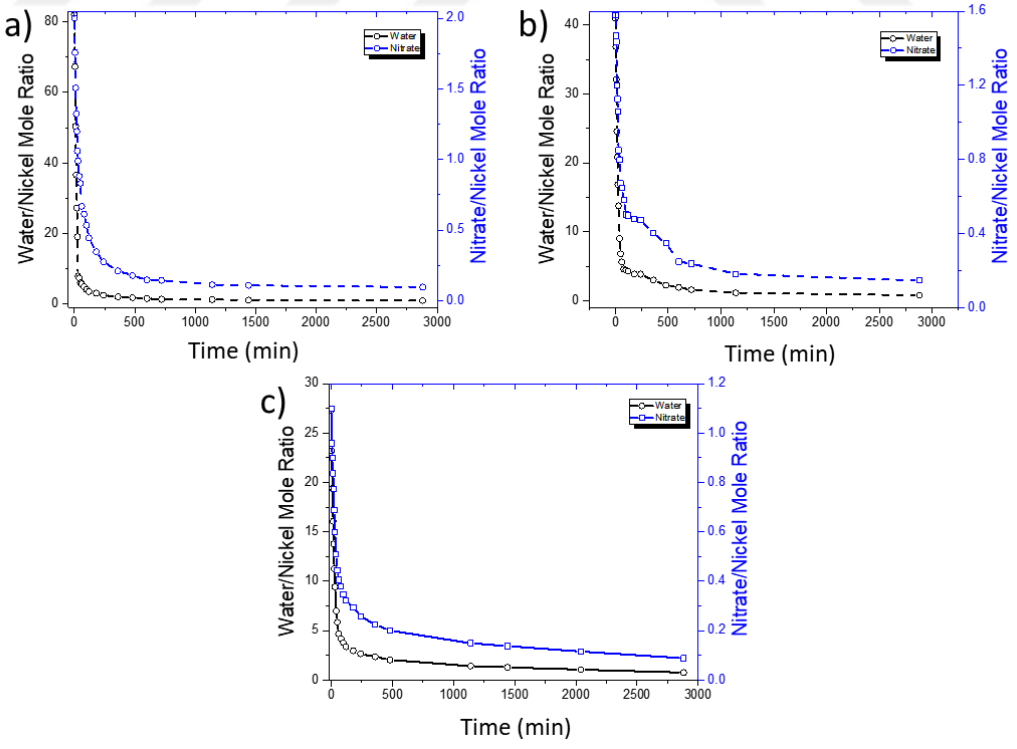

Figure 3.8: Water/nickel and nitrate/nickel mole ratios versus time graphs derived from the normalized ATR-FTIR spectra of a) NiPP-30, b) NiPP-60, and c) NiPP-90 solutions.

The gelation and solidification processes were also followed by weight-lost measurement by putting about 1 g of a solution and monitoring the change of the sample's weight under ambient conditions over a 4-digit balance. The solution loses its water quickly in the first 200 min, see Figure 3.9. The range I indicates the evaporation of excess water in the solution. Then, the weight of the solution continues to decrease at a slow rate due to the polymerization of the pyrophosphate species upon the solidification process. As discussed in the ATR-FTIR section, the more volatile species in ranges II and III leave the system as mainly nitrate decomposition products. Gravimetric measurements are further proof of the gelation and solidification processes. Figure 3.9 compares the samples of NiPP-60 prepared by PA and PPA. The range I is almost identical in each acid system. There are slight differences between PA and PPA solutions in the ranges II and III, which shows that the chemical reaction for removing volatile species from the media differs with the acid type and acidity of the solutions.

Also, note that the thickness of the mesophases is different for the coated samples over a microscope slide (for POM and XRD analysis) and the dropped samples (ATR-FTIR and gravimetric analysis), which are thicker than those. Therefore, the time difference for the gelation and solidification processes should be considered to compare those processes with different techniques sensibly.

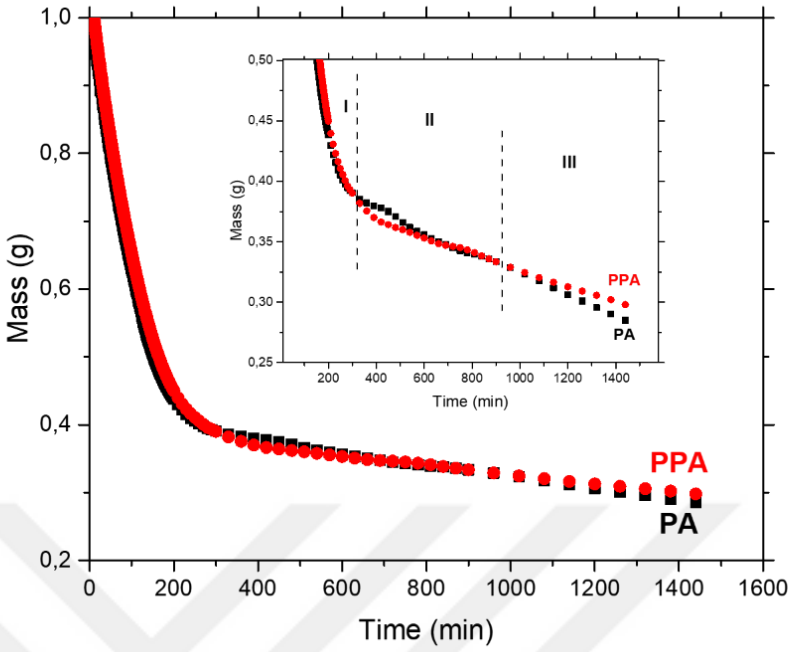

Figure 3.9: Gravimetric measurements: Mass versus time plots during water evaporation on the balance of NiPP-60 prepared by PA and PPA.

The mesophases obtained from the NiPP solutions were also analyzed after heat treatments. Figure 3.10 shows the small-angle XRD patterns of NiPP-30, -60, and -90 samples upon heating the samples after 1 day of aging. The 1 day-aged samples were put in a preheated furnace for 15 min intervals between 40-100 ^{o}C with an increment of 10 ^{o}C, and the patterns of the heated samples were recorded. As shown in Figure 3.10, the mesophase formed at RT is oriented up to 50 ^{o}C, 70 ^{o}C, and 90 ^{o}C in the NiPP-30, -60, and -90 samples, respectively. Above those temperatures, they lose their orientation by losing the diffraction intensity at around 1.6^{o}, 2θ. However, the mesophases are still stable even after heating above those temperatures. The high intensity around 1^{o}, 2θ, is likely due to the (100) line and is proof of the existence of the mesophase/mesostructure.

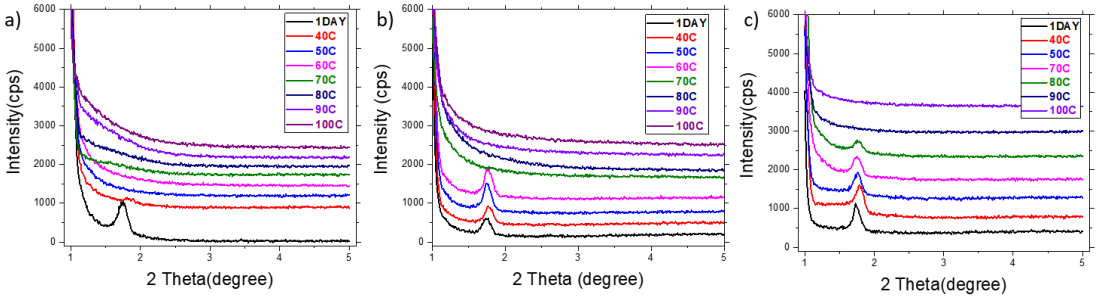

Figure 3.10: Small-angle XRD patterns of the a) NiPP-30, b) NiPP-60, and c) NiPP-90 mesophases after 1 day of aging, followed by heating at (bottom to top) RT, 40 to 100 ºC with 10 ºC increments.

The effect temperature on the mesophases is also followed using an ATR-FTIR spectroscopy by heating the sample on the ATR diamond crystal. Heating of the 48 h aged samples further reduces the nitrate and water species from the mesophase, see Figure 3.11. There are some minor differences between the 3 compositions of NiPP mesophases, resulting from the initial compositional differences. The mesophase of NiPP-60 was analyzed in more detail to elucidate the spectral changes between RT and 100 ºC, see Figure 3.12a. The peaks at around 1300 and 1409 cm^{-1} (with a splitting of 119 cm^{-1}, due to monodentate nitrate) shift to 1289 and 1506 cm^{-1} (with a splitting of 217 cm^{-1}, due to bridge-coordinated nitrate) by heating the sample. The water peak completely disappears at around 80 ºC, indicating a complete drying and mainly leaving bridged-coordinated nitrates in the media. Figure 3.12b shows the plots of x (nitrate amount) and n (water amount) values of $Ni_2H_xP_2O_7(NO_3)_x{\cdot}nH_2O$ with increasing temperature. The sample composition of NiPP-60 becomes $Ni_2H_{0.4}P_2O_7(NO_3)_{0.4}$ at 100 ºC. Notice also that a complete water removal from the sample stops the nitrate decomposition.

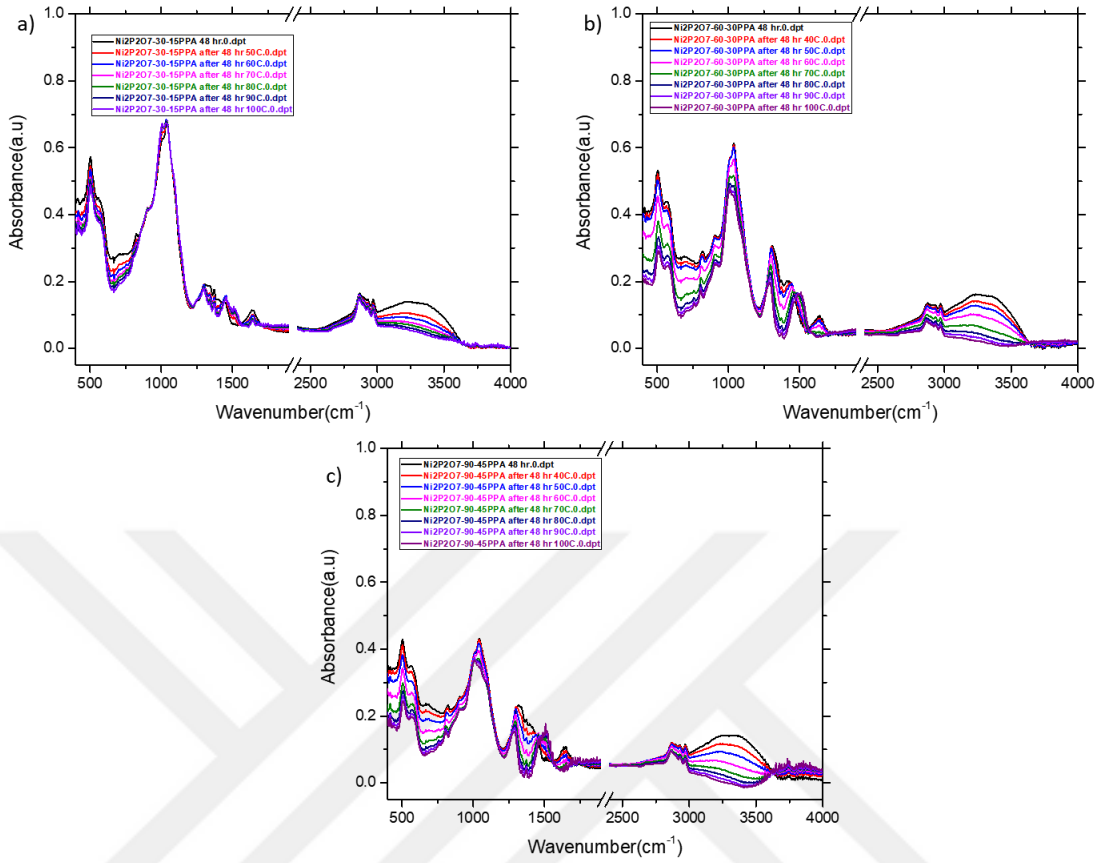

Figure 3.11: Temperature-dependent ATR-FTIR spectra of the a) NiPP-30, b) NiPP-60, and c) NiPP-90 solutions after 2 days aging followed by heating at (top to bottom) RT, 40 to 100 ^{o}C with 10 ^{o}C increments.

Note also that it is possible to further reduce the nitrate content of the mesophase by exposing it to a humid environment. Figures 3.12c and 13.2d display some ATR-FTIR spectra recorded at various conditions. Heating the sample at the end of 24 h aging to 40 and 100 ^{o}C causes a reduction of nitrate species to around 0.2 nitrate/nickel, as previously shown, see Figure 3.8b. The sample is exposed to 85 % humidity using a vial of saturated KCl solution sealed around the ATR diamond. [159] At 85 % humidity, the sample absorbs some water that appears in the spectrum; the intensity at around 3600-3000 and 1640 cm^{-1} increases, and the bridged nitrates become monodentate nitrates. Heating this sample at 40 and 100 ^{o}C makes the water peaks disappear, reducing the nitrate peaks and changing the remaining monodentate nitrates back to bridged nitrates. Therefore, it is reasonable to conclude that the adsorbed water molecules are in a very close vicinity to nitrate species and react with

each other to reduce the nitrate content of the sample further. With the 2nd cycle of heating and cooling, the sample loses its nitrate species from 0.4 to 0.08, and at the end, the product $Ni_2H_{0.08}P_2O_7(NO_3)_{0.08}$ is obtained. The pure P123 spectrum is also shown in Figure 3.12d, green spectrum, for comparison purposes. Notice that the spectrum of 2nd cycle of heating and cooling in the nitrate region is very similar to the P123 spectrum, meaning that most of the nitrate species have been removed from the sample by humidity and heat treatment. The cycling of heating and cooling under 85 % humidity was repeated 5 times; however, the 5th and 2nd cycles gave almost the same result. Therefore, removing all nitrates and some protons even at 100 °C and further humidity treatment is impossible. The presence of the remaining protons (which can be as P-OH species after further calcination/annealing process) in the samples makes the product amorphous and keeps it amorphous up to 700 °C (see latter).

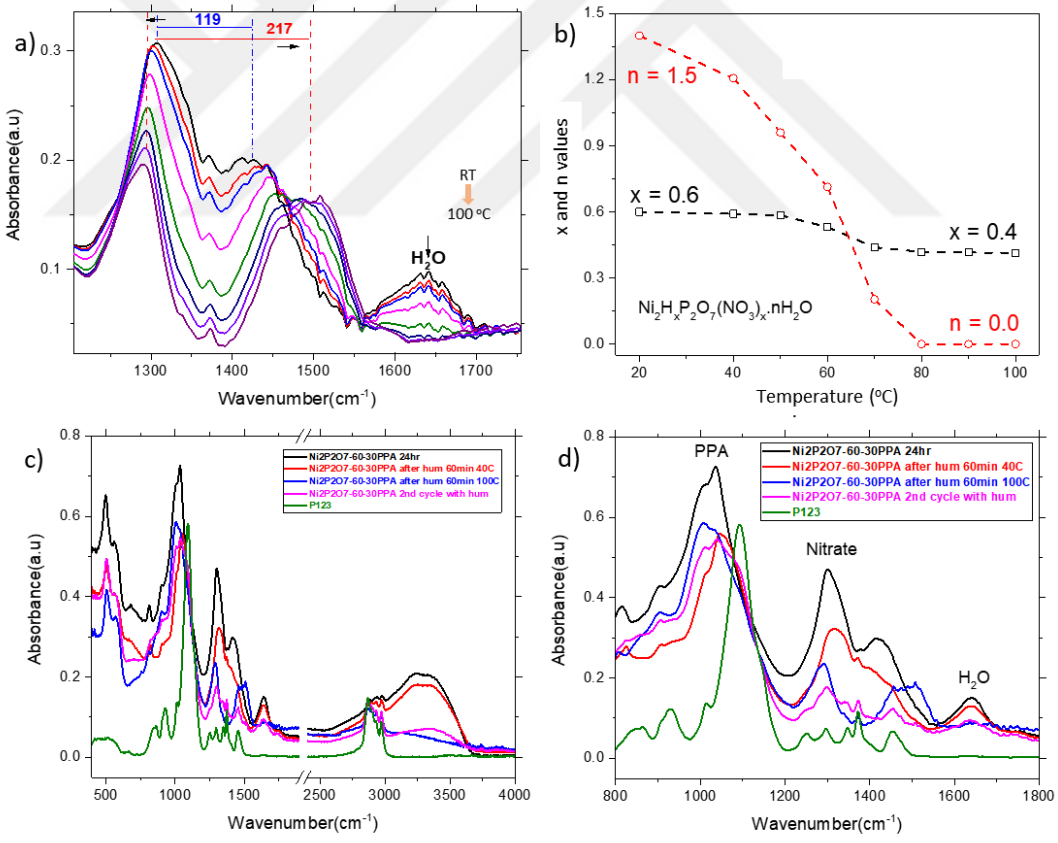

Figure 3.12: a) ATR-FTIR spectra of the NiPP-60 solutions after 2 days of aging followed by heating at (top to bottom) RT, 40 to 100 °C with 10 °C increments in the nitrate region, b) the graph of x and n values of $Ni_2H_xP_2O_7(NO_3)_x \cdot nH_2O$ versus temperature of the NiPP-60 sample, c) and d) spectral changes, humidity dependent changes, of 24 h aged sample under the following conditions, (black) at RT, (red) at 40 °C, (blue) at 100 °C, (pink) 2nd cycle after exposing 85 % humidity followed by heat at 100 °C then cooling to RT, and (green) P123.

3.1.2. Synthesis and Characterization of Mesoporous $Ni_2P_2O_7$

Calcination of spin-coated, dip-coated, or drop-casted samples at 300 ^oC produces mesoporous $Ni_2P_2O_7$ particles (denoted as m-NiPP-n-X, m stands for mesoporous, n is the nickel/P123 mole ratio, and X is the calcination temperature in Celsius). The m-NiPP-n-300 samples were annealed at higher temperatures (400, 500, 600, and 700 ^oC) and characterized using XRD, ATR-FTIR, SEM, EDX, TEM, N_2 adsorption-desorption measurement, XPS, and electrochemical techniques.

Figure 3.13 shows the powder XRD patterns of the m-NiPP-60 samples heated or calcined/annealed at various temperatures. The diffraction pattern shows no diffraction line(s) up to 700 ^oC; this sample is amorphous and becomes crystalline at 700 ^oC, see Figure 3.13 (left one). The pattern of m-NiPP-60-700 can be indexed to a mixture of α-NiPP and a small amount of δ-NiPP, Figure 3.13 (right one).[160] The α-phase is the dominant phase in the spectrum, having the most intense line (12-2) of the phase. The δ-phase coexists with the α-phase; however, the amount of this phase is not worthwhile even as the most intense line (-121) is like a shoulder near the most intense line of the α-phase.

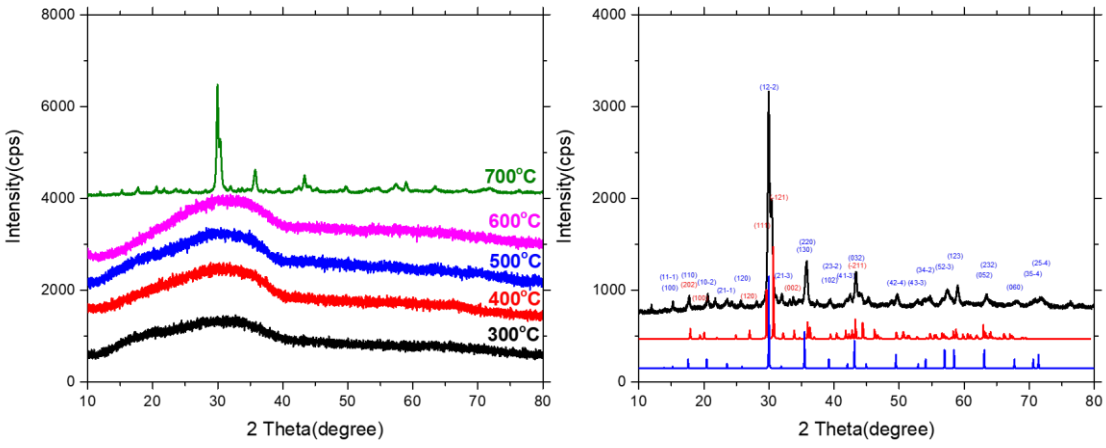

Figure 3.13: Wide-angle XRD patterns of the (left) m-NiPP-60-X (X is 300, 400, 500, 600, and 700 ^oC) and (right) indexed XRD pattern of the NiPP-60-700 sample with reference patterns of (blue) α-$Ni_2P_2O_7$ (ICDD 00-039-0710) and (red) δ-$Ni_2P_2O_7$ (ICDD 00-049-1082).

Figure 3.14 shows the ATR-FTIR spectra of the m-NiPP-60 samples heated or calcined/annealed at various temperatures. The ATR-FTIR spectra display a decrease in the peaks of nitrate and surfactant species up to 200 ^oC; no peaks are observed from

the nitrate and surfactant species at 300 °C and higher annealing temperatures. The only peaks at 300 °C and higher annealing temperatures result from the NiPP species. The peaks at high frequency (1050-1200 cm^{-1}) correspond to PO_3 units, the peaks at around 750 and 930 cm^{-1} correspond to symmetric and asymmetric modes of the bridging P-O (P-O-P) group, and the intense peaks at about 500-600 cm^{-1} originate from the bending modes of pyrophosphate group and Ni-O stretching modes. [161], [162]. All the phosphate peaks are broad up to 700 °C, get sharper by increasing the annealing temperatures, and become more resolved at 700 °C. This change corresponds to the crystallization of nickel pyrophosphate particles at 700 °C, see Figure 3.14. The spectral features show that the local pyrophosphate structure in the amorphous phase is very similar to the crystalline phase.

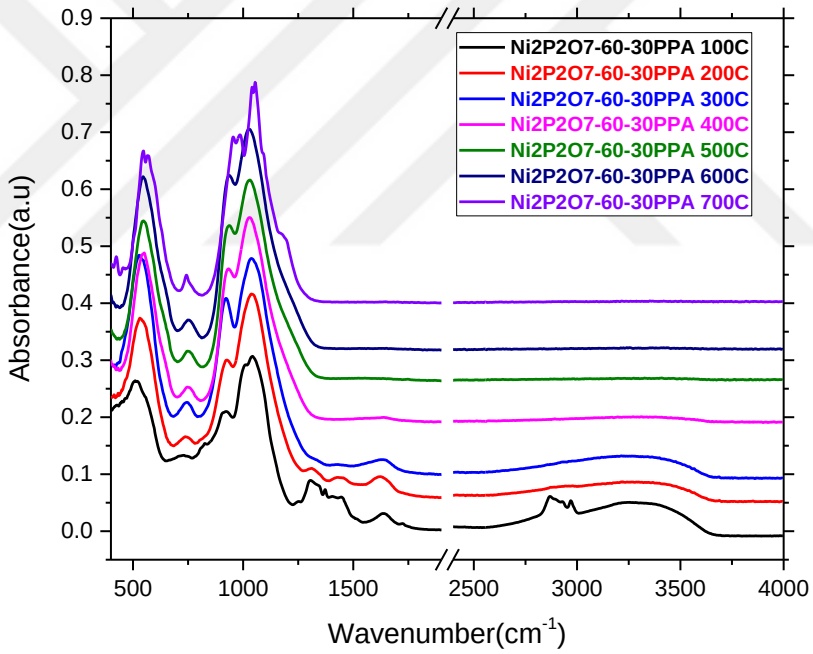

Figure 3.14: ATR-FTIR spectra of the m-NiPP-60 heated or calcined/annealed at various temperatures.

N_2 adsorption-desorption isotherms are collected, and Barrett-Joyner-Halenda (BJH) pore size distribution plots (from the desorption part) are calculated for the low, intermediate, and high compositions of m-NiPP calcined at 300 °C and annealed at 400, 500, 600, and 700 °C samples (see Figure 3.15). The isotherms are type IV, characteristic of mesoporous materials.[163][164] The pore-size distribution of the m-

NiPP-30-300 sample is relatively more uniform than that of the m-NiPP-60-300 and m-NiPP-90-300 samples (see Figure 3.15b). Brunauer-Emmett-Teller (BET) surface area, pore volume, and pore sizes of m-NiPP-30-300, m-NiPP-60-300, and m-NiPP-90-300 samples are given in Table 3.1. The highest surface area is obtained from the m-NiPP-30-300 sample and chosen for the electrochemical analysis later. The surface area of m-NiPP-60-X gradually decreases with increasing annealing temperature and becomes 31, 25, 5, and 5 m^2/g at 400, 500, 600, and 700 ^oC, respectively; see Figure 3.15c and Table 3.1.

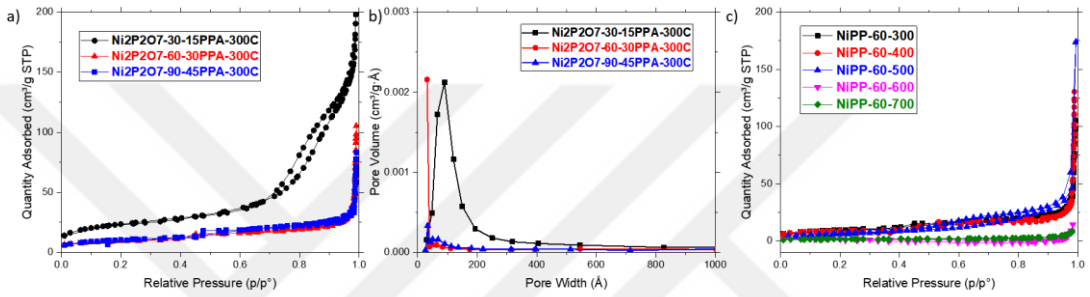

Figure 3.15: N_2 (77 K) adsorption and desorption isotherms of the a) m-NiPP-n-300 (n is 30, 60, and 90) and c) m-NiPP-60-X (X is 300, 400, 500, 600, and 700 ^oC), b) the pore size distribution plots of m-NiPP-n-300 (n is 30, 60 and 90).

Table 3.1: (Left) BET surface area, pore volume, and pore size values of the m-NiPP-n-300 (n is 30, 60, and 90) samples and (right) the BET surface area of the m-NiPP-60-X (X is 300, 400, 500, 600, and 700 ^oC) samples.

Mole Ratio	BET Surface Area (m^2/g)	Pore Volume (cm^3/g)	Pore Size (nm)
m-NiPP-30-300	60	0.40	17.8
m-NiPP-60-300	35	0.15	11.2
m-NiPP-90-300	38	0.17	12.4

Calcination Temperature (^oC)	BET Surface Area (m^2/g)
	m-NiPP-60
300	35
400	31
500	25
600	5
700	5

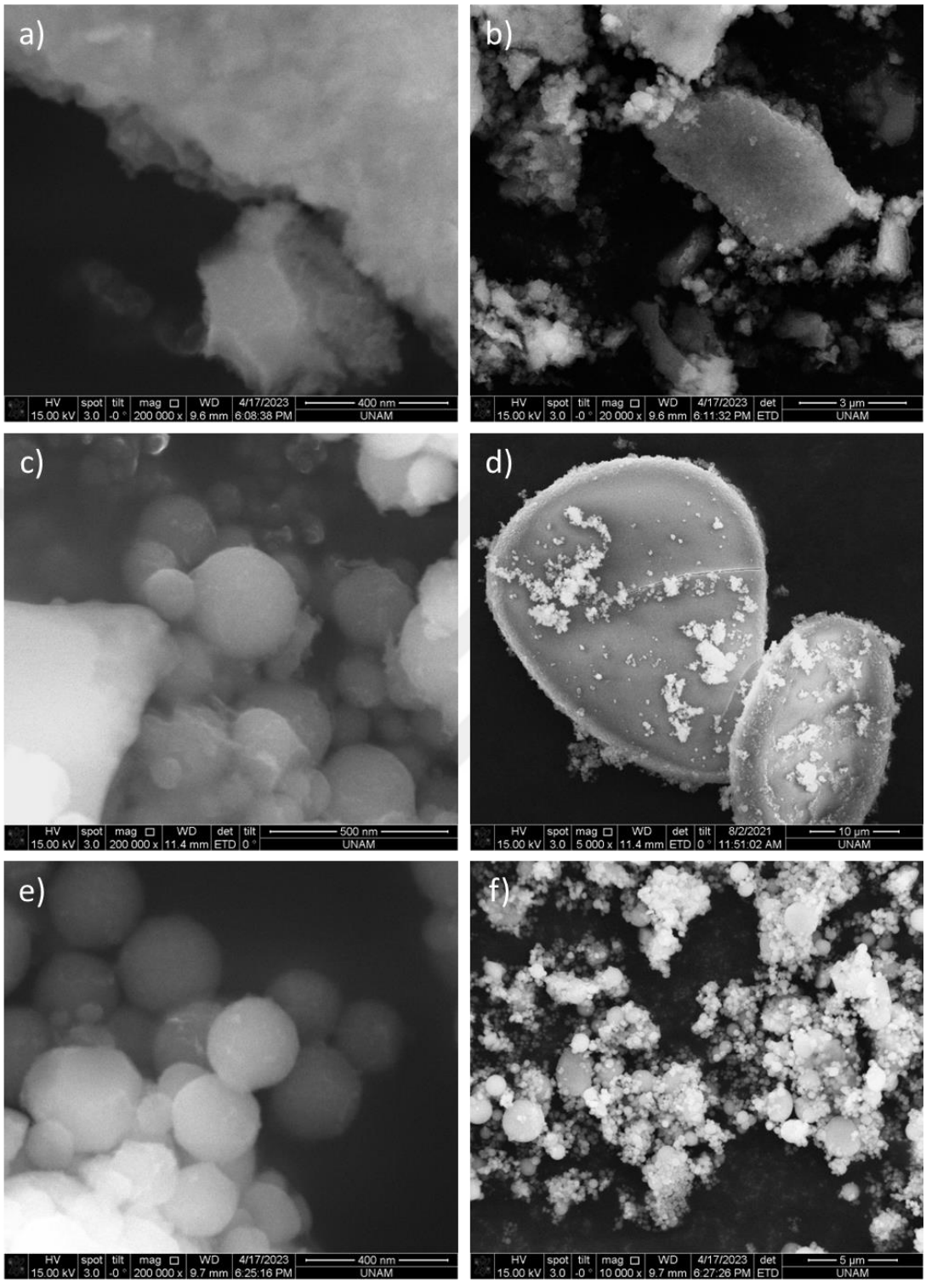

Figure 3.16: SEM images of the a) and b) m-NiPP-30-300, c) and d) m-NiPP-60-300, e) and f) m-NiPP-90-300 samples with scale bars 400 nm, 3 µm, 500 nm, 10 µm, 400 nm, and 5 µm, respectively.

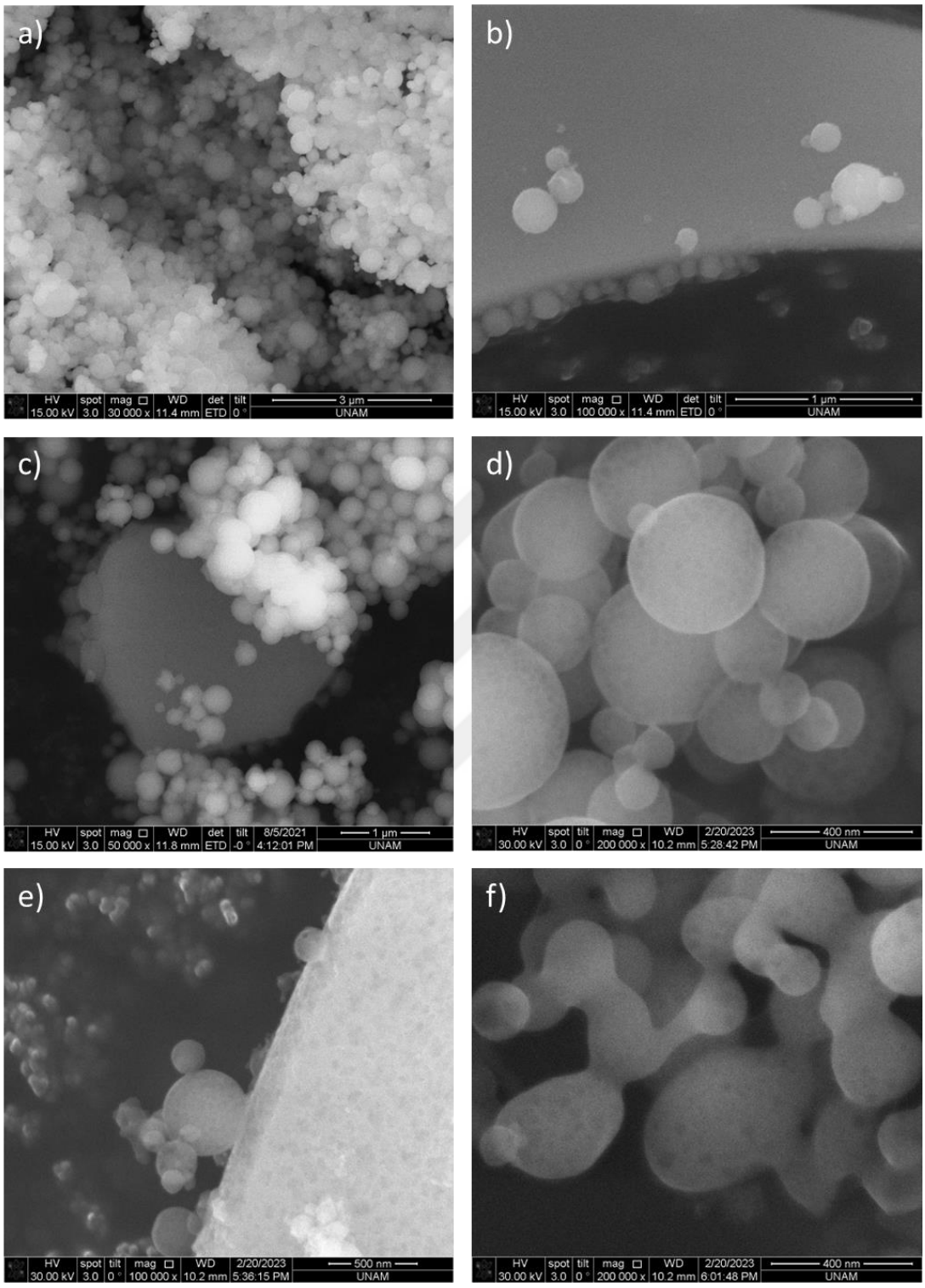

Figure 3.17: SEM images of the a) and b) m-NiPP-60-300, c) m-NiPP-60-400, d) and e) m-NiPP-60-600, and f) m-NiPP-60-700 samples, with scale bars 3 µm, 1 µm, 1 µm, 400 nm, 500 nm, and 400 nm, respectively.

The m-NiPP-n-X samples were further investigated using SEM and TEM imaging techniques to determine their morphology and porosity. Figures 3.16, 3.17, and 3.18 show SEM and TEM images of the m-NiPP-n samples calcined/annealed at different temperatures. Images display two distinct morphologies: spherical particles ranging from 50 to 300 nm in size and film-like particles. There is a morphology change when the mole ratio of the sample is varied from 30 to 90 for the m-NiPP-n-300 samples. The m-NiPP-30-300 sample displays both film-like particles and individual (not perfect) particles, see Figures 3.16 a and b. These particles become mostly perfect spheres by increasing the mole ratio of inorganic ingredients. The m-NiPP-60-300 samples have mostly spherical particles ranging from 50 to 300 nm in size. There are also film-like particles, which are spherical and relatively bigger than other spherical particles, see Figures 3.16 c and d. The m-NiPP-90-300 samples display almost only spherical particles, and the sizes can reach up to 3 μm, given in Figures 3.16 e and f. The effect of the calcination/annealing temperature on the morphology is also illustrated using the m-NiPP-60-X samples since they contain both spherical and film-like particles. There is almost no change in the pore appearance up to 600 ^{o}C. Expansion in the pore size in the samples with increasing the calcination/annealing temperature is clearly visible over 600 ^{o}C even in the SEM images (Figures 3.17 d, e, and f). Since the surface area decreases with increasing annealing temperature, the pores expand and become large enough to observe from both spherical particles and films. The m-NiPP-60 sample is aggregated to each other when calcined at 700 ^{o}C, and the pores are expanded more, which correlates with the N_2-adsorption desorption data. Figure 3.18 shows the TEM images of the spherical particles of m-NiPP-60-300 and m-NiPP-60-700. The particles are perfect spheres at 300 ^{o}C but get distorted and aggregated to each other at 700 ^{o}C. Figure 3.18d shows a high-resolution TEM image of m-NiPP-60-700. The lattice fringes are visible in the image with a lattice distance of 0.298 nm, corresponding (12-2) plane, and the most intense line in the XRD pattern of alpha m-NiPP, see Figure 3.13.

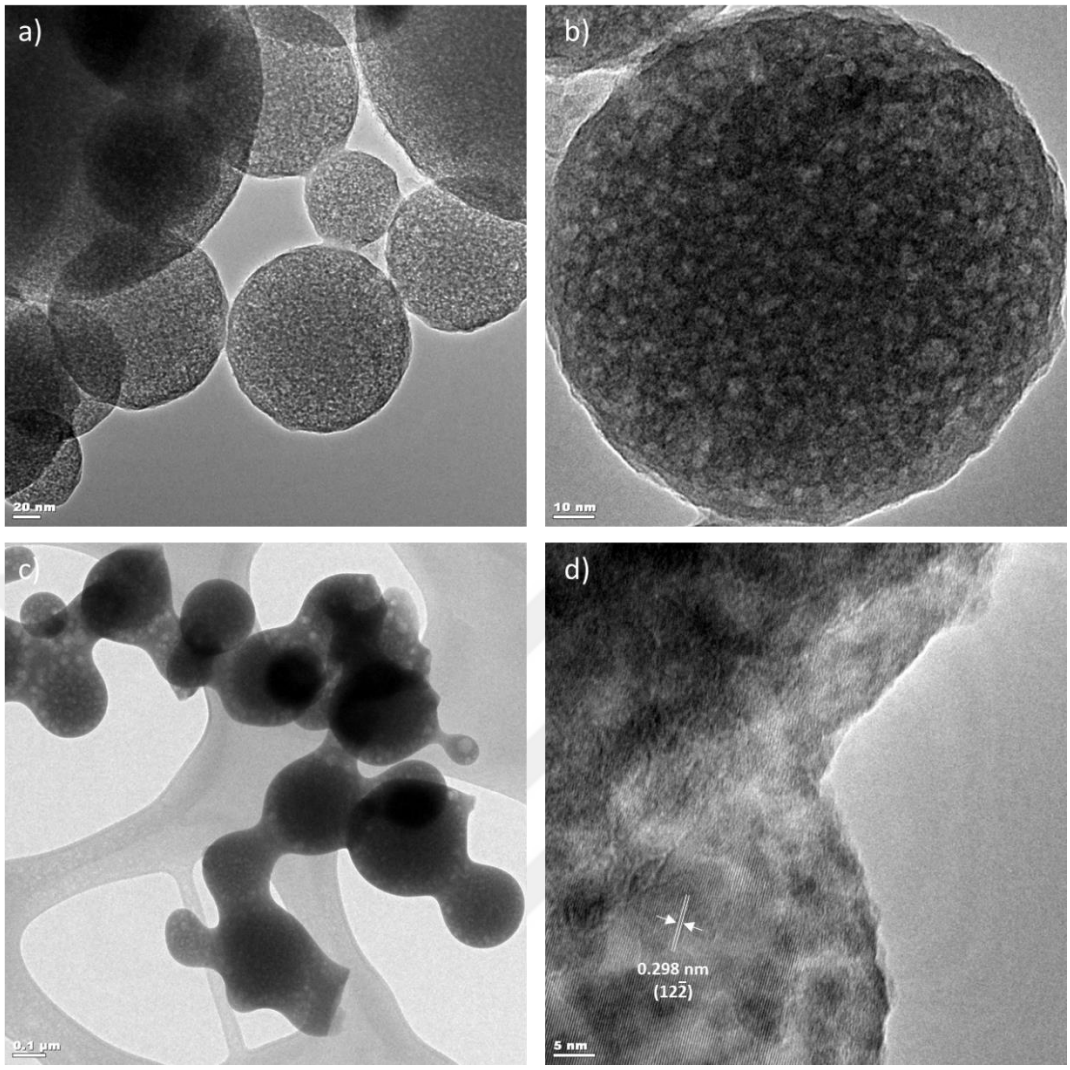

Figure 3.18: TEM images of the a) and b) m-NiPP-60-300 and c) and d) m-NiPP-60-700 spherical particles, with scale bars 20 nm, 20 nm, 100 nm, and 5 nm, respectively.

3.1.3. Electrochemical Characterization of m-NiPP and its Transformation to β-$Ni(OH)_2$

The clear solutions of Ni(II):Acid:P123 are spin-coated over fluorine doped tin oxide (FTO) coated glasses or dip-coated over graphite rods (GR) and calcined at a desired temperature (300 to 700 ^oC) to obtain 1 cm^2 FTO, and GR coated electrodes, abbreviated as FTO-NiPP-n-X and GR-NiPP-n-X (n is Ni(II)/P123 mole ratio in the initial solution, and X is calcination/annealing temperature in Celsius). A 3-electrode system is used in a 3M KOH solution to conduct electrochemical measurements. Three sets of electrodes were fabricated using solutions of NiPP-n, where n is 30, 60, or 90, that display very similar electrochemical behaviors.

Firstly, the FTO-NiPP-n-X electrodes were prepared to collect cyclic voltammograms (CVs), scan rate-dependent CVs, and galvanostatic charge-discharge (GCD) curves at various current densities to evaluate their electrochemical behaviors. Figure 3.19 shows the CVs of the FTO-NiPP-60-X electrodes with a scan rate of 50 mV/s for a potential window of -0.5-2.0 V versus NHE (normal hydrogen electrode) in 3 M KOH solution as an electrolyte. The peaks are the oxidation and reduction peaks of the Ni(II) species at 0.5 and 0.1 V, respectively. The water oxidation reaction starts at around 0.9 V. The oxidation peak potential shifts to more positive potentials while cycling (the oxidation peak overlaps with the water oxidation and makes it difficult to follow). Also, the current density increases due to the transformation of NiPP to nickel hydroxide (which will be discussed later). In further use of the electrode, the current density vanishes over time and disappears in the later cycles, see Figure 3.19. Similarly, there is a shift in the reduction peak potential and a decrease in the current density. The decline of the current densities and disappearance of the peaks indicate that the electrodes, coated on the FTO surface, are unstable to electrochemical cycling, and the electrode material starts falling/dissolving into the electrolyte solution (degradation of the sample).

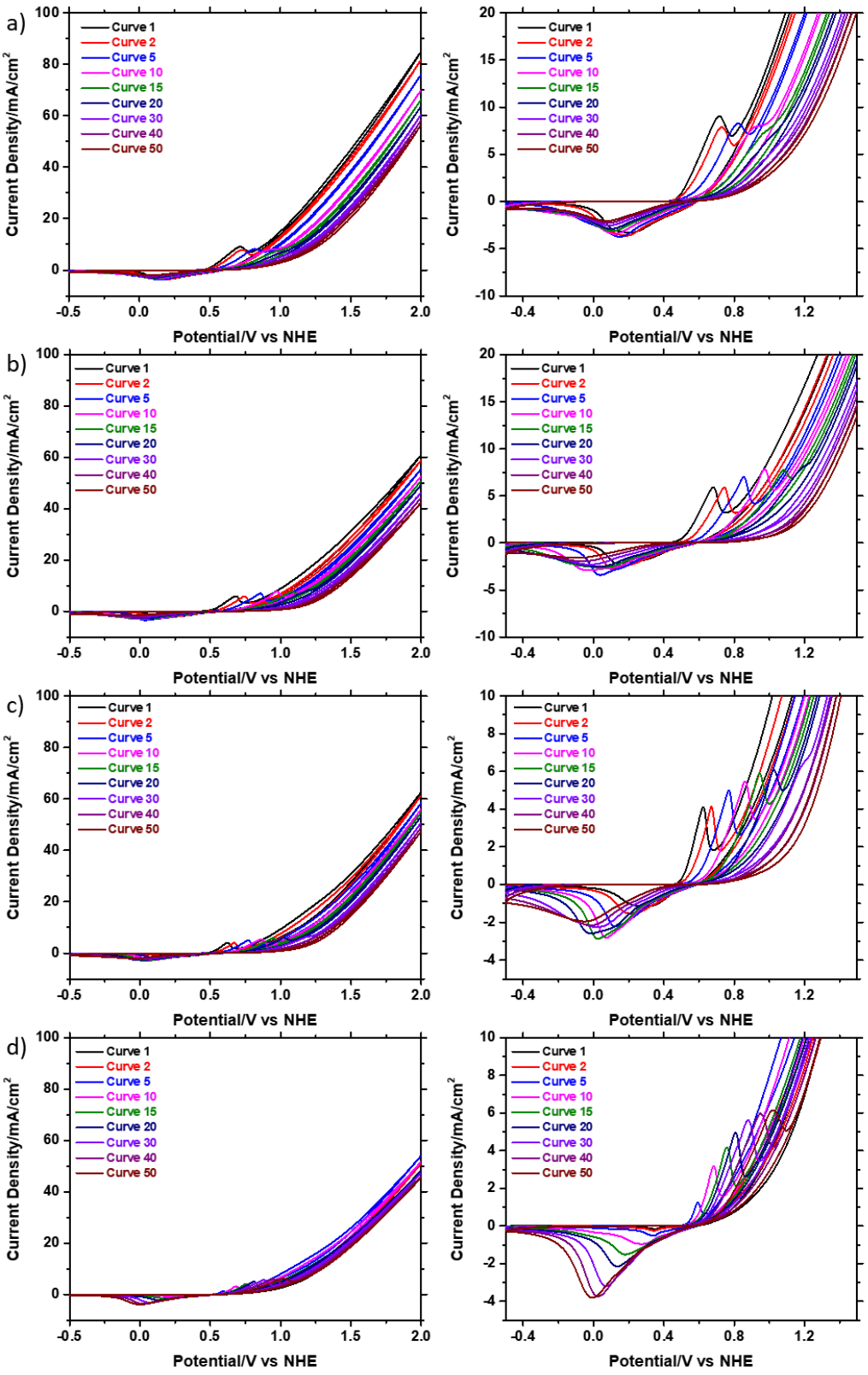

Figure 3.19: 50 CV cycles with a scan rate of 50 mV/s of the FTO-NiPP-60-X electrodes, X is a) 300, b) 400, c) 500, and d) 600 (Right column shows the smaller potential windows of the same CVs in the oxidation-reduction region).

Figure 3.20a shows the current density at the peak maxima of reduction peaks versus time (or cycle number) graph for the FTO-NiPP-60 electrodes, calcined at various temperatures. These plots show that the peak current of the FTO-NiPP-60-300, FTO-NiPP-60-400, and FTO-NiPP-60-500 electrodes first increases (up to the 5th cycle) and then gradually decreases over time (with an increasing number of CV cycles), indicating the transformation and degradation, respectively. The peak current of the FTO-NiPP-60-600 electrode shows only an increasing regime while cycling. The increasing trend proves the transformation of NiPP to $Ni(OH)_2$ and shows that the transformation is slower for the samples calcined at 600 ^oC. It is essential to conclude that increasing the annealing temperature (over 600 ^oC) makes the electrodes more robust to degradation.

The scan rate-dependent CVs are collected from the FTO-NiPP-60-300 electrode for a narrow potential window (-0.1-0.9 V). The measurements are carried in the order of fast (50 mV/s) to slower scan rates by collecting 5 cycles at each scan rate. However, since the electrode is unstable on the FTO surface, the faradaic peaks disappear during cycling after the scan rate of 10 mV/s (see Figure 3.20b).

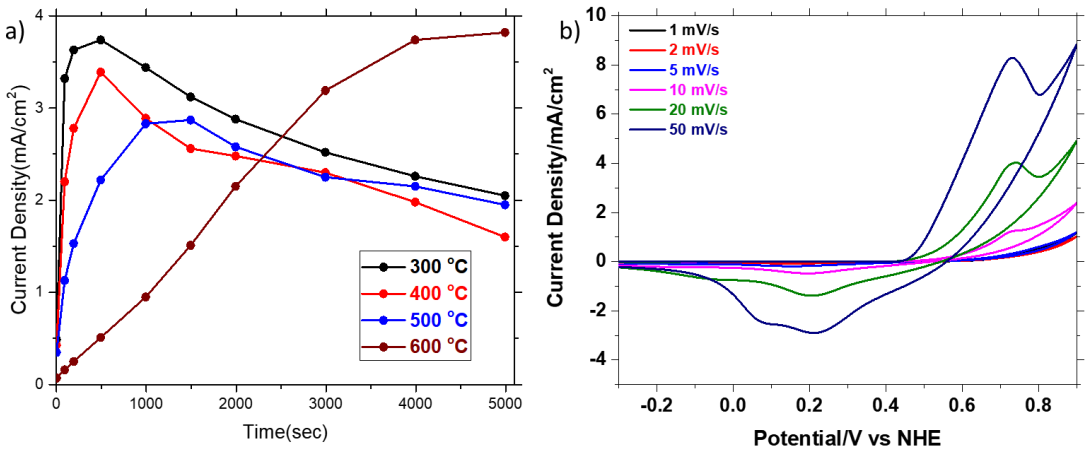

Figure 3.20: Graphs of a) the current density of reduction peak of the FTO-NiPP-60-X (X is 300 to 600^{o}C) versus time and b) the scan rate dependent CVs of the FTO-NiPP-60-300.

Since the FTO is not a suitable substrate for stable electrodes to use in the electrochemical measurements, the pure graphite rod has been used to prepare the working electrodes. The dip-coating method was used to fabricate the graphite electrodes with a pulling speed of 1.45 mm/s. The dip-coating process produces very

thick particles on the graphite surface after calcination and causes material degradation during electrochemical measurement, compare the Figures 3.21 a and b. Therefore, a dilution is needed to the mother solution of Ni(II):P123:PPA. Different concentrations were tested to adjust the optimum thickness by diluting the original solution to avoid large particle formation during calcination. 2-, 5-, 10-, 20- and 50-times diluted solutions were coated for this purpose. The thickness-dependent problem (having big visible particles on graphite) is also encountered from the 2-times diluted solution. The thin films of NiPP-30-300 were obtained using the 10-, 20- and 50-times diluted solutions. The current density in the CVs follows the dilution and drops with dilution number; the film thickness gradually decreases with the dilution, see Figure 3.22.

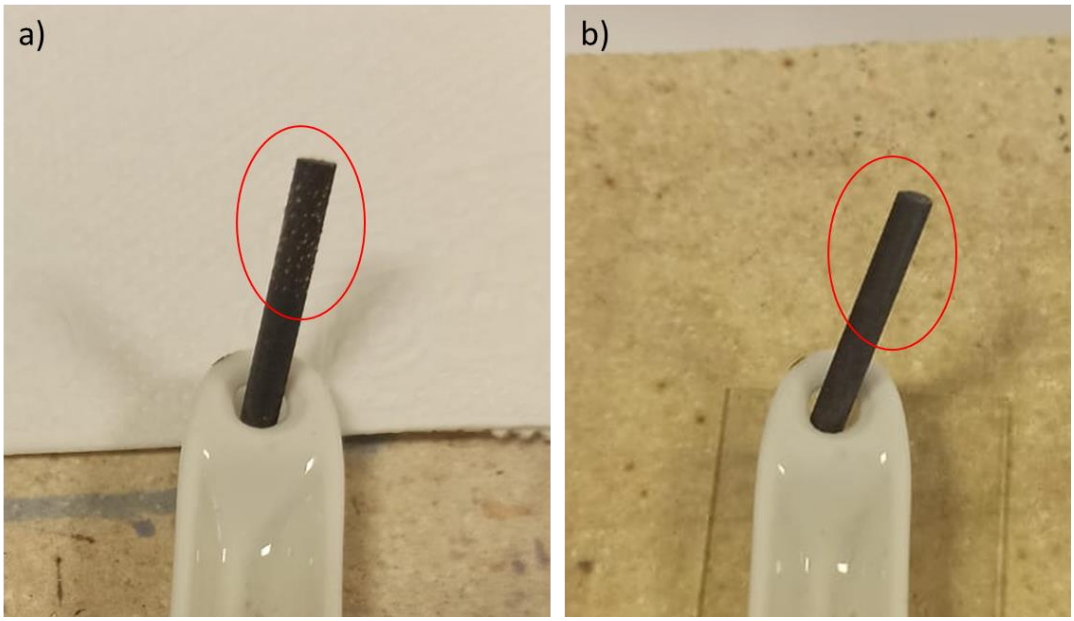

Figure 3.21: Photographs of the GR-NiPP-30-300 electrodes obtained from a) mother liquor and b) 5 times diluted solution.

Since the dilution gives very thin films on the substrate, a very broad additional oxidation peak (at around 0.2 V) appears in the CVs in addition to the faradaic couple of Ni(II) species, which might be originated from the deintercalation of potassium ions that are intercalated during application of the negative potentials (reverse process) to the electrodes. The CVs of pure graphite, calcined at 300 ^{o}C, are also collected to elucidate the origin of this broad peak. The same oxidation peak appears with cycling in a potential window of -0.5-1.5 V vs. NHE, see Figure 3.23c. Moreover, this is also

tested using the GR-NiPP-30-300 electrode, prepared from a 20-times diluted solution. The same broad peak is visible in the CVs of this electrode in the range of -0.5-1.5 V vs. NHE. Without changing the setup, the same electrode is used in the potential window of 0.0-1.5 V vs. NHE, and it is found that the broad peak disappears in the CVs if the reverse cycle is not carried, compare Figures 3.23 a and b. This proves that the broad peak comes from the graphite-originated (or potassium intercalation to the graphite) species when the negative potentials are applied. After these analyses, the 5-times diluted solutions are selected for the GR-NiPP-30 electrode preparations and electrochemical tests. Note also that the 10- and 15-times diluted solutions were used to fabricate the GR-NiPP-60 and GR-NiPP-90 electrodes, respectively.

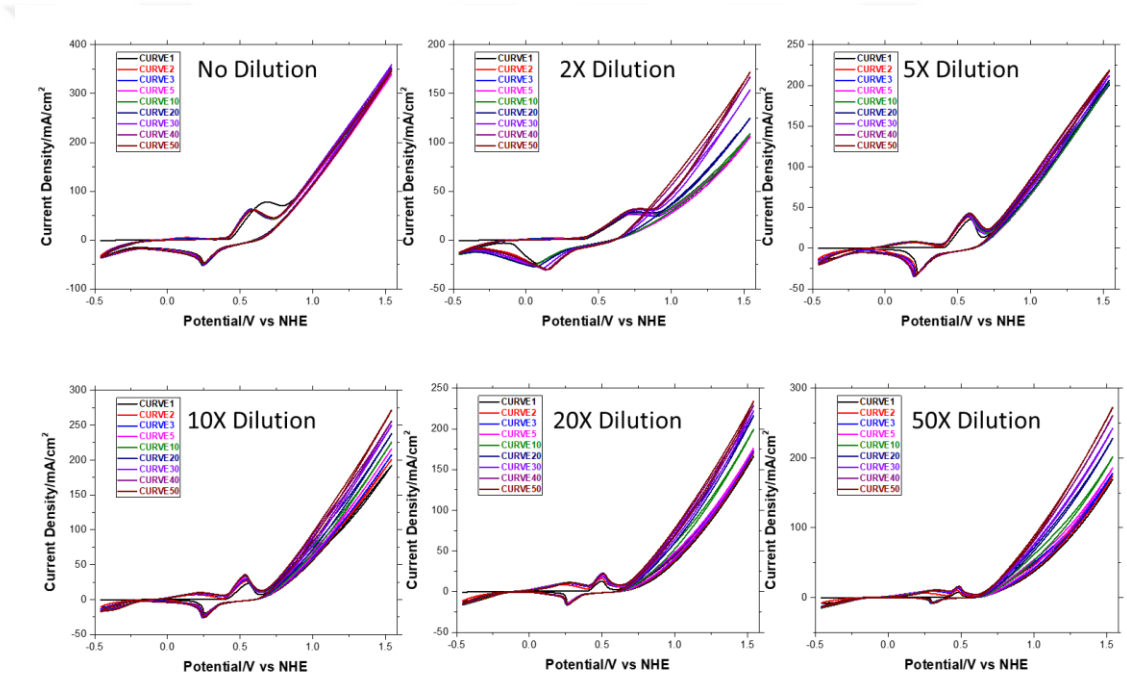

Figure 3.22: CV cycles of the GR-NiPP-30-300 electrodes, prepared from different concentrations of the same solution.

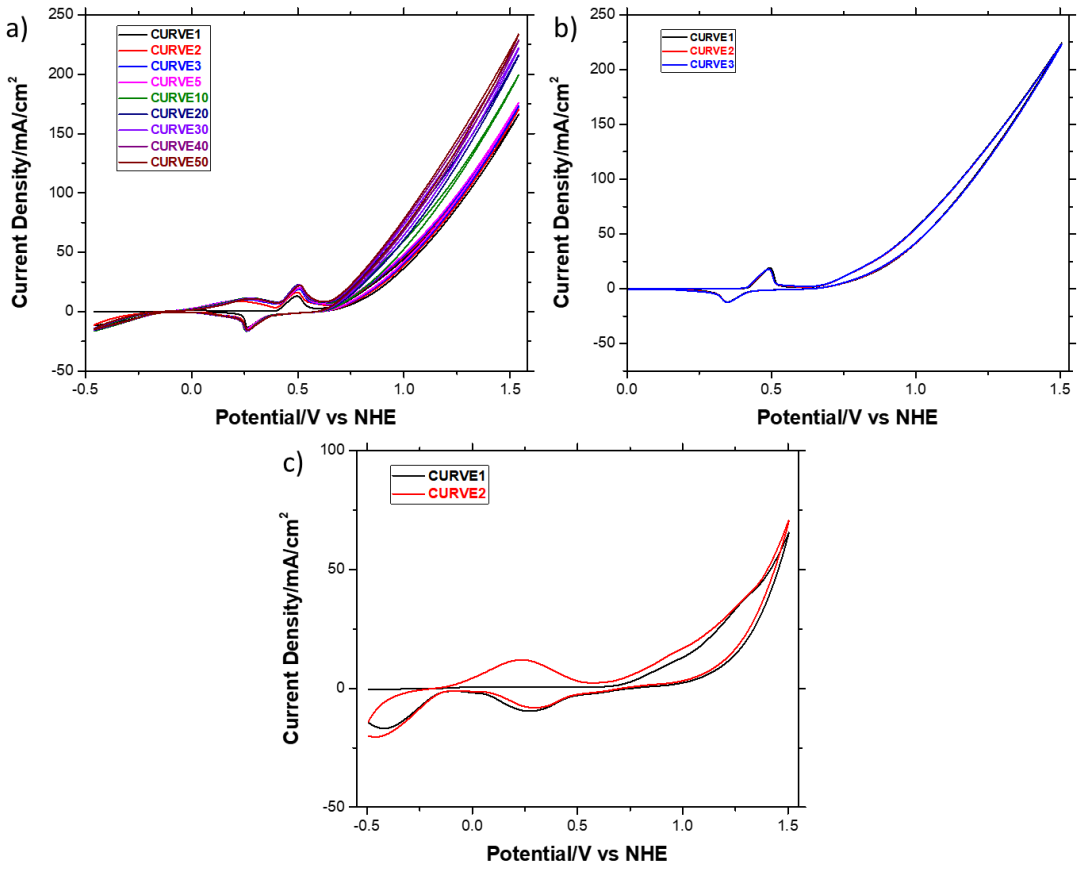

Figure 3.23: CV cycles of the GR-NiPP-30-300 electrode, fabricated from 20-times diluted solution in the potential windows of a) -0.5-1.5 V, b) 0.0-1.5 V, after 50 cycles, c) the CV cycles of the pure graphite electrode, calcined at 300 ^{o}C.

The weights of the NiPP over 1 cm^2 FTO electrodes are measured as 0.2, 0.3, and 0.4 mg (calculated by taking the average of 10 same electrodes) in the FTO-NiPP-30-300, FTO-NiPP-60-300, and FTO-NiPP-90-300 electrodes, respectively. Moreover, the weight of a 1 cm^2 coated GR-NiPP-30-300 electrode, using 5 times diluted solution, is measured as 0.4 mg (by taking the average of 4 coated electrodes). It is consistent with the electrochemically calculated value. The current density of the oxidation peak of the electrodes fabricated from each diluted solution is plotted against the number of dilutions. A linear correlation was found between the ln(1/ND) (ND is the number of dilutions) and current density, see Figure 3.24. The plot, shown in Figure 3.24b, can be used as a calibration curve to determine the electrodes' relative thickness (or amount of material on GR) and could also be used by simply measuring the current density of the electrode made using any solution.

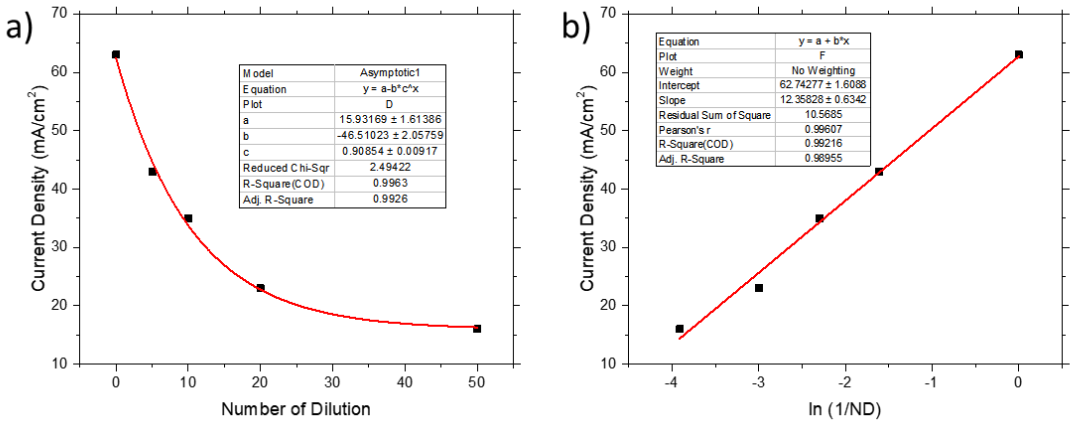

Figure 3.24: Graphs of a) current density versus the number of dilutions and b) current density versus ln(1/ND).

CV curves of the GR-NiPP-30-X (X varies between 300 and 700 ^{o}C) are collected to understand the role of the annealing/calcination temperature on the electrochemical behaviors, see Figure 3.25. For this purpose, 5 times diluted 30 Ni(II)/P123 solution was coated over pure graphite rods and calcined at different temperatures. Generally, the NiPP-30 sample was used for the electrochemical process since this sample's surface area is the highest in the nickel system. The electrodes, prepared at desired temperatures, were tested with a scan rate of 50 mV/s for 50 cycles in a potential window of -0.5-1.5 V vs. Ag/AgCl in 3M KOH solution. The peak maxima of oxidation current gradually increases with use (with cycle number) and becomes stable in further cycles. The faradaic oxidation peak, observed at around 0.6 V in the CVs at all annealing temperatures, is due to the oxidation of Ni^{2+} to Ni^{3+} and maybe Ni^{3+} to Ni^{4+}.[25] The sharp increase in the current density after 0.8 V is due to water oxidation. High current density at a relatively low overpotential indicates that the electrodes are also excellent electro-catalysts for the water oxidation reaction. It has been shown that the CV curves differ slightly with increasing calcination temperature of the electrodes, even though the surface area of the NiPP material decreases gradually while increasing the calcination temperature. The oxidation peak of the Ni^{2+} species of the GR-NiPP-30-300 electrode is first observed at a relatively high current density that slightly increases. At higher temperatures, the oxidation peak of Ni^{2+} species displays lower current densities at an early stage of cycling but increases in later cycling to similar values. Therefore, it is reasonable to conclude that

the amorphous electrodes (GR-NiPP-30-X, X is between 300 and 600 ºC) transform quickly to a more active form. In contrast, the crystalline electrode (GR-NiPP-30-700) produces the same active material in a much longer use (see latter). Moreover, water oxidation efficiency is enhanced by cycling the electrodes prepared at a higher temperature. Since the oxidation peak current density increases by cycling, the current density vs. cycle number was also plotted to elucidate the likely reaction mechanism, see Figure 3.26. The transformation reaction gets slower by increasing the calcination temperature. At 300 and 400 ºC, the reaction is almost complete after a few cycles. However, the electrodes prepared at higher temperatures take much longer to reach the same current density.

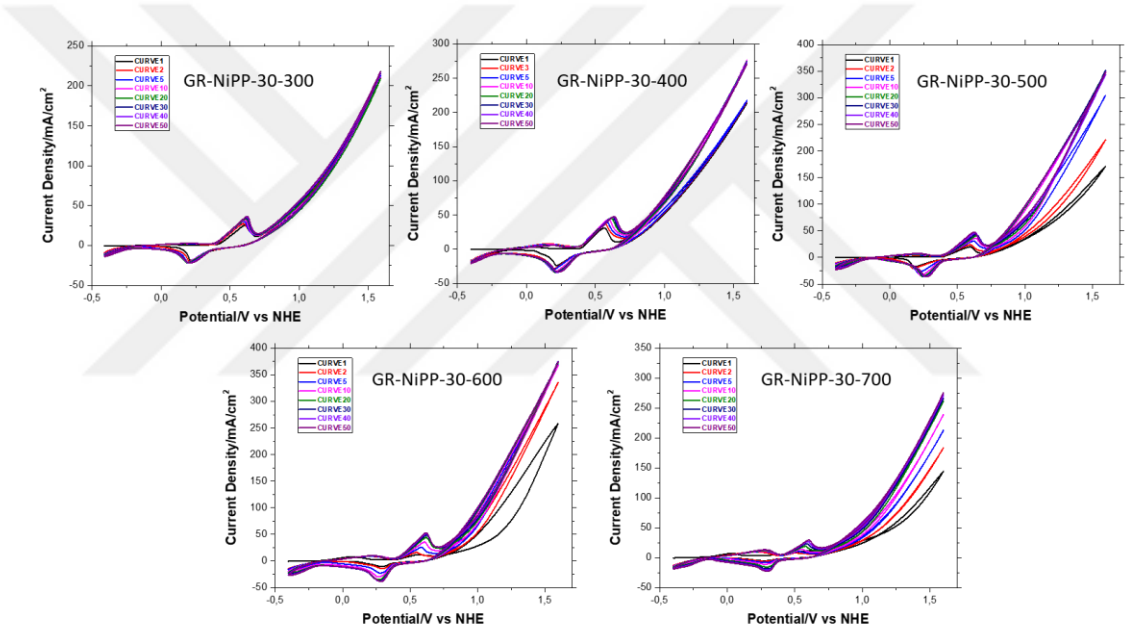

Figure 3.25: CV cycles with a scan rate of 50 mV/s of the GR-NiPP-30-X electrodes (X is indicated on each panel).

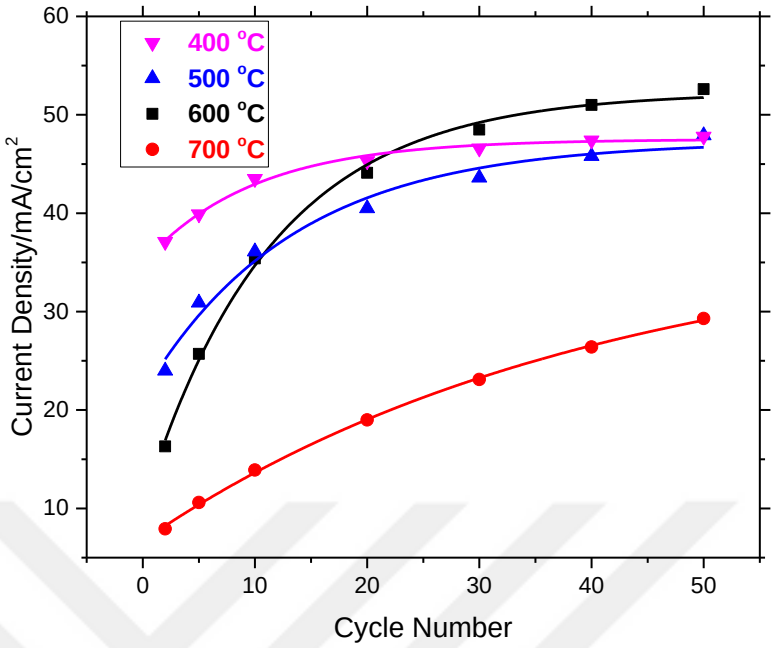

Figure 3.26: Graph of current densities of oxidation peak maxima of the GR-NiPP-30-X electrodes (X is 400, 500, 600, and 700) versus cycle number.

After 50 CV cycles at a scan rate of 50 mV/s, the same electrode was used to perform scan rate-dependent measurements in a narrow potential window that includes oxidation-reduction peaks. This analysis aimed not only to find the proper potential range for the galvanostatic charge-discharge measurements but also to get information about the active surface coverage of the material. If the scan rate versus current density is plotted, it gives a linear relationship with a slope that provides information on the surface coverage (Γ), see eq. 1.2 and 1.3 in the introduction part. Suppose the scan rate versus the current density plot is not linear. In that case, the oxidation/reduction process may be diffusion-limited, having linearity in the current density versus the square root of the scan rate plot, see eq. 1.4. Figure 3.27 displays the scan rate-dependent CV curves (left column), plots of current density versus scan rate (middle column), and the square root of scan rates (right column) of the GR-NiPP-30-X electrodes (X varied between 300 and 700 ^{o}C). The scan rate-dependent CV curves were collected from the fast scan rate (50 mV/s) to the slower ones. Since the scan rate versus current density is not linear, the square root of scan rate versus current density is plotted and found a linear relationship, indicating a diffusion-controlled mechanism

in the oxidation process, see the right column in Figure 3.27. It could be the diffusion of OH^- ions into the electrode in the oxidation process. This diffusion could be between ultra-thin nanoflakes of $Ni(OH)_2$ particles. When the plots of all electrodes, calcined at all temperatures, are compared in the same graph, it is found that there are some differences among these electrodes. They differ in oxidation and reduction regions in terms of both the shape of the peaks and current densities. Moreover, the graphs of scan rate and the square root of scan rate versus current density are also slightly different at each temperature. These may originate due to differences in the resistance of the electrodes that are hard to control even for the same composition and annealing temperature and also some changes in the transformation of NiPP to $Ni(OH)_2$.

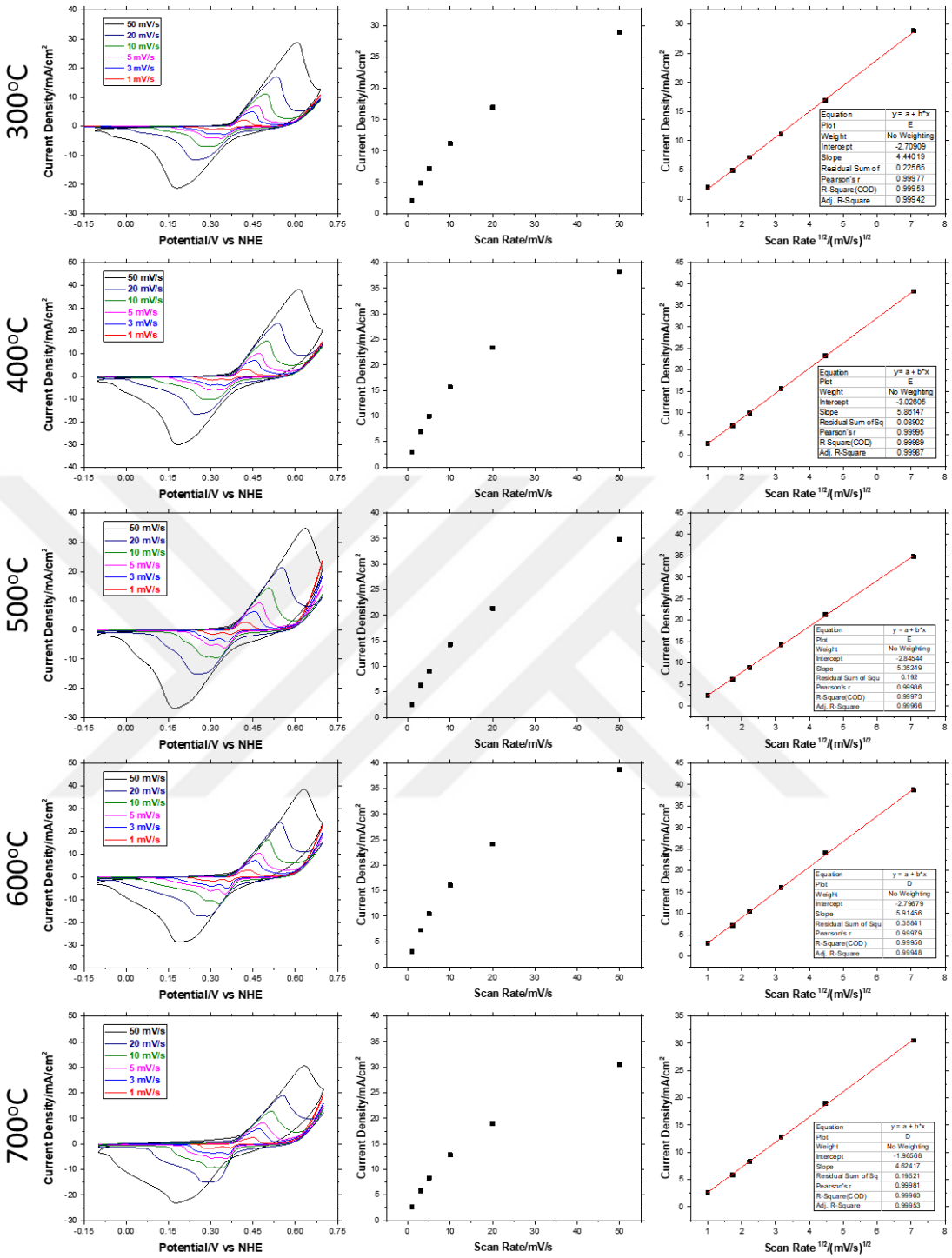

Figure 3.27: (Left column) Scan rate dependent CV curves, (middle column) the plots of current density versus scan rate, and (right column) the plots of current density versus square root of scan rate of the GR-NiPP-30-X electrodes (X values are shown on the left).

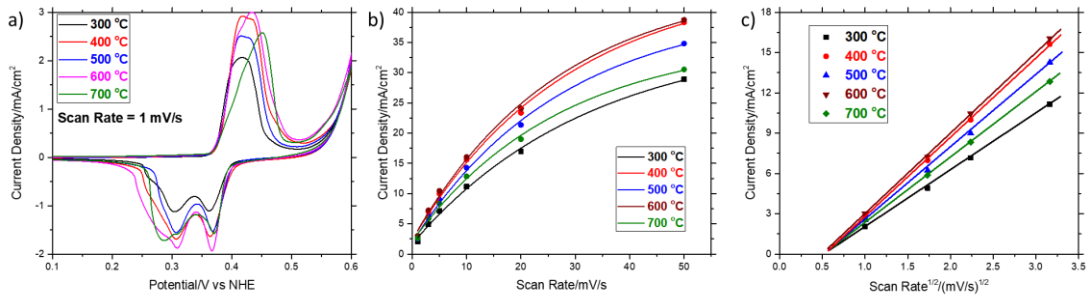

Figure 3.28: Comparison of calcination temperatures on a) CV at a 1 mV/s scan rate (recorded after 50 cycles at 50 mV/s), b) current density vs. scan rate, and c) current density vs. square root of scan rate (lines are best fits).

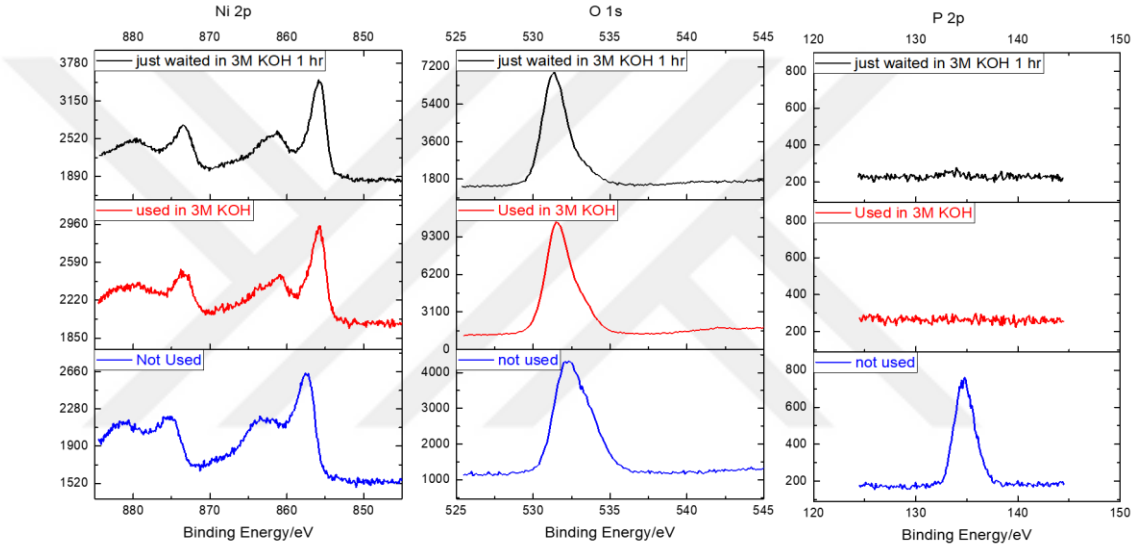

Figure 3.29: XPS spectra of the m-NiPP electrodes: (blue) before CVs, (red) m-NiPP after CVs, and (black) after keeping in 3M KOH for 1 h with (left) Ni 2p, (middle) O 1s, and (right) P 2p regions.

The used m-NiPP electrodes were further characterized to fully understand the origin of the changes (increases of the current densities) in the CVs by recording their XPS spectra, see Figure 3.29. Surprisingly, the phosphorus 2p peak in spectra disappeared after using the electrode in the CV measurements. Figure 3.29 shows the XPS spectra in the Ni 2p, O 1s, and P 2p regions before (blue spectra) and after CVs (red spectra). The Ni 2p peaks almost do not change before and after CVs (it only shifts about 2 eV). This could be due to the oxidation of Ni^{2+} species after CVs. The O 1s peak becomes sharper and shifts to higher binding energy and is observed at 532.2 and 531.5 eV for the electrodes before and after CVs, respectively. However, the P 2p peak completely disappears, indicating a transformation of NiPP to phosphorous-free

material (likely $Ni(OH)_2$, see latter). Note also that the Ni 2p and O 1s regions are very similar to the spectra of $Ni(OH)_2$.[165] Moreover, the O 1s region peaks at 531.5 eV with a shoulder on the high-energy side due to hydroxide and coordinated water. [166] Furthermore, the electrodes were aged in a 3M KOH solution for 1 h without potential application. Then, their XPS spectrum was also collected (see black spectra in Figure 3.29) to show that this is a chemical reaction of NiPP in a KOH solution, not an electrochemical transformation. The spectra in all three regions are identical in electrochemically (after CVs) and chemically (just aged in basic medium) obtained samples. Therefore, it is reasonable to suggest the following chemical equilibrium reaction (eq. 3.3) for the chemical transformation reaction.

$$Ni_2P_2O_7(s) + 4OH^-(aq) \leftrightarrow 2Ni(OH)_2(s) + P_2O_7^{4-}(aq) \qquad \text{eq. 3.3}$$

The disappearance of phosphorous from the NiPP sample after electrochemical measurements is also confirmed by EDX analysis. Figure 3.30a shows that the P and Ni amounts are comparable (almost 1 to 1 to keep stoichiometry) in the EDX spectrum regarding their intensities before use. However, the phosphorous peak completely disappears after CV measurements since the reaction in eq. 3.3 takes place, see Figure 3.30b. Note that a trace amount of potassium in the spectrum (Figure 3.30b) originates from the unwashed KOH crystals or $KHCO_3$ formation (see latter).

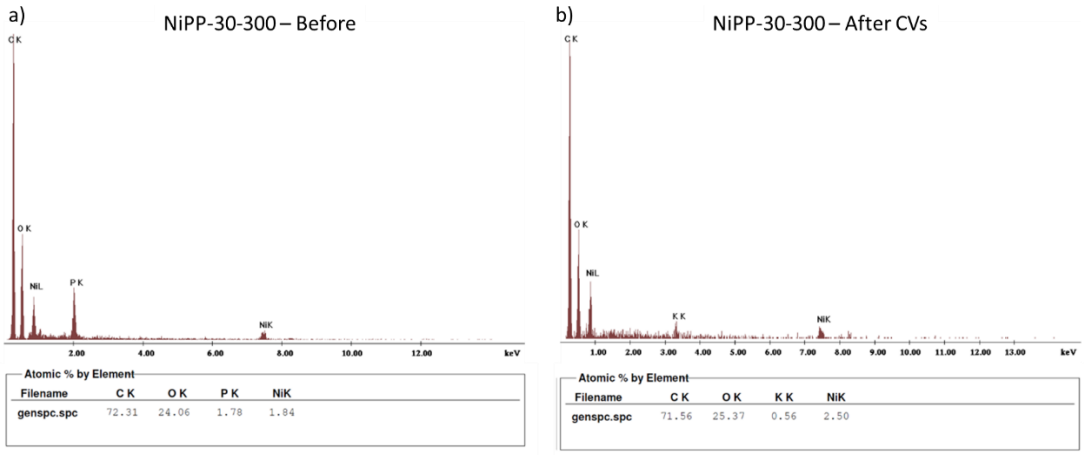

Figure 3.30: EDX spectra of the m-NiPP-30-300 electrode (a) before and (b) after CV measurements with atomic percentages of elements.

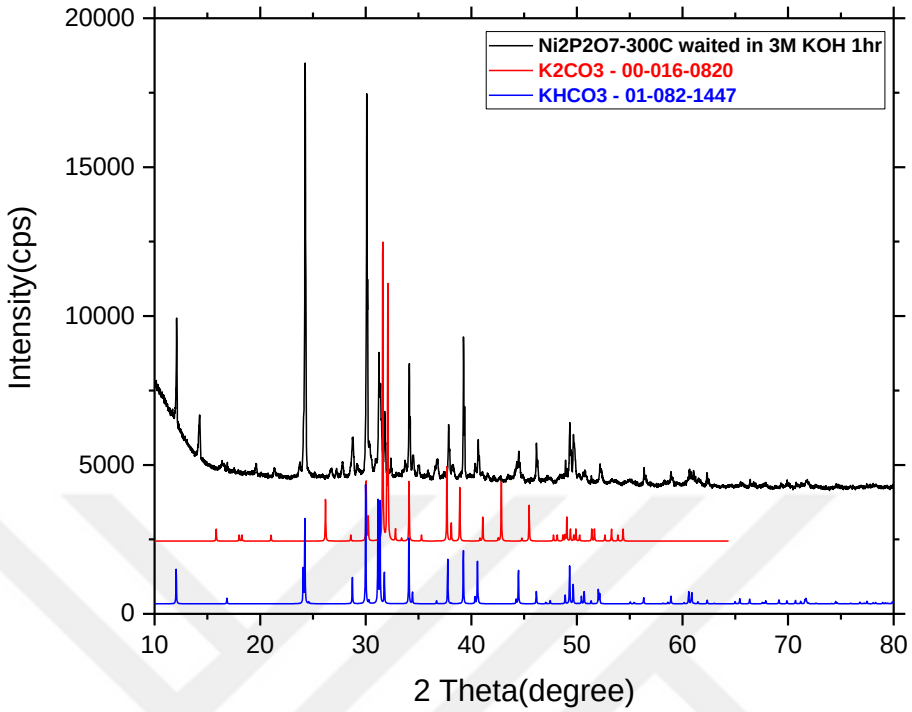

Figure 3.31: Wide-angle XRD pattern of the m-NiPP-60-300 after treatment in 3M KOH for 1 h (black) at the laboratory conditions with the corresponding references of $KHCO_3$ (ICDD-01-082-1447) (blue) and K_2CO_3 (ICDD- 00-016-0820) (red).

The used electrodes and large amounts of NiPP powder samples were further analyzed using XRD, ATR-FTIR, and TEM imaging techniques to elucidate details of the above chemical transformation of NiPP to $Ni(OH)_2$ (see eq. 3.3). Firstly, the calcined m-NiPP sample is kept in 3M KOH solution without scratching from the glass slide in laboratory conditions without covering the top of the solution. In that case, it is hard to prevent the formation of crystalline carbonate species (namely K_2CO_3 and $KHCO_3$) from the sample even after several washing processes. The XRD pattern of this sample shows only the big crystals of those undesired materials, see Figure 3.31. Instead, the calcined sample should be collected from the substrate to obtain a powder form. A closed system (like a centrifuge tube with its cap) is used to transform m-NiPP to its hydroxide in a 3M KOH solution to achieve a pure hydroxide structure without undesired crystals. Time-dependent XRD patterns of the powder samples for aging in 3M KOH solution in a closed system were collected to understand the transformation mechanism more deeply, see Figure 3.32. The carbon dioxide protected transformation

produces a pure beta nickel hydroxide. The transformation takes longer since the amount of m-NiPP is much larger than a single electrode. After 30 minutes of aging, m-NiPP just starts converting into a nickel hydroxide structure that displays very broad diffraction lines due to (100), (101), and (110) planes. However, after 1 h, it is completely converted to the beta phase, see Figure 3.32. When the XRD lines are analyzed, it is found that the planes related to the c-axis are pretty broad compared to the others (compare sharp (100) and (110) planes with the planes related to the c-axis). This means that only a few nanometers thick $Ni(OH)_2$ flakes are produced after complete transformation. Fitting the (100) and (101) lines give a full-width half-maximum (FWHM) of 1.25 and 5.85^o along the a, b, and c axis, respectively. Calculation using the Scherer equation (eq. 3.4);

$$\boldsymbol{D(nm) = \frac{K\lambda}{\beta \cos\theta} = \frac{0.94 \times 1.5406}{FWHM \times \cos\theta}} \qquad \textbf{eq. 3.4}$$

Where D is the mean size of the crystalline domains, K is a dimensionless shape factor, λ is the wavelength of the X-ray, β is the line broadening at half the maximum intensity (FWHM), and θ is the Bragg's angle. The FWHM gives that the β-$Ni(OH)_2$ nanoparticles are 7 nm wide (a = b = 3.125 Å) and 1.5 nm thick (c-axis, c = 4.605 Å).[121] This corresponds to only 3-4 layers thick and about 20-22 unit cell-wide particles.

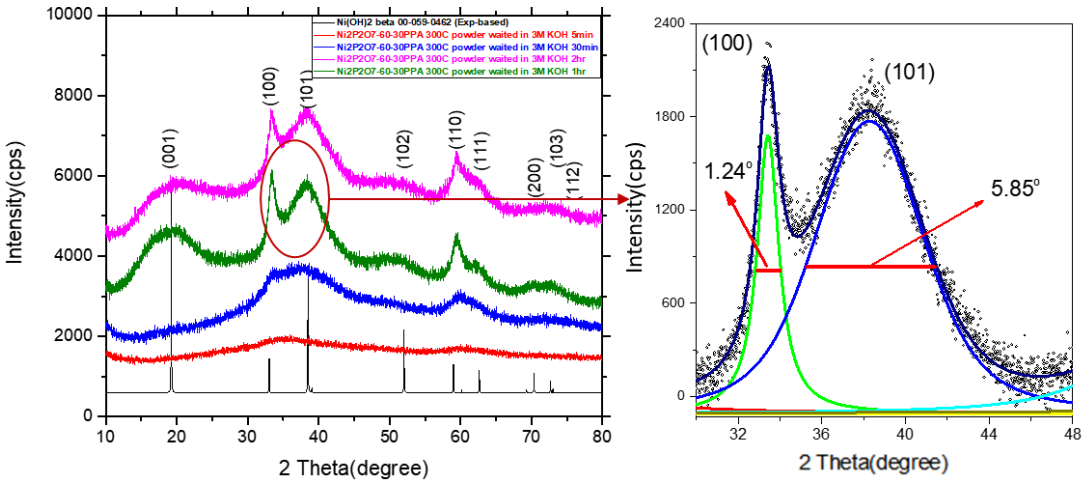

Figure 3.32: Wide-angle XRD patterns of the m-NiPP-60-300 after treatment in 3M KOH for 5 min, 30 min, 1 h, and 2 h in a close system and corresponding to reference of β-$Ni(OH)_2$ (ICDD- 00-059-0462).

The carbonate formation during the transformation reaction of metal pyrophosphate to hydroxide was also analyzed by ATR-FTIR spectroscopy. Figure 3.33a shows the ATR-FTIR spectra of the m-NiPP-300 before and after aging the sample on a microscope slide in a 3M KOH solution and a drop of the KOH solution upon drying. Spectra of the aged and pure dried KOH samples have similar features at around 1400 cm^{-1} and originate from the same species ($KHCO_3$ and K_2CO_3 crystals), formed during the drying step by absorbing carbon dioxide from the laboratory atmosphere. [167] This also accords well with the XRD data that the sharp diffraction lines originate from the $KHCO_3$ and K_2CO_3 crystals. The ATR-FTIR spectra of the calcined samples scratched from the substrate, aged in a closed system, and washed carefully were also collected and compared with the sample before being aged in 3 M KOH solution. Time-dependent ATR-FTIR spectra display a gradual decreasing PP peaks (at 1030, 928, 744, and 548 cm^{-1}), an increasing peaks at 3643 cm^{-1} due to $Ni(OH)_2$ (water-free), and strongly hydrogen-bonded water and hydrated hydroxides (at 2976 and 3125, and 1645 cm^{-1}), carbonate, bicarbonate peaks (at around 1400 and 1580 cm^{-1}) and Ni-O peaks (at about 440-650 cm^{-1}), see Figure 3.33b. Even though the powder samples are aged in a closed system and washed carefully, there is still a carbonate and bicarbonate formation (see around 1400 and 1580 cm^{-1}), which is hard to eliminate. However, since the amounts of those species are relatively low, they are under the detection limits of XRD, or these carbonate species are surface carbonates

and bicarbonates. Therefore, $KHCO_3$ and K_2CO_3 crystals are not visible in the XRD patterns of those samples, see Figure 3.32.

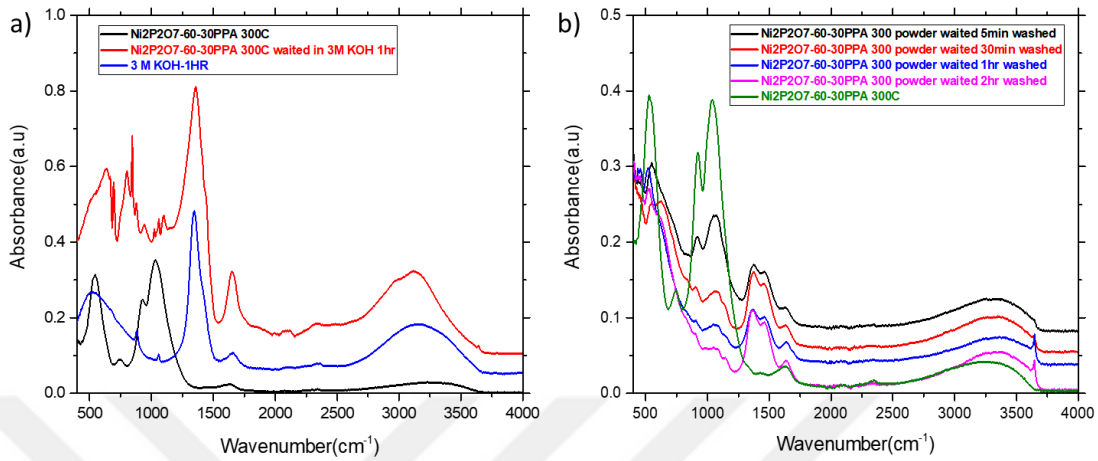

Figure 3.33: ATR-FTIR spectra of the m-NiPP-60-300 a) before hydroxide treatment (black) and after aging in 3M KOH without scraping the powder (red) and 1 h aging on ATR diamond (blue) and b) the time-dependent spectra of the m-NiPP-60-300 aged in 3 M KOH as a powder form.

There is a significant difference between the m-NiPP-300 and m-NiPP-700 samples regarding the transformation reaction. The NiPP samples, calcined at 300 ^oC, transform to their hydroxides much faster than their 700 ^oC calcined sample. Aging of the m-NiPP-700 in 3M KOH solution for 1 h is not enough to convert all pyrophosphates to hydroxide. The NiPP-700 sample has no hydroxide formation in the same period, see the XRD patterns in Figure 3.34. The NiPP-700 sample aged in 3M KOH solution for a very long time (about 3 days), and only a small amount of beta nickel hydroxide is observed in the XRD pattern. The aging process was repeated by changing the KOH solution every 1 h with a fresh KOH solution; the repeating process did not help to convert all NiPP to $Ni(OH)_2$ (not shown). It isn't easy to completely transform the NiPP-700 sample if a large amount of NiPP is used. Using the XRD and ATR-FTIR data, we estimated the solubility product of the NiPP sample, which is around 10^{-29} (see later) and much lower than the solubility product of $Ni(OH)_2$, which is 5.48×10^{-16}.[168] The transformation strongly depends on the amount of NiPP powder and the concentration and volume of the KOH solution. Almost 3 L of 3M KOH solution is needed to fully convert all pyrophosphates for 40 mg of NiPP powder to the hydroxide (see later).

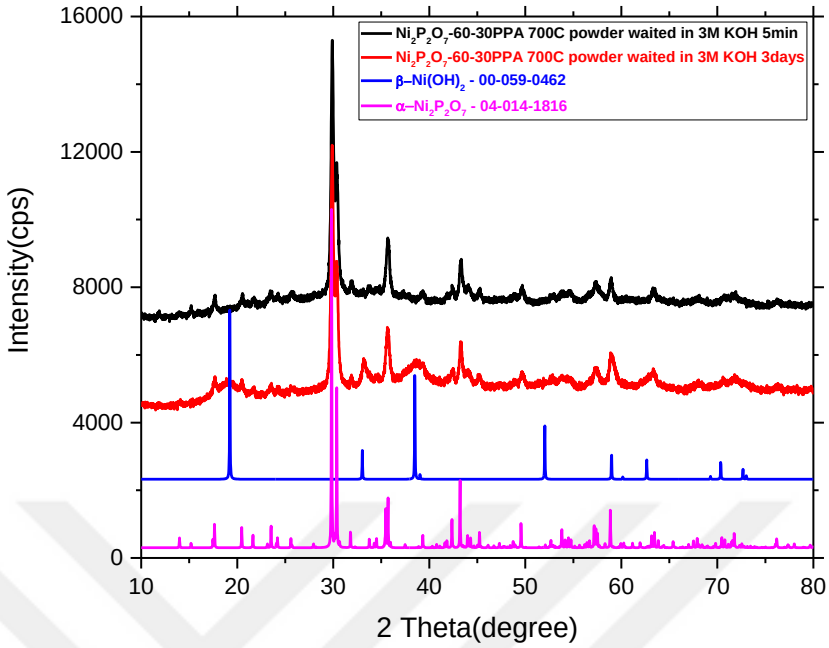

Figure 3.34: Wide-angle XRD patterns of the m-NiPP-60-700 sample after treatment in 3M KOH (black) for 5 min, (red) 3 days in a close system and corresponding references of β-$Ni(OH)_2$ (ICDD- 00-059-0462) and α-$Ni_2P_2O_7$ (ICDD 00-039-0710).

The m-NiPP-300 and m-NiPP-700 samples were aged in a 3M KOH solution separately for 5 min and 1 h, and their TEM images were also collected, see Figure 3.35. After 5 min aging in 3M KOH solution, the spherical morphology of the NiPP-300 particles was preserved with additional flake-like particles on the surface due to the formation of the $Ni(OH)_2$ particles. After 1 h aging in the KOH solution, the particles of NiPP-300 still keep their spherical morphology, but a clear majority is converted into β-$Ni(OH)_2$ particles, which is also demonstrated by the XRD patterns and ATR-FTIR spectra, compare Figures 3.32 and 3.33b. TEM image of the m-NiPP-700 sample aged for 1 h in KOH solution also shows needle/flake-like features of $Ni(OH)_2$ particles on top of the m-NiPP sample since in the m-NiPP-700 sample there is no complete conversion.

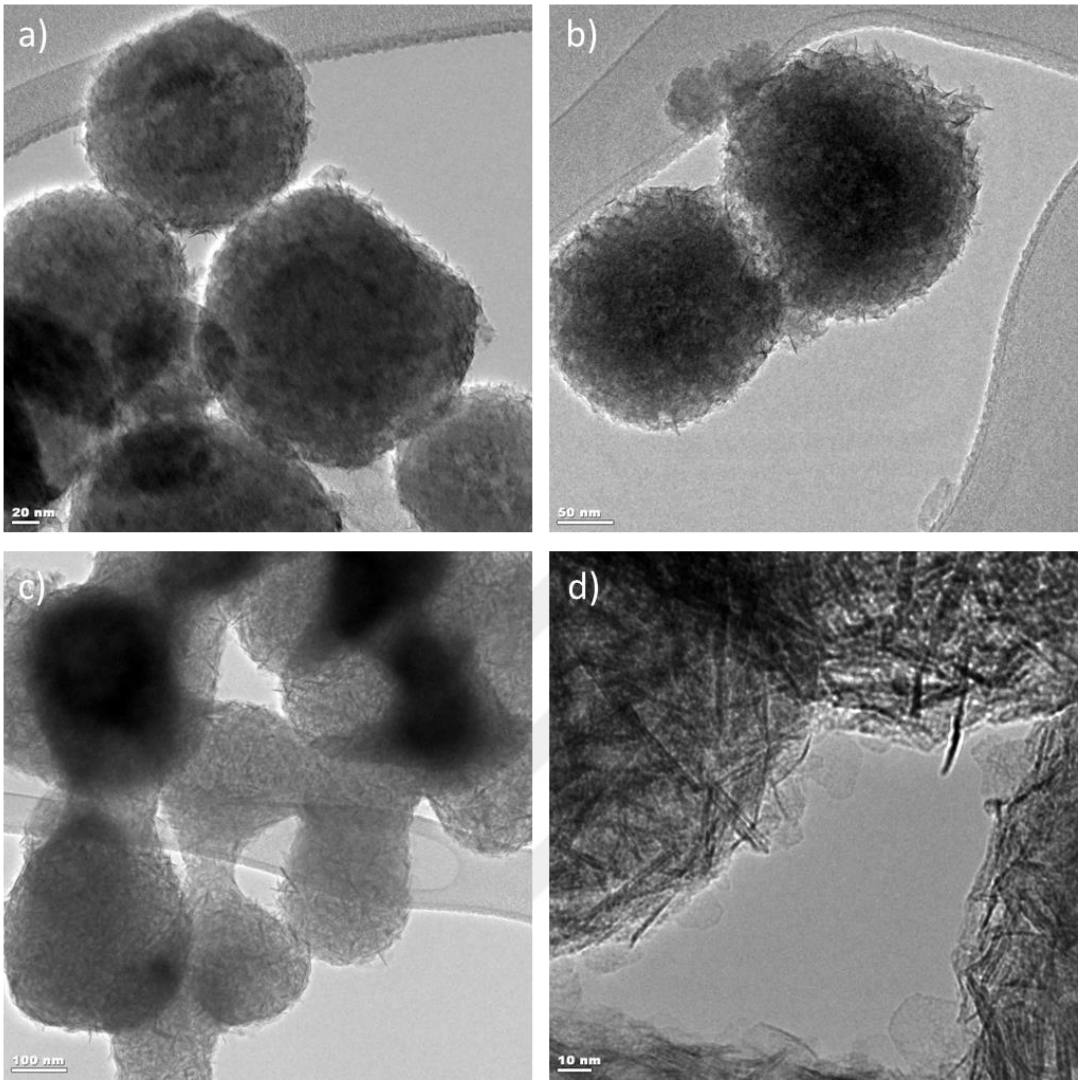

Figure 3.35: TEM images of the m-NiPP-60-300 aged in 3M KOH solution for (a) 5 and (b) 60 mins and (c and d) m-NiPP-60-700 aged in 3M KOH for 60 min, with scale bars 20 nm, 50 nm, 100 nm, and 10 nm, respectively.

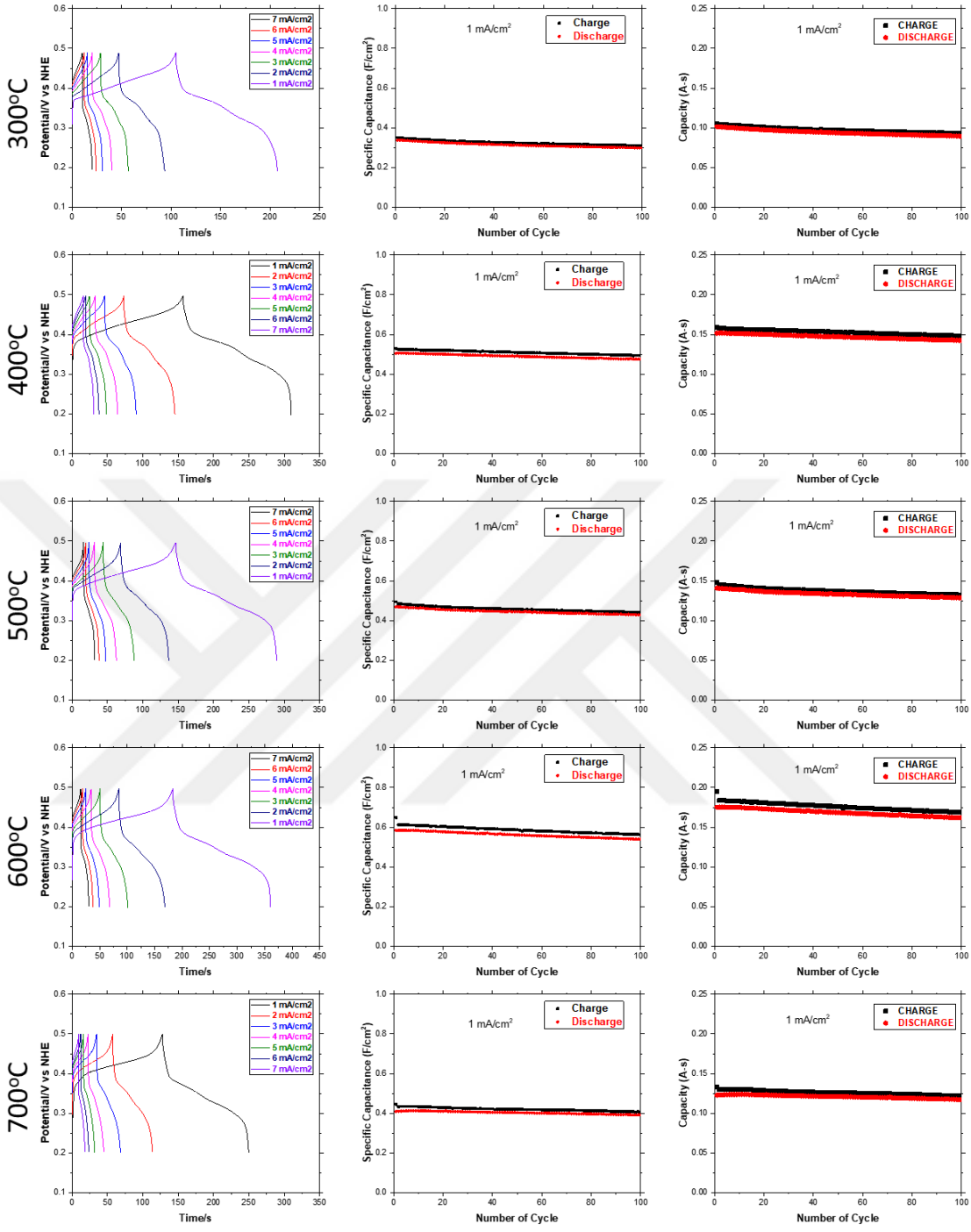

Figure 3.36: Electrochemical properties: (right column) GCD graphs, (middle column) specific capacitance versus the number of cycle plots, and (left column) capacity versus the number of cycle plots of GR-NiPP-30-X (X is denoted on the left).

The NiPP electrodes completely transformed to $Ni(OH)_2$ material were also used for the GCD measurements. It is essential to mention that the electrodes, calcined at low temperatures, must be cycled for at least 50 cycles (which takes almost 1 h) or

kept in KOH solution for 1 h before GCD measurements to start from the fully converted electrodes. For the higher temperatures, the number of cycles must be more (around 200 cycles or 3-4 h aging) to convert all NiPPs to β-$Ni(OH)_2$ particles. The electrode, which was used for 50 cycles, and then scan rate-dependent analysis, is used to collect the GCD data. Note that the time of these measurements is more than enough to convert all the NiPP to $Ni(OH)_2$ particles. After the scan rate-dependent CV curves are collected, the potential range is determined for GCD measurements for all the samples prepared at all temperatures. Figure 3.36 (left column) shows the charge-discharge behaviors of the electrodes. The specific capacitance and capacity values are plotted against the number of cycles to check the stability of the electrodes over 100 cycles of charging and discharging, see Figure 3.36 (middle and right column). Both specific capacitance and capacity values of all the samples, prepared at all temperatures, almost stay stable during the charging/discharging process. The specific capacitance and capacity values are reported as mF/cm^2 and mA·s (mC) at different current densities in Table 3.2. In addition, the percent coulombic efficiency, which indicates the ratio of the discharge capacity to the charge capacity within the same cycle, is calculated for all electrodes that were calcined at temperatures ranging from 300 to 700 ^oC, see Figure 3.37. The coulombic efficiency of all electrodes is approximately 97%, demonstrating excellent charge efficiency.

Table 3.2: Specific capacitance and capacity values of the electrodes calcined at indicated temperatures of the GR-NiPP-30-X (X is shown on the top).

	300 °C		400 °C		500 °C		600 °C		700 °C	
Current Density (mA/cm^2)	Capacity (mA.s)	Specific capacitance (mF/cm^2)	Capacity (mA.s)	Specific capacitance (mF/cm^2)	Capacity (mA.s)	Specific capacitance (mF/cm^2)	Capacity (mA.s)	Specific capacitance (mF/cm^2)	Capacity (mA.s)	Specific capacitance (mF/cm^2)
1	102	368	152	538	142	501	177	631	122	436
2	93	362	144	538	135	505	167	639	112	435
3	85	358	135	535	131	514	151	623	101	430
4	80	368	128	537	124	523	136	611	89	416
5	76	377	120	534	119	526	123	594	79	406
6	72	387	113	533	114	540	113	595	70	400
7	69	414	107	530	110	571	105	606	62	407

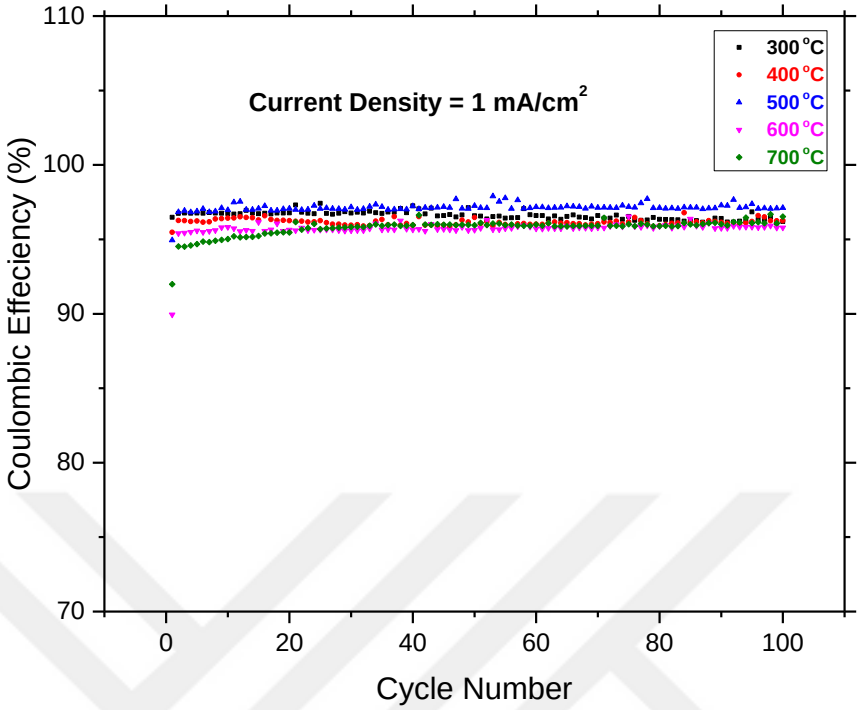

Figure 3.37: Graph of coulombic efficiencies of the GR-NiPP-30-X electrodes (X is 300, 400, 500, 600, and 700) versus cycle number.

The transformation mechanism is followed by 1000 cycles of CVs of the m-NiPP-30 electrodes to observe the changes during the transformation. As shown in Figure 3.38, the oxidation and reduction peaks of the m-NiPP sample reach their absolute maxima in the early cycles at 300 and 400 ºC calcination/annealing temperatures. However, the NiPP-700 sample starts with a very low current density for the oxidation and reduction peaks and gradually increases. This also proves that the transformation rate is much slower when calcined at 700ºC. After 1000 cycles, the NiPP-700 sample is almost entirely converted to β-$Ni(OH)_2$, reaching a similar current density as the NiPP-300 and NiPP-400 samples. It should be remembered that the complete transformation for the NiPP-700 sample requires lots more KOH solution; however, during the electrochemical tests, the amount of used sample is around 0.4 mg (dip-coated on a graphite rod), and the volume of KOH solution is about 30 ml which is more than enough for a complete transformation.

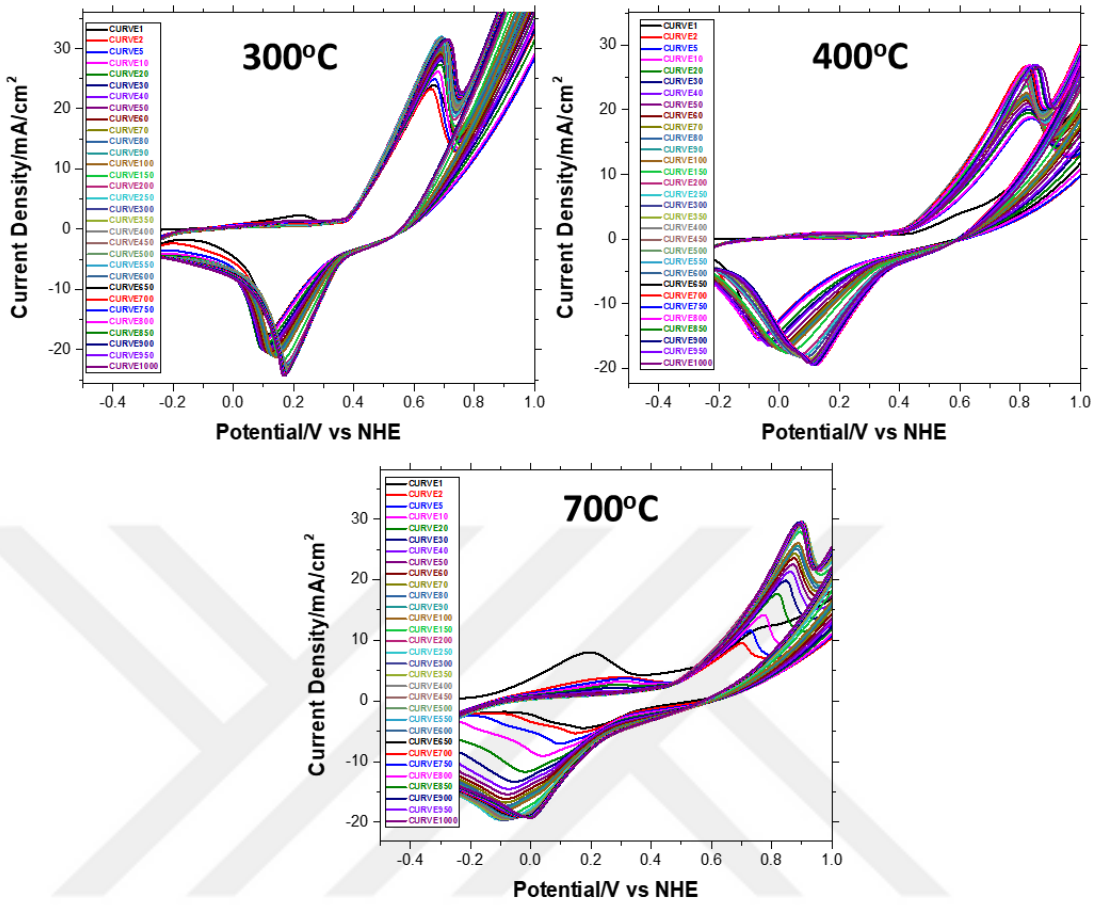

Figure 3.38: CV curves of the GR-NiPP-30-X electrodes (X is shown on each panel) with a scan rate of 50 mV/s for a potential window of -0.5-1.0 V vs. NHE in 3M KOH solution.

To further understand the electrochemical behaviors, the electrolyte composition is changed by adding known amounts of PPA to the KOH solution, which may prevent the transformation of NiPP to $Ni(OH)_2$. For this purpose, GR-NiPP-30-300 electrodes were tested in different electrolytes (3M KOH, 2.9M KOH + 0.1M PPA, and 2.6M KOH + 0.4M PPA) for 1000 cycles. In the electrolyte consisting of 2.9M KOH and 0.1M PPA, the behavior of the GR-NiPP-30-300 sample is identical to testing in 3M KOH, showing the faradaic oxidation and reduction peaks of β-$Ni(OH)_2$. The PPA amount is insufficient to stop the transformation because the electrolyte contains 2.5M OH^- ion concentration, and all the pyrophosphoric acid is neutralized by the KOH. Then, 2.4M KOH and 0.6M PPA containing electrolyte (neutralized solution), in which all $H_4P_2O_7$ is converted to $P_2O_7^{4-}$ ion, was prepared. The hydroxide concentration is around 10^{-4} M due to the association reaction of $P_2O_7^{4-}$

with water to produce $HP_2O_7^{3-}$ and OH^- ions. Clearly, the hydroxide concentration is too low to convert NiPP to $Ni(OH)_2$. The CVs of the GR-NiPP-30-300 electrode in 2.4M KOH and 0.6M PPA electrolyte displays capacitive feature in a potential window of 0 and 1.4 V. Moreover, there is a faradaic peak at around 1.6 V due to the oxidation of NiPP and OER at more positive potentials. However, no characteristic faradaic peaks of β-$Ni(OH)_2$ features are observed (see Figure 3.39), indicating no transformation. This electrode displays a 40 mA·s charge capacity and 40 mF/cm^2 specific capacitance at 2 mA/cm^2 current density in the 0.2-1.2 V potential window in an above neutralized electrolyte solution, which is much lower than the capacity of β-$Ni(OH)_2$ (93 mA·s charge capacity and 309 mF/cm^2 specific capacitance at 2 mA/cm^2 current density in the 0.2-0.5 V potential window, see Table 3.2.

Several CVs are collected by changing the electrolyte composition to determine the minimum amount of KOH solution as an electrolyte in the presence of PPA for the transformation reaction. Since the GR-NiPP-30-300 and GR-NiPP-30-700 samples display only capacitive behavior in the neutral electrolyte (2.4M KOH + 0.6M PPA), no characteristic faradaic peaks, 1 ml of 3M KOH solution is added to the electrolyte in every 10 CV cycles. The faradaic oxidation peak starts to appear when 2.98 and 3.78 ml of KOH are added for the GR-NiPP-30-300 and GR-NiPP-30-700 electrodes, respectively, see Figure 3.40.

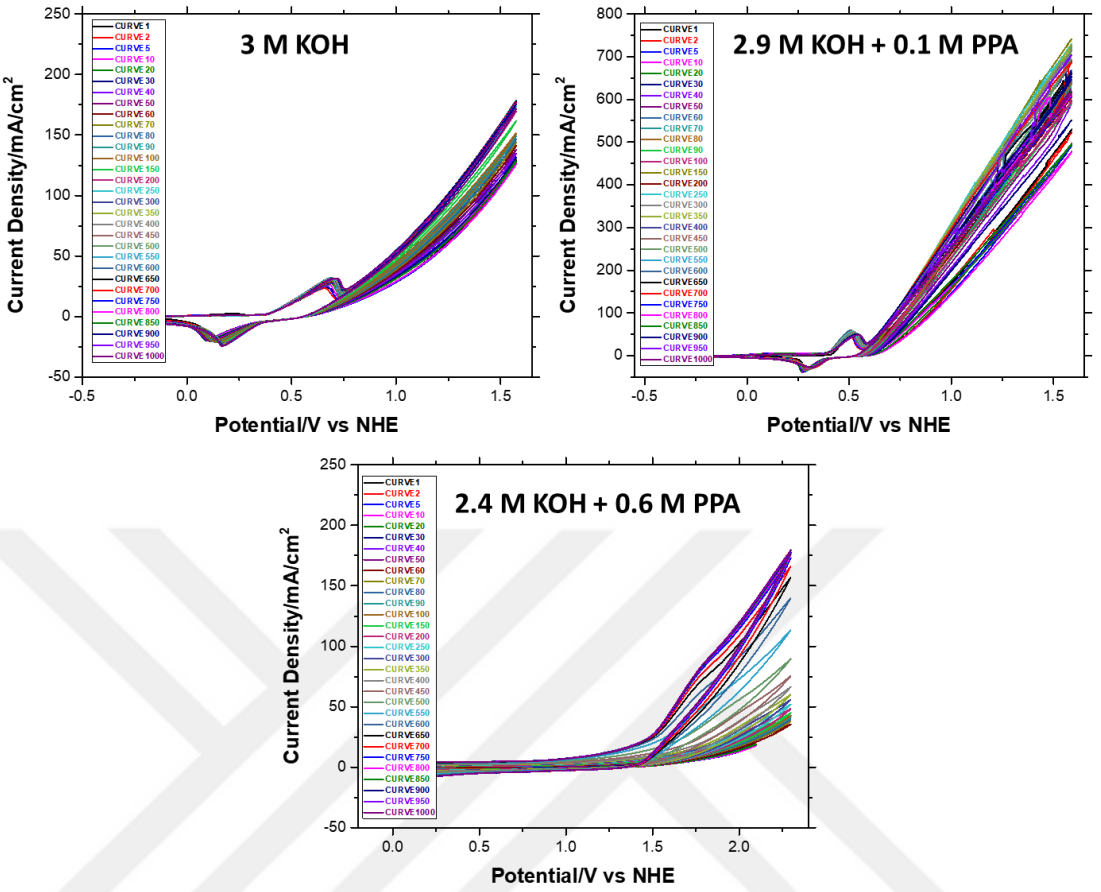

Figure 3.39: CV curves of GR-NiPP-30-300 sample with a scan rate of 50 mV/s in various electrolytes.

The current density of the oxidation and reduction peaks of the samples from Figure 3.40 are plotted versus the volume of KOH added, see Figure 3.41. The current densities are evaluated by subtracting the capacitive feature of the sample. Since the oxidation peaks originating from the $Ni(OH)_2$ particles are near the water oxidation region, the reduction part might be more reliable for determining the exact volume of KOH needed for the transformation. According to that approximation, the GR-NiPP-30-300 electrode starts to form $Ni(OH)_2$ after 2.98 ml of 3M KOH is added to 30 ml of neutral electrolyte, whereas the GR-NiPP-30-700 electrode needs 3.78 ml of 3M KOH for the same transformation.

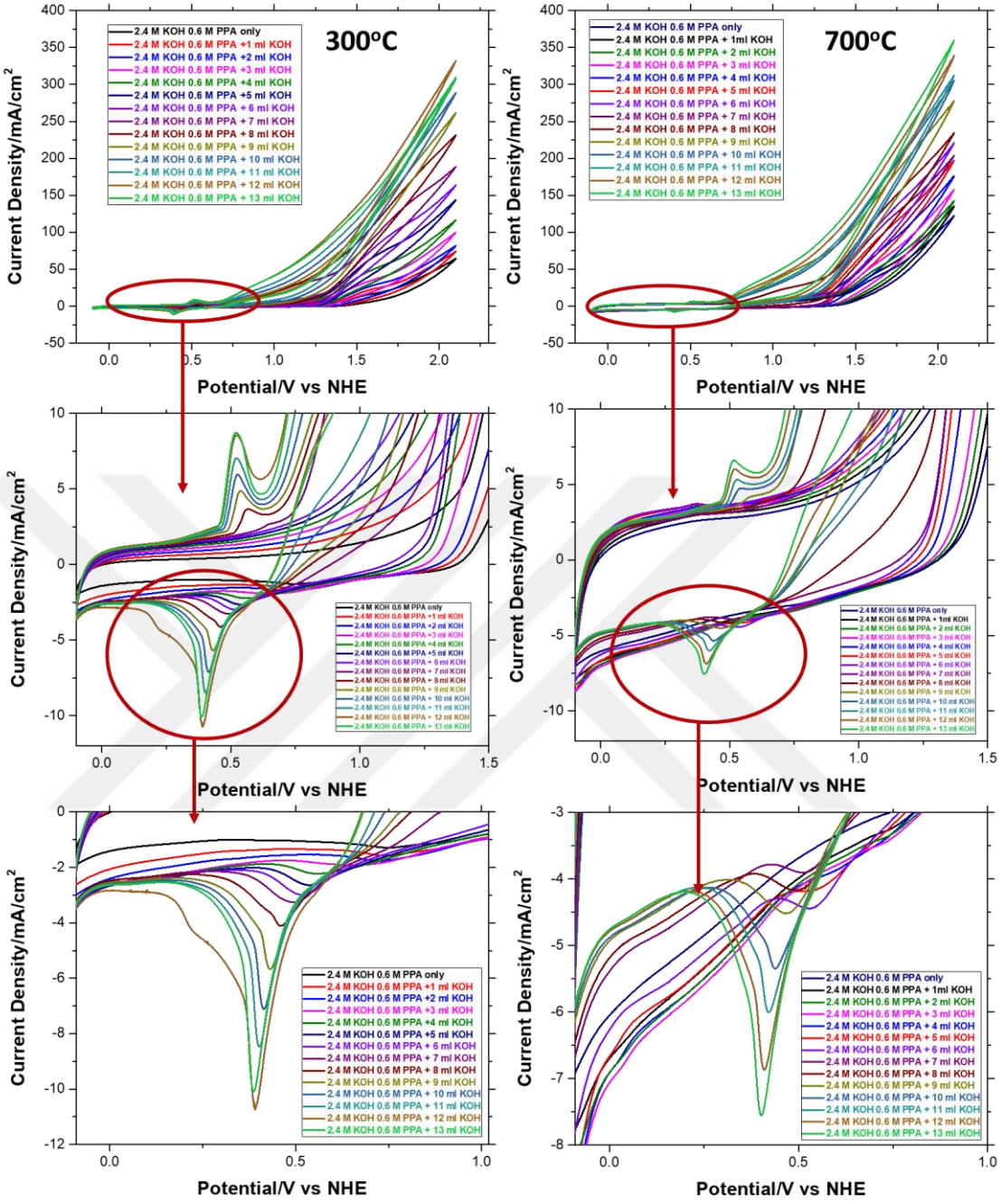

Figure 3.40: CV curves of the GR-NiPP-30-300 and GR-NiPP-30-700 electrodes with a scan rate of 50 mV/s for a potential window -0.2-2.0 V vs. Ag/AgCl in a neutral electrolyte by the addition of KOH solution.

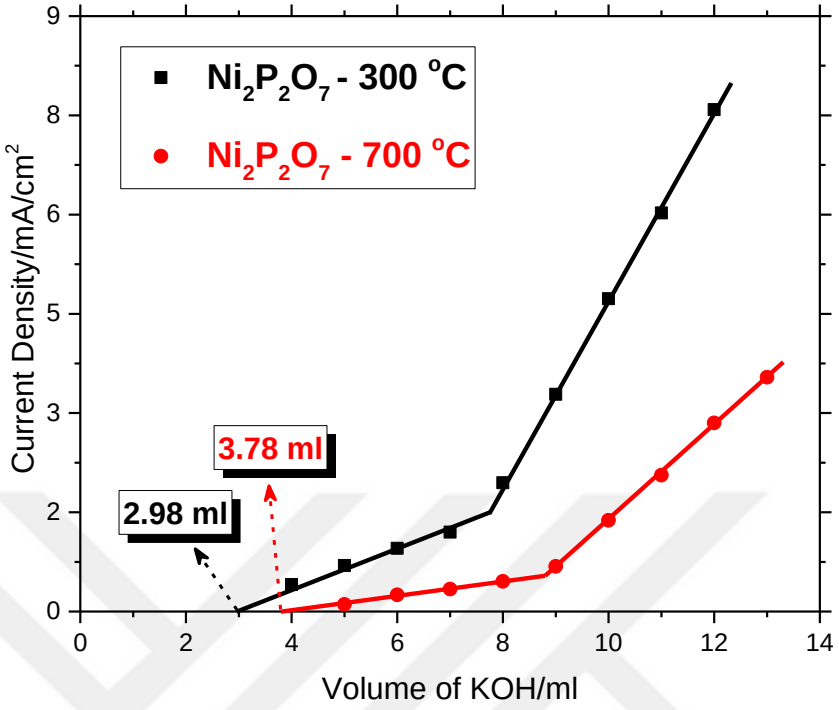

Figure 3.41: Graph of current densities on the reduction peak maxima of the GR-NiPP-30-300 and GR-NiPP-30-700 electrodes versus the volume of 3M KOH solution added.

These data can be used to determine the K_{sp} of the amorphous and crystalline NiPP since no K_{sp} values are reported for the transition metal pyrophosphates in the literature. In order to calculate the K_{sp} values, the transformation reaction (remember eq. 3.3) and solubility reaction (eq. 3.5) of NiPP are used.

$$\mathbf{Ni_2P_2O_7(s) \rightarrow 2Ni^{2+}(aq) + P_2O_7^{4-}(aq)} \qquad \textbf{eq. 3.5}$$

The hydroxide concentrations after the addition of 2.98 and 3.78 ml to the amorphous and crystalline NiPP, respectively, become 0.271M ($[OH^-]$ = (2.98 ml x 3.0 M)/32.98 ml) and 0.336M ($[OH^-]$=(3.78 ml x 3.0 M)/33.78 ml). Since the K_{sp} value of $Ni(OH)_2$ is known in the literature as 5.84×10^{-16} M^3, the Ni^{2+} ion concentrations are calculated as 7.95×10^{-15} and 5.17×10^{-15} M for the amorphous and crystalline NiPP electrodes, respectively. With the addition of 3M KOH, the $P_2O_7^{4-}$ ion concentration is reduced from 0.6 M to 0.546 and 0.533M in the electrolyte solutions, after the addition of 2.98

and 3.78 ml, used for the GR-NiPP-300 and GR-NiPP-700 electrodes, respectively. Using the relation of

$$\mathbf{K_{sp} = [Ni^{2+}]^2[P_2O_7^{4-}]} \qquad \textbf{eq. 3.6}$$

derived from eq. 3.5, K_{sp} values are evaluated as 3.45×10^{-29} and 1.42×10^{-29} M^3 for the amorphous and crystalline NiPPs. There is only a small difference between the two K_{sp} values (more than 2 times). However, this is why the transformation process differs in time for the amorphous and crystalline NiPPs.

3.2. Synthesis and Characterization of m-$Co_2P_2O_7$ Samples

3.2.1. Preparation and Characterization of Co(II):Acid:P123 Mesophases

Homogeneous solutions of Co(II):Acid:P123 are prepared using PA or PPA with compositions given in Table 2.1. Ratios of the ingredients are calculated to be stoichiometric according to the acid (mole ratio of Co(II)/P123 is the same as the acid mole ratio for PA, half for PPA). Three mole ratios of Co(II)/P123 are investigated, namely 30, 60, and 90. The homogenous solutions of the Co(II):Acid:P123 mixtures are first drop-cast coated on microscope slides to form the mesophases of the above compositions. Then, the mesophases are characterized using the XRD, POM, and ATR-FTIR techniques while aging at room temperature before further calcination processes.

The mesophases are characterized by small-angle XRD, ranging between 1 and 5^o, 2θ, to analyze their stability during aging at RT. Figure 3.42 shows the XRD patterns of all three ratios of the Co(II):Acid:P123 mesophases aged at RT. The 30-mole ratio sample diffracts at small angles, indicating that the mesophase has an ordered structure, and almost all are stable for up to 2 days. The diffraction lines are not too intense because they originated from the higher hkl planes having the most intense line below 1^o, 2θ, which is characteristic of LLC mesophases. A slight shift in the diffraction lines is observed while aging at RT because of the differences in the evaporation of excess water. The diffraction lines in the XRD patterns of the Co(II):Acid:P123 mesophases with 60 and 90-mole ratios are visible only up to 10 min aging. The diffraction lines of high hkl planes disappear in 10 min. The most intense line below 1^o, 2θ, is likely still at below 1^o, as evidenced by the intensity rises below 1^o. Therefore, the mesophase/mesostructure must hold its ordered structure.

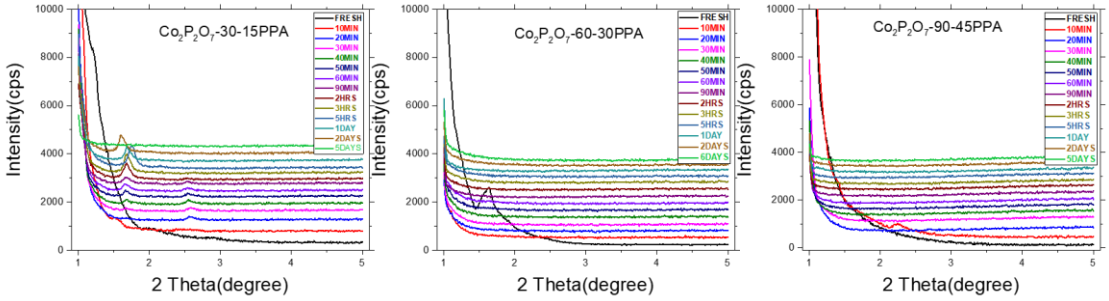

Figure 3.42: Small-angle XRD patterns of the Co(II):Acid:P123 mesophases with (left) 30, (middle) 60, and (right) 90-mole ratios of Co(II)/P123, prepared using PPA.

Figure 3.43 shows the POM images of the Co(II):Acid:P123 mesophases prepared using PA and PPA as the acid sources and aged in the laboratory conditions at RT. A typical mesophase (LLC) texture is not observed in the POM images. Instead, particle-like domains are observed in the POM images. With further aging, some cracks appear, and particle-like morphology covers the entire image. The cracks in the sample indicate that solid-like particles are forming during aging under ambient conditions with a composition of $Co_2H_xP_2O_7(NO_3)_x{\cdot}nH_2O$ (see eq. 3.7). Similar solid-like particles are observed from the mesophases prepared from both PA and PPA systems. The diffraction line of the mesophase, obtained from the PPA system, is not observed during aging, with an assumption that the most intense line is below 1^o, 2θ; however, the mesophase of the PA system has an ordered and oriented structure even after 1 day, see Figure 3.45. This means solid-like particles still preserve their mesostructure. Note also that there are no salt species over the mesophases during the formation of solid-like particles, even after 5 days of aging, see Figure 3.44.

$$\mathbf{2Co(NO_3)_2(aq) + H_4P_2O_7(aq) + nH_2O \leftrightarrow Co_2H_xP_2O_7(NO_3)_x.nH_2O(s) + (4-x)HNO_3(g)} \quad \mathbf{eq.3.7}$$

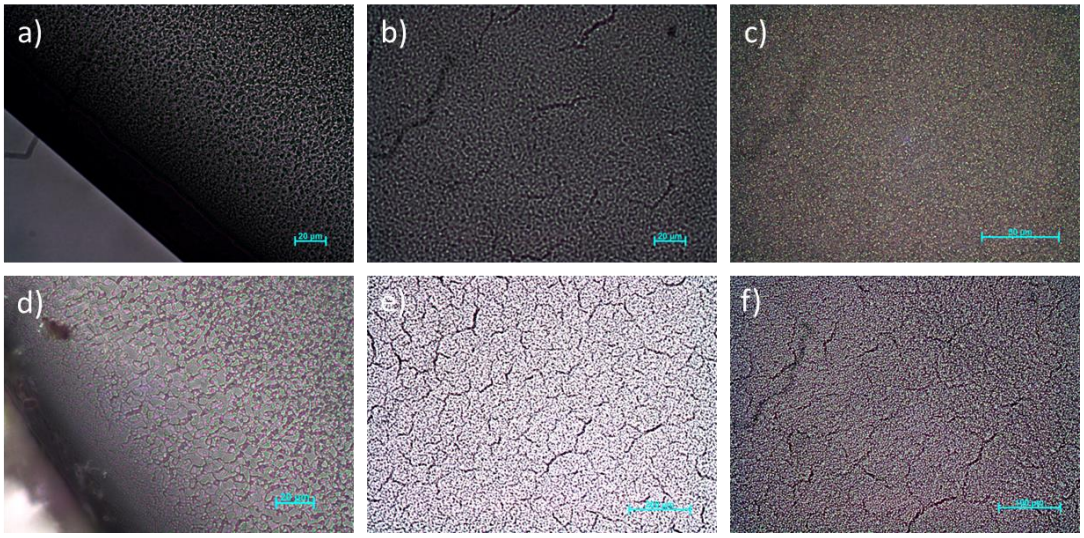

Figure 3.43: POM images of the $Co_2P_2O_7$-60-30PPA mesophases a) and b) 2 h aged, c) and d) 6 h aged. e) and f) Images of the $Co_2P_2O_7$-60PA mesophases after 4 h aging at room temperature, with scale bars 20, 20, 50, 20, 200, and 100 μm, respectively.

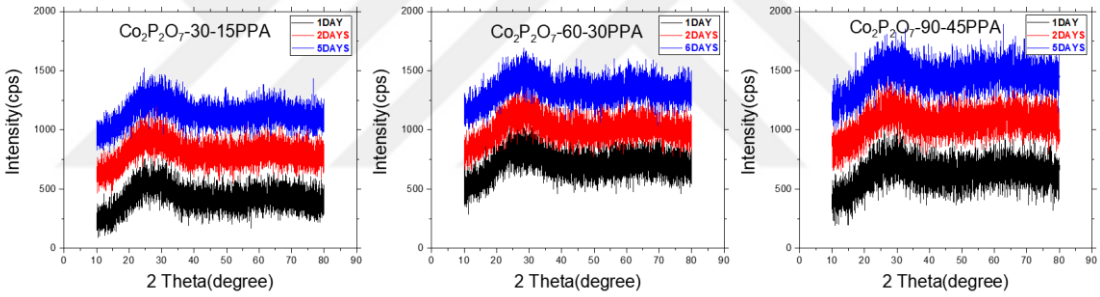

Figure 3.44: Wide-angle XRD patterns of 1, 2, and 5 days aged mesophases of the Co(II):PPA:P123 (left) 30, (middle) 60, and (right) 90 mole ratios at RT.

Mesophases of the Co(II):Acid:P123 mixture are also characterized by small-angle XRD considering the acid precursors, phosphoric acid (PA), or pyrophosphoric acid (PPA) during aging at RT, see Figure 3.45. There are some differences between the patterns for PA and PPA samples. The higher hkl planes are visible in the pattern for the mesophases prepared using PA precursor. However, like the PPA system, the most intense line might still be below 1^o, 2θ. The interaction between acid and metal ions can differ in the gelation process since the acidity of PPA ($pK_a = 0.91$) is slightly higher than PA ($pK_a = 2.16$).

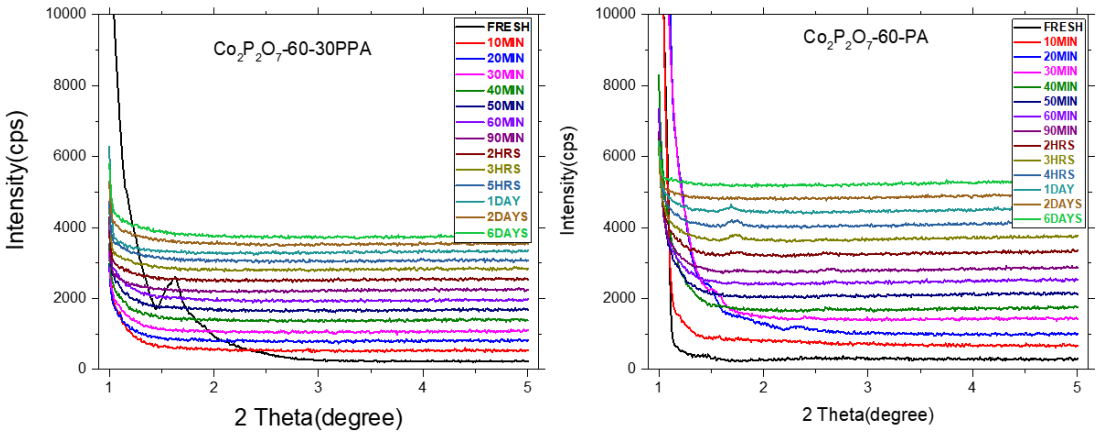

Figure 3.45: Small-angle XRD patterns of the 60-Co(II):Acid:P123 samples, prepared using (left) PPA and (right) PA acid precursors.

The aging process of the mesophase of Co(II):Acid:P123 was also followed by weight-lost measurement by putting about 1 g of a solution prepared using PA and PPA. The weight changes are recorded under ambient laboratory conditions over a 4-digit balance. Solution of the Co(II):Acid:P123 mixture loses its excess water quickly in the first 200 min, see Figure 3.46. The range I in the inset of Figure 3.46 indicates the evaporation of excess water in the solution by losing most water. In this range, there is a slight difference between the solutions prepared by PA and PPA; the PA systems lose their water more quickly than the PPA systems. Then, in the range II and III of both systems, continue to lose weight at a slow rate. These ranges show the solidification process, which is due to the polymerization of the phosphate/pyrophosphate and metal ion species. During the polymerization process, the weight loss of the volatile species is more in the PPA system than in the PA system, see Figure 3.46 inset. Since the acidity of the solutions is different (PPA is more acidic than PA), the chemical reaction over the solidification process differs for the removal of volatile species from the media.

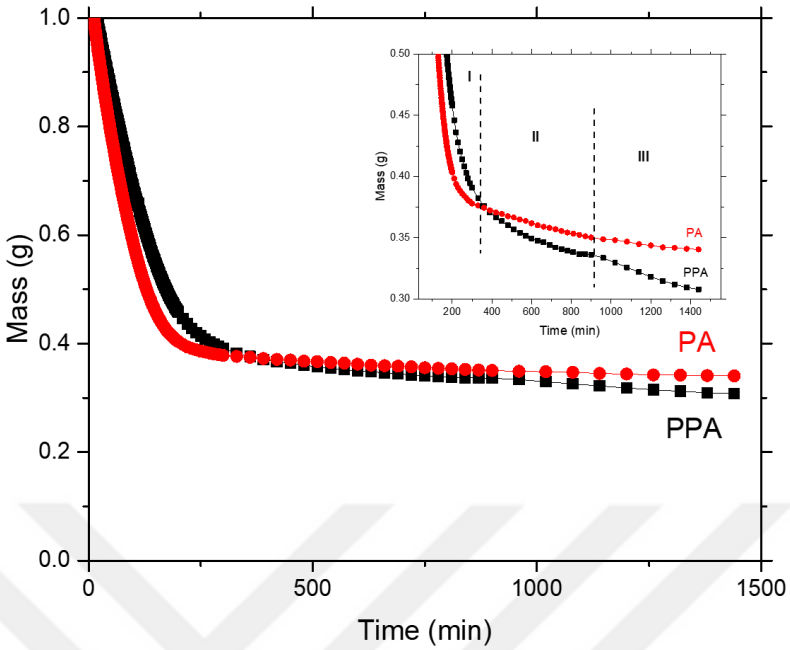

Figure 3.46: Gravimetric measurements: Mass versus time plots during water evaporation on balance from the CoPP-60 solutions, prepared using PA and PPA.

The Co(II):Acid:P123 solutions are also investigated using ATR-FTIR spectroscopy to follow the gelation and solidification processes at RT. The spectra are collected by adding one drop of the Co(II):Acid:P123 solution on the ATR diamond, starting from the time of dropping (0 min) till 48 hours. Figure 3.47a shows the raw ATR-FTIR spectra of a CoPP solution. As discussed in the NiPP section, the spectra should be normalized before quantitative analysis. Figure 3.47b shows the normalized spectra of the CoPP-30. The peaks at around 3600-3000 and 1640 cm^{-1} originate from the stretching and bending modes of water species, respectively; the peaks at about 1470-1290 cm^{-1} are due to the nitrate ion, and the peaks at around 1200-800 cm^{-1} result from the phosphate species. There is a decrease in the intensities of the water and nitrate regions similar to the NiPP system while aging the mesophase at RT. These spectral changes indicate the evaporation of water and the leaving of the nitrate species from the media as nitric acid or its decomposition products, see eq. 3.7.

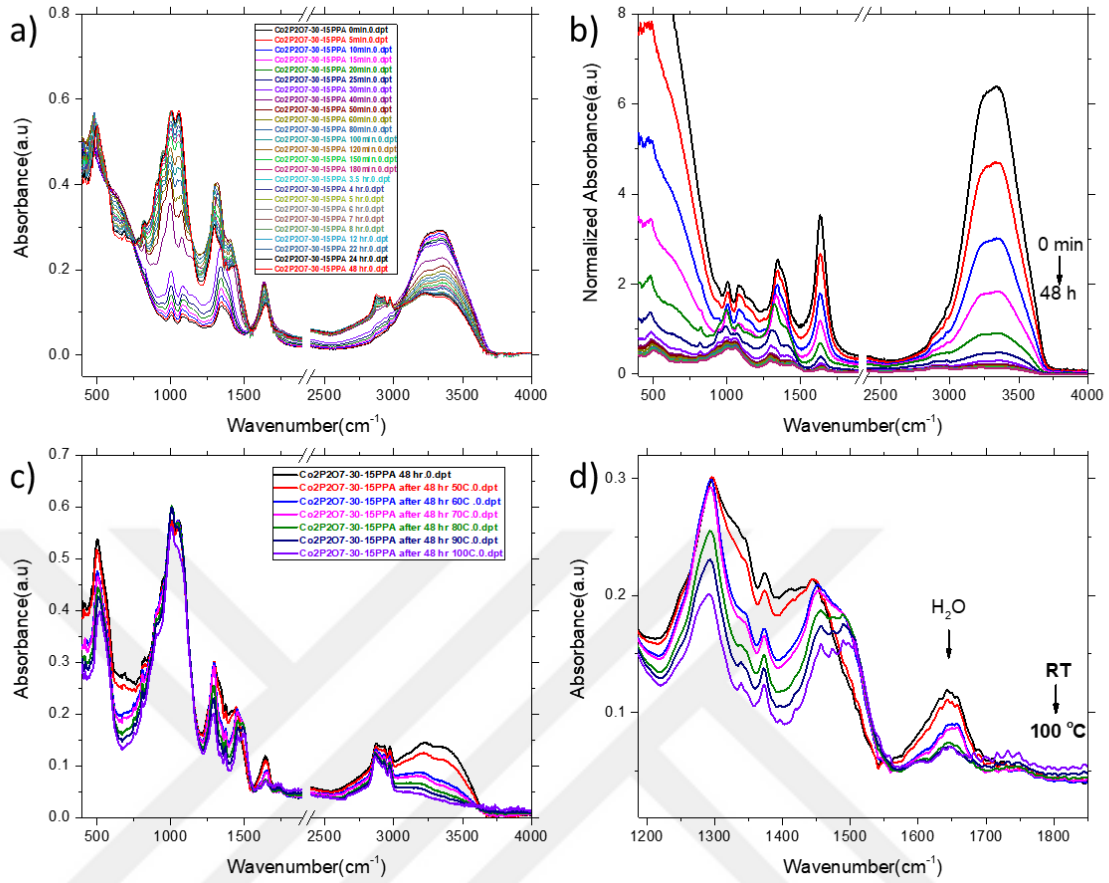

Figure 3.47: Time-dependent ATR-FTIR spectra of the CoPP-30 aging process: a) raw spectra, b) normalized spectra. c) and d) The temperature-dependent ATR-FTIR spectra of the 2 days aged CoPP-30 and followed by heating at (top to bottom) RT, 40 to 100 °C with 10 °C increments.

The first spectrum (at 0 min) of CoPP-30 is assumed to be the initial composition of the solution and calculated to have 113 water per cobalt ion in the media. The nitrate to cobalt mole ratio is considered to be 2 in the fresh CoPP-30 solution. Figure 3.48 shows the relationship between mole ratios of water/cobalt and nitrate/cobalt versus time in the CoPP-30 mesophase during aging at RT. The CoPP-30 sample loses its water quickly (in the first 30 minutes). The decay of nitrate species is similar and correlates with the water evaporation process, meaning that nitrate decomposition depends on the water content of the solution, like in the nickel system. The composition of the CoPP-30 mixture after 48 h of aging is calculated to be $Co_2H_{0.6}P_2O_7(NO_3)_{0.6}\cdot 4.8H_2O$.

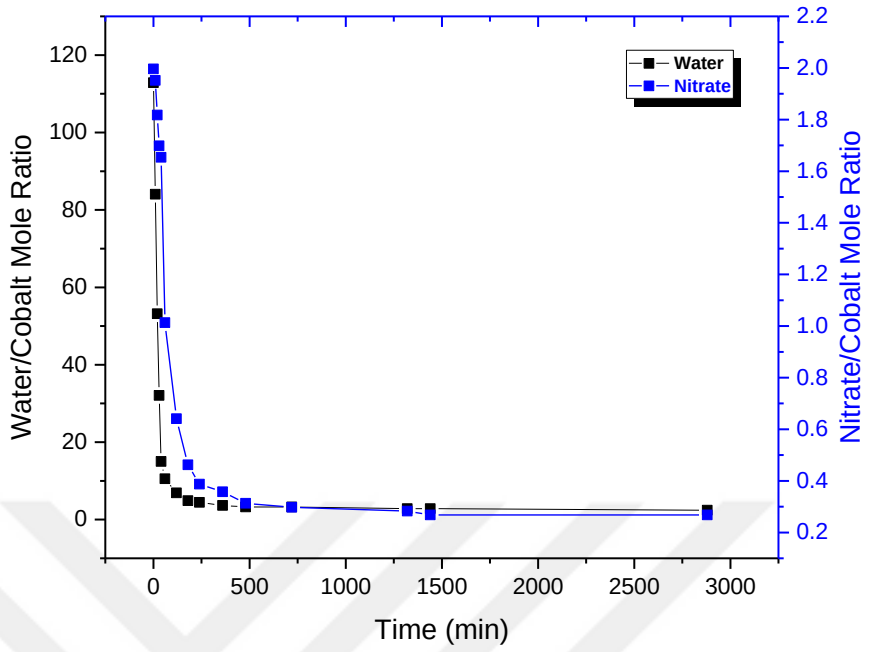

Figure 3.48: Water/cobalt and nitrate/cobalt mole ratios versus time graphs derived from normalized ATR-FTIR spectra of the CoPP-30 solution.

The heating effect on the mesophases is also monitored using ATR-FTIR spectroscopy by heating the sample on the ATR diamond. Heating after 48 h causes further reduction of the nitrate and water species from the mesophase, see Figures 3.47 c and d. The mesophase of the CoPP-30 mixture was analyzed in more detail to elucidate the spectral changes between RT and 100 °C. The peaks of nitrate species shift by heating the sample due to the formation of the bridged nitrate species. The water peak almost completely disappears at around 80 °C, indicating a complete drying of the sample.

3.2.2. Synthesis and Characterization of Mesoporous $Co_2P_2O_7$

The Co(II):Acid:P123 mesophases that are spin-coated, dip-coated, or drop-casted samples are calcined at 300 °C to synthesize the mesoporous $Co_2P_2O_7$ particles (denoted as m-CoPP-n-X, where m stands for mesoporous, n is for mole ratio of Co(II)/P123, and X is the calcination temperature in Celsius). The m-CoPP-n-300 samples are further annealed at higher temperatures and characterized by various techniques at each calcination step.

Powder XRD patterns of the m-CoPP-60 samples that were prepared by calcining/annealing at various temperatures are given in Figure 3.49. No diffraction line is observed up to 600 °C, meaning that the sample is amorphous and becomes crystalline over 600 °C. The crystalline phase of the m-CoPP-60 sample can be indexed to α-$Co_2P_2O_7$ with the unit cell parameters of a of 8.9236 Å, b of 8.3656 Å, and c of 9.0158 Å, see Figure 3.49 (right one). [169]

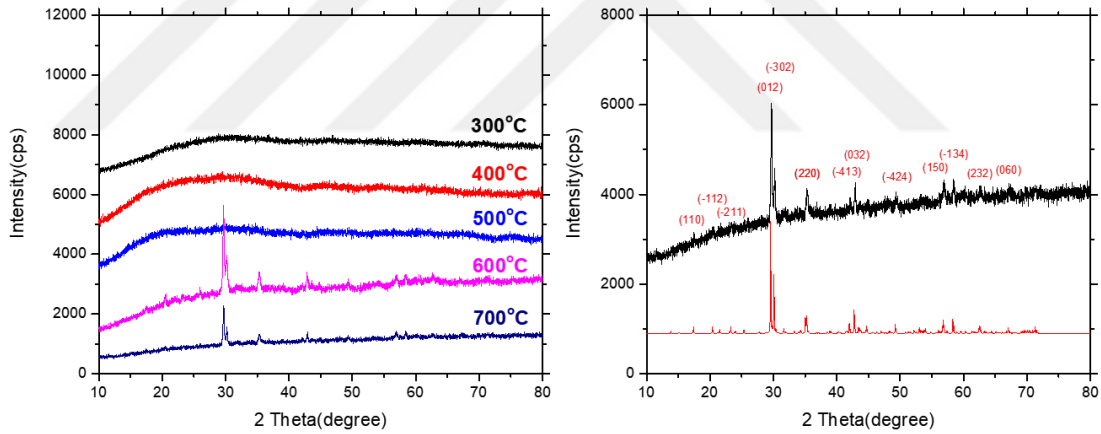

Figure 3.49: Wide-angle XRD patterns of the (left) m-CoPP-60-X (X is 300, 400, 500, 600, and 700 °C) samples and (right) indexed XRD pattern of the CoPP-60-700 sample together with reference α-$Co_2P_2O_7$ (red, ICDD - 00-049-1091).

ATR-FTIR spectra of the m-CoPP-n samples, calcined/annealed at various temperatures, are recorded to evaluate the spectral changes during the calcination process. Spectra of the CoPP-n-300 (n is 30, 60, and 90) samples were collected to compare the spectral differences among low, intermediate, and high compositions. The spectra of those compositions are almost identical, indicating that the structures of the m-CoPP samples for each composition are the same, see Figure 3.50a. Only the peaks

originating from the phosphate species are visible at 300 °C and higher annealing temperatures. There are no peaks originating from nitrate and surfactant species after the calcination process. The peaks at high-frequency region (1050-1200 cm^{-1}) correspond to PO_3 units, and the peaks at around 750 and 930 cm^{-1} result from the symmetric and asymmetric modes of the bridged P-O (P-O-P) group (where the angle between P-O-P is not equal to 180°) and strong indication for cobalt pyrophosphate formation, and the intense peaks at around 500-600 cm^{-1} originate from the bending modes of pyrophosphate group and Co-O stretching modes. [161], [162]. All the phosphate peaks are broad up to 600 °C and become sharp and better resolved at 600 °C. This change corresponds to the crystallization of cobalt pyrophosphate particles at 600 °C (see Figure 3.49) and is consistent with the XRD data. Even though there is a change in the broadness of the peaks, the pyrophosphate structure is very similar for both amorphous and crystalline phases of the CoPP sample, indicating that the local structure around Co(II) ions is very similar.

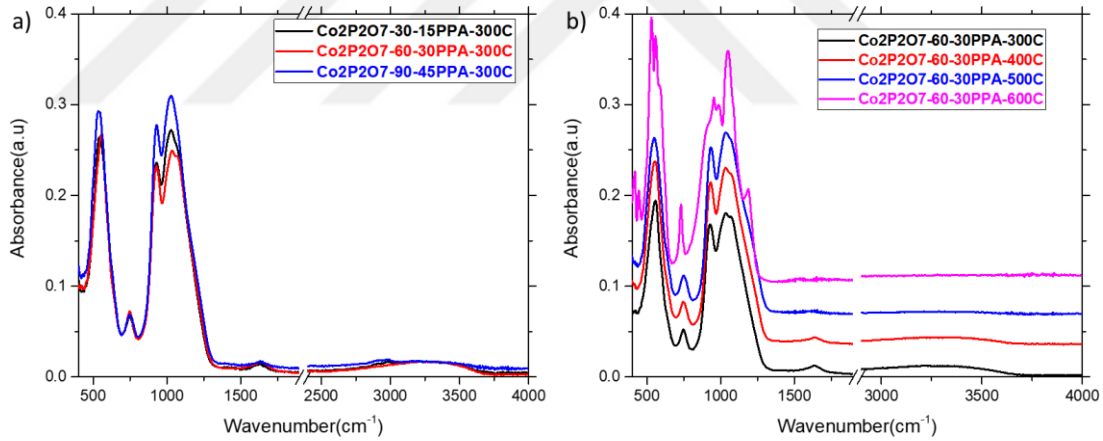

Figure 3.50: ATR-FTIR spectra of a) the m-CoPP-n-300 (n is 30, 60, and 90) and b) the m-CoPP-60-X (X is 300, 400, 500, and 600).

N_2-adsorption-desorption isotherms are collected to investigate the porosity details of the calcined samples. Barrett-Joyner-Halenda (BJH) pore size distribution plots and Brunauer-Emmett-Teller (BET) surface area of the m-CoPP samples calcined at 300 °C and annealed at 400, 500, 600, and 700 °C are evaluated and shown in Figure 3.51 and Table 3.3, respectively. The isotherms with a type IV hysteresis are characteristic of mesoporous materials. [163][164] Brunauer-Emmett-Teller (BET)

surface area, pore volume, and pore sizes of m-CoPP-30-300, m-CoPP-60-300, and m-CoPP-90-300 samples are given in Table 3.3. The m-CoPP-60-300 sample has more uniform porosity than the 30 and 90 compositions, see Figure 3.51b. The BET surface areas of m-CoPP-30-300, m-CoPP-60-300, and m-CoPP-90-300 samples are 49, 111, and 56 m^2/g, respectively. The highest surface area is obtained from the m-CoPP-60-300 sample and chosen for the electrochemical analysis later. The surface area of the m-CoPP-60 sample gradually decreases with increasing annealing temperature and becomes 26 and 18 m^2/g at 400 and 500 ^oC, respectively, Figure 3.51c. The BET surface area could not be measured from the 600 and 700 ^oC annealed samples since these samples are crystalline and the pores are collapsed.

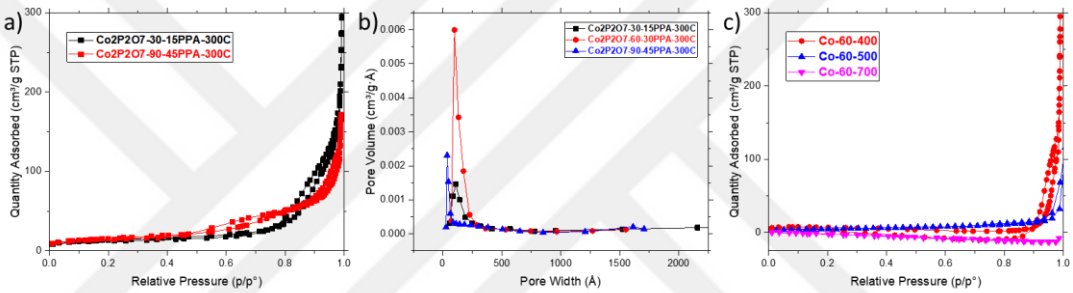

Figure 3.51: N_2 (77 K) adsorption and desorption isotherms of the a) m-CoPP-n-300 (n is 30 and 90) and c) m-CoPP-60-X (X is 400, 500, and 700 ^oC), b) the pore size distribution plots of the m-CoPP-n-300 (n is 30, 60 and 90) samples.

Table 3.3: (Left) BET surface area, pore volume, and pore size values of the m-CoPP-n-300 (n is 30, 60, and 90) and right the BET surface area the m-CoPP-60-X (X is 300, 400, 500, 600, and 700 ^oC).

Mole Ratio	BET Surface Area (m^2/g)	Pore Volume (cm^3/g)	Pore Size (nm)
m-CoPP-30-300	49	0.50	29.8
m-CoPP-60-300	111	0.60	15.4
m-CoPP-90-300	56	0.26	13.5

Calcination Temperature (^oC)	BET Surface Area (m^2/g)
	m-CoPP-60
300	111
400	26
500	18
600	-
700	-

SEM and TEM images of the m-CoPP-n-X samples are also collected to investigate their morphology and porosity. There are some morphologic changes when the mole ratio of cobalt salt is varied from 30 to 90 for the m-CoPP-n-300 samples.

The m-CoPP-30-300 sample displays film-like particles; on top, there are individual spherical (not perfect) particles, see Figures 3.52 a and b. When the mole ratio of cobalt salt is increased to 60, the particles become almost perfect spheres, which displays the highest surface area in the set. When analyzed with lower magnifications, they have some film-like morphology formed by the aggregation of many spherical particles shown in Figures 3.52 c and d. The m-CoPP-90 sample shows distorted spherical particles when calcined at 300 ^{o}C. Since the highest surface area is obtained from the 60-mole ratio, the m-CoPP-60-300 sample is analyzed in more detail using the TEM imaging technique. The TEM images display mesoporous spherical m-CoPP-60-300 particles with a size between 50 and 350 nm, see Figure 3.53. However, it was observed that some deformations occur on the m-CoPP-300 particles under the TEM beam during imaging, see Figures 3.53 c and d. This means that the m-CoPP-300 particles are beam-sensitive and should be considered during imaging. Figure 3.54 displays a set of SEM images of the m-CoPP-60 samples, calcined/annealed at different temperatures. The m-CoPP particles are spherical up to 600 ^{o}C. The pores are visible even in the m-CoPP-300 and m-CoPP-400 samples. The particles get distorted, and the pores expand with increasing annealing temperature to 500 ^{o}C. When the crystalline phase was obtained at 600 ^{o}C, the particles aggregated with each other and became larger particles. Note also that the particles had film-like morphology when the samples were imaged at lower magnifications, which ensures visualization of the larger particles in the sample, see Figure 3.54, right column.

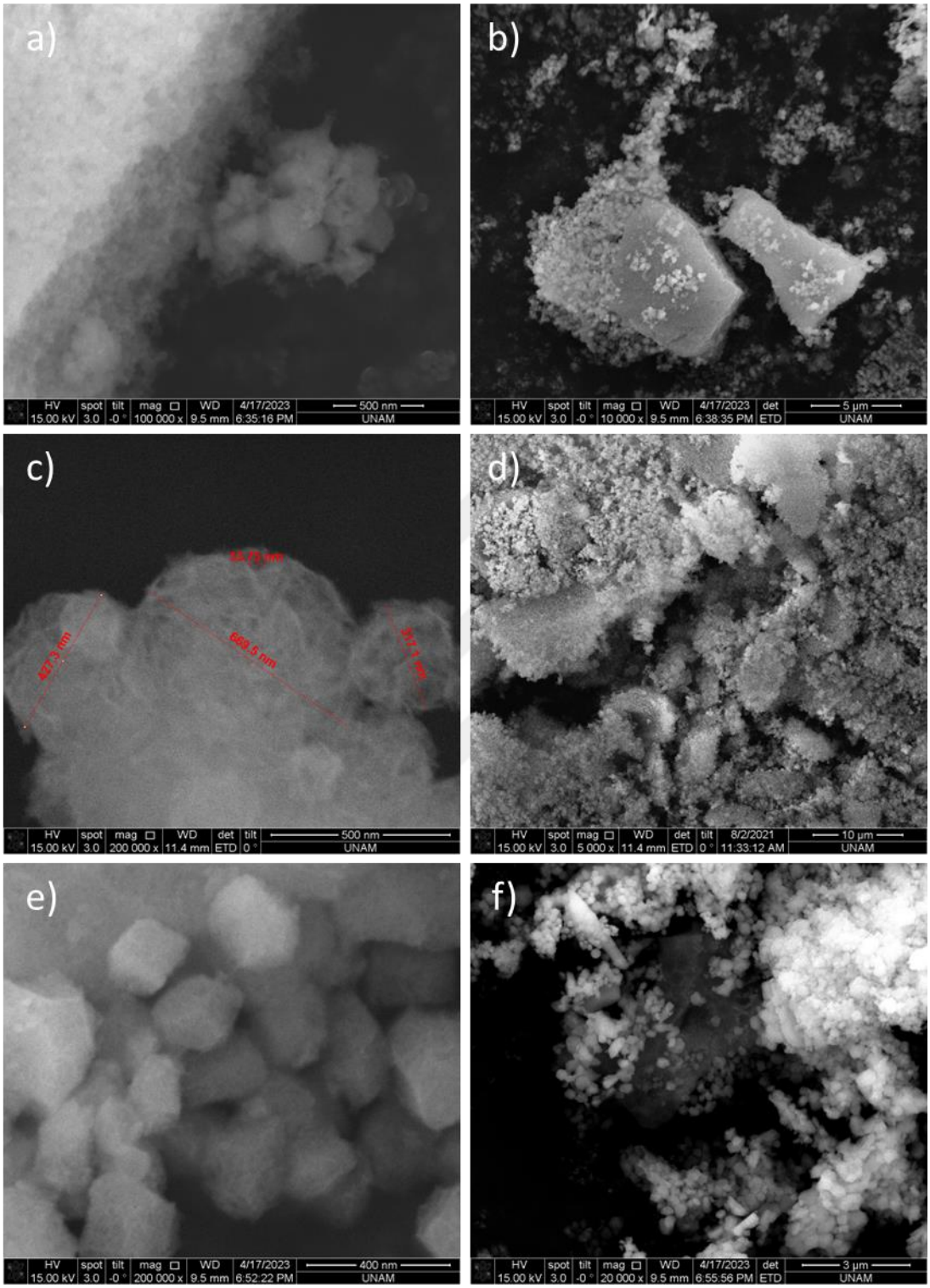

Figure 3.52: SEM images of the a) and b) m-CoPP-30-300, c) and d) m-CoPP-60-300, e) and f) m-CoPP-90-300 samples, with scale bars 500 nm, 5 μm, 500 nm, 10 μm, 400 nm, and 3 μm, respectively.

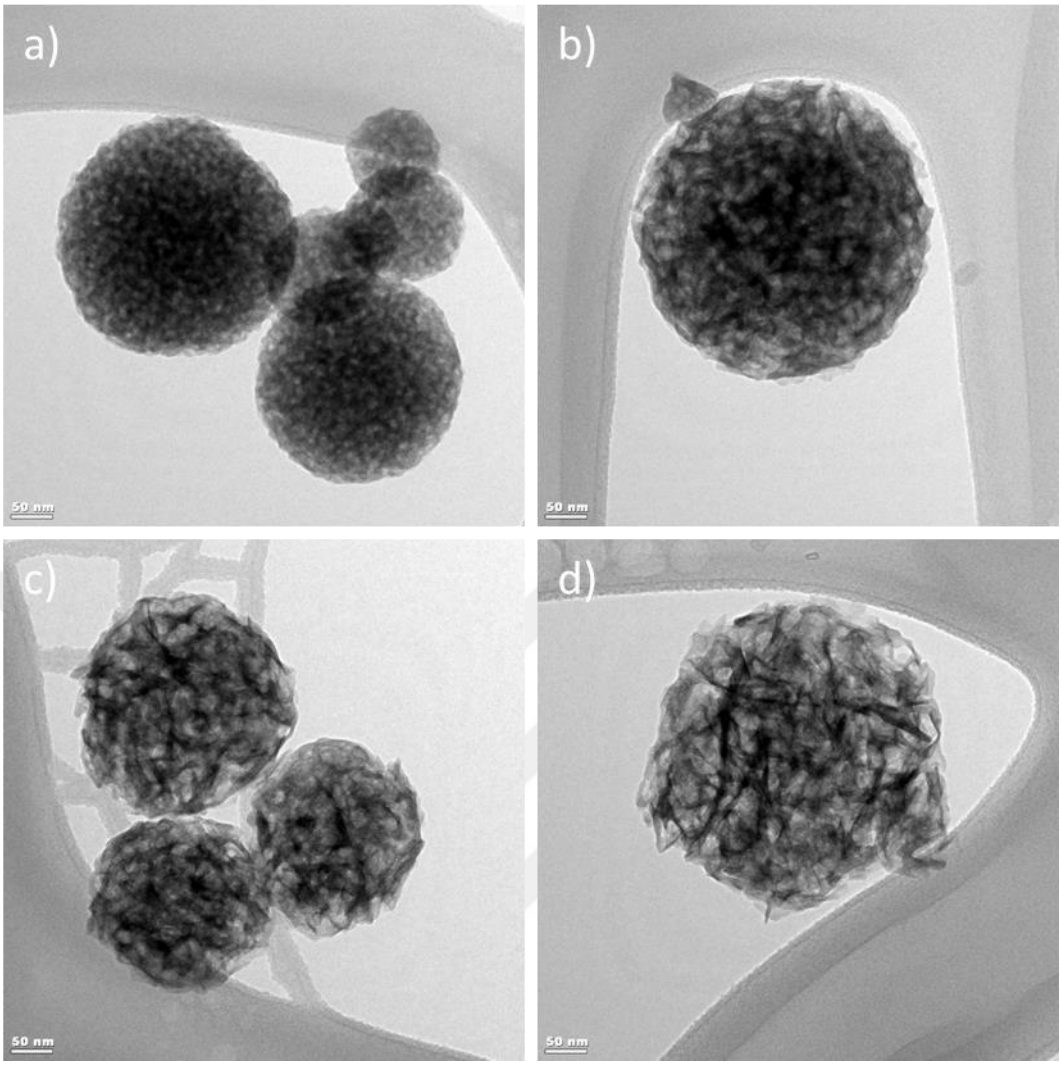

Figure 3.53: TEM images of the m-CoPP-60-300 a) and b) not damaged, c) and d) damaged under the beam (all scale bars are 50 nm).

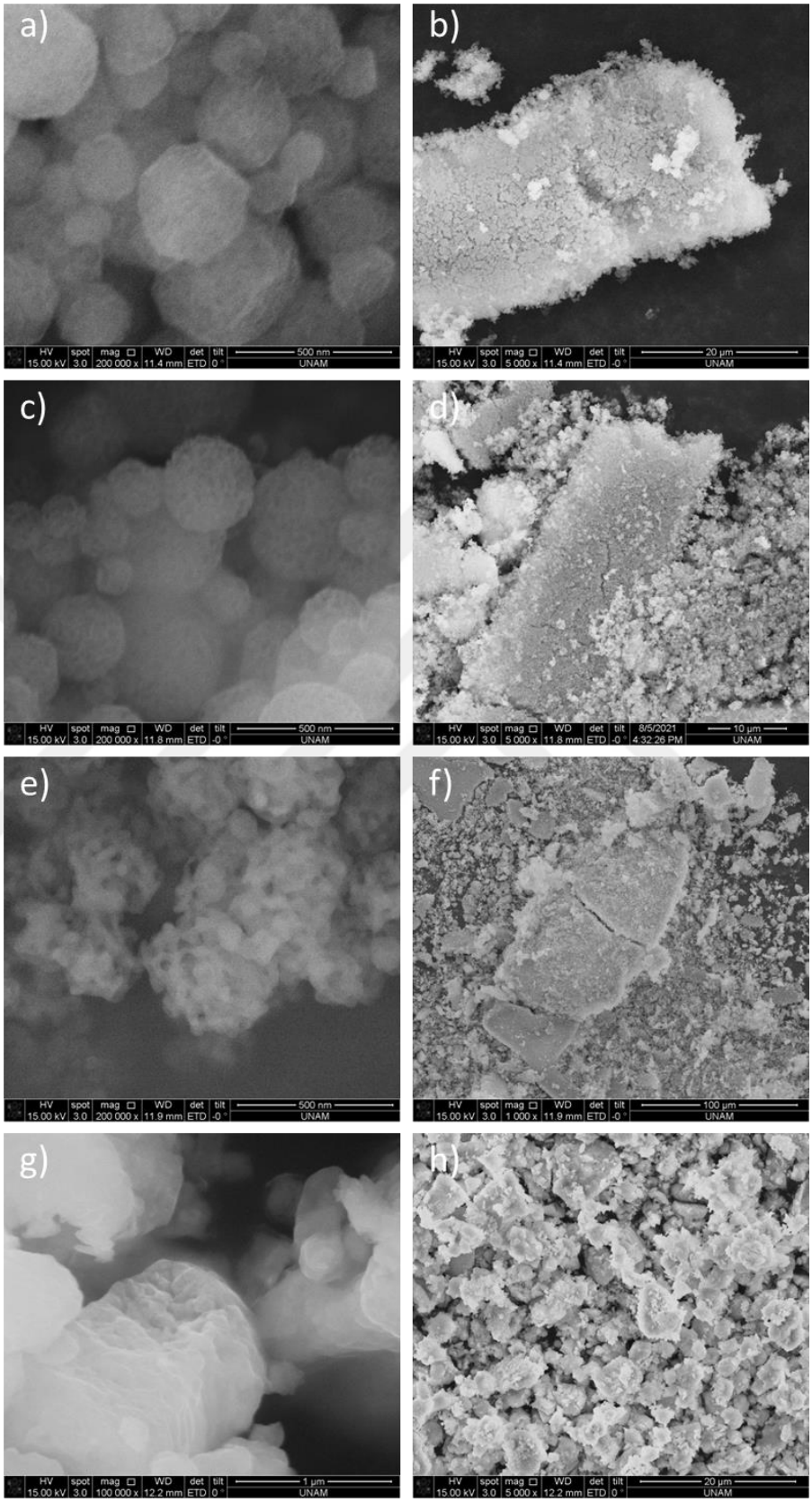

Figure 3.54: SEM images of the a) and b) m-CoPP-60-300, c) and d) m-CoPP-60-400, e) and f) m-CoPP-60-500, and g) and h) m-CoPP-60-600 samples, with scale bars 500 nm, 20 μm, 500 nm, 10 μm, 500 nm, 100 μm, 1 μm and 20 μm, respectively.

3.2.3. Electrochemical Characterization of m-CoPP and its Transformation to β-$Co(OH)_2$

The clear solutions of Co(II):Acid:P123 are spin-coated over an FTO coated glasses or dip-coated over graphite rods (GR) and calcined at a desired temperature (300 to 700 ^oC) to obtain 1 cm^2 FTO (denoted as FTO-CoPP-n-X, CoPP is $Co_2P_2O_7$, n is Co/P123 ratio in the initial solution, and X is calcination/annealing temperature in Celsius) and GR-coated electrodes (denoted as GR-CoPP-n-X). These electrodes are used to carry out the electrochemical measurements using a 3-electrode system in 3M KOH solution as an electrolyte.

Firstly, the FTO-CoPP-n-X electrodes were prepared to collect CVs at various current densities to evaluate their electrochemical properties. Figure 3.55 shows the CVs of the FTO-CoPP-60-X electrodes with a scan rate of 50 mV/s in a potential window of -0.5-2.0 V versus NHE. One oxidation peak is observed at around 0.5 V in the first cycle of the FTO-CoPP-60 electrodes, calcined at 300, 400, and 500 ^oC. This peak disappears in further consecutive cycles. Peaks due to oxidation and reduction of cobalt species with very low current density appear in the second and additional cycles up to 600 ^oC. With CV cycling, there is a slight decrease in the current density. Note also that there is a decline in the current density in the OER potential region. As observed in the nickel system, the reason for this decline in the current density for both the redox couple and the water oxidation part is the degradation of the electrode during cycling. Here, the degradation is slower than in the nickel system, but there is instability with cycling. The FTO-CoPP-60-600 electrode, which is crystalline, is relatively more stable compared to the amorphous phases. There is a gradual increase in the current density during CV cycling, indicating that the transformation of CoPP to $Co(OH)_2$ is slower (see later).

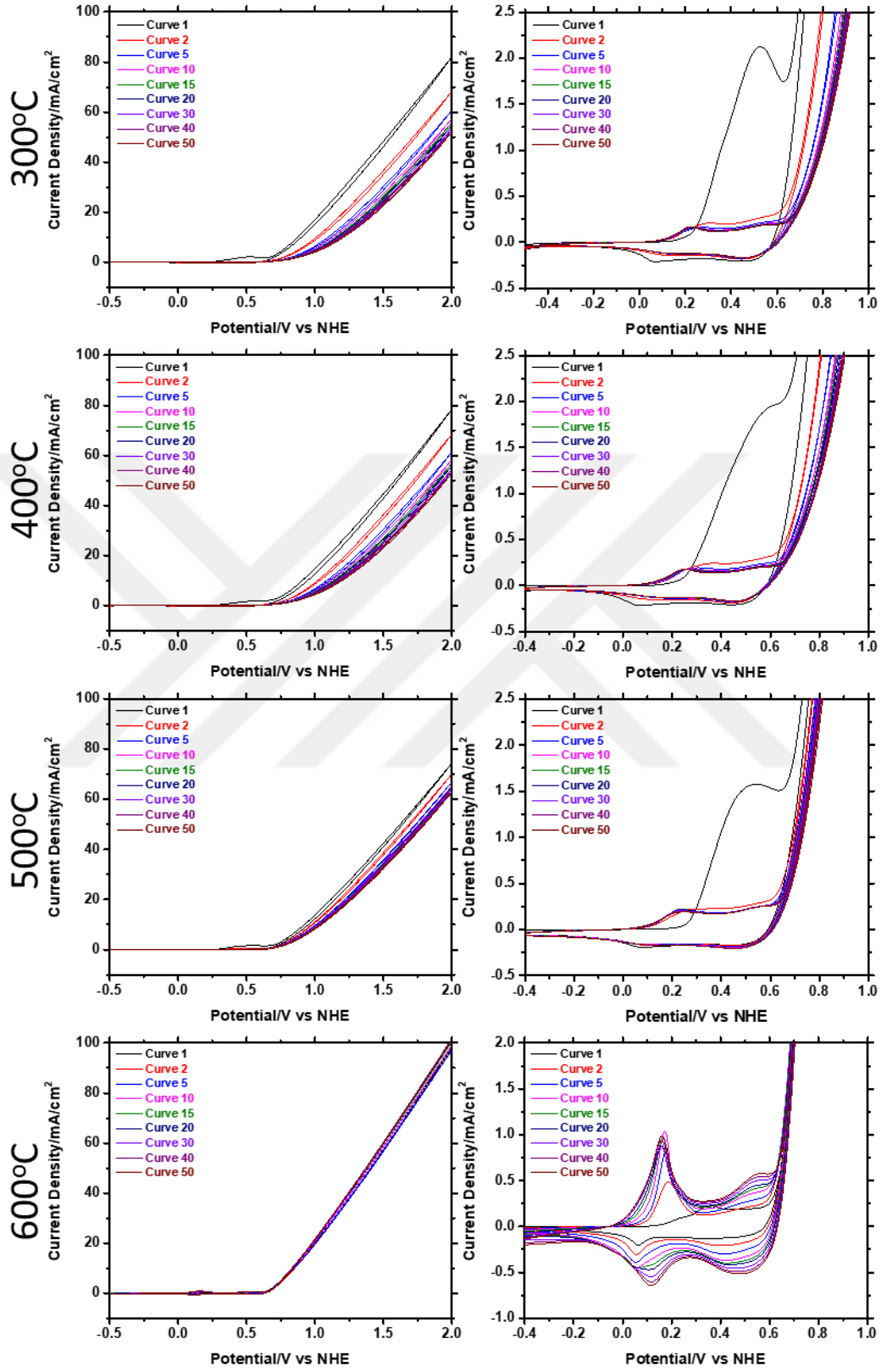

Figure 3.55: 50 CV cycles of FTO-CoPP-60-X (X values are shown on the left) electrodes with a scan rate of 50 mV/s (The right column shows the zoomed plots in the oxidation-reduction region).

Pure graphite rods are also used to prepare the CoPP-60 electrodes since the FTO is not good as a substrate for the working electrode. As discussed before, the dilution of the mother liquors is necessary to use the graphite rod as a substrate. Since the highest surface area is obtained from the 60-mole ratio in the CoPP system, the electrodes are prepared using the 60-mole ratio solution. This solution is diluted 10 times to get an almost similar thickness to the electrodes to compare with the nickel system (remember that 5 times dilution was used for a 30-mole ratio for the nickel system). Figure 3.56 shows the CV curves of the GR-CoPP-60-X (X is 300, 400, 500, 600, and 700) electrodes. There are slight changes in the oxidation and reduction peaks over cycling. The water oxidation region is relatively stable for the GR-CoPP-60-300 working electrode. With increasing calcination temperature, the water oxidation region (0.75 and 1.5 V) becomes sharper by increasing the number of CV cycles. This means the material is converted to a more active material for the OER process by increasing the calcination temperature.

After using the electrodes for CV measurements in a wide potential window at a scan rate of 50 mV/cm^2, the scan rate dependence was tested in a narrow potential window, namely the oxidation-reduction region. The scan rate-dependent analysis provides information about the active surface coverage and helps to determine a proper range for the GCD measurements. The current density versus scan rate relationship is linear, unlike the NiPP system. This means the only surface is used as the active side in the CoPP electrodes. Note also that, with the help of eq. 1.2 (see introduction part), the surface coverage of the CoPP electrodes can be calculated as 4.15, 3.72, 3.51, 4.47, and 6.17 $\mu mol/cm^2$ for the electrodes prepared at 300, 400, 500, 600, and 700 ^oC, respectively. Interestingly, the surface coverage drops first by annealing in the amorphous samples and increases with temperature in the crystalline samples. Figure 3.57 displays the scan rate-dependent CV curves (left column) and plots of current density versus scan rate (right column) of the GR-CoPP-60-X electrodes (X varied between 300 and 700 ^oC). The scan rate-dependent CV curves are collected from the fast scan rate (50 mV/s) to the slower ones. There are only slight differences between the electrodes prepared by different calcination temperatures. It indicates that during the electrochemical process, the reaction mechanism of the transformation of CoPP to $Co(OH)_2$ slightly differs with calcination temperatures.

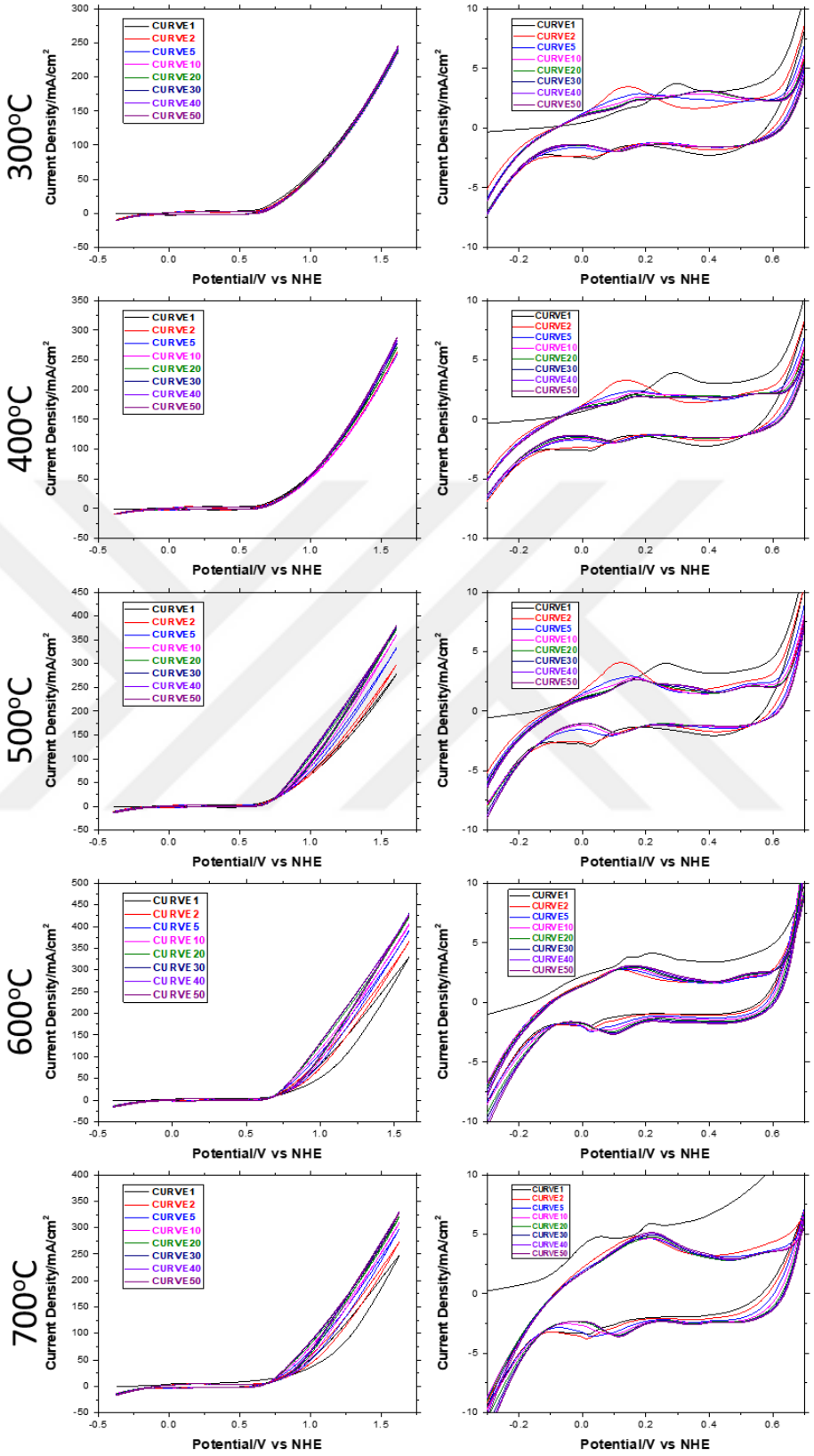

Figure 3.56: 50 CV cycles of the GR-CoPP-60-X (X values are shown on the left) electrodes with a scan rate of 50 mV/s (the right column shows the zoomed plots in the oxidation-reduction region).

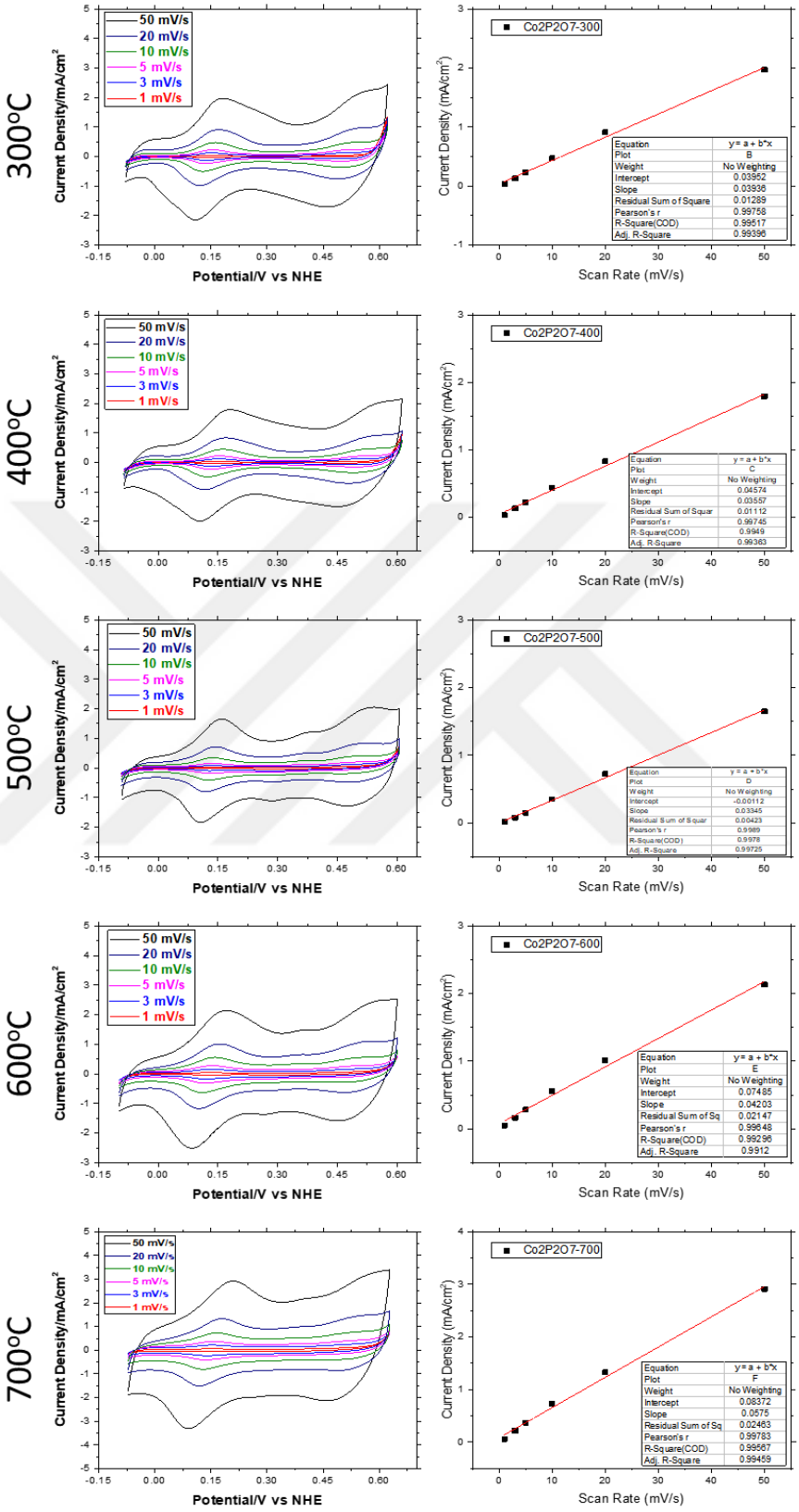

Figure 3.57: (Left column) Scan rate dependent CV curves and (right column) the plots of currents density versus scan rate of the GR-NiPP-30-X electrodes (X values are shown on the left).

The used m-CoPP electrodes, like in the nickel system, are further characterized after electrochemical tests. The XPS spectra were recorded before and after CVs and compared with the electrode only aged in a 3M KOH solution. Figure 3.58 shows the XPS spectra in the Co 2p, O 1s, and P 2p regions before (blue spectra), after CVs (red spectra), and only the aged electrode (black spectra). As expected, the phosphorus 2p peak in the spectrum completely disappears after using the electrode in the CV measurements and aging in a 3M KOH solution, indicating a transformation of the CoPP to phosphorous-free material (likely $Co(OH)_2$, see latter). The Co $^2P_{3/2}$ peak appears at around 782.4 eV before use for CoPP material. [170] After transformation to the $Co(OH)_2$ materials with aging or use for CVs, the same peak shifts to the 780.7 eV for the $Co(OH)_2$ material, similar to the Ni 2p region in the NiPP electrodes. [171] The O 1s peak becomes sharper and shifts to a lower binding energy, from 532.2 to 531.5 eV, for the electrodes before and after CVs, respectively. However, the P 2p peak completely disappears, indicating the transformation. Moreover, there is a shoulder in the region of the O 1s peak at 531.5 eV on the high-energy side due to hydroxide and coordinated water. [166] The spectra in all three regions (Co 2p, O 1s, and P 2p) are identical in electrochemically (after CVs) and chemically (just aged in 3M KOH) transformed samples. Therefore, it is reasonable to suggest the following chemical equilibrium reaction (eq. 3.8).

$$\mathbf{Co_2P_2O_7(s) + 4OH^-(aq) \leftrightarrow 2Co(OH)_2(s) + P_2O_7^{4-}(aq)} \qquad \mathbf{eq.\ 3.8}$$

EDX analysis also proved the transformation of the CoPP material to a phosphorous-free material. Figure 3.59 shows the EDX spectra of the CoPP electrode before and after CVs. Before electrochemical measurements, the CoPP material has cobalt and phosphorous elements in a stoichiometric ratio. However, the phosphorous disappears entirely after the electrochemical measurements.

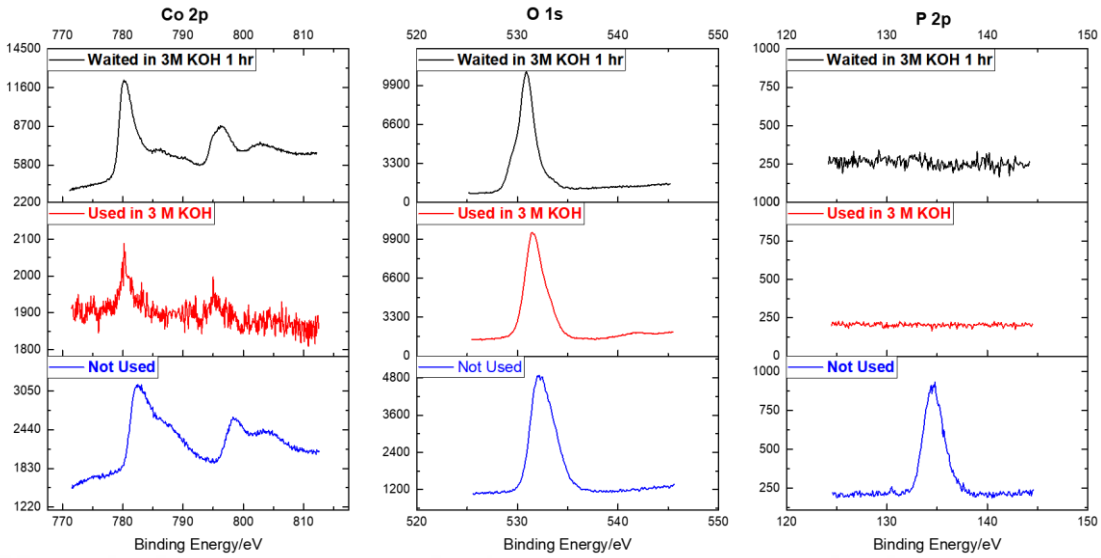

Figure 3.58: XPS spectra of (blue) of the m-CoPP before CVs, (red) m-CoPP after CVs, and (black) m-CoPP aged in 3M KOH for 1 h:(left) Co 2p, (middle) O 1s, and (right) P 2p regions.

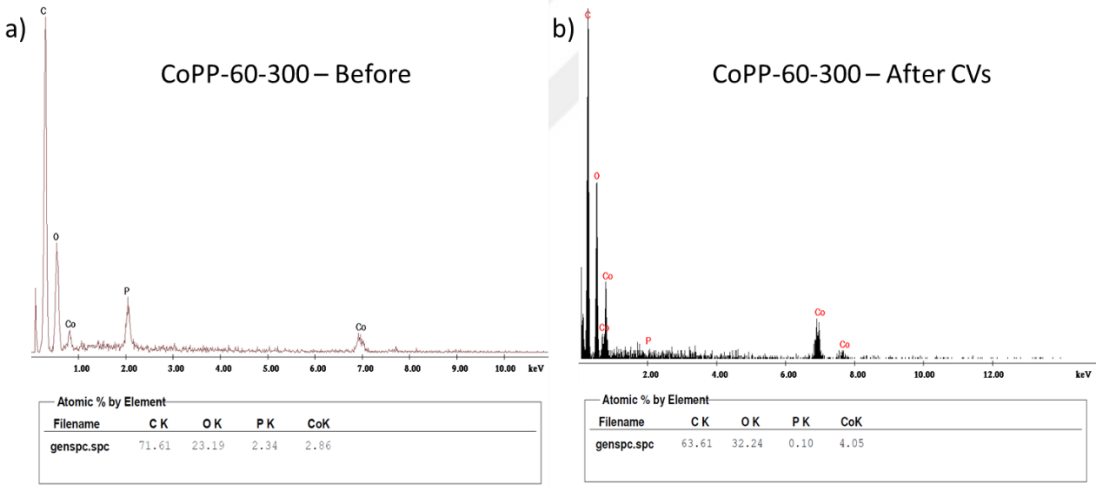

Figure 3.59: EDX spectra of the m-CoPP-30-300 electrode (a) before and (b) after CV measurements with atomic percentages of elements.

A large amount of m-CoPP-60 powder is further analyzed using XRD, ATR-FTIR, and SEM imaging techniques to elucidate details of the chemical transformation of CoPP to $Co(OH)_2$ (see eq. 3.8). The m-CoPP-60-300 sample, collected from the substrate as a powder, is aged in a 3M KOH solution to observe the transformation. As it is clarified in the nickel system, the powders of CoPP are also aged in a closed system to achieve the pure hydroxide phase. The aging process in the basic medium was followed by changing the aging time; the XRD patterns and ATR-FTIR spectra

were collected for each step, see Figure 3.60. The transformation of CoPP to cobalt hydroxide in a 3M KOH solution is a relatively fast process; in 5 min, aging in the 3 M KOH solution, the transformation is complete. The XRD patterns of 5 min and 1 h aged samples are identical, and the diffraction lines can be indexed to pure beta cobalt hydroxide, see Figure 3.60a. Remember that transforming NiPP to $Ni(OH)_2$ takes about 1 h, which is a slower process than the CoPP transformation. The β-$Co(OH)_2$ particles are much larger than the β-$Ni(OH)_2$ particles. Therefore, the growth is faster in the CoPP to $Co(OH)_2$ transformation. The seeding process is likely more rapid in the NiPP to $Ni(OH)_2$ transformation, leading to too many smaller particles.

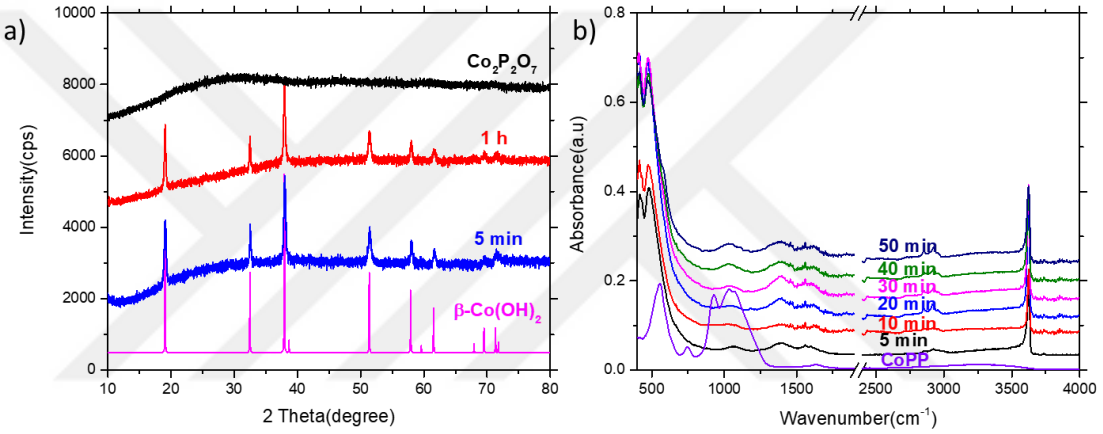

Figure 3.60: a) Wide-angle XRD patterns of the m-CoPP-60-300 sample after treatment in 3M KOH for 5 min and 1 h and corresponding to reference of β-$Co(OH)_2$ (ICDD - 00-030-0443) and b) ATR-FTIR spectra of the m-CoPP-60-300 sample and after its aging in 3M KOH for 5, 10, 20, 30, 40, and 50 min.

The ATR-FTIR spectra of the CoPP samples, aged in 3M KOH solution, also show that the transformation is complete in 5 min, see Figure 3.60b. The peaks at 3643 cm^{-1} due to $Co(OH)_2$ (water-free hydroxyl group) and Co-O peaks (at about 440-650 cm^{-1}) appear, whereas the PP peaks at 1030, 928, 744, and 548 cm^{-1} entirely disappear. In addition, there is a trace amount of carbonate and bicarbonate species (at around 1400 and 1580 cm^{-1}), which are like some impurities and are not visible in the XRD patterns of those samples since they are under the detection limits of XRD.

The changes in morphology during the transformation of pyrophosphates to hydroxide are also investigated by SEM imaging technique using the m-CoPP-60-300 samples. When it is converted to hydroxide, the m-CoPP-60-300 sample changes its

morphology from spherical porous like-particles to plate-like particles, compare Figures 3.61a and 3.61b. The image of the aged sample is consistent with the highly sharp diffraction lines in the XRD pattern, see Figure 3.60a. The plate-like large nanoparticles are crystalline β-$Co(OH)_2$, as evidenced by both XRD patterns and ATR-FTIR spectra.

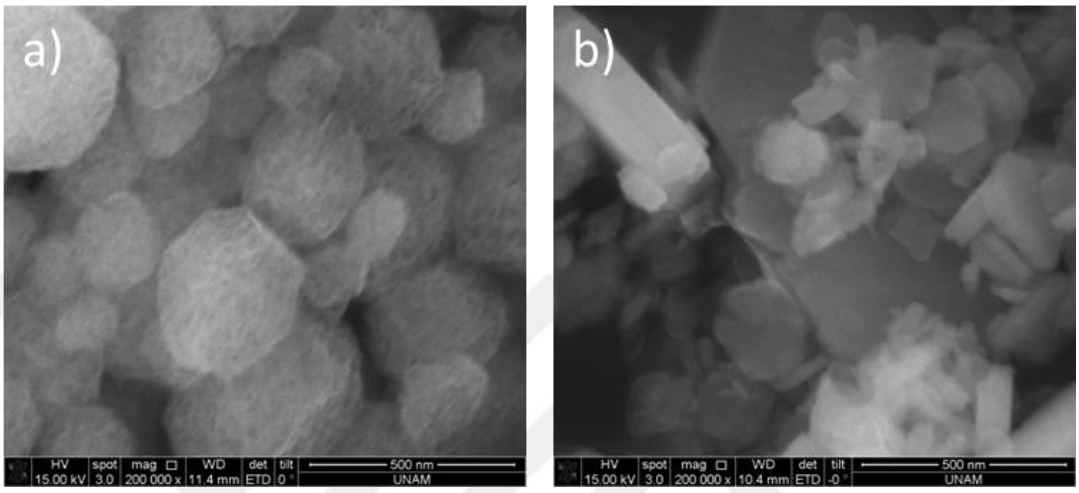

Figure 3.61: SEM images of m-CoPP-60-300 a) before, b) after aging in 3 M KOH solution for 5 min (the scale bars are 500 nm).

Since the reaction of the m-CoPP-300 sample undergoes an extremely fast transformation in KOH solution, it is possible to observe real-time transformation by recording a video. The CoPP sample calcined at 300 ^oC on a microscope slide has a purple-blue color before reacting with a KOH solution. When the KOH solution is poured into the sample, the sample becomes turquoise-blue colored. This color may originate from tetrahedrally coordinated cobalt species forming during the transformation.[172] Note also that the blue color is characteristic of tetrahedral Co(II) species. But 30 sec later, the sample turns completely to a pale pink color, which is the color of pure β-$Co(OH)_2$. After obtaining β-$Co(OH)_2$, a small amount of concentrated PPA (pyrophosphoric acid) is added to the transformed film to see its reversibility. Since concentrated PPA is used, it dissolves some of the β-$Co(OH)_2$ particles. However, it is enough to observe the back transformation to purple-blue colored CoPP, meaning that the process is reversible, see Figure 3.62.

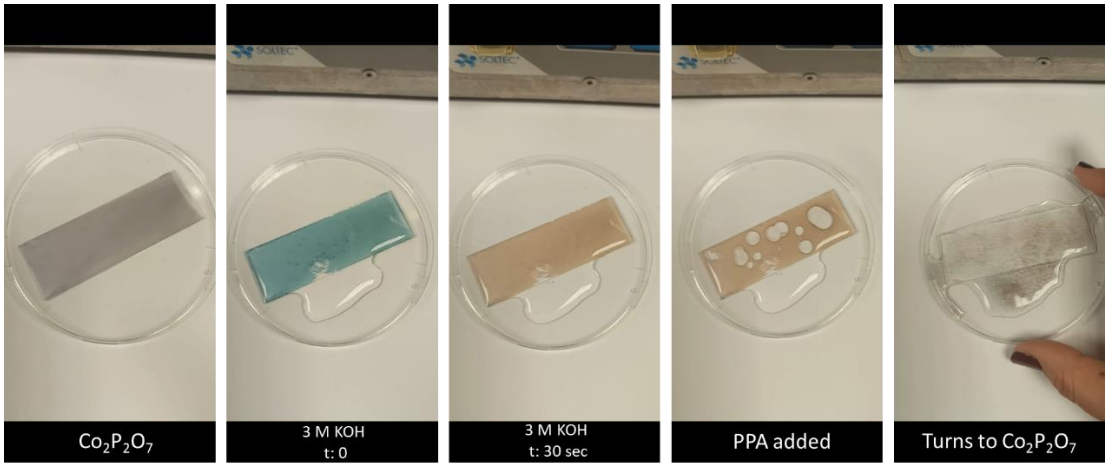

Figure 3.62: Photographs of the m-CoPP-60-300 film over a microscope slide during the transformation and its reversibility.

The m-CoPP-60-300 sample transforms to its hydroxides much faster than the m-CoPP-60-700 sample. Aging the m-CoPP-60-700 in 3M KOH solution for 5 min is not sufficient to convert all pyrophosphates to hydroxide. Transformation of the CoPP-60-700 sample starts in 5 min, but a large portion of the sample is still CoPP, see the XRD pattern in Figures 3.63a. Diffraction lines of both α-CoPP and β-$Co(OH)_2$ coexist in the XRD pattern. The colors of the sample in the 3M KOH solution, kept for 5 min, are also proof of the transformation; the CoPP-300 is converted to pale pink, which is the color of β-$Co(OH)_2$, whereas the CoPP-700 preserves its color of CoPP, which is purple-blue, see Figure 3.63b.

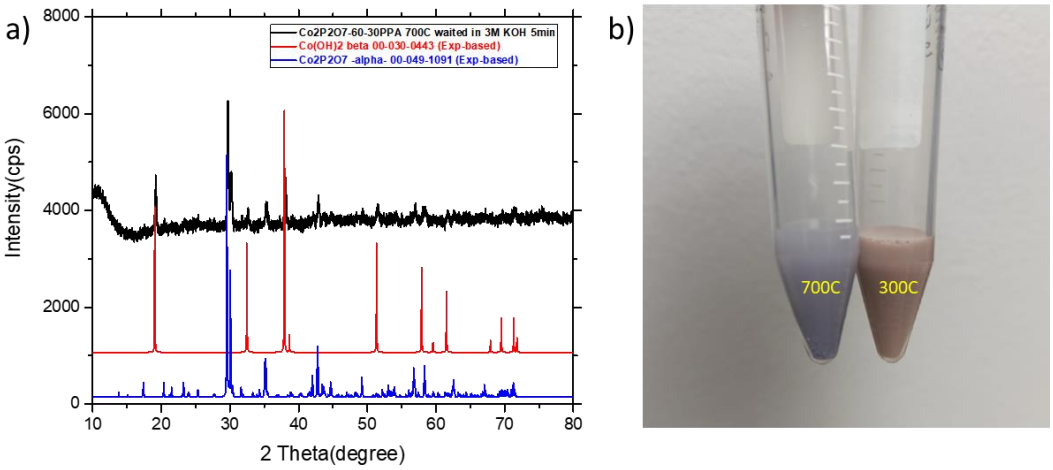

Figure 3.63: a) Wide-angle XRD pattern of the CoPP-60-700 aged in 3 M KOH solution for 5 min and the reference patterns of β-$Co(OH)_2$ (ICDD - 00-030-0443) and α-$Co_2P_2O_7$ (ICDD - 00-049-1091) and b) photographs of the m-CoPP-60-300 and m-CoPP-60-700 samples, aged in 3M KOH solution for 5 min.

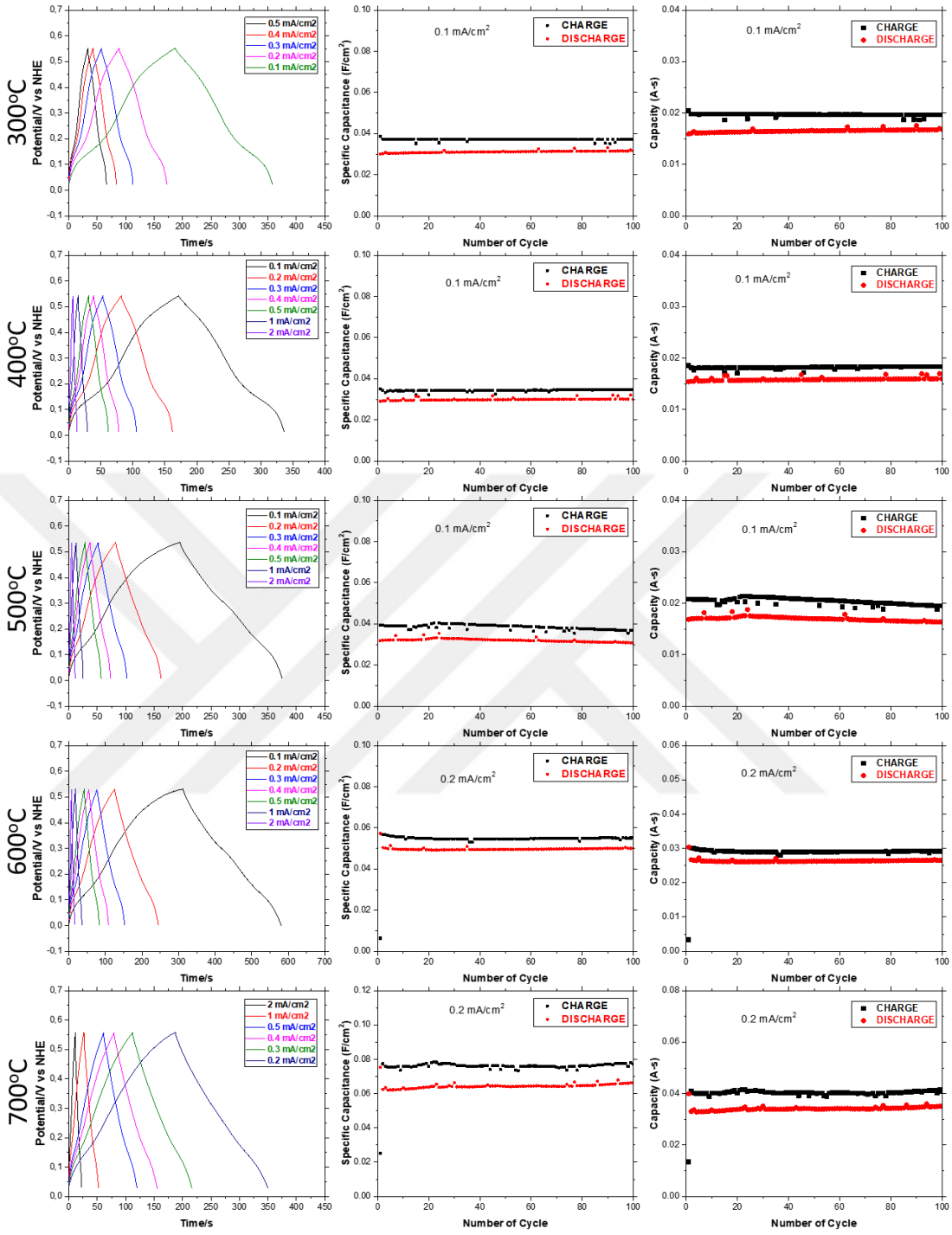

Figure 3.64: Electrochemical properties: (right column) GCD graphs, (middle column) specific capacitance versus the number of cycle plots, and (left column) capacity versus the number of cycle plots of the GR-CoPP-60-X (X is denoted on the left) electrodes.

The electrodes are completely transformed to the $Co(OH)_2$ material and used for the GCD measurements. Remember that the electrodes calcined at higher temperatures must be cycled for at least 50 cycles (which takes almost 1 h) or kept in

KOH solution for 1 h before GCD measurements in order to start from the fully converted electrodes. Each electrode, used for 50 CV cycles and scan rate-dependent analysis, is used to record the GCD curves. Note that the time required for these measurements is more than enough to convert all CoPP, calcined at each temperature, to $Co(OH)_2$. Figure 3.64 shows the GCD behaviors at different current densities and specific capacitance and capacity values versus the number of cycles to see the stability of the electrodes over 100 cycles of charging and discharging. Both specific capacitance and capacity values of all the samples remain constant during charging/discharging in each electrode, annealed at each temperature, see Figure 3.63. The specific capacitance and capacity values are given in mF/cm^2 and $mA \cdot s$ units, respectively, at each current density in Table 3.4. The capacity and specific capacitance values of fully converted CoPP samples are almost 10 times less than $Ni(OH)_2$, which might be related to the particle sizes of their hydroxides. Furthermore, the percent coulombic efficiency is calculated for the electrodes that were subjected to calcination temperatures ranging from 300 to 700 ^oC, see Figure 3.65. The coulombic efficiency varies depending on the calcination temperature. The percent coulombic efficiency of the GR-CoPP-60-300 electrode is reported to be around 80% in the first cycles. With subsequent cycling, this value increases to approximately 85%. When the calcination temperature increases to 600 ^oC, the coulombic efficiency reaches 90% and further improves by 92% with cycling. The GR-CoPP-60-700 electrode exhibits similar efficiency compared to the low-temperature electrodes.

Table 3.4: Specific capacitance and capacity values of the electrodes calcined at indicated temperatures of the GR-CoPP-60-X (X is shown on the top).

	300 °C		400 °C		500 °C		600 °C		700 °C	
Current Density (mA/cm^2)	Capacity ($mA \cdot s$)	Specific capacitance (mF/cm^2)	Capacity ($mA \cdot s$)	Specific capacitance (mF/cm^2)	Capacity ($mA \cdot s$)	Specific capacitance (mF/cm^2)	Capacity ($mA \cdot s$)	Specific capacitance (mF/cm^2)	Capacity ($mA \cdot s$)	Specific capacitance (mF/cm^2)
0.1	16.81	33.62	15.48	30.96	16.85	33.70	25.13	50.26	-	-
0.2	16.31	32.62	15.55	31.10	15.98	31.96	23.11	46.22	31.61	63.22
0.3	16.27	32.54	15.41	30.82	14.83	29.66	21.99	43.98	30.56	61.12
0.4	16.16	32.32	15.26	30.52	14.29	28.58	21.06	42.12	29.66	59.32
0.5	16.02	32.04	15.08	30.16	13.82	27.64	20.19	40.38	28.84	57.68
1	-	-	14.26	28.52	12.35	24.70	17.60	35.20	25.59	51.18
2	-	-	12.64	25.28	10.84	21.68	15.34	30.68	22.14	44.28

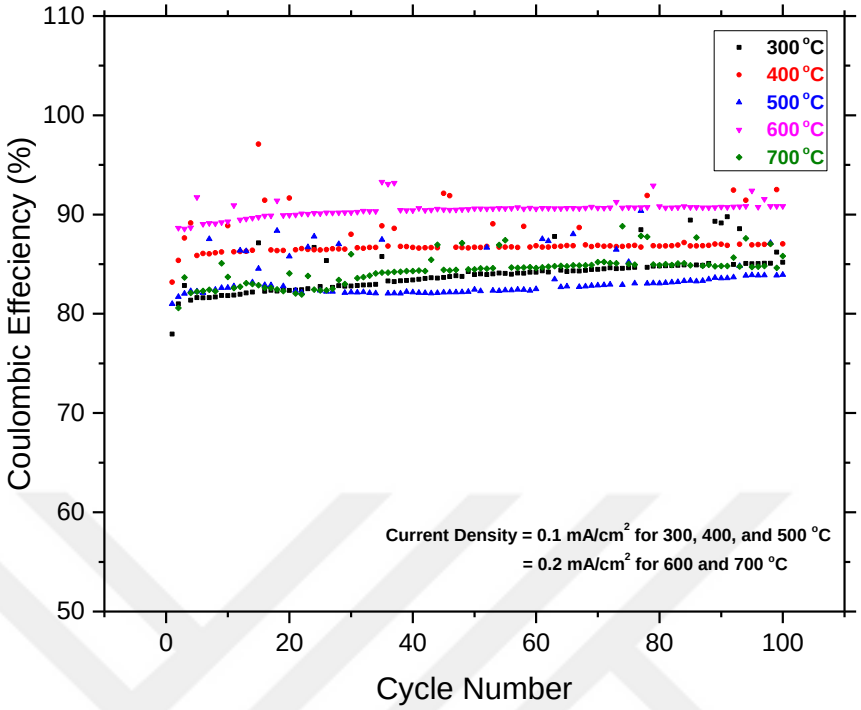

Figure 3.65: Graph of coulombic efficiencies of the GR-CoPP-60-X electrodes (X is 300, 400, 500, 600, and 700) versus cycle number.

As mentioned before, the transformation of the CoPP-300 to β-$Co(OH)_2$ is a much faster reaction. Figure 3.66 shows the 1000 CV curves of the electrodes, calcined at various temperatures. Till 600 °C, the first curves of the sample have the highest oxidation current density at around 0.3 V. For the higher calcination/annealing temperatures, the first curves do not display the same oxidation peak current density. Since in 30 sec, the transformation is almost complete, till starting the CV measurement, the large portion of the sample is already converted to cobalt hydroxide structure. After the water oxidation reaction, the oxidation peak at around 0.3 V diminishes, and with cycling, it again begins to enhance. With the applied potential, the material might change its structure upon cycling.

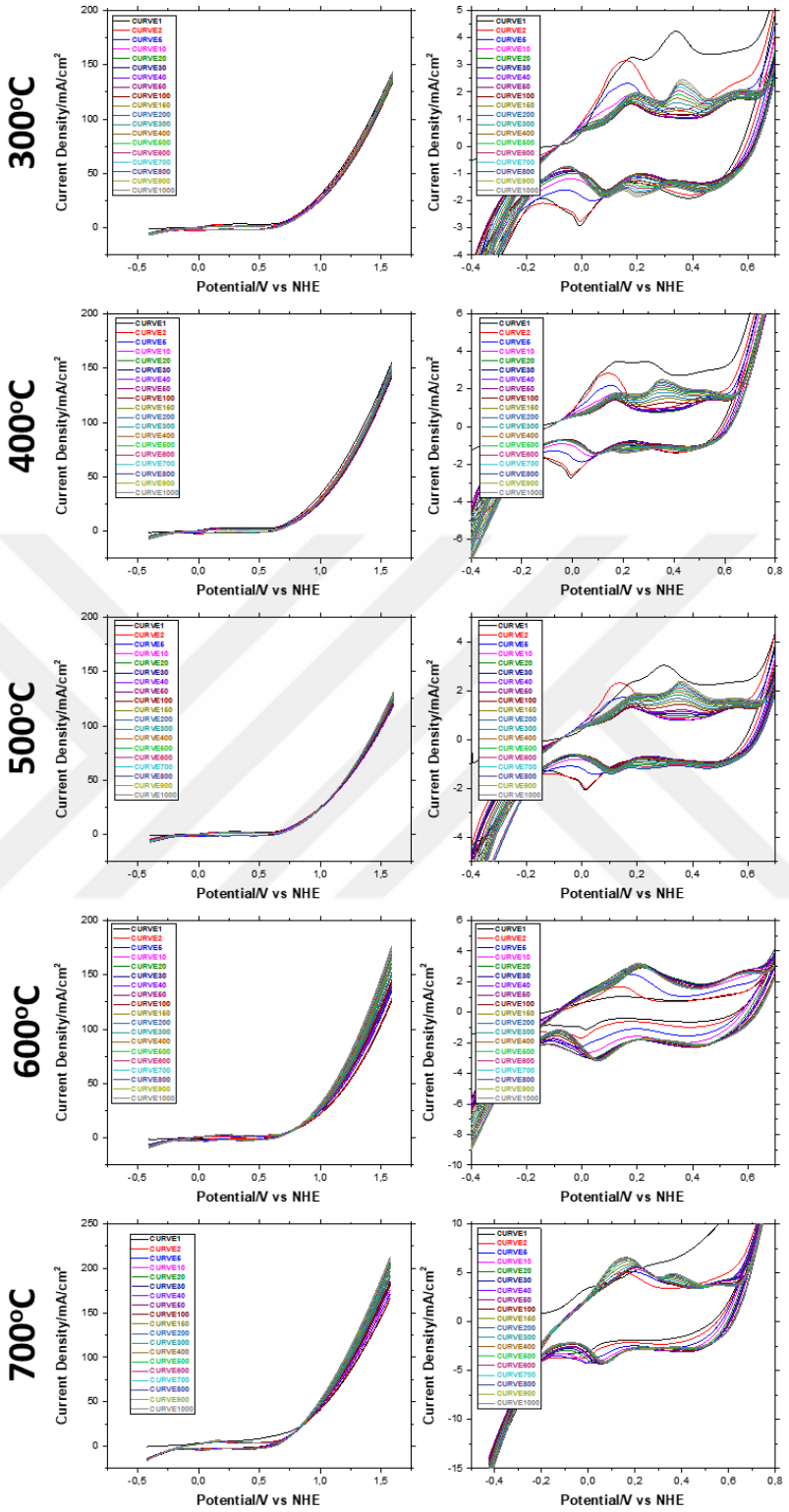

Figure 3.66: 1000 CV cycles of the m-CoPP-60-X (X is indicated on the left) electrodes at a scan rate of 50 mV/s for a potential window of -0.5-1.5 V vs. Ag/AgCl in 3M KOH electrolyte.

3.3. Synthesis and Characterization of m-$Mn_2P_2O_7$ Samples

3.3.1. Preparation and Characterization of Mn(II):Acid:P123 Mesophases

The clear solutions of Mn(II):Acid:P123 are prepared using PA or PPA in tabulated amounts in Table 2.1. The mesophases of Mn(II):Acid:P123 can be obtained by drop-casting method over microscope slides and characterized by XRD, gravimetric measurements, and ATR-FTIR techniques during aging (solvent evaporation) at RT to determine their stabilities and monitor spectral changes.

Small-angle XRD patterns of the mesophases of Mn(II):PPA:P123 for low, intermediate, and high mole ratios (30, 60, and 90, respectively) are collected during aging at RT, see Figure 3.67. A couple of diffraction lines of the 30 and 60-mole ratios of Mn(II):PPA:P123 mesophases are observed at small angles, indicating that the mesophases have an ordered/oriented mesostructure, and almost all are stable up to 5-6 days. The diffraction line at around 1.9°, 2θ, shifts to a lower angle (to 1.63°, 2θ) while aging at laboratory conditions, meaning that the unit cell of the mesophase enlarges in the 30-mole ratio. The shift in the 60-mole ratio mesophase is negligible compared to the 30-mole ratio, meaning there is almost no change in the unit cell parameters. The mesophase of the 90-mole ratio is not oriented like lower compositions; no diffraction line is observed between 1 and 5°, 2θ. However, the tailing in the patterns indicates that there might be diffraction below 1°, 2θ. Notice that, like the Ni and Co systems, the diffraction lines are not very intense, meaning the visible diffractions belong to the higher-order planes. The most intense line might still be below 1°, 2θ.

The stability of the mesophases is compared by changing the acid precursor. Mesophase of the Mn(II):PPA:P123 solutions are relatively more stable during aging at RT (evaporation of excess solvent) than that of the Mn(II):PA:P123 mesophases. The diffraction line of the Mn(II):PA:P123 mesophase, at around 1.3°, 2θ, appears in 30 min aging at RT, shifts to 1.7°, 2θ while aging, and disappears after 1 day, see Figure 3.68. The reason can be related to the acidity of the solutions and polymerization reactions between pyrophosphate and metal ions.

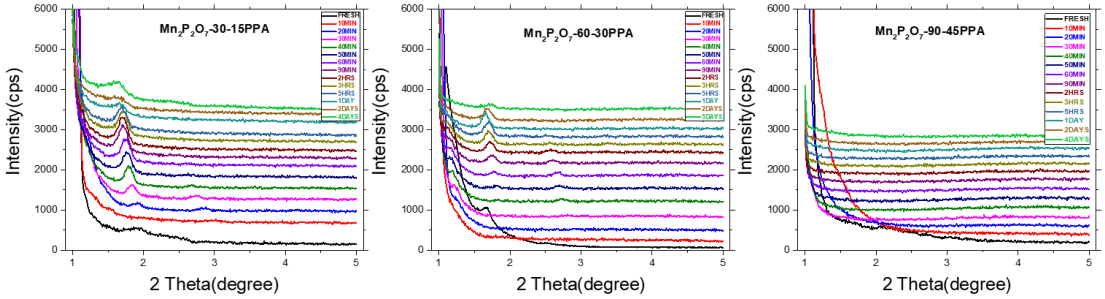

Figure 3.67: Small-angle XRD patterns of the Mn(II):PPA:P123 mesophases with a composition of (left) 30, (middle) 60, and (right) 90 mole ratios of Mn(II)/P123.

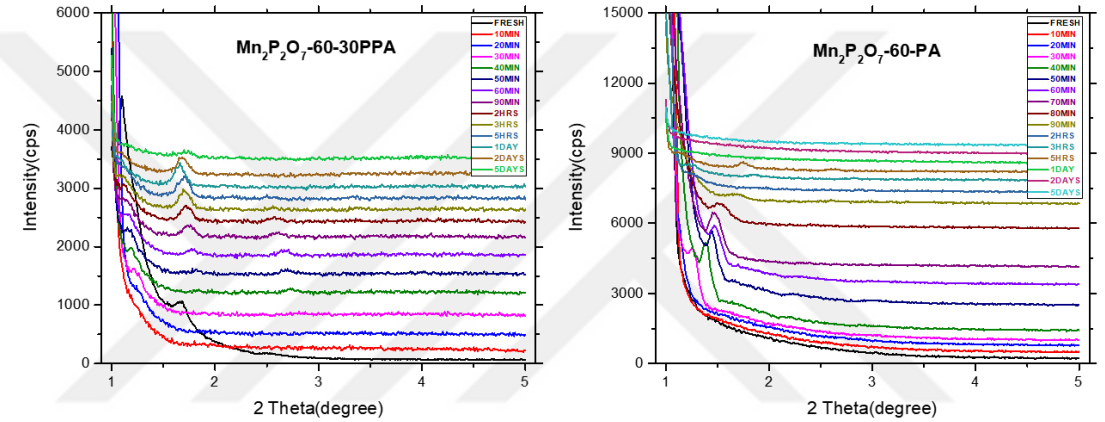

Figure 3.68: Small-angle XRD patterns of 60-mole ratio Mn(II):Acid:P123, prepared using (left) PPA and (right) PA acid precursors.

Evaporation of the solvent from the Mn(II):Acid:P123 solution was also followed by gravimetric measurement using both PA and PPA solutions. The excess water is quickly lost in the first 200 min (range I, gelation), and evaporation continues slowly after this point (ranges II and III, solidification), see Figure 3.69. Slow decay is due to the removal of the volatile species from the media (like nitric acid and its decomposition products). This step corresponds to a solidification reaction (polymerization of the pyrophosphate and metal ions). There are slight differences between PA and PPA systems since the acidity of the solutions is different (PPA is more acidic than PA) and affects the chemical reactions during the solidification process.

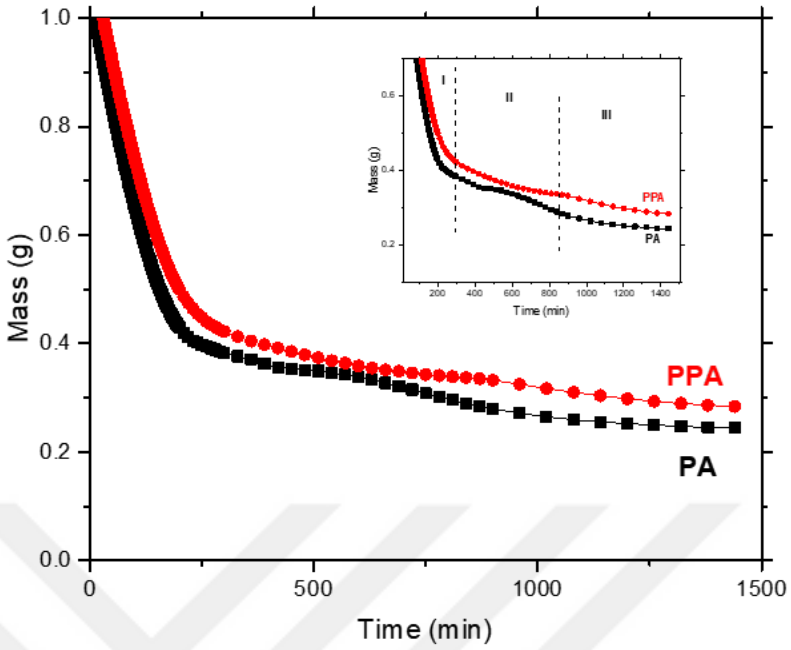

Figure 3.69: Gravimetric measurements: Mass versus time plots during water evaporation on the balance of the Mn(II):Acid:P123 solutions prepared by PA and PPA.

The MnPP mesophases are also characterized by ATR-FTIR spectroscopy to understand the gelation and solidification mechanism further. The spectra are recorded by putting a drop of each solution of the Mn(II):PPA:P123 mixture on the ATR crystal, starting from dropping (0 min) to 48 hours. Figure 3.70a shows the raw ATR-FTIR spectra of a Mn(II):PPA:P123 solution. Since the refractive index and concentration of the solution change during the evaporation of excess water (see NiPP section for details), the spectra must be normalized to analyze quantitatively. The normalized spectra using the phosphate peak are given in Figure 3.70b. The peaks at around 3600-3000 and 1640 cm^{-1} originate from the stretching and bending modes of water species, respectively. The intensity of the water peaks decreases during the aging process. Peaks at around 1470-1290 cm^{-1} are due to nitrate species, and the peaks at around 1200-800 cm^{-1} result from the phosphate species. A similar reduction is also observed in the nitrate peaks, meaning the nitrate species decay in time, likely as nitric acid or its decomposition products, similar to the Ni(II) and Co(II) systems, see eq.3.9

$$2Mn(NO_3)_2(aq) + H_4P_2O_7(aq) + nH_2O \leftrightarrow Mn_2H_xP_2O_7(NO_3)_x.nH_2O(s) + (4-x)HNO_3(g) \quad \textbf{eq. 3.9}$$

The normalized spectra are used to obtain quantitative results for the gelation and polymerization processes. The first spectrum (0 min) of MnPP-30 is assumed to be the initial composition of the solution and calculated to have 115 water per manganese ion in the media. The nitrate to manganese mole ratio is supposed to be 2 in the first spectrum of the MnPP-30 solution. Figure 3.71 shows the plots of water/manganese and nitrate/manganese mole ratios versus time during the aging of the MnPP-30 sample at RT. The sample loses its water quickly (in the first 50 min). Decay of the nitrate species follows water loss, showing that the nitrate decomposition depends on the water content of the solution, similar to nickel and cobalt systems. First, fast decay corresponds to a gelation process. In contrast, the decline is slow after this point and corresponds to the polymerization of pyrophosphate species and manganese ions, a solidification process. The composition of MnPP-30 after 48 h of aging is calculated to be $Mn_2H_{0.4}P_2O_7(NO_3)_{0.4}\cdot 3.6H_2O$.

Effect of heating on the Mn(II):PPA:P123 mesophase is also monitored using ATR-FTIR spectroscopy by heating the sample on the ATR diamond. Heating after 48 h aging causes further reduction of the nitrate and water species from the mesophase, see Figures 3.70 c and d. The spectra were recorded between RT and 100 ^oC to identify further the chemical species forming during the heating/drying process. The water peak almost completely disappears at around 80 ^oC, indicating a complete drying of the sample. A clear shift in the peaks of nitrate species, observed in the nickel and cobalt systems by heating the sample due to the formation of bridged nitrate species, is not observed in the manganese system, indicating no change in the nitrate binding during heating. The only change is a decay in the free and monodentate nitrate peaks, leaving only bidentate nitrate species.

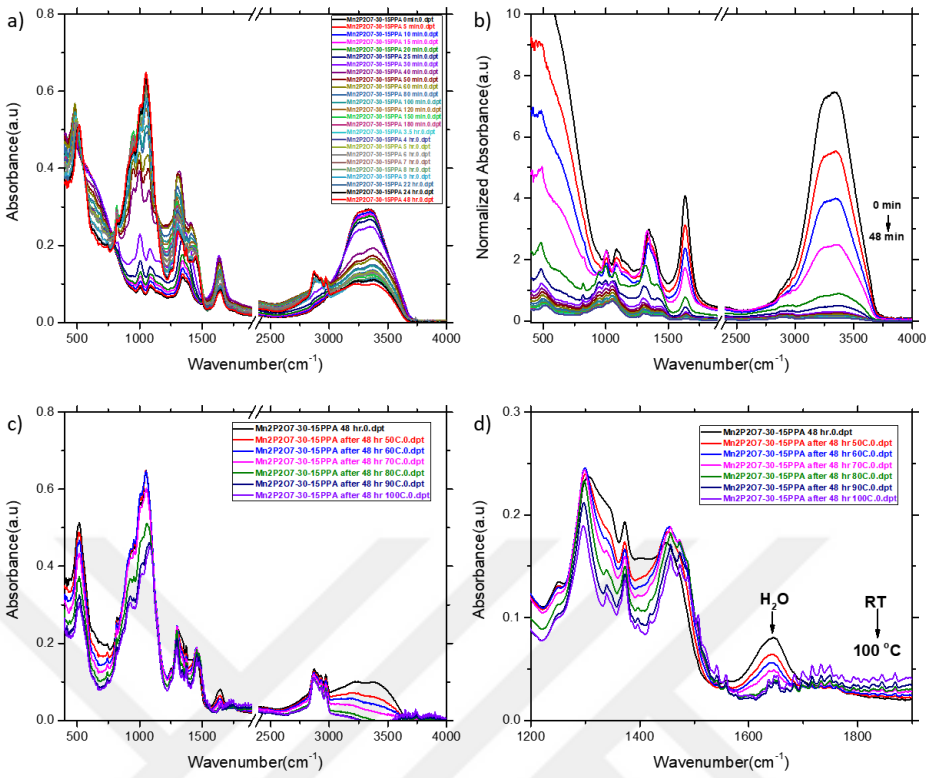

Figure 3.70: Time-dependent ATR-FTIR spectra of the MnPP-30 a) raw spectra, b) normalized spectra. c) and d) The temperature-dependent ATR-FTIR spectra of the MnPP-30 after 2 days aging and followed by heating at (top to bottom) RT, 40 to 100 ºC with 10 ºC increments.

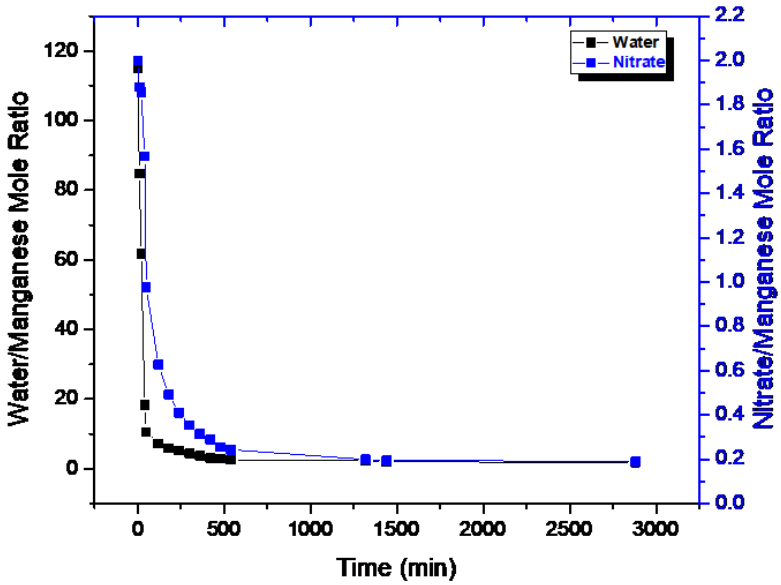

Figure 3.71: Water/manganese and nitrate/manganese mole ratios versus time graphs derived from the normalized ATR-FTIR spectra for the MnPP-30 solution.

3.3.2. Synthesis and Characterization of Mesoporous $Mn_2P_2O_7$

The mesophases of Mn(II):Acid:P123, obtained by various methods (spin-coating, dip-coating, or drop-casting), are calcined at 300 °C to obtain mesoporous $Mn_2P_2O_7$ particles (denoted as m-MnPP-n-X, where m stands for mesoporous, n is for mole ratio of Mn(II)/P123, and X is the calcination temperature in Celsius). The m-MnPP-n-300 samples are further annealed at higher calcination temperatures and characterized by various techniques at each annealing step.

Figure 3.72 shows the powder XRD patterns of the m-MnPP-60-X samples. No diffraction lines are observed up to 600 °C, meaning the sample is amorphous and becomes crystalline above 600 °C. The diffraction pattern of the crystalline phase of the m-MnPP-60 sample can be indexed to monoclinic β-$Mn_2P_2O_7$ with unit cell parameters of a, b, and c of 6.636, 8.584 Å, and 4.546 Å, respectively, see Figure 3.72 (right one).

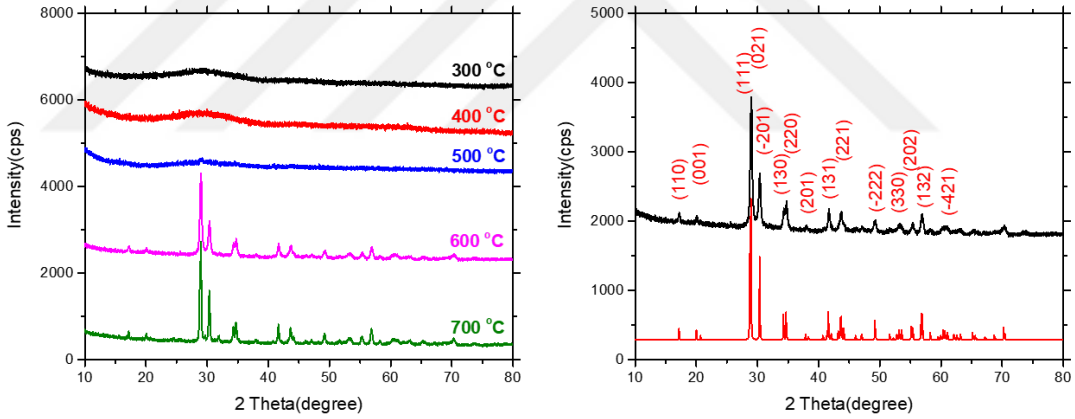

Figure 3.72: Wide-angle XRD patterns of (left) m-MnPP-60-X (X is 300, 400, 500, 600, and 700 °C) and (right) indexed XRD pattern of the MnPP-60-600 with (red) $Mn_2P_2O_7$ (ICDD - 00-029-0891).

The ATR-FTIR spectra of the m-MnPP-n-X samples are collected to evaluate the spectral changes during the calcination/annealing process. Figure 3.73a displays ATR-FTIR spectra of the MnPP-n-300 (n is 30, 60, and 90) samples. The spectra are almost identical, indicating that the structures of m-MnPP for each composition are the same in the samples calcined at 300 °C, see Figure 3.73a. There are no peaks originating from nitrate and surfactant species after the calcination process, indicating

the decomposition of those species at high temperatures (300 ^{o}C and above), see Figure 3.73b. Only peaks originate from the pyrophosphate species at 300 ^{o}C and higher annealing temperatures. The peaks at high frequency (1050-1200 cm^{-1}) correspond to PO_3 units, The peak at 930 cm^{-1} is from the asymmetric stretching modes of the bridged P-O (P-O-P) group, and the intense peaks at around 500-600 cm^{-1} originate from the bending modes of pyrophosphate group and Mn-O stretching modes. [161], [162] The peak at around 750 cm^{-1} resulted from symmetric modes of the bridged P-O (P-O-P) group (where the angle between P-O-P is not equal to 180^{o}) is visible up to 600 ^{o}C and disappears at 600 ^{o}C upon crystallization because the P-O-P angle is smaller than 180^{o} till 600 ^{o}C. With crystallization (at higher temperatures), the material changes its phase to where this angle equals 180^{o} (from alpha to beta phase transformation).[173], [174] Since the P-O-P group is linear in the beta phase, the peak at around 750 cm^{-1} is not observed because the dipole change during this motion is zero. All other phosphate peaks are broad up to 600 ^{o}C and become sharp and resolved at 600 ^{o}C. This change corresponds to a crystallization of the manganese pyrophosphate particles at 600 ^{o}C (see Figure 3.72) and is consistent with the XRD data. The ATR-FTIR spectra also prove that the structure of the material is different in the amorphous and crystalline phases of the MnPP sample, which could not be detected by the XRD.

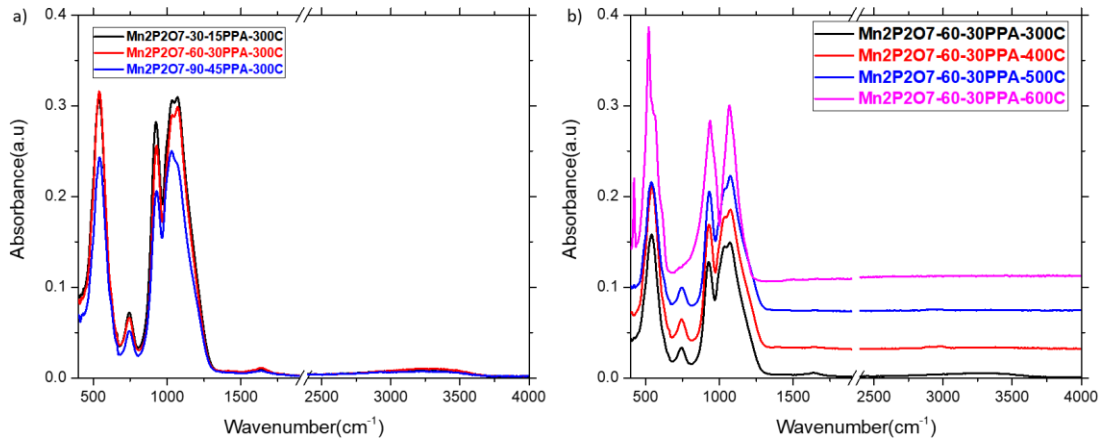

Figure 3.73: ATR-FTIR spectra of the a) m-MnPP-n-300 (n is 30, 60, and 90) and b) m-MnPP-60-X (X is 300, 400, 500, and 600).

N_2-adsorption-desorption isotherms of the m-MnPP-n-X samples are also collected to investigate the porosity. Linear isotherms and Barrett-Joyner-Halenda

(BJH) pore size distribution plots of the m-MnPP samples calcined at 300 °C and annealed at 400, 500, 600, and 700 °C are evaluated and shown in Figure 3.74. Brunauer-Emmett-Teller (BET) surface area, pore volume, and pore sizes of m-MnPP-30-300, m-MnPP-60-300, and m-MnPP-90-300 samples are given in Table 3.5. The isotherms are characteristic of mesoporous materials with a type IV hysteresis. [163][164] The BET surface areas of the m-MnPP-30-300, m-MnPP-60-300, and m-MnPP-90-300 samples are 39, 41, and 26 m^2/g, respectively. The highest surface area is obtained from the m-MnPP-60-300 sample and was chosen for the electrochemical analysis later. The surface area of m-MnPP-60 gradually decreases with increasing annealing temperature and becomes 13, 8, and 2 m^2/g at 400, 500, and 600 °C, respectively, see Figure 3.74c and Table 3.5. Since the pores collapsed, the BET surface area could not be measured from the 700 °C annealed samples.

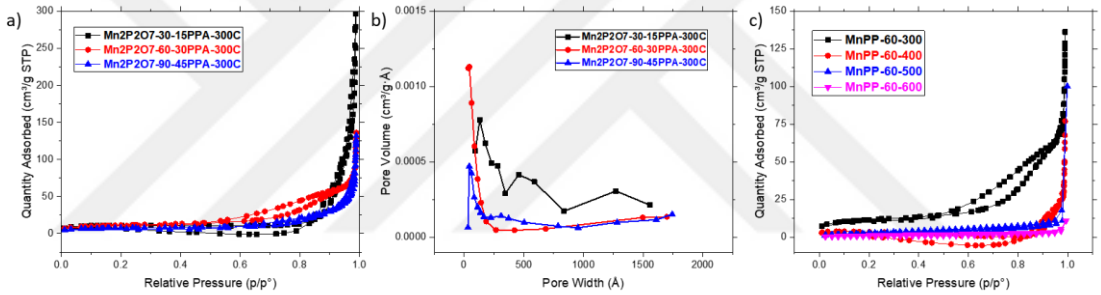

Figure 3.74: N_2 (77 K) adsorption and desorption isotherms of a) m-MnPP-n-300 (n is 30, 60, and 90) and c) m-MnPP-60-X (X is 300, 400, 500, and 600 °C), b) the pore size distribution plots of m-MnPP-n-300 (n is 30, 60 and 90).

Table 3.5: (Left) BET surface area, pore volume, and pore size values of m-MnPP-n-300 (n is 30, 60, and 90) and (right) BET surface area of the m-MnPP-60-X samples (X is 300, 400, 500, 600, and 700 °C).

Mole Ratio	BET Surface Area (m^2/g)	Pore Volume (cm^3/g)	Pore Size (nm)
m-MnPP-30-300	39	0.51	38.4
m-MnPP-60-300	41	0.20	13.6
m-MnPP-90-300	26	0.19	25.0

Calcination Temperature (°C)	BET Surface Area (m^2/g)
	m-MnPP-60
300	41
400	13
500	8
600	2
700	-

The SEM and TEM images of the m-MnPP-n-X samples are also collected to elucidate their morphology and porosity. The images of low, intermediate, and high compositions of m-MnPP-300 are shown in Figure 3.75. There is almost no change in the morphology for all compositions, having spherical and distorted-spherical particles. Since the highest surface area is obtained from the 60-mole ratio, the detailed images are collected using the intermediate composition. The high-quality TEM images show that m-MnPP-60-300 particles range between 50 and 350 nm and have 2 different morphologies: one perfect spherical and some distorted shapes, see Figure 3.76. Unfortunately, the manganese samples are beam sensitive; some deformation occurs under the TEM beam during imaging, see Figures 3.76d. The pores get expanded due to beam damage. The SEM images of the m-MnPP-60 samples, calcined/annealed at different temperatures, are collected to observe the morphological changes while annealing, given in Figure 3.77. The m-MnPP particles display separate spherical particles at calcination temperatures of 300 and 400 ^{o}C. The pores are visible even in the m-MnPP-60-300 and m-MnPP-60-400 samples. The spherical particles aggregate with each other when calcined at 500 ^{o}C and higher temperatures, and the pores expand with increasing annealing temperature. When the crystalline phase is obtained at 600 ^{o}C, the particles become more prominent and bulk-like with no porosity. Note also that the particles had film-like morphology when the samples were imaged at lower magnifications, see Figure 3.77, right column.

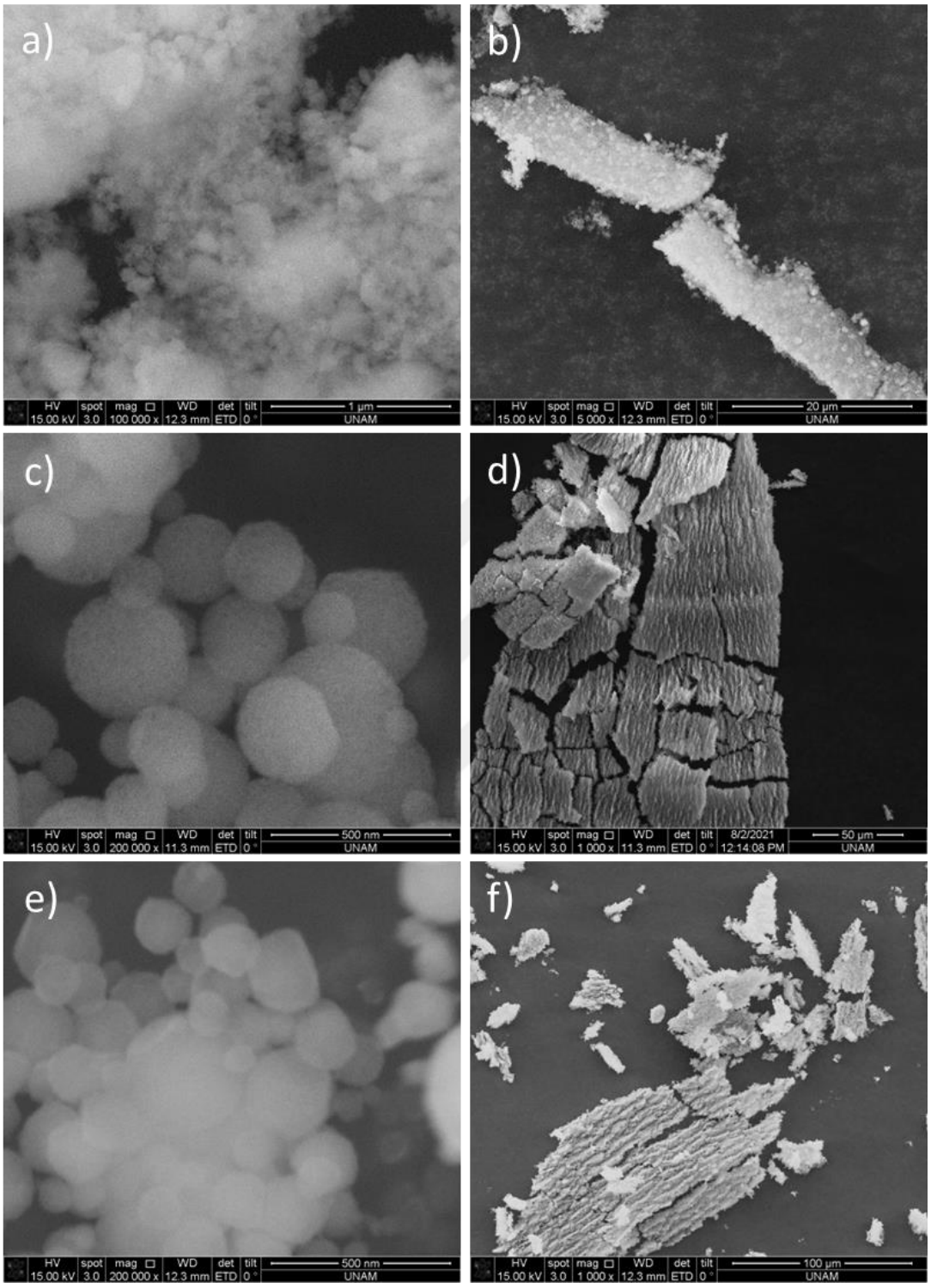

Figure 3.75: SEM images of the a) and b) m-MnPP-30-300, c) and d) m-MnPP-60-300, e) and f) m-MnPP-90-300 samples, with the scale bars 500 nm, 50 μm, 500 nm, and 100 μm, respectively.

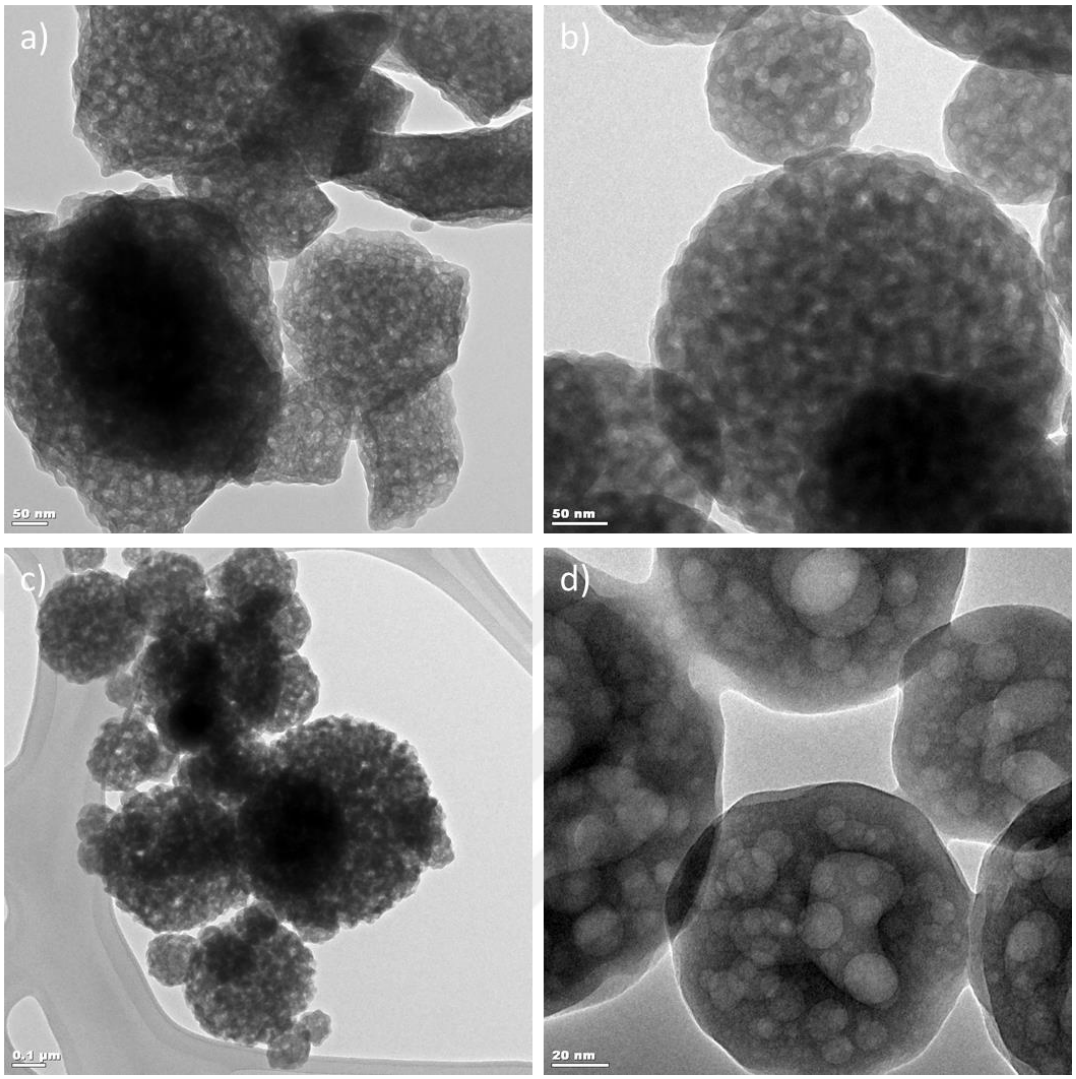

Figure 3.76: TEM images of the m-MnPP-60-300 a), b), c) not damaged, and d) damaged under the beam, with scale bars 50, 50, 100, and 20 nm, respectively.

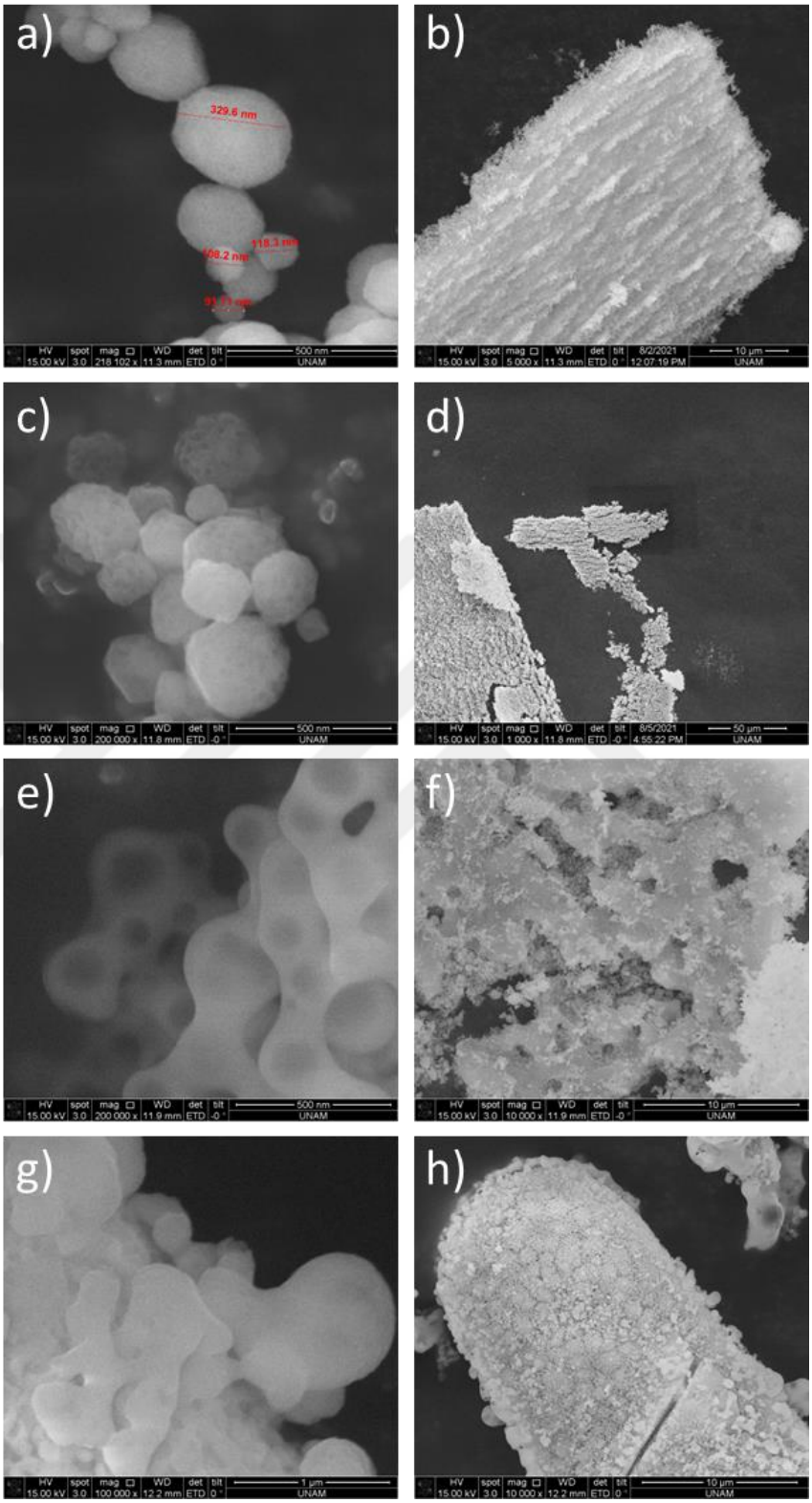

Figure 3.77: SEM images of the a) and b) m-MnPP-60-300, c) and d) m-MnPP-60-400, e) and f) m-MnPP-60-500, and g) and h) m-MnPP-60-600 samples, with the scale bars 500 nm, 10 μm, 500 nm, 50 μm, 500 nm, 10 μm, 1 μm and 10 μm, respectively.

3.3.3. Electrochemical Characterization of m-MnPP and its Transformation to β-$Mn(OH)_2$

The homogeneous solutions of Mn(II):Acid:P123 are spin-coated over fluorine doped tin oxide (FTO) coated glasses or dip-coated over graphite rods (GR) and calcined at a desired temperature (300 to 700 ^oC) to fabricate the electrodes of FTO-MnPP-n-X and GR-MnPP-n-X. Similarly, like nickel and cobalt systems, the electrochemical measurements are performed using a 3-electrode system in a 3M KOH solution. Three sets of electrodes were fabricated using solutions of MnPP-n, where n is 30, 60, or 90, that display very similar electrochemical behaviors. Since the BET surface area of MnPP-60-300 is higher than other compositions, the electrochemical characterization is illustrated using the electrodes obtained from a 60-mole ratio.

Firstly, the FTO-MnPP-60-X electrodes are fabricated to record CVs at various current densities to evaluate their electrochemical behaviors. Figure 3.78 shows the CVs of the FTO-MnPP-60-X electrodes with a scan rate of 50 mV/s in a potential window of -0.5-2.0 V versus NHE. A couple of irreversible oxidation peaks are observed at around 0.0, 0.2, and 0.6 V in the first cycle of the FTO-MnPP-60-300 electrode. These peaks disappear in further consecutive cycles. Similar behavior is observed for the electrodes prepared at 400 and 500 ^oC. The oxidized species in the first cycle might be irreversibly used in the OER region. No oxidation or reduction peaks are observed from the FTO-MnPP-60-600 electrode. Notice also that there is a decline in the current density in the OER potential region. As observed in the nickel and cobalt systems, the reason for this decline in the current density of the water oxidation part is the degradation of the sample during cycling. The degradation gets slower with increasing the calcination temperature.

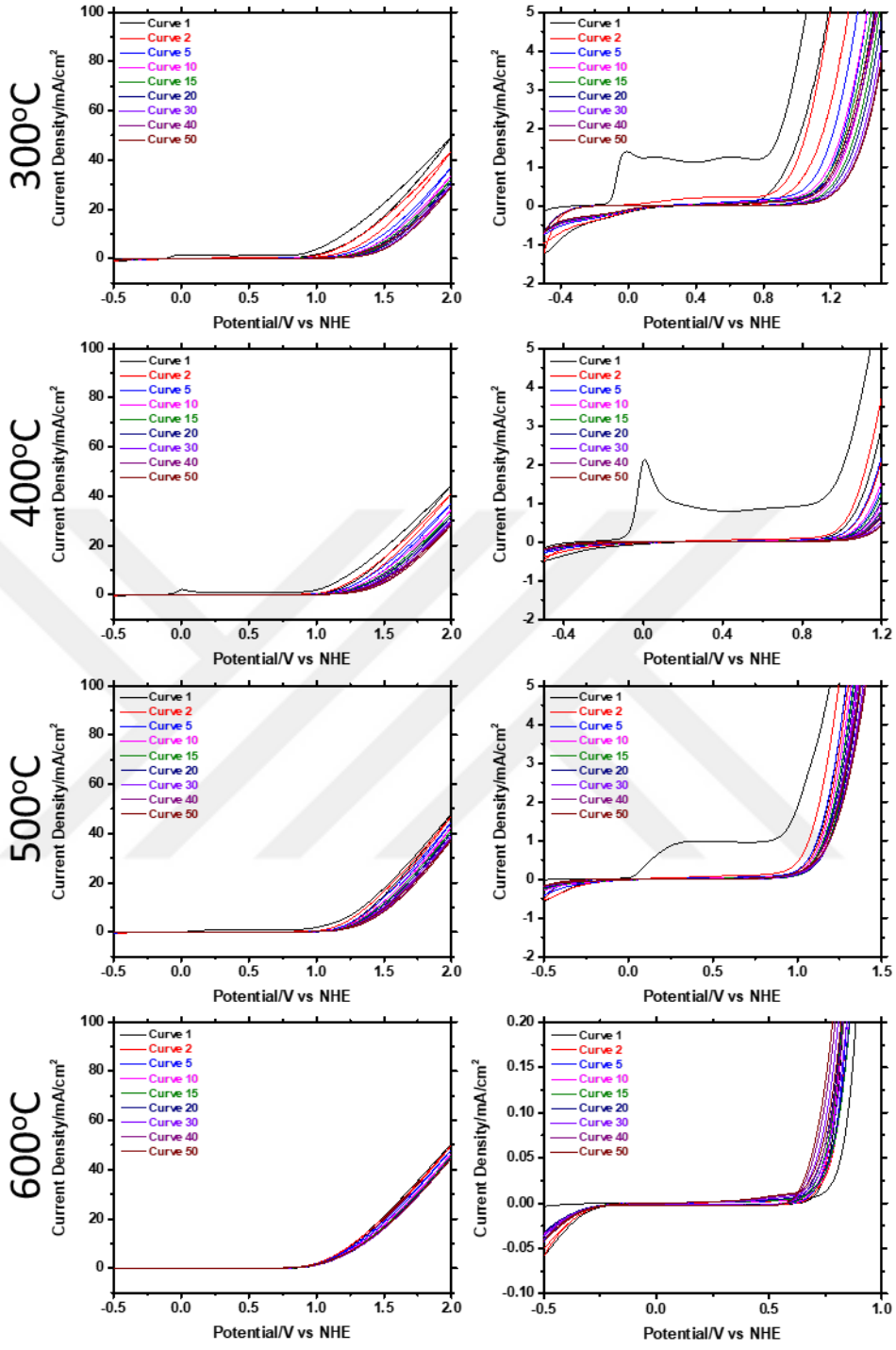

Figure 3.78: 50 CV cycles of FTO-MnPP-60-X (X values are shown on the left) electrodes with a scan rate of 50 mV/s (The right column shows the zoomed plots in the oxidation-reduction region).

Since there is a degradation problem when FTO is used as a substrate for the working electrode, pure graphite rods are also coated to prepare the MnPP-60 electrodes using 10 times diluted mother liquor of MnPP-60 solution, as mentioned

before. Figure 3.79 shows the CV curves of the GR-MnPP-60-X (X is 300, 400, 500, 600, and 700) electrodes. Some changes in the oxidation and reduction peaks over cycling are observed. However, these electrodes behave quite differently compared to the NiPP and CoPP electrodes. The changes in the water oxidation region of the GR-MnPP-60-X electrodes are significantly sharper than the degradation of FTO-NiPP and FTO-CoPP.

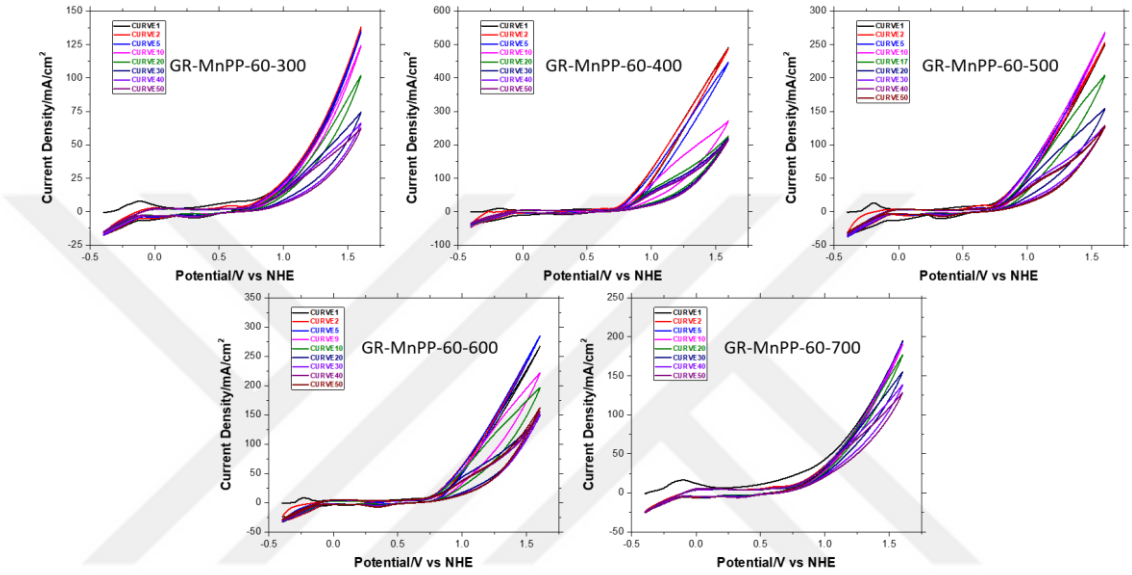

Figure 3.79: 50 CV cycles with a scan rate of 50 mV/s of GR-MnPP-60-X electrodes (X is indicated on each panel).

It is observed that during cyclic voltammetry measurements at around 1.0 V, where the OER takes place, a pink-colored specie disperses from the electrode surface to the electrolyte solution, see Figure 3.80a. This color indicates that the MnPP electrode decomposes to permanganate ion (MnO_4^-) at high potentials. The UV spectrum of the pink-colored specie is recorded to confirm the formation of permanganate ions, which exhibit a unique fingerprint spectrum, see Figure 3.81a.[175] Since the permanganate ion is unstable in the alkaline media, the pink solution is immediately transferred into an acidic medium to record the spectrum as it disperses from the electrode surface. Even in the acidic solution, the permanganate species are not stable for a long time, see inset of Figure 3.81a. The pink-colored permanganate ions continue to leach until the 10^{th} cycle during cyclic voltammetry. After the 10^{th} cycle, either decomposition stops due to transformation, or it may be a

minimal amount coming out so that it cannot be observed by the naked eye. After approximately the 20th cycle, the electrolyte solution turns green, see Figure 3.80b, indicating the decomposition of MnO_4^-, where the manganese ion is in a 7+ oxidation state, to manganate (MnO_4^{2-}) ion, where the manganese ion is in a 6+ oxidation. The UV spectrum of the green solution is also recorded to illustrate this decomposition from permanganate to manganate ions, see Figure 3.81b. [175] Following the completion of 50 cycles of CV measurements, the decomposed electrode is removed from the electrolyte, and the electrochemical cell is left at rest to observe the color of the electrolyte solution over time. It is noted that the MnO_4^{2-} species further decompose to MnO_2, resulting in brown solids accumulating at the bottom of the electrochemical cell (not shown).

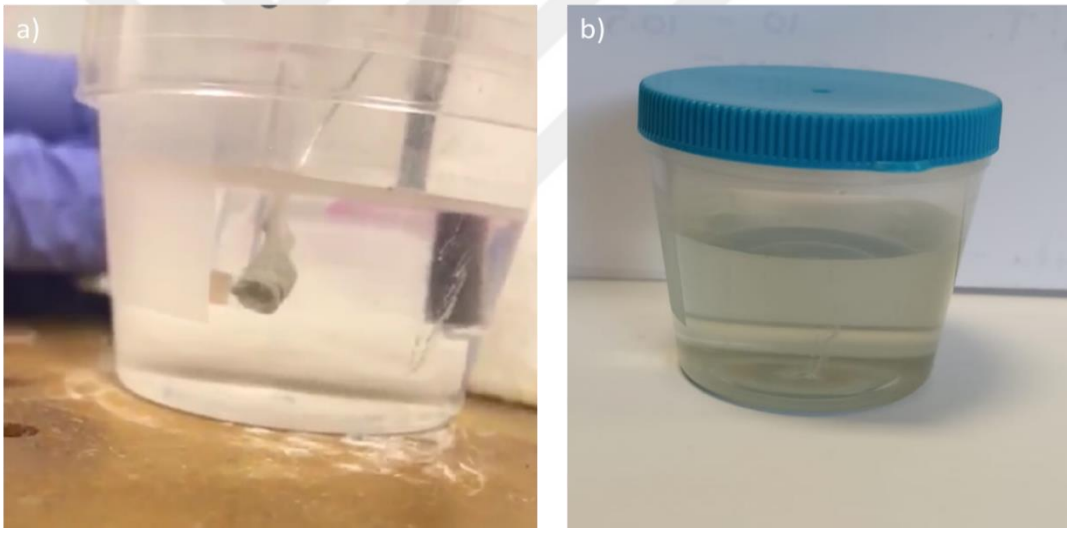

Figure 3.80: Photographs of a) the electrochemical setup for the GR-MnPP-60-300 during the CV measurement and b) the electrolyte after 50 CV cycles of the GR-MnPP-60-300.

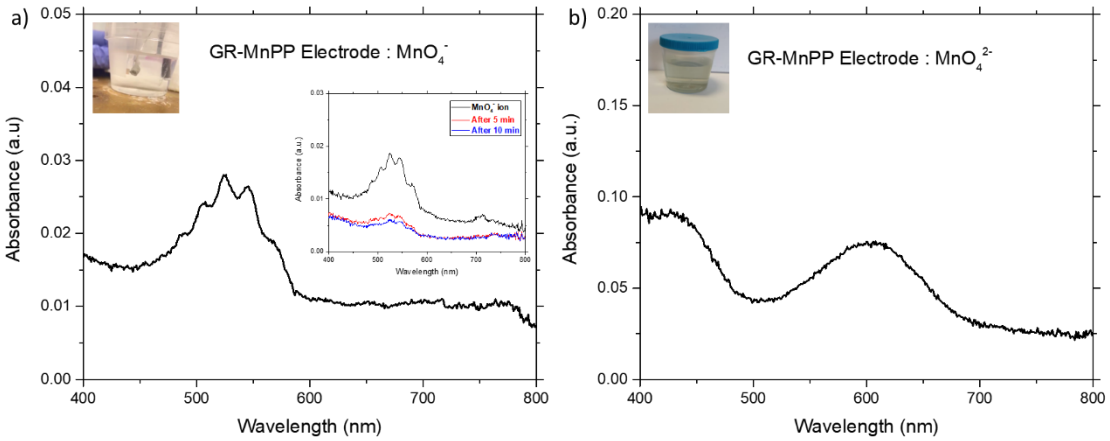

Figure 3.81: UV spectra of a) MnO_4^- ion and degradation by time (inset), and b) MnO_4^{2-} ion.

Since the electrodes of GR-MnPP-60 decompose to permanganate ions at the OER potentials, these electrodes are not used in further CV and CD measurements, like in the nickel and cobalt samples. Instead, new electrodes of GR-MnPP-60 are used to test the scan rate dependency and to collect GCD and long-term CD cycles. Figure 3.82 shows the scan-rate dependent CV curves of GR-MnPP-60-X (X is 300, 400, 500, 600, and 700 ^oC) in a narrow potential window, namely the oxidation-reduction region. A couple of oxidation and reduction peaks are observed from each electrode calcined at various temperatures with very low current densities. This means the manganese ion oxidizes to different oxidation states (might be 3+, 4+, 5+, and 6+). The scan rate-dependent analysis provides information about the active surface coverage and helps to determine a proper range for the GCD measurements. However, since the current densities of redox peaks are not well resolved, the plots of scan rate versus current density could not be created. Instead, only the potential window is determined by using these CVs.

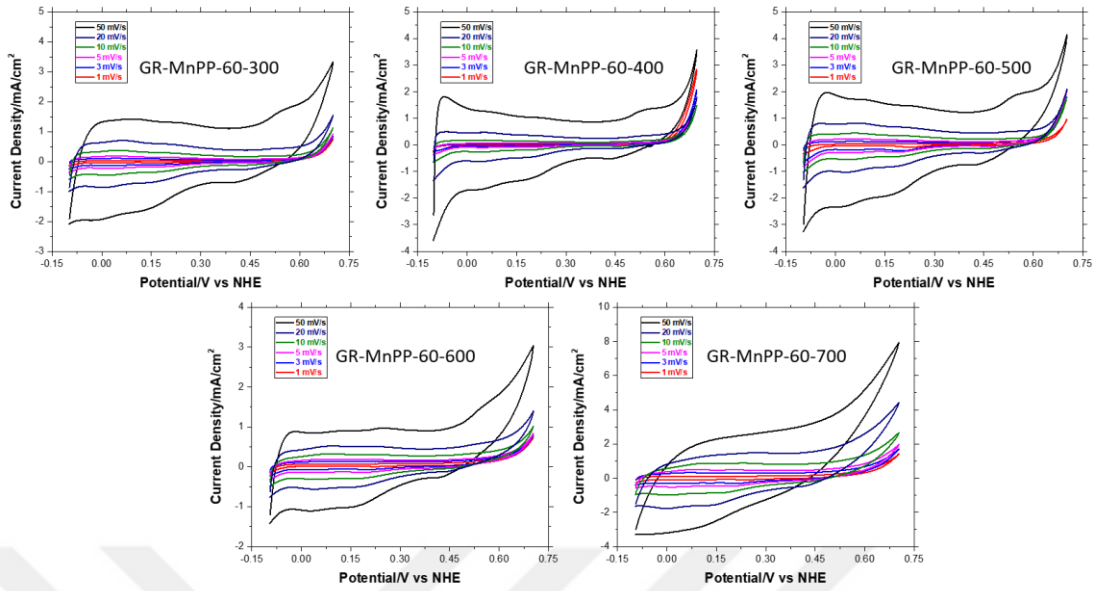

Figure 3.82: Scan rate-dependent CV curves of the GR-MnPP-60-X electrodes (X is indicated on each panel).

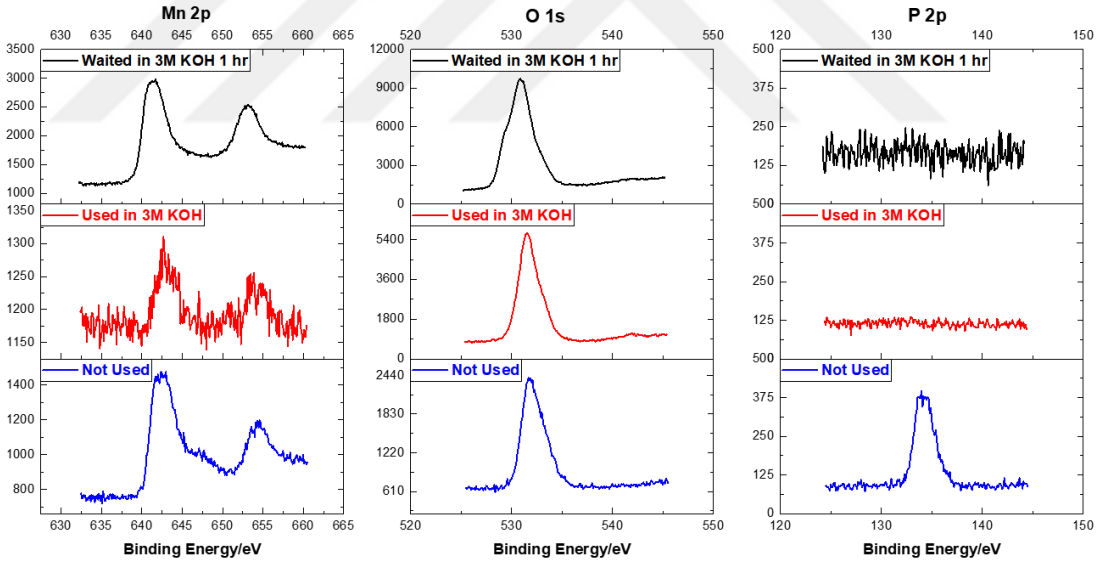

Figure 3.83: XPS spectra of (blue) m-MnPP before CVs, (red) m-MnPP after CVs, and (black) m-MnPP aged in 3M KOH for 1 h with (left) Mn 2p, (middle) O 1s, and (right) P 2p regions.

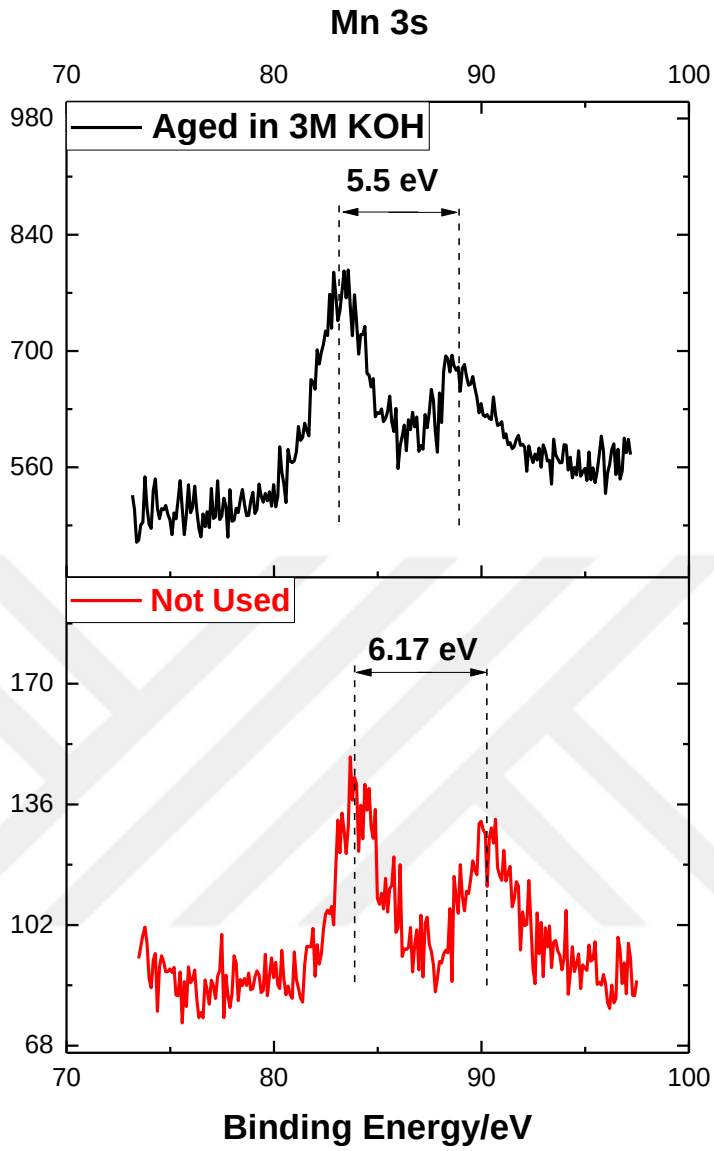

Figure 3.84: XPS spectra of m-MnPP (red) not used and (black) aged in 3M KOH for 1 h for Mn 3s region.

The used m-MnPP electrodes, like in the nickel and cobalt systems, are further characterized after usage in the electrochemical analysis. The XPS spectra were recorded before and after CVs and compared with the sample only aged in a 3M KOH solution. Figure 3.83 shows the XPS spectra in the Mn 2p, O 1s, and P 2p regions before (blue spectra), after CVs (red spectra), and only the aged sample (black spectra). As expected, the phosphorus 2p peak in the spectrum completely disappears after using the electrode in the CV measurements and aging in a 3M KOH solution, indicating a transformation of MnPP to a phosphorous-free material (likely $Mn(OH)_2$, see latter).

The Mn $^2P_{3/2}$ and $^2P_{1/2}$ peaks appear at around 642.5 eV and 654.2 eV, respectively, before the use of MnPP material, in which Mn is only in a 2+ oxidation state. [176] In addition, a shake-up peak (at around 647.5 eV) originates from the interaction between outgoing and valence electrons that are excited to higher energy levels. As a result, the energy of the core electron is reduced, and a satellite structure is showing below the core level energy. [177] After CVs, those peaks appear almost in the same energy; however, in the aged sample, there is a 1eV shift to the lower energy side, showing the oxidation state of manganese is increased. Moreover, the Mn 3s regions are also analyzed to compare the oxidation state of the manganese species, see Figure 3.84. Two peaks appear in the Mn 3s region due to the spin coupling between 3s electrons and unpaired 3d electrons during the photoelectron ejection. The difference in the Mn 3s binding energy splitting strongly depends on the oxidation state of the manganese ions. [177]–[179] The splitting is 6.1, 5.4, and 4.8 eV in the Mn(II), Mn(III), and Mn(IV) species, respectively.[176], [178], [180] The splitting energy of the sample before use in the CVs measurement and aging process is 6.17 eV, which means all manganese ions are in their 2+ oxidation state. However, when the MnPP sample is aged in 3M KOH solution for 1 h, the splitting becomes 5.5 eV, meaning there are Mn(III) species (might be MnOOH). The color of the sample after transformation, which is brownish, is also proof of having 3+ species since the pure $Mn(OH)_2$ should be a very light color because of the d^5 electron configuration, in which d-d transitions are spin-forbidden.

The O 1s peak shifts to lower binding energy, from 531.9 to 531.5 and 530.8 eV, for the electrodes before, after CVs, and aged in 3M KOH solutions, respectively. However, the P 2p peak completely disappears, indicating the transformation. Moreover, a shoulder appears in the region of the O 1s peak at 531.5 eV on the high-energy side due to hydroxide and coordinated water. [166] The spectra in all three regions (Mn 2p, O 1s, and P 2p) are very similar in electrochemically (after CVs) and chemically (just aged in 3M KOH) transformed samples. Therefore, it is reasonable to suggest the following chemical equilibrium reaction (eq. 3.10).

$$\mathbf{Mn_2P_2O_7(s) + 4OH^-(aq) \leftrightarrow 2Mn(OH)_2(s) + P_2O_7^{4-}(aq)} \qquad \textbf{eq. 3.10}$$

To further prove the transformation of MnPP material to phosphorous-free material, as a bulk technique, EDX spectra were also collected using the electrodes before and after electrochemical measurements. Figure 3.85 shows the EDX spectra of MnPP before and after CVs. Before electrochemical measurements, the MnPP material has manganese and phosphorous elements in a stoichiometric ratio. However, the phosphorous disappears entirely after the electrochemical measurements. The potassium peak appears in the spectrum after CVs because the KOH electrolyte is not appropriately washed after electrochemical usage.

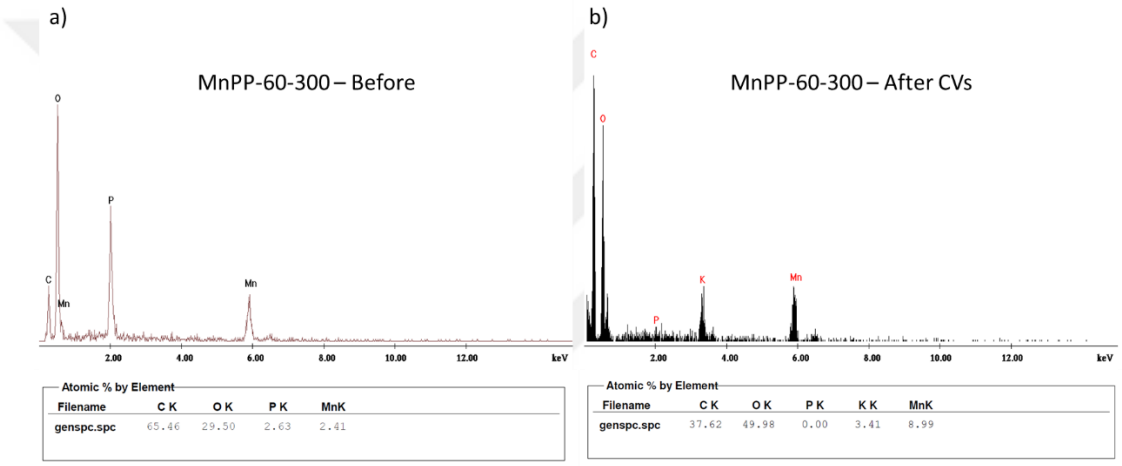

Figure 3.85: EDX spectra of m-MnPP-60-300 (a) before and (b) after CV measurements with atomic percentages of elements.

A large amount of m-MnPP-60 powder is further characterized using XRD, ATR-FTIR, and SEM imaging techniques to elucidate details of the chemical transformation of MnPP to $Mn(OH)_2$ (see eq. 3.10). The m-MnPP-60-300 sample, collected from the substrate as a powder form, is aged in a 3M KOH solution to obtain a large amount of transformed product. As clarified in the nickel and cobalt systems, the powder of MnPP is also aged in a closed system to get the pure hydroxide phase without any impurities like carbonates, see section 3.13 and Figure 3.31. 5 min aged sample in the basic medium was first followed using the m-MnPP-60-300 sample to check that the transformation was complete in this period. The transformation of MnPP to manganese hydroxide in a 3M KOH solution is a relatively fast process; in 5 min, aging in the 3M KOH solution, the transformation is complete, like the cobalt system.

The XRD patterns and ATR-FTIR spectra are collected from the 5 min aged samples in 3 M KOH solution, see Figure 3.86. The XRD patterns of the 5 min aged sample can be indexed to pure beta manganese hydroxide, see Figure 3.86a. Remember that the particles in the β-$Ni(OH)_2$ sample are much smaller because of the rapid seeding process. However, the β-$Mn(OH)_2$ particles are much more extensive compared to nickel hydroxide particles, like $Co(OH)_2$, where the growth is faster, leading to big particles.

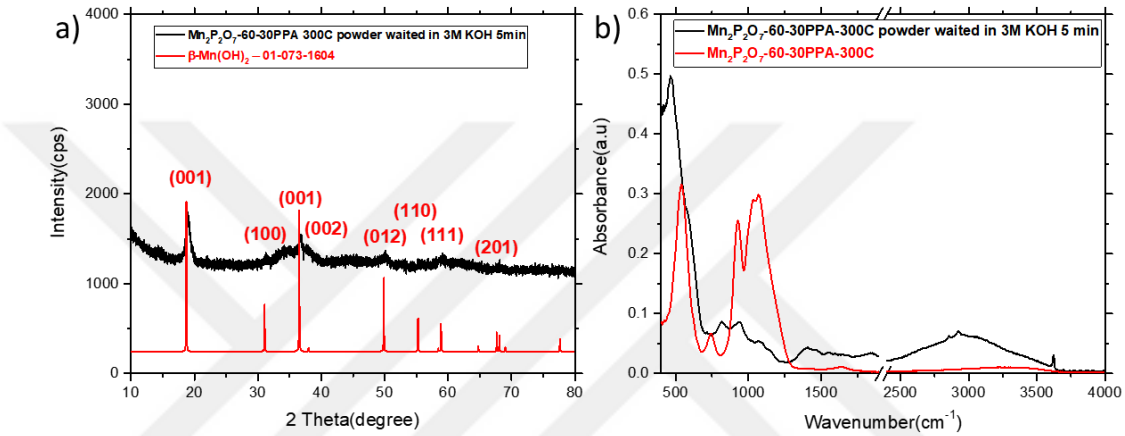

Figure 3.86: a) Wide-angle XRD patterns of m-MnPP-60-300 after treatment in 3 M KOH for 5 min and corresponding reference of β-$Mn(OH)_2$ (ICDD - 01-073-1604) and b) ATR-FTIR spectra of m-MnPP-60-300 and after its aging in 3 M KOH for 5 min.

The ATR-FTIR spectrum of the m-MnPP-60-300 sample aged in 3M KOH solution also shows that the transformation is complete in 5 min, see Figure 3.86b. The sharp peak at 3622 cm^{-1} is due to $Mn(OH)_2$ (water-free), and the peaks (at about 440-650 cm^{-1}) due to Mn-O stretching mode(s) appear, whereas the PP peaks at 1030, 928, 744, and 548 cm^{-1} entirely disappear (see red spectrum for MnPP). Moreover, a trace amount of carbonate and bicarbonate species are observed at around 1400 and 1580 cm^{-1}, which are like some impurities and are not detected in the XRD patterns of the same samples since they are either in small amounts or amorphous. In addition, the minor peaks at around 2900 cm^{-1} originate from ethanol, adsorbed during the washing of the sample.

The SEM images of the m-MnPP-60-300 samples before and after base treatment were collected to investigate the changes in morphology during the

transformation of pyrophosphates to hydroxide. The spherical m-MnPP-60-300 sample changes its morphology to plate-like particles when completely converted to its hydroxide, compare Figures 3.87 a and b. The bulk-like large nanoparticles are crystalline β-$Mn(OH)_2$, as evidenced by both XRD patterns and ATR-FTIR spectra.

The m-MnPP-60-300 sample transforms to its hydroxides much faster than the m-MnPP-60-700 sample. Aging the m-MnPP-60-700 in 3M KOH solution for 5 min is insufficient to convert all pyrophosphates to hydroxide. Transformation of the MnPP-60-700 sample starts in 5 min, but a significant portion is still MnPP. Diffraction lines of both MnPP and β-$Mn(OH)_2$ coexist in the XRD pattern, see Figure 3.88. However, the transformation period is much shorter if the m-MnPP-60-700 electrode (a typical weight of 0.1-0.2 mg) is directly dipped into a 3M KOH solution.

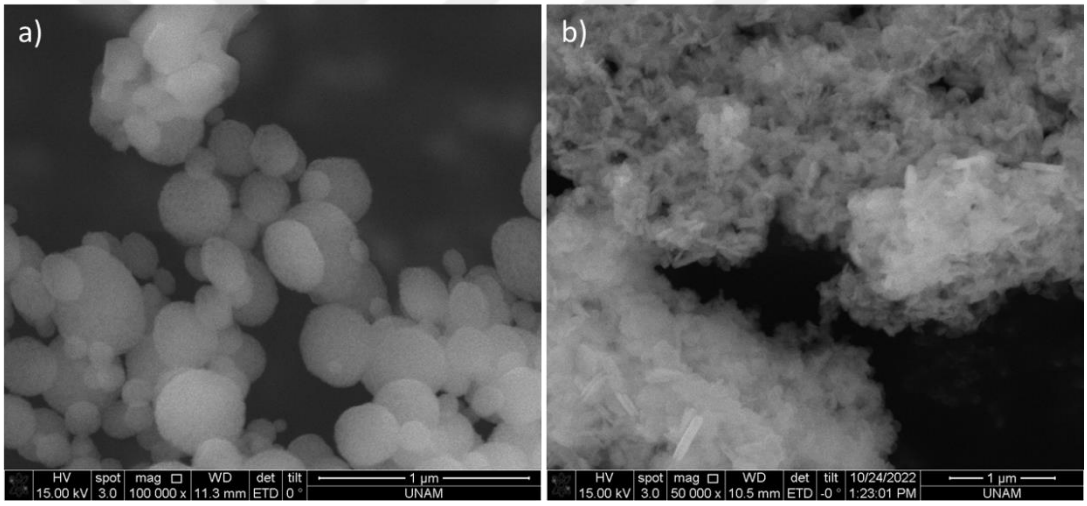

Figure 3.87: SEM images of the m-MnPP-60-300 a) before, b) after aging in 3M KOH solution for 5 min (The scale bars are 1 μm).

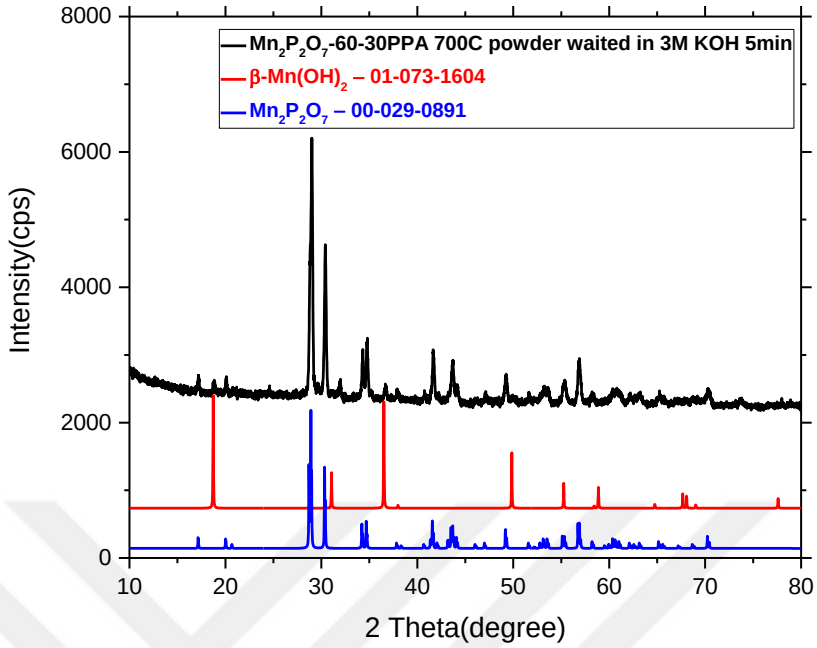

Figure 3.88: Wide-angle XRD pattern of the MnPP-60-700 aged in 3M KOH solution for 5 min and the reference patterns of β-$Mn(OH)_2$ (ICDD - 01-073-1604) and β-$Mn_2P_2O_7$ (ICDD – 00-029-0891).

The GCD measurements are performed using the electrodes used for scan rate-dependent CVs (not the ones used for the full potential window, including the water oxidation region since there is a decomposition reaction for the manganese). Remember that scan-rate dependent CVs also take around 1 h, enough time to convert all MnPP to $Mn(OH)_2$ on the graphite electrodes, calcined at each temperature. Figure 3.89 shows the GCD behaviors at different current densities and specific capacitance and capacity values versus the number of cycles to see the stability of the electrodes over 100 cycles of charging and discharging. The specific capacitance and capacity values up to 100 cycles are quite reproducible, up to 600 ^oC, with a slight decrease by cycling. The specific capacitance and capacity values are reported in mF/cm^2 and mA·s units, respectively, at each current density and collected in Table 3.6. Like CoPP electrodes, the capacity and specific capacitance values of fully converted MnPP samples are almost 10 times less than $Ni(OH)_2$, which might be related to the particle sizes of their hydroxides. Additionally, the discharge/charge capacity ratio is calculated for all electrodes that were calcined at various temperatures to observe their coulombic efficiencies, see Figure 3.90. The GR-MnPP-60-X electrodes display a

decreasing coulombic efficiency trend as the calcination temperature increases up to 700 °C. Both GR-MnPP-60-300 and GR-MnPP-60-700 electrodes demonstrate similar efficiencies, each at around 90%.

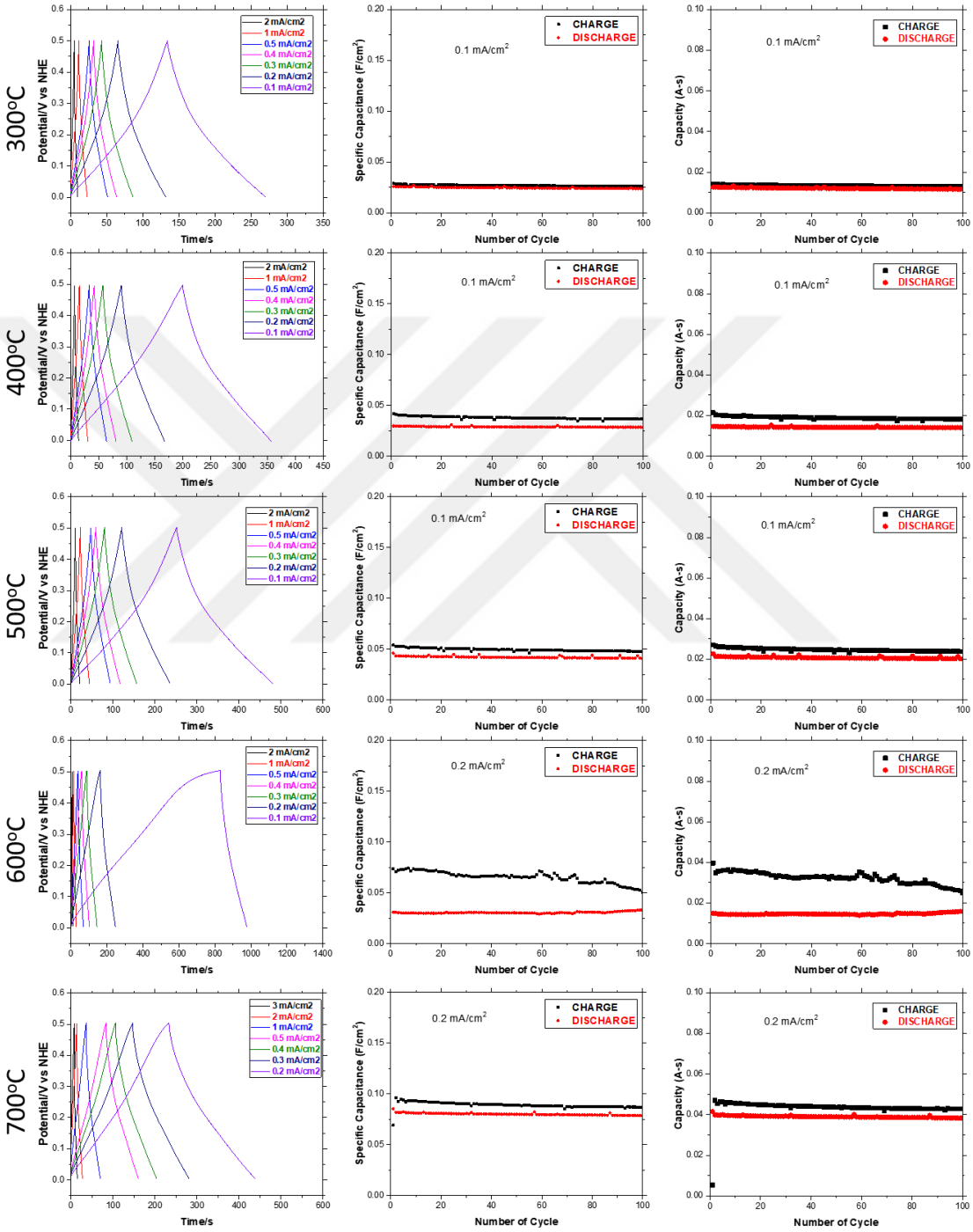

Figure 3.89: Electrochemical properties: (right column) the GCD graphs, (middle column) specific capacitance versus the number of cycle plots, and (left column) capacity versus the number of cycle plots of the GR-MnPP-60-X (X is denoted on the left) electrodes.

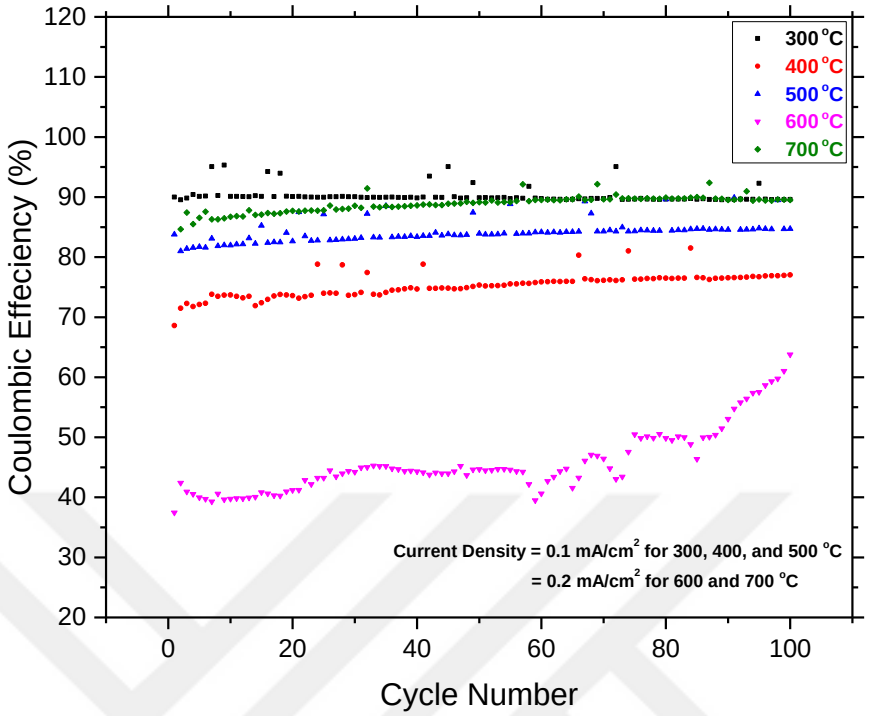

Figure 3.90: Graph of coulombic efficiencies of the GR-MnPP-60-X electrodes (X is 300, 400, 500, 600, and 700) versus cycle number.

Table 3.6: Specific capacitance and capacity values of the electrodes calcined at indicated temperatures of the GR-MnPP-60-X (X is shown on the top).

Current Density (mA/cm^2)	300 °C		400 °C		500 °C		600 °C		700 °C	
	Capacity (mA·s)	Specific capacitance (mF/cm^2)	Capacity (mA·s)	Specific capacitance (mF/cm^2)	Capacity (mA·s)	Specific capacitance (mF/cm^2)	Capacity (mA·s)	Specific capacitance (mF/cm^2)	Capacity (mA·s)	Specific capacitance (mF/cm^2)
0.1	12.78	25.56	14.80	29.60	21.49	42.98	13.86	27.72	-	-
0.2	12.78	25.56	14.94	29.88	22.28	44.56	16.42	32.84	39.67	79.34
0.3	12.67	25.34	15.19	30.38	22.46	44.92	16.85	33.70	39.38	78.76
0.4	12.49	24.98	15.26	30.52	22.51	45.02	16.67	33.34	38.63	77.26
0.5	12.49	24.98	15.26	30.52	22.54	45.08	14.79	29.58	38.05	76.10
1	11.38	22.76	14.76	29.52	21.35	42.70	12.99	25.98	33.77	67.54
2	9.792	19.58	13.86	27.72	19.91	39.82	9.76	19.52	26.42	52.84

However, the capacity and specific capacitance of the m-MnPP-60-700 electrode is more than 2 times higher. This might be due to not completing the transformation. Note that the capacity of NiPP is about 40 mC if tested in a 2.4M KOH and 0.6M $H_4P_2O_7$ solution and consistent with the XRD pattern. In the XRD pattern of the m-MnPP-60-700, a significant component of the 5 min aged sample is MnPP. Further investigation is needed to elucidate the observed difference fully.

3.4. Synthesis and Characterization of m-$M_xM'_{2-x}P_2O_7$ (M and M'=Ni(II), Co(II), Mn(II)) Samples

3.4.1. Preparation and Characterization of $M_xM'_{2-x}$:Acid:P123 Mesophases

Homogeneous solutions of binary salt system ($M_xM'_{2-x}$:Acid:P123) are also prepared using PPA as a phosphate precursor since the mesophases with PPA are more stable and provide a high surface area for their mesoporous structures. The ratios of ingredients are calculated to be stoichiometric according to the acid. First, binary metal salt mixtures with a 50% composition of $M_xM'_{2-x}$ (Ni(II)/Co(II) and Mn(II)/Co(II) where x is 1) are prepared with a total salt/P123 ratio of 30, 60, and 90 (will be demonstrated as MM'PP-n:t where n and t are the mole ratios of the first metal (M) and the second metal (M'), respectively. The homogenous solutions of $M_xM'_{2-x}$:PPA:P123 are first drop-cast coated on microscope slides to form the mesophases of the above compositions. Then, the gelation behaviors of mesophases are characterized by XRD, POM, and ATR while aging at room temperature before further calcination processes.

The mesophases are characterized by small-angle XRD, ranging between 1 and 5^o, 2θ, to analyze their stability during aging at RT. Figure 3.91 shows the XRD patterns of all three ratios of Mn(II)Co(II):PPA:P123 and Ni(II)Co(II):PPA:P123 mesophases aged at RT. The gelation behaviors of binary salt systems (both Ni(II)/Co(II) and Mn(II)/Co(II)) are very similar to the one salt systems. The diffraction lines in the small angle show that the mesophases of binary systems have ordered structures. Since the number of diffraction lines is limited, it is hard to identify the form of mesophases. Similarly, with the one salt systems, the intensities of the diffraction lines are not too high because they originated from the higher-order planes having the most intense line below 1^o, 2θ. The mesophases obtained from the 30 and 60-mole ratios of total salt amounts are stable for up to 5 days, keeping the diffraction lines. However, the mesophases prepared from the 90-mole ratio keep the stable phase up to only 20-30 min. Note that 20-30 min is still enough for further production of metal pyrophosphates.

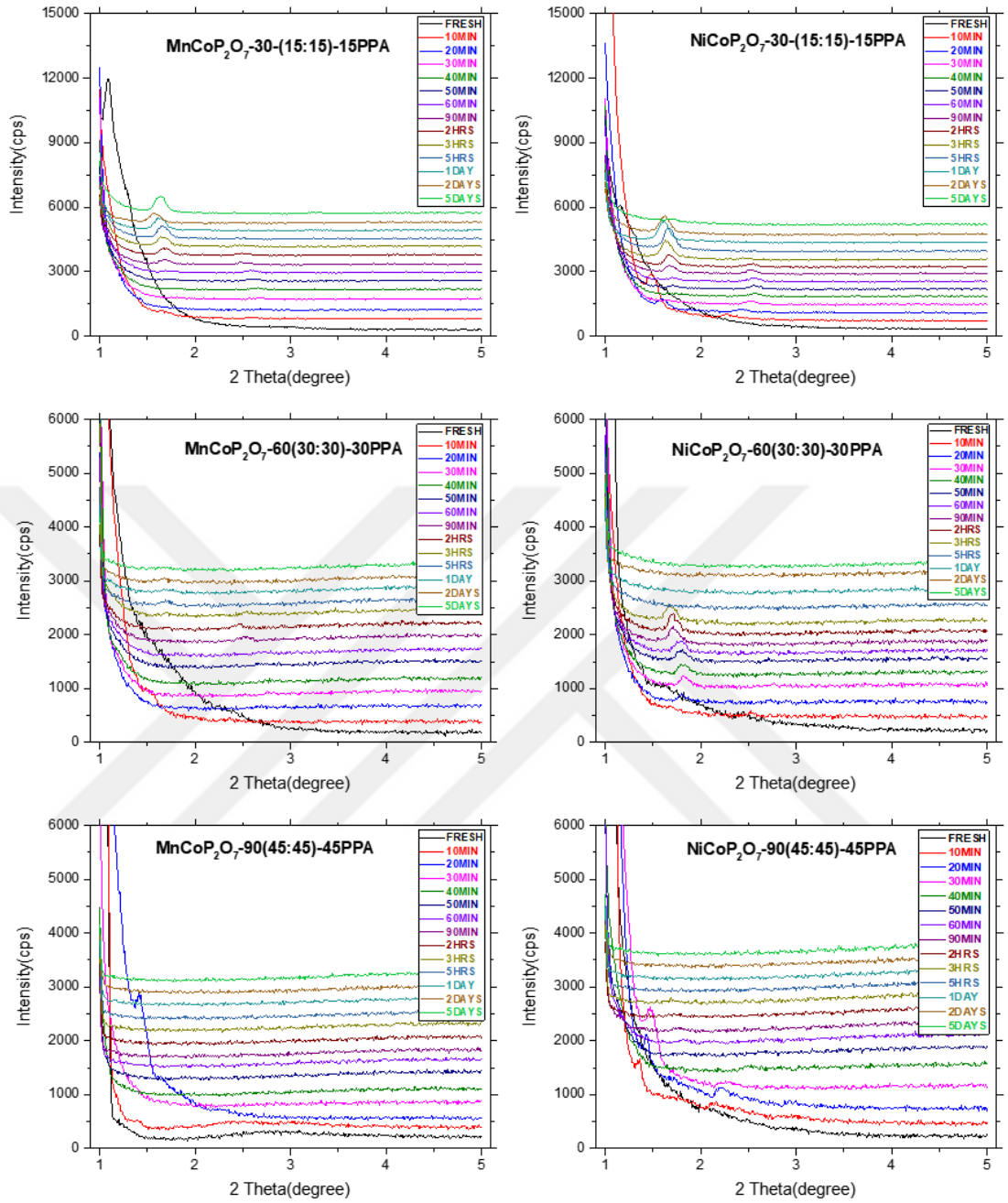

Figure 3.91: Small-angle XRD patterns of the (left column) Mn(II):Co(II):PPA:P123 and (left column) Ni(II):Co(II):PPA:P123 mesophases with (upper row) 15:15 (middle row) 30:30, and (bottom row) 45:45 mole ratios of binary systems.

Figure 3.92 shows the POM images of the Mn(II):Co(II):PPA:P123 and Ni(II):Co(II):PPA:P123 mesophases prepared using PPA as the acid sources and 5 h aged in the laboratory conditions at RT. There is no typical mesophase (LLC) texture in the POM images for those mesophases. Instead, there is a particle-like domain in

the POM images. Moreover, some cracks can appear, and particle-like morphology covers the entire image, see Figure 3.92b. The cracks in the sample indicate that solid-like particles are forming during aging under ambient conditions with a composition of $MnCoH_xP_2O_7(NO_3)_x{\cdot}nH_2O$ and $NiCoH_xP_2O_7(NO_3)_x{\cdot}nH_2O$ (see eq. 3.11 and 3.12). Similar solid-like particles are observed from the mesophases prepared from both Mn(II):Co(II):PPA:P123 and Ni(II):Co(II):PPA:P123 systems. The diffraction line of the mesophases, obtained from both systems, is not perfectly visible during aging, assuming that the most intense line is below 1°, 2θ, see Figure 3.91. This means solid-like particles still preserve their mesostructure. Note also that there are no salt species over the mesophases during the formation of solid-like particles, even after 5 days of aging, see Figure 3.93.

$$\mathbf{Mn(NO_3)_2(aq) + Co(NO_3)_2(aq) + H_4P_2O_7(aq) \leftrightarrow MnCoH_xP_2O_7(NO_3)_x.nH_2O(s) + HNO_3(g)} \quad \textbf{eq. 3.11}$$

$$\mathbf{Ni(NO_3)_2(aq) + Co(NO_3)_2(aq) + H_4P_2O_7(aq) \leftrightarrow NiCoH_xP_2O_7(NO_3)_x.nH_2O(s) + HNO_3(g)} \quad \textbf{eq. 3.12}$$

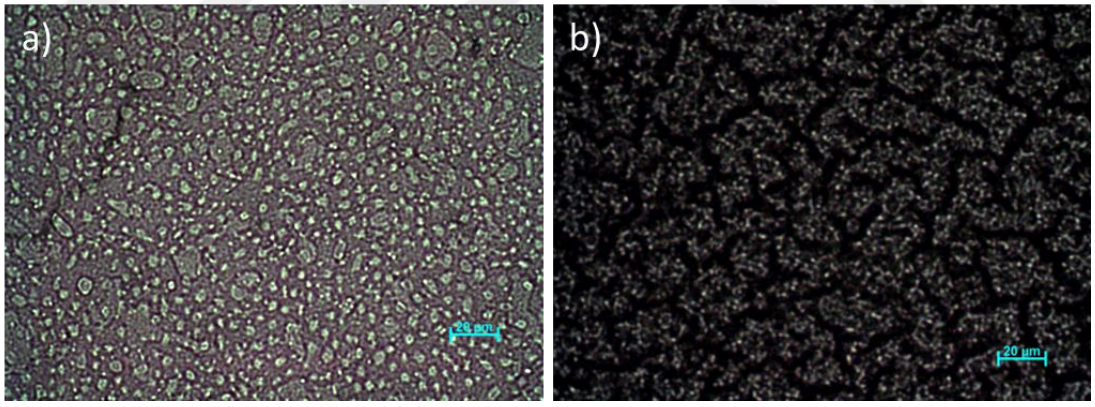

Figure 3.92: POM images of the a) MnCo-30:30 and b) NiCo-30:30 mesophases 5 h aged at room temperature (The scale bars are 20 µm).

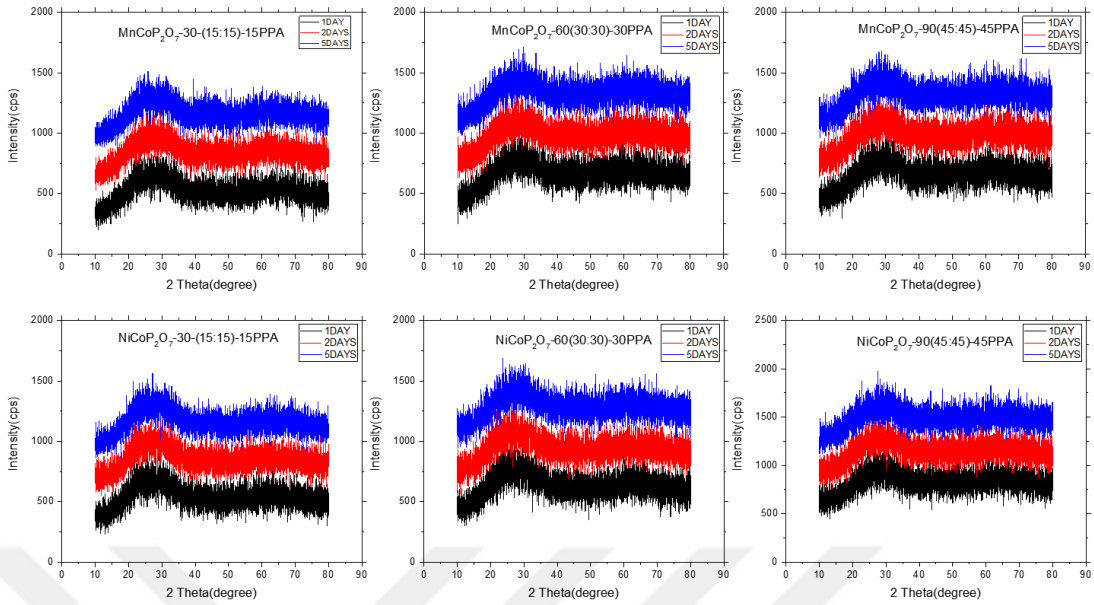

Figure 3.93: Wide-angle XRD patterns of 1, 2, and 5 days aged mesophases of the (top column) Mn(II)Co(II):PPA:P123 and (bottom column) Ni(II)Co(II):PPA:P123 (left row) 30, (middle row) 60, and (right row) 90-mole ratios at RT.

The gelation process of the mesophases of Mn(II):Co(II):PPA:P123 and Ni(II):Co(II):PPA:P123 systems was followed by gravimetric measurement by putting about 1 g of a solution. The weight changes of the mesophase starting from the solution phase are recorded under ambient laboratory conditions over a 4-digit balance. The solutions of Mn(II):Co(II):PPA:P123 and Ni(II):Co(II):PPA:P123 systems lose their excess water quickly in the first 200 min like one salt systems, see Figure 3.94. The range I in the inset indicates the evaporation of excess water in the solution by losing most water. Then, in the range II and III, both systems continue to lose weight at a slow rate. These ranges show the solidification process, which is due to the polymerization of the pyrophosphate species with the metal ions, see eq. 3.8 and 3.9. There is a slight difference between the two binary systems related to the chemical reaction over the solidification process that can differ for each transition metal.

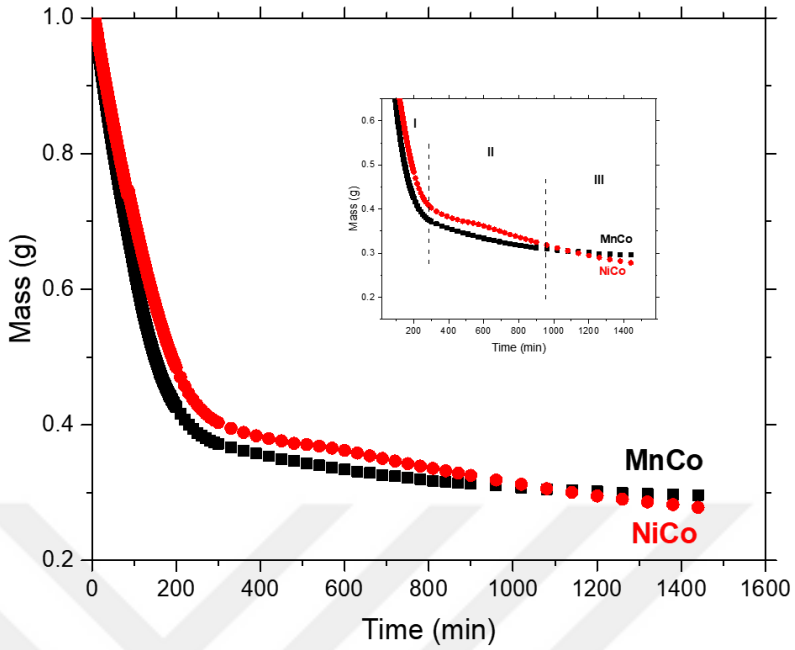

Figure 3.94: Gravimetric measurements: Mass versus time plots during water evaporation on the balance of NiCoPP-30:30 and MnCoPP-30:30 mesophases.

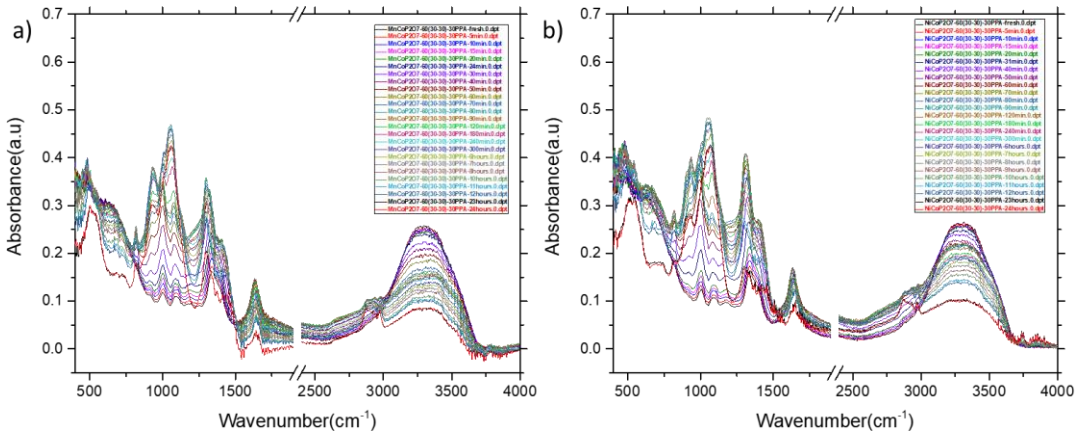

Figure 3.95: Time-dependent ATR-FTIR spectra of the a) MnCoPP-30:30 and b) NiCoPP-30:30 solution at RT.

3.4.2. Synthesis and Characterization of Mesoporous $M_xM'_{2-x}P_2O_7$

The mesophases of Mn(II):Co(II):PPA:P123 and Ni(II):Co(II):PPA:P123 obtained by various methods (spin-coating, dip-coating, or drop-casting), are calcined at 300 °C to obtain mesoporous $MnCoP_2O_7$ and $NiCoP_2O_7$ particles (denoted as m-MM'PP-n:t-X, where m stands for mesoporous, n and t are for mole ratio of M(II)/P123 and M'(II)/P123, respectively, and X is the calcination temperature in Celsius). The mesoporous binary samples are further annealed at higher calcination temperatures and characterized by various techniques at each annealing step.

Figure 3.96 shows the powder XRD patterns of the m-MnCoPP-30:30-X samples. There are no diffraction lines observed up to 600 °C, which means the sample is amorphous and becomes crystalline above 600 °C. The diffraction pattern of the crystalline phase of the m-MnCoPP-30:30 sample can be indexed to monoclinic β-$Mn_{0.9}Co_{1.1}P_2O_7$ with unit cell parameters of a, b, and c of 6.61, 8.48, and 4.55 Å, respectively, see Figure 3.96 (right one). Even though the ratio of metal species is kept as 1 in the beginning, it becomes a Co(II) rich phase during crystallization. Like in the m-MnPP system, the structure forms a beta phase, which is the feature of the manganese metal.

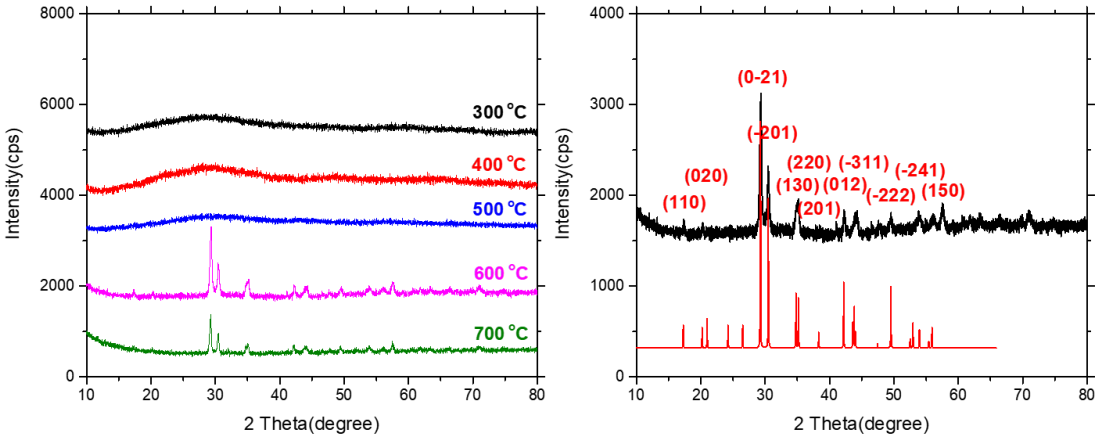

Figure 3.96: Wide-angle XRD patterns of the (left) m-MnCoPP-30:30-X (X is 300, 400, 500, 600, and 700 °C) and (right) indexed XRD pattern of the MnCoPP-30:30-700 sample with (red) β-$(Mn_{0.45}Co_{0.55})_2P_2O_7$ (ICDD - 00-050-0653).

Similarly, the powder XRD patterns of the m-NiCoPP-30:30-X samples show that the material is amorphous up to 600 °C and starts to be crystalline above 600 °C,

see Figure 3.97. The diffraction pattern of the crystalline phase of the m-NiCoPP-30:30 sample can be indexed to monoclinic α-$NiCoP_2O_7$ with unit cell parameters of a, b, and c of 6.97, 8.30, and 8.98 Å, respectively, see Figure 3.97 (right one).

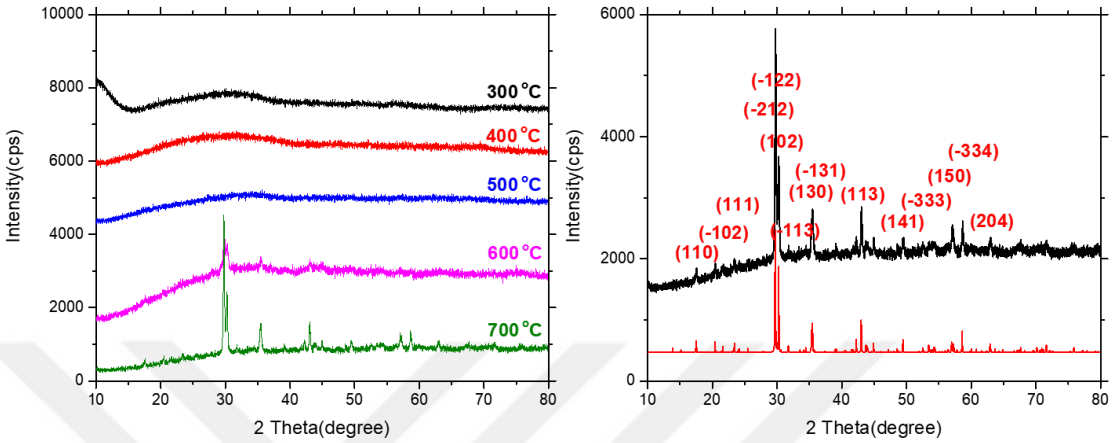

Figure 3.97: Wide-angle XRD patterns of the (left) m-NiCoPP-30:30-X (X is 300, 400, 500, 600, and 700 °C) and (right) indexed XRD pattern of the NiCoPP-30:30-700 with (red) α-($NiCoP_2O_7$ (ICDD - 04-025-4666).

The ATR-FTIR spectra of the m-MnCoPP-30:30-X and m-NiCoPP-30:30 samples are collected to illustrate the spectral changes during the calcination/annealing process. In both spectra, no peaks originating from nitrate and surfactant species after the calcination process at 300 °C and above, which indicates that those species decompose at high temperatures, see Figures 3.98 a and b. The only peaks originating from the phosphate species are visible at 300 °C and higher annealing temperatures. The peaks at high frequency (1050-1200 cm^{-1}) correspond to PO_3 units, The peak at 930 cm^{-1} is from the asymmetric stretching modes of the bridged P-O (P-O-P) group, and the intense peaks at around 500-600 cm^{-1} originate from the bending modes of pyrophosphate group and metal-oxygen stretching modes. [161], [162] The peak at around 750 cm^{-1} has resulted from the symmetric stretching modes of the bridged P-O (P-O-P) group (where the angle between P-O-P is not equal to 180°). This peak, in the spectra of MnCoPP-30:30-X, is visible up to 600 °C and disappears at 600 °C upon crystallization because the P-O-P angle is smaller than 180° till 600 °C. Like in the pure manganese system, the material changes its alpha phase (stable up to 600 °C) to beta phase (600 °C) with crystallization. The angle between P-O-P equals 180° in the

beta phase. [173], [174] The ATR-FTIR spectra of MnCoPP also prove that the structure of the material is different in the amorphous and crystalline phases of the MnCoPP sample, which could not be detected by the XRD. The same peak is visible in the spectra of NiCoPP-30:30-X, where X is 300, 400, 500, and 600 ^{o}C, Figure 3.98b. There is no phase transition in the case of the NiCoPP sample, even at crystallization temperature. All other pyrophosphate peaks are broad up to 600 ^{o}C and become sharp and resolved at 600 ^{o}C for each binary metal system. This change in the sharpness corresponds to a crystallization of the binary metal pyrophosphate particles at 600 ^{o}C and is consistent with their XRD data, see Figures 3.96 and 3.97.

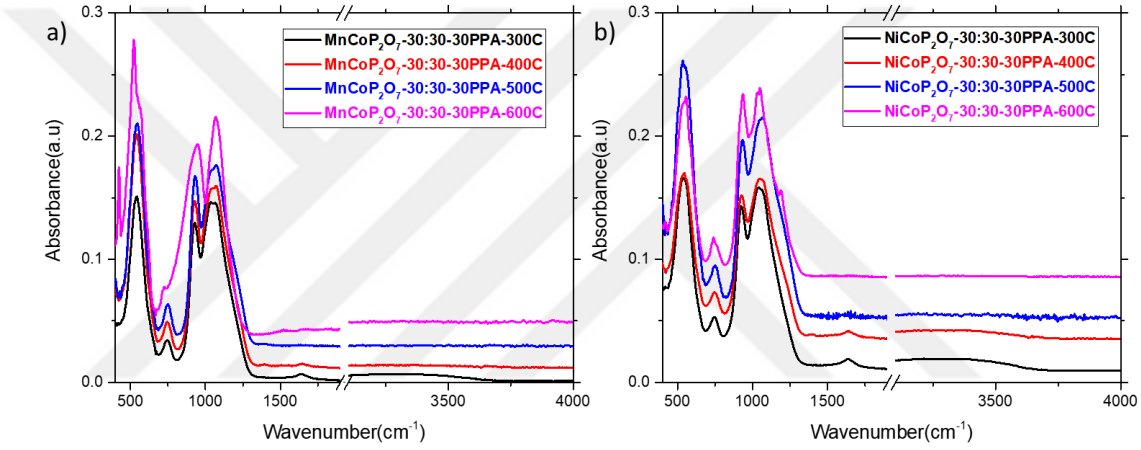

Figure 3.98: ATR-FTIR spectra of the a) MnCoPP-30:30-X and b) NiCoPP-30:30-X (X is 300, 400, 500, and 600) samples.

N_2-adsorption-desorption isotherms of the binary metal pyrophosphates (MnCoPP and NiCoPP) are collected to evaluate the porosity of the materials. The BET surface area of the m-MnCoPP-n:t-300 and m-NiCoPP-n:t-300 samples are given in Table 3.7. The highest surface area is obtained from the sample where the total metal ratio is 60 (n:t is 30:30). This ratio for both binary systems is chosen for the electrochemical analysis later.

Table 3.7: BET surface areas of m-MnCoPP-n:t-300 and m-NiCoPP-n:t-300 (n and t are 15, 30, and 45).

Sample	Bet Surface Area (m^2/g)		
	15:15	30:30	45:45
$MnCoP_2O_7$	48	70	42
$NiCoP_2O_7$	60	68	30

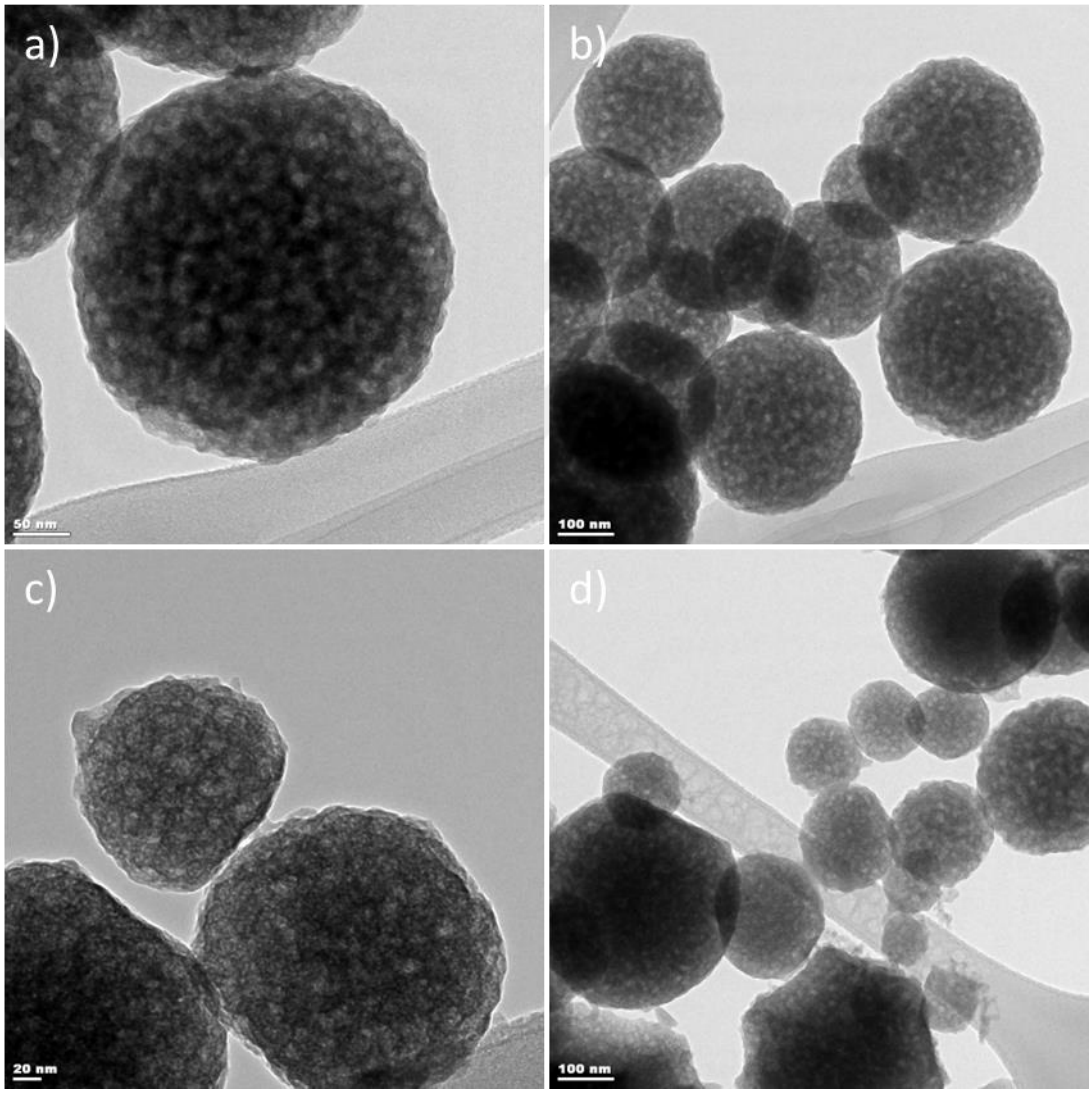

Figure 3.99: TEM images of the a) and b) m-MnCoPP-30:30-300, and c) and d) m-NiCoPP-30:30-300 samples, with the scale bars 50, 100, 20, 100 nm, respectively.

The TEM and SEM images of the m-M(II)M'(II)PP-n-X samples are collected to illustrate their morphology and porosity in detail. Since the highest surface area of

the binary metal system is obtained from the sample where the total mole ratio is equal to 60 (50% of each metal), TEM images are collected from those ratios, see Figure 3.99. Likely, in one metal system, the particles of m-MnCoPP-30:30-300 and m-NiCoPP-30:30-300 samples are primarily spherical in shape with 50-350 nm sizes, and the pores are visible for both samples in the TEM images. The SEM images of the m-MnCoPP-30:30-X and m-NiCoPP-30:30-X, calcined/annealed at different temperatures, are also collected to observe the morphological changes while annealing, given in Figures 3.100 and 3.101, respectively. The SEM images show that, for the m-MnCoPP-30:30-X samples, the particles are not perfect spheres (plate-like) at 300 ^{o}C (see Figure 3.100a) but become spherical with annealing to 400 ^{o}C (see Figure 3.100c). The particles start to aggregate with each other at 500 ^{o}C, keeping the spherical shape and porous structure with expanded pores, see Figure 3.100e. At 600 ^{o}C, the particles display bulk-like big particles losing their porous structure, accompanied by their XRD and ATR-FTIR data, see Figures 3.100 g and h. At all temperatures, with higher magnifications, it is observed that the powder samples are made up of individual particles. However, when they are analyzed by lower magnification, the samples display a film-like structure since particles stay together, compare the left and columns in Figure 3.100. Differently, the m-NiCoPP-30:30-X particles are perfect spheres at 300 ^{o}C, see Figure 3.101a. Some particles preserve their spherical shapes with annealing to 400 ^{o}C (Figure 3.101c), while some become distorted. The distorted particles become more prominent when the sample is annealed to 500 ^{o}C with expanded pores, as shown in Figure 3.101e. Like in the other binary system, the particles become bulk-like with no porosity when the crystalline phase is obtained at 600 ^{o}C. Similarly, with the MnCoPP system, the samples have film-like morphology when observed with lower magnification, see Figure 3.101, right column.

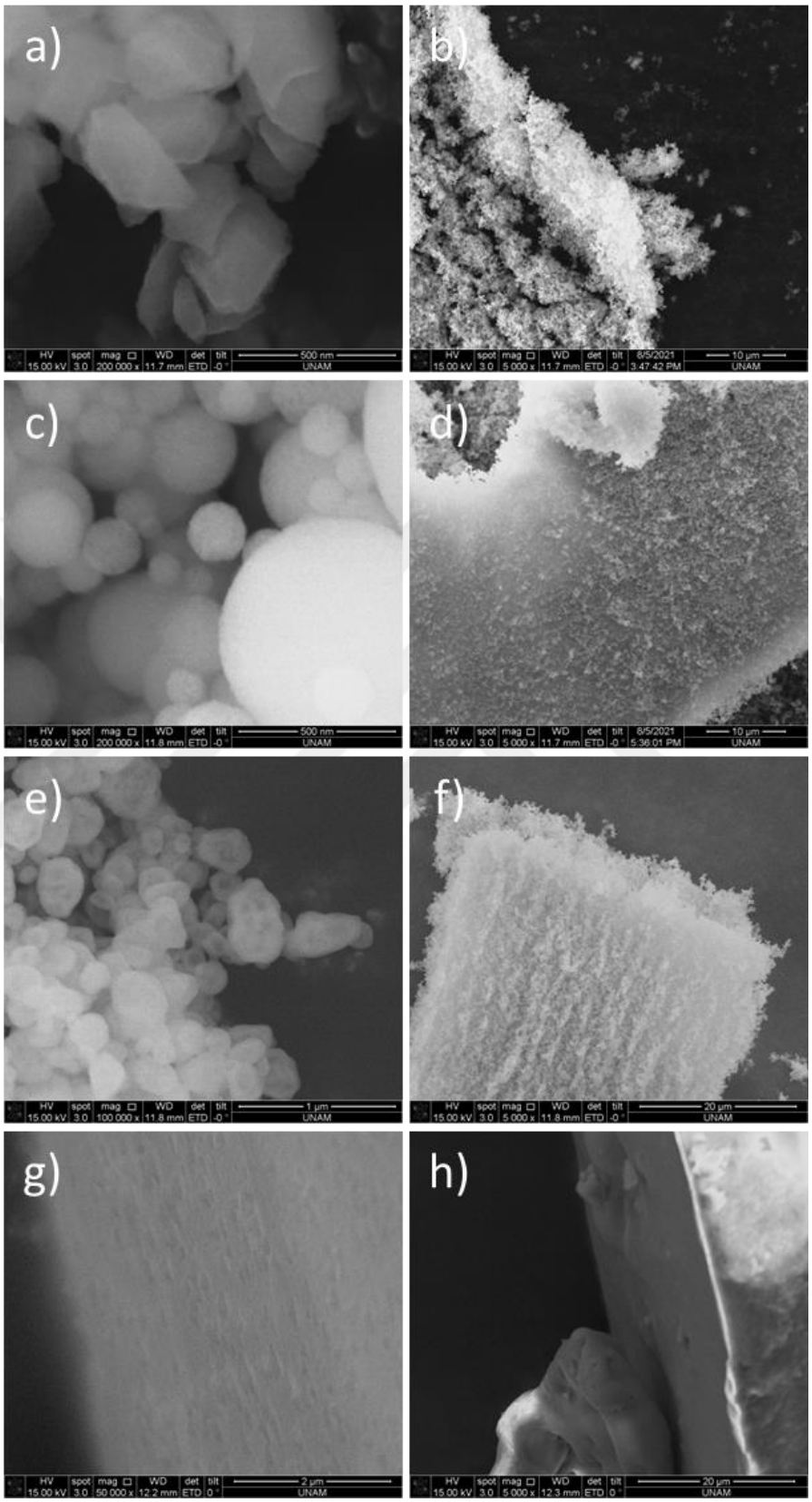

Figure 3.100: SEM images of the a) and b) m-MnCoPP-30:30-300, c) and d) m-MnCoPP-30:30-400, e) and f) m-MnCoPP-30:30-500, and g) and h) m-MnCoPP-30:30-600 samples, with the scale bars 500 nm, 10 μm, 500 nm, 10 μm, 1 μm, 20 μm, 2 μm, and 20 μm, respectively.

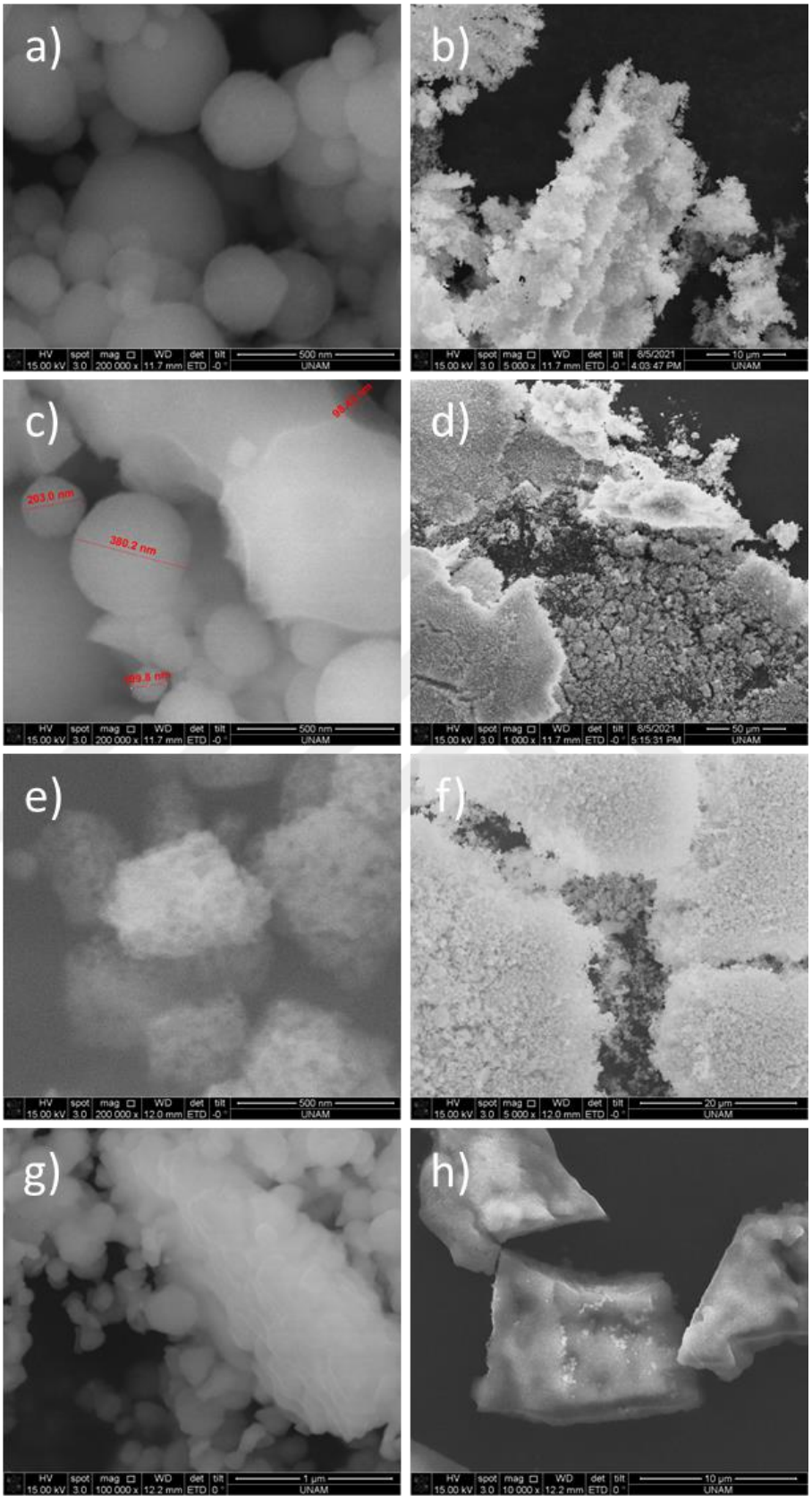

Figure 3.101: SEM images of the a) and b) m-NiCoPP-30:30-300, c) and d) m-NiCoPP-30:30-400, e) and f) m-NiCoPP-30:30-500, and g) and h) m-NiCoPP-30:30-600 samples, with the scale bars 500 nm, 10 μm, 500 nm, 50 μm, 500 nm, 20 μm, 1 μm, and 10 μm, respectively.

.

3.4.3. Electrochemical Characterization of m-$M_xM'_{2-x}P_2O_7$ and its Transformation to β-$M_xM'_{2-x}(OH)_2$

The clear solutions of binary metal systems are spin-coated over FTO glasses or dip-coated over GR and calcined at various temperatures (300 to 700 ^oC) to produce the electrodes of FTO-$M_xM'_{2-x}$PP-n:t-X and GR- $M_xM'_{2-x}$PP-n:t-X. Similarly, like one metal system, the electrochemical measurements are performed using a 3-electrode system in a 3M KOH solution. Since the BET surface area of the samples having a 60-mole ratio for total metal amount is higher than other compositions, the electrochemical characterization is illustrated using the electrodes obtained from the samples having a 60-mole ratio metal in total.

Firstly, the FTO-MnCoPP-30:30-X and FTO-NiCoPP-30:30-X electrodes are fabricated to record CVs at various current densities to evaluate their electrochemical behaviors. Figures 3.102 and 3.103 show the CVs of the FTO-MnCoPP-30:30-X and FTO-NiCoPP-30:30-X electrodes with a scan rate of 50 mV/s in a potential window of -0.5-2.0 V versus NHE, respectively. The oxidation and reduction peaks for the FTO-MnCoPP-30:30-X sample, observed in the first cycle of the measurements, are changing in the further consecutive cycles (after reaching the water oxidation reaction and coming back). Note also that there is an apparent decline in the water oxidation region (slope of 0.8-2.0 V region). The reason for this decrease, as discussed in the one metal systems, is the degradation of the sample during cycling. The degradation gets slower with increasing the calcination temperature, see Figure 3.102. For the FTO-NiCoPP-30:30-X sample, the reversible oxidation and reduction peaks are observed at around 0.5 and 0.2 V, respectively, originating from the oxidation-reduction behavior of $Ni(OH)_2$ species, as discussed in the NiPP part. However, similarly, with other metal systems, with cycling, there is a decomposition of the sample, evidenced by shifting and disappearing of the oxidation and reduction peaks over cycling in each calcination temperature.

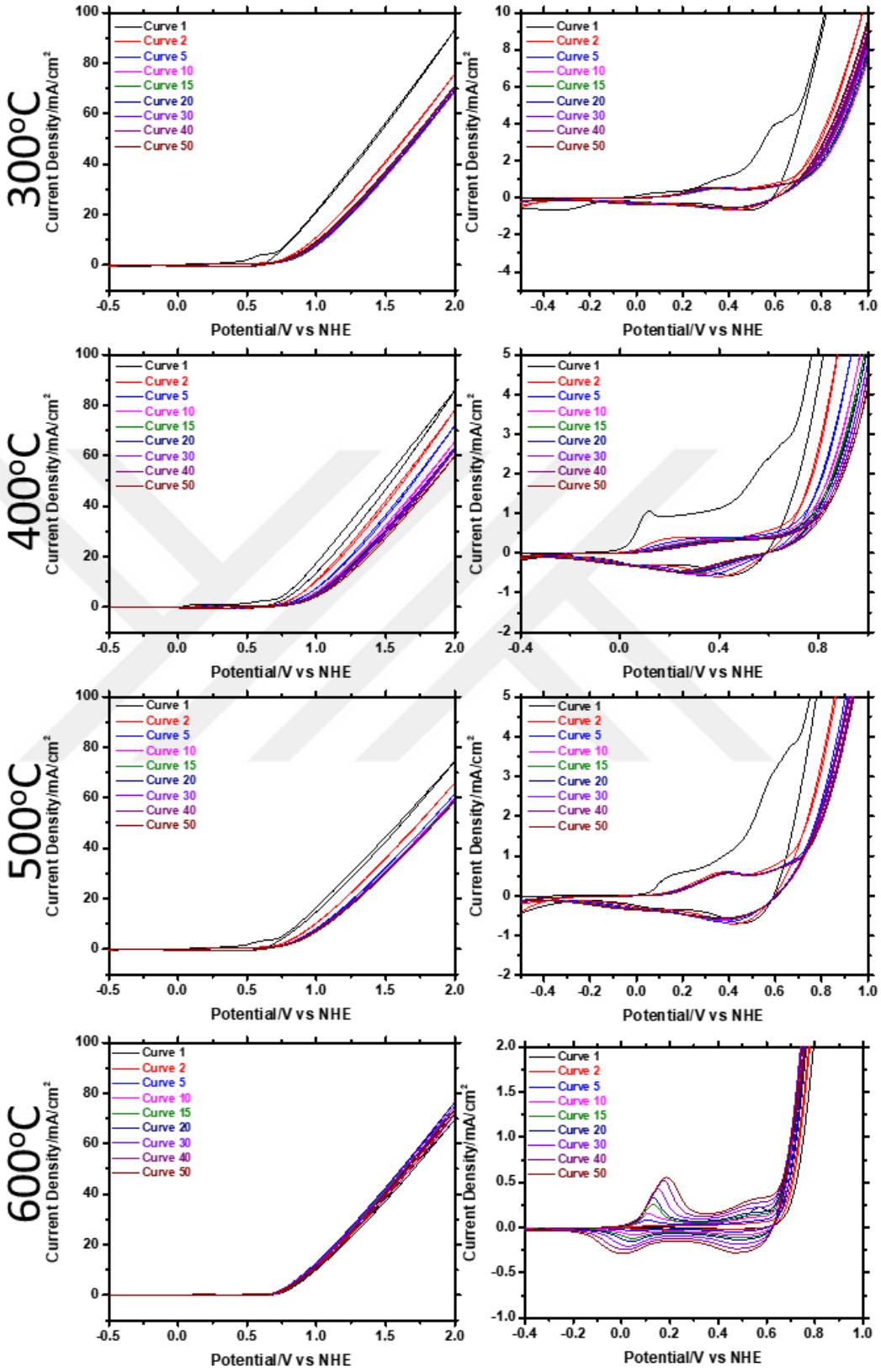

Figure 3.102: 50 CV cycles of FTO-MnCoPP-30:30-X (X values are shown on the left) electrodes with a scan rate of 50 mV/s (The right column shows the zoomed plots in the oxidation-reduction region).

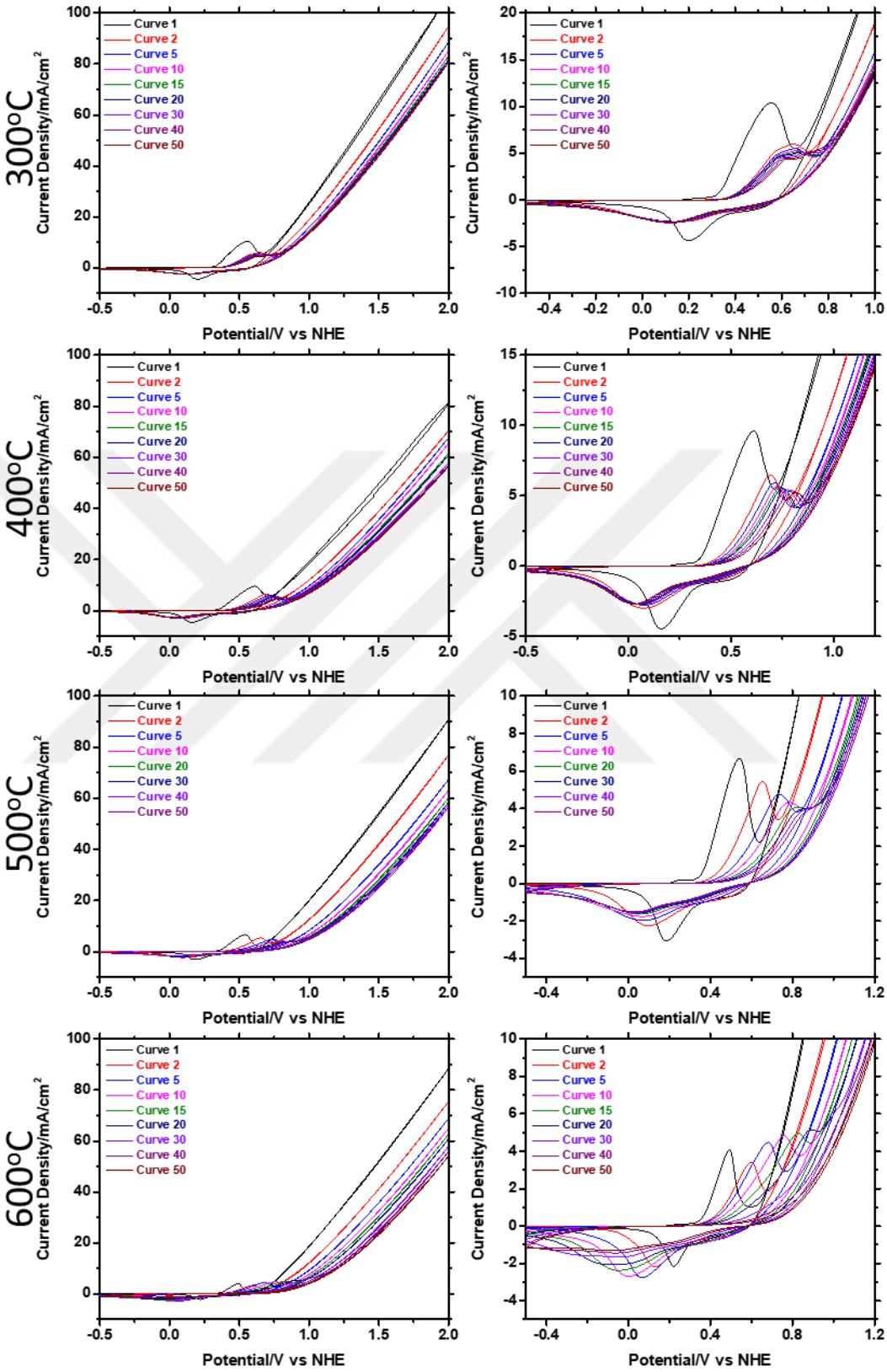

Figure 3.103: 50 CV cycles of the FTO-NiCoPP-30:30-X (X values are shown on the left) electrodes with a scan rate of 50 mV/s (The right column shows the zoomed plots in the oxidation-reduction region).

Since there is a degradation problem when FTO is used as a substrate for the working electrode, pure graphite rods are also coated to prepare the electrodes of binary metal systems. For the electrode fabrication, 10 times diluted mother liquor of MnCoPP-n:t and NiCoPP-n:t solutions are used since the total mole ratio (n+t is equal to 60) of metal is 60, as mentioned in the Mn(II) and Co(II) systems. Figure 3.104 shows the CVs of the GR-MnCoPP-n:t-300 (n and t are changed by the increments 10, keeping n+t equal to 60) electrodes. As mentioned, in the MnPP electrodes, there is a decomposition problem of manganese species during cycling. When the water oxidation reaction starts, the manganese species reach their 7+ oxidation state and decompose as MnO_4^- ion (the pink color is observed in electrolyte solution), see Figure 3.80. The decomposition of manganese species is considerably diminished by adding Co(II) to the system. The decomposition is only observed in a few cycles (2-3 cycles) with a quite pale color; then, the electrode stays stable during the cycling. The observation of pink color is completely stopped when the manganese and cobalt compositions are the same (n and t are equal to 30 each). Similarly, there is no decomposition in the cobalt-rich electrodes, meaning that adding Co(II) in a manganese system makes the electrodes more stable and robust in water oxidation reactions. The stability of the electrodes is also analyzed in the water oxidation region of the CVs. When the pure manganese system is tested, there is an apparent decrease in the water oxidation region; however, the binary systems (all compositions) of MnCoPP display relatively stable behavior in the same region. Moreover, the oxidation and reduction peaks of MnCoPP-n:t-300 electrodes are not very intense regarding current densities, see the zoomed region in Figure 3.104 (right column). The behaviors of the first cycles are different in the further cycles, meaning the starting material is changing while cycling, namely transformation to the mixed metal hydroxides, like one metal systems, see details later. With increasing of the Co(II) composition in the system, the oxidation and reduction behavior of Co(II) species (namely $Mn_xCo_{2-x}(OH)_2$) materials become more visible (oxidation peaks at around 0.1 and 0.55 V, and reduction peaks at around -0.05 and 0.4 V, respectively, see Figure 3.104.

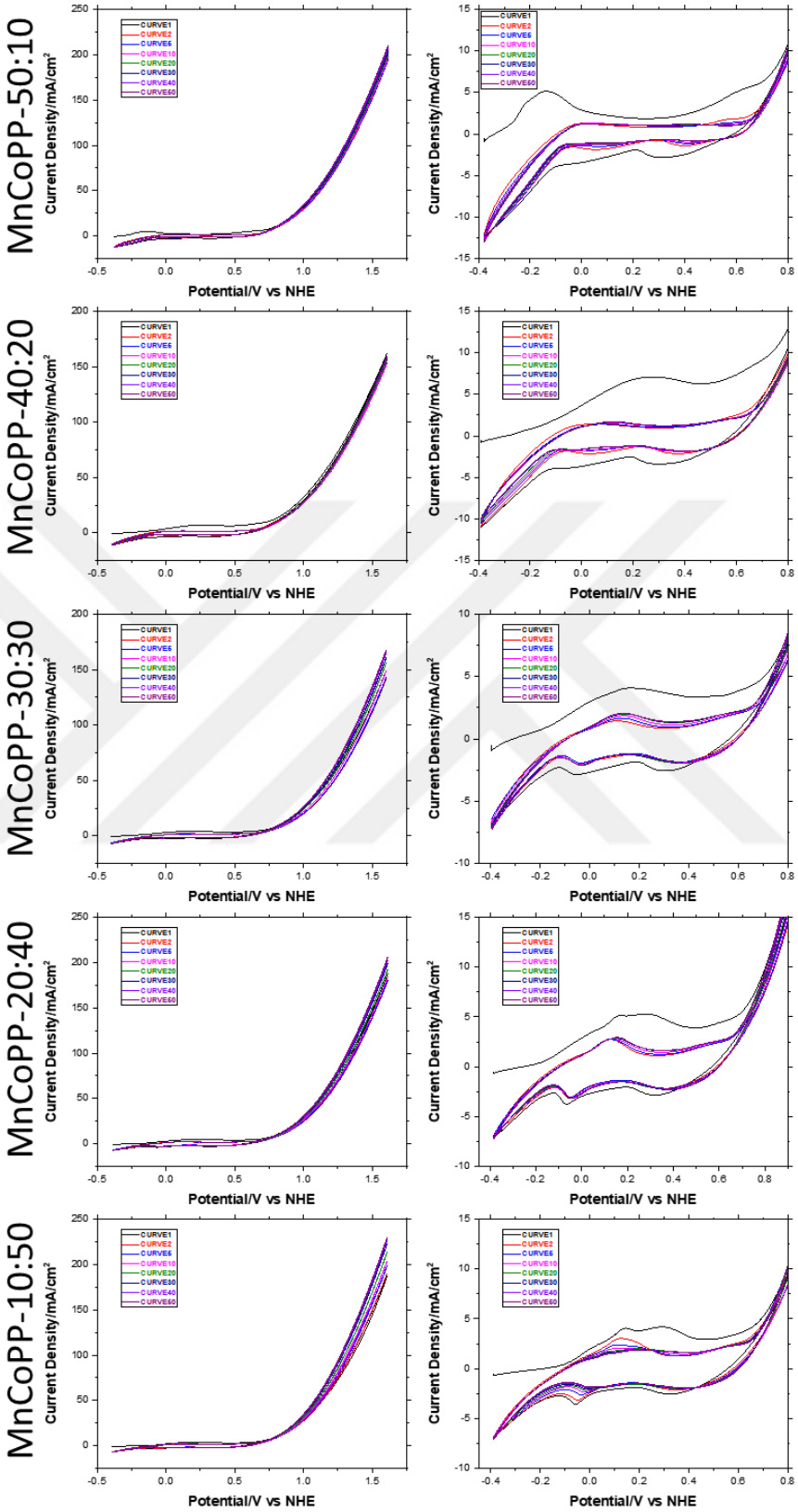

Figure 3.104: 50 CV cycles of the GR-MnCoPP-n:t-300 (n and t values are shown on the left) electrodes with a scan rate of 50 mV/s (the right column shows the zoomed plots in the oxidation-reduction region).

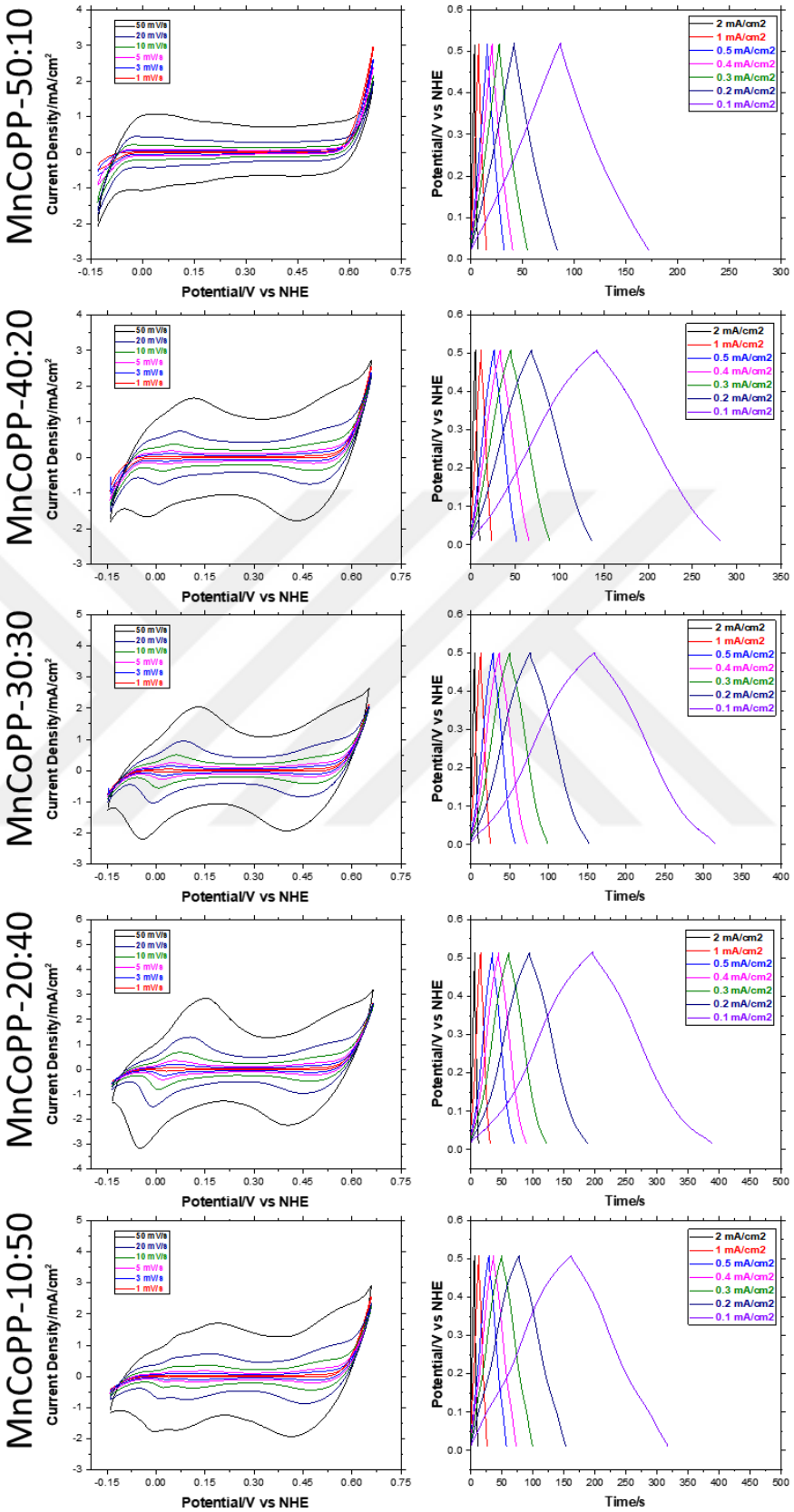

Figure 3.105: (Left column) Scan rate-dependent CV curves and (right column) GCD graphs of the GR-MnCoPP-n:t-300 electrodes (n and t are indicated on the left).

Since these electrodes are stable, they are also used to perform the scan rate dependent measurements and GCD cycling after the CV measurements in a 3M KOH electrolyte solution. As discussed in the one metal systems, the electrodes used in the CV measurements are essential to ensure that the pyrophosphate materials are fully converted to their hydroxides. Figure 3.105 shows the scan rate dependent CVs (left column) and GCD measurements (right column) of MnCoPP-n:t-300 electrodes. Likely in the 50 CVs, with the addition of the Co(II), the oxidation and reduction peaks become more prominent, where the oxidation and reduction behavior of Mn(II) species are very weak. The GCD measurements start from fast to slow charging-discharging cycles at 2, 1, 0.5, 0.4, 0.3, 0.2, and 0.1 mA/cm^2 current densities and are tabulated in Table 3.8. Moreover, the percent coulombic efficiency of each electrode is plotted for the electrodes with varying mole ratios of the metal species, see Figure 3.106. The coulombic efficiency varies across all electrodes within the 80-95% range. Increasing the amount of cobalt in the sample leads to greater stability in terms of efficiency through cycling. The binary system demonstrates higher coulombic efficiency (around 90%) compared to the pure metal systems, which exhibit approximately 80% efficiency.

Table 3.8: Specific capacitance and capacity values of the electrodes calcined at indicated temperatures of the GR-MnCoPP-n:t-300 (n and t are shown on the top) electrodes.

	MnCoPP-50:10		MnCoPP-40:20		MnCoPP-30:30		MnCoPP-20:40		MnCoPP-10:50	
Current Density (mA/cm^2)	Capacity ($mA \cdot s$)	Specific capacitance (mF/cm^2)	Capacity ($mA \cdot s$)	Specific capacitance (mF/cm^2)	Capacity ($mA \cdot s$)	Specific capacitance (mF/cm^2)	Capacity ($mA \cdot s$)	Specific capacitance (mF/cm^2)	Capacity ($mA \cdot s$)	Specific capacitance (mF/cm^2)
0.1	8.06	16.12	13.14	26.28	14.69	29.38	18.58	37.16	15.23	30.46
0.2	8.06	16.12	13.14	26.28	14.69	29.38	18.47	36.94	14.76	29.52
0.3	7.99	15.98	13.25	26.5	14.47	28.94	17.89	35.78	14.76	29.52
0.4	7.92	15.84	12.82	25.64	14.22	28.44	17.53	35.06	14.26	28.52
0.5	7.81	15.62	12.60	25.2	13.93	27.86	17.17	34.34	13.97	27.94
1	7.34	14.68	11.59	23.18	12.46	24.92	15.30	30.6	12.74	25.48
2	6.44	12.88	9.58	19.16	9.72	19.44	11.99	23.98	10.58	21.16

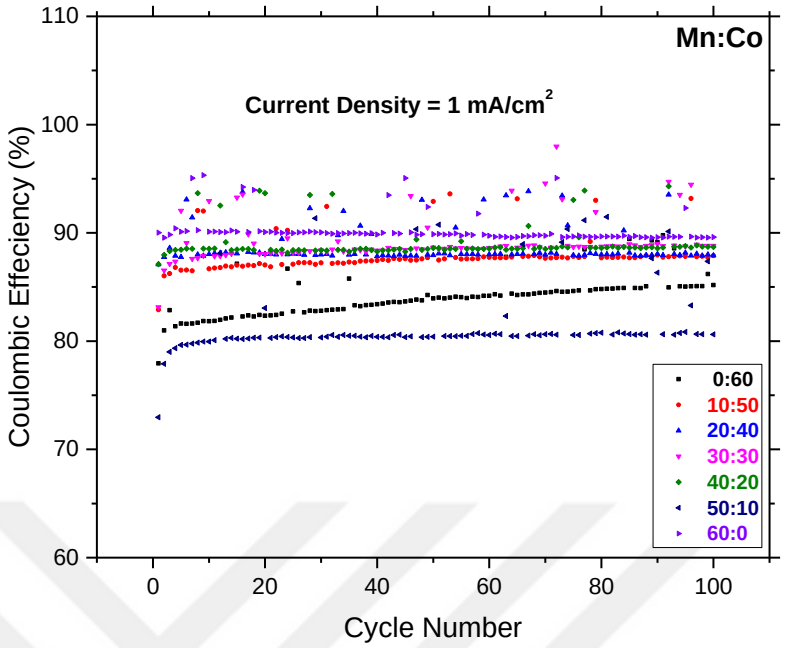

Figure 3.106: Graph of coulombic efficiencies of the GR-MnCoPP-n:t-300 electrodes (n and t are indicated on the graph) versus cycle number.

The capacity values at 0.1 mA/cm^2 current density of MnCoPP-n:t-300 electrodes are compared to pure MnPP-60-300 and CoPP-60-300 electrodes, see Figure 3.107. The pure MnPP-60-300 electrode is slightly better than the electrode of MnCoPP-10:50-300 in terms of capacity. However, the capacity values increase with increasing Co species in the sample up to a 20:40 mole ratio for Mn:Co ratio (where n and t are 20 and 40, respectively). Further increasing of Co amount in the sample reaches almost the value of the pure CoPP-60-300 electrode.

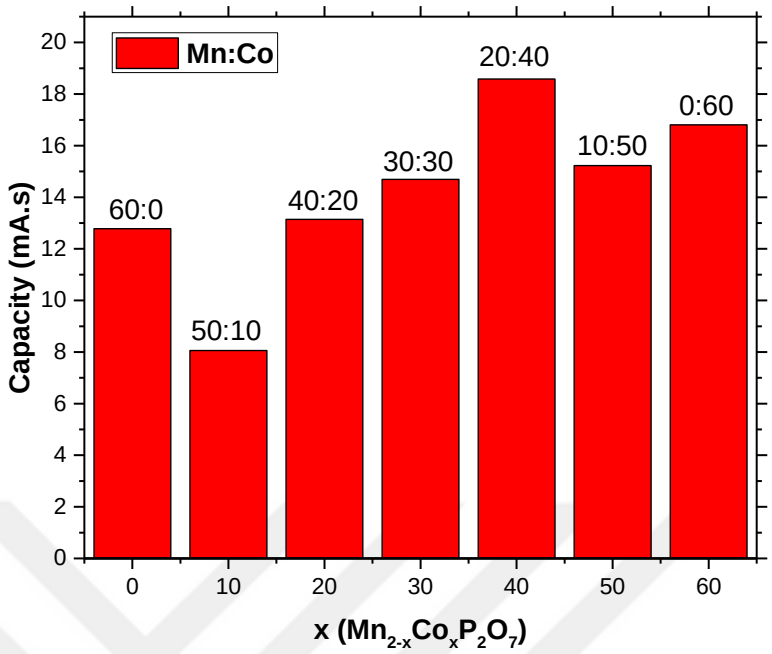

Figure 3.107: Graph of capacity values versus mole ratio of cobalt in the MnCoPP-300 electrodes.

Similarly, the GR-NiCoPP-n:t-300 are fabricated to elucidate the electrochemical behaviors of the binary systems. Figure 3.108 shows the CVs of the GR-NiCoPP-n:t-300 electrodes collected using a 3-electrode system in 3M KOH solution for a potential window of -0.5-1.5 V vs. Ag/AgCl by changing the n:t ratio by increments of 10. Since the oxidation (at around 0.5 V) and reduction (at about 0.1 V) peak currents of NiPP (more correctly, $Ni(OH)_2$ species because of transformation) are higher than Co(II) species, the only observed peaks are originated from the $Ni(OH)_2$ species. The oxidation and reduction peaks of Co(II) ($Co(OH)_2$ species) are encapsulated by the dominant Ni(II) species. However, with the addition of Co content to the Ni system, the water oxidation reaction becomes more prominent, and the slope of this region increases during cycling. Note also that for some mixed metal systems (for example, 30:30 and 10:50 ratios for NiCo), the current density reaches an outstanding current density of 600-700 mA/cm^2 at relatively low potentials, showing that the material is fascinating electro-catalysts for the water oxidation reaction, see Figure 3.108.

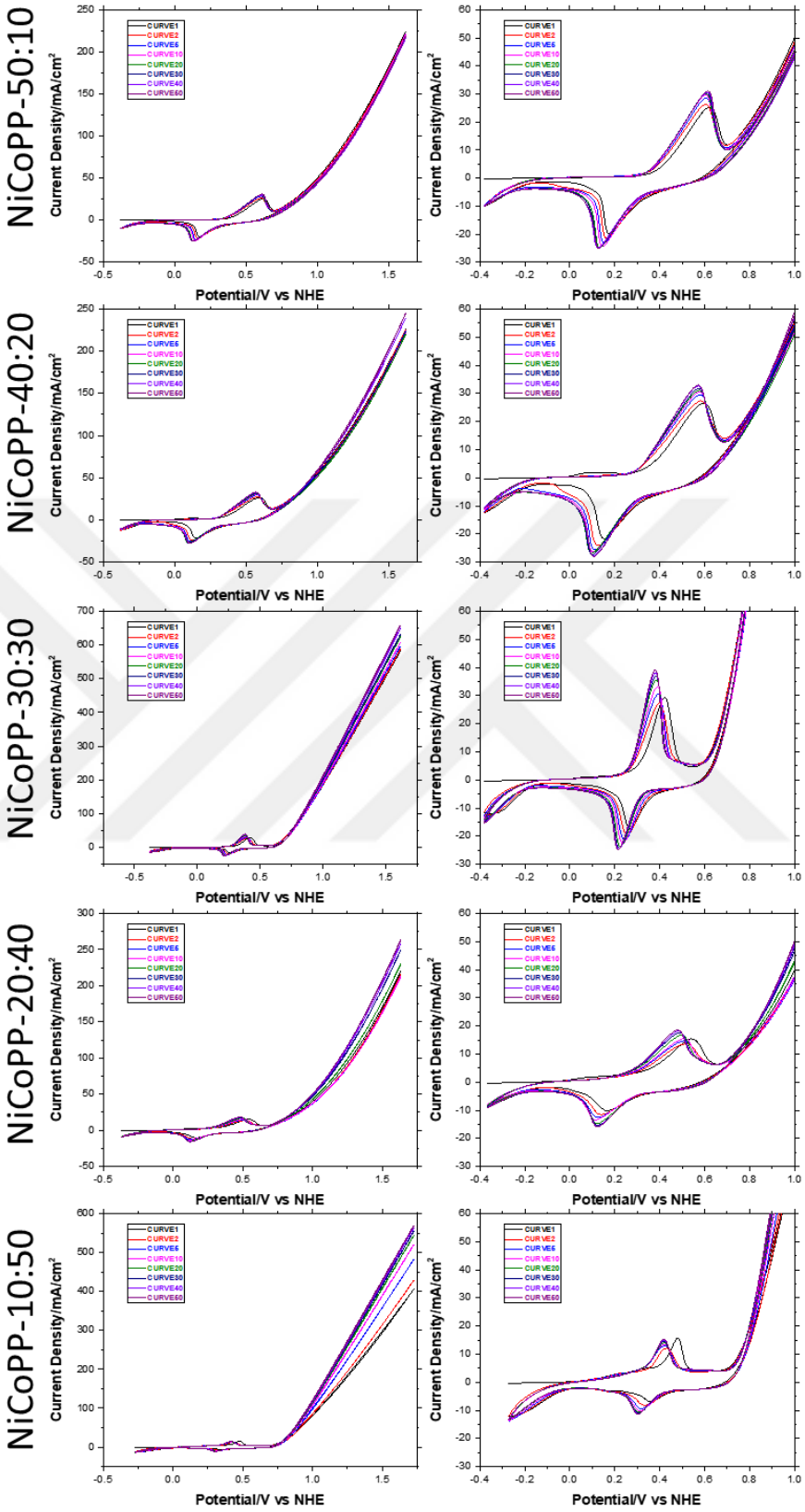

Figure 3.108: 50 CV cycles of the GR-NiCoPP-n:t-300 (n and t values are shown on the left) electrodes with a scan rate of 50 mV/s (the right column shows the zoomed plots in the oxidation-reduction region).

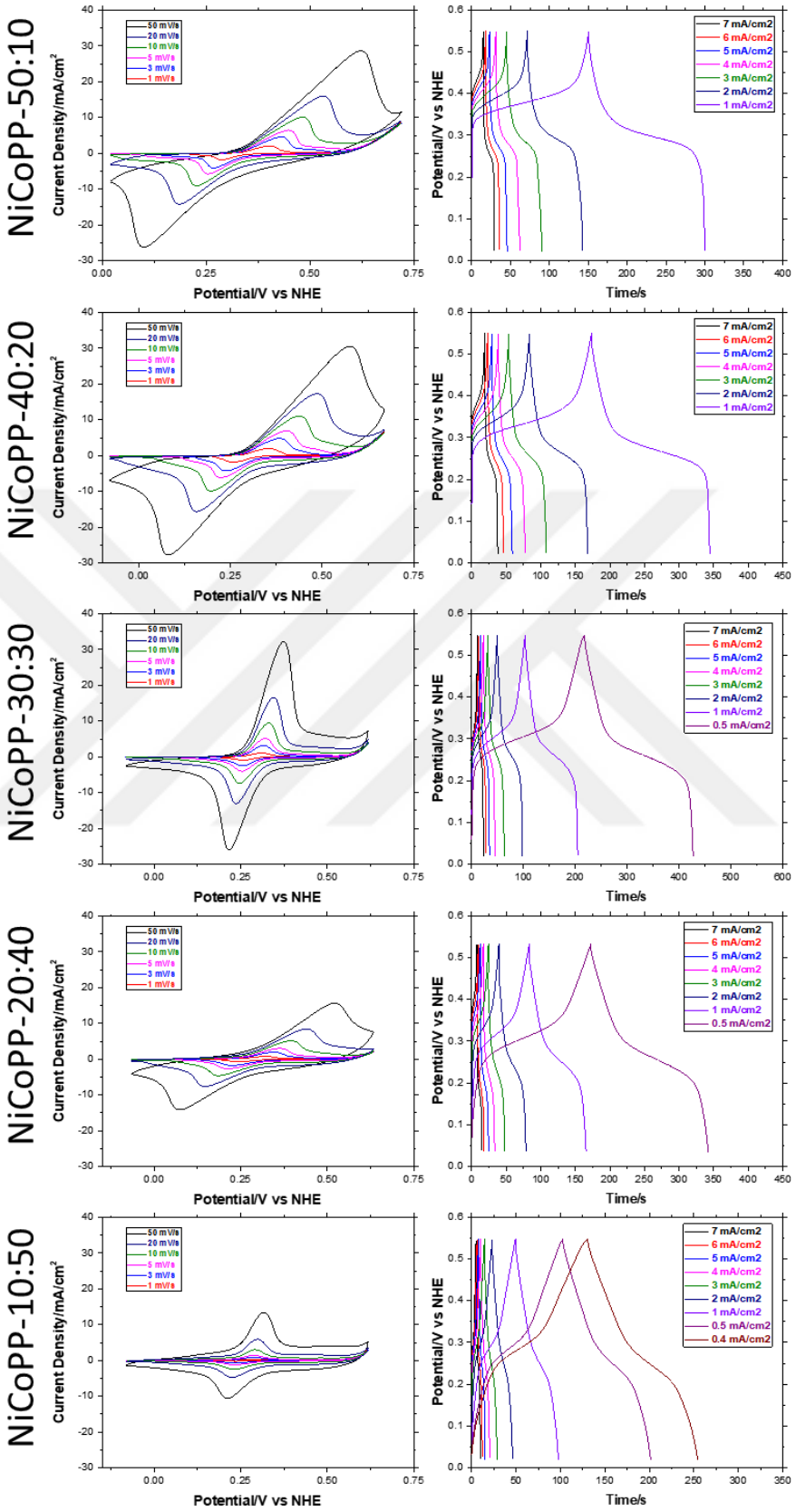

Figure 3.109: (Left column) Scan rate-dependent CV curves and (right column) GCD graphs of GR-NiCoPP-n:t-300 electrodes (n and t are indicated on the left).

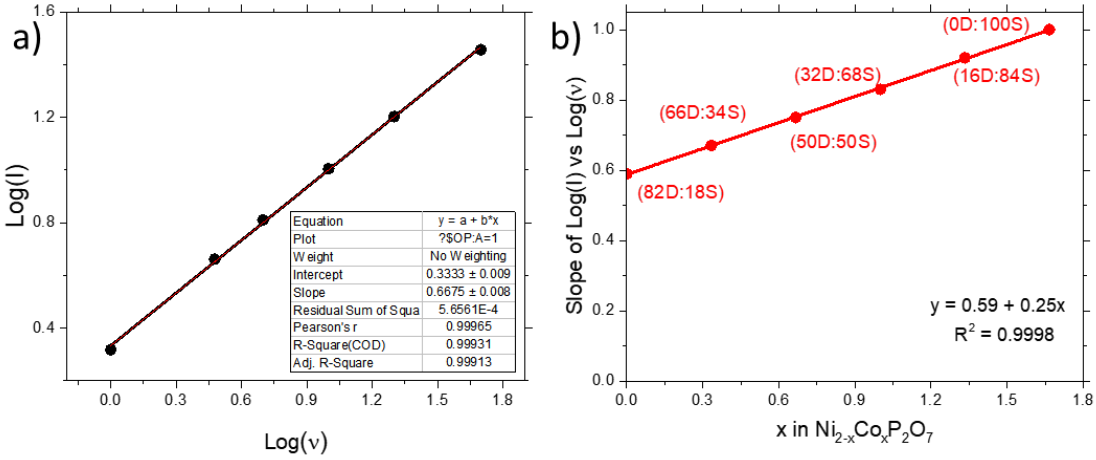

Figure 3.110: a) Logarithm of current density (log(I)) versus logarithm of scan rate (log(ν)) from NiCoPP-30:30-300 electrode, and b) slopes of log(I) versus log(ν) of all compositions versus x in $Ni_{2-x}Co_xP_2O_7$ (D stands for diffusion, and S stands for surface).

The scan rate dependent CVs and GCD measurements are collected from the used electrodes (50 cycles of CV measurements) to ensure the complete transformation of the PP to hydroxide, see Figure 3.109. The only faradaic current observed in the scan rate-dependent CV curves results from the Ni(II) species, which dominates the oxidation and reduction regions of Co(II) species, see the left column of Figure 3.109. From the scan rate-dependent measurements, the logarithm of current density versus the logarithm of scan rate plots are produced to elucidate information about the oxidation process. Remember that the oxidation process is diffusion-controlled (where the current density versus square root of scan rate is linear) process for the NiPP (more correctly, $Ni(OH)_2$, after transformation), see Figure 3.27 (right column). In contrast, it is a surface-controlled (where the current density versus scan rate is linear) process for the pure Co(II) system, see Figure 3.57 (right column). In other words, if the slope of log(I) versus log(ν) (denoted as b in the equation) is equal to 0.5, it corresponds to a diffusion-controlled process, and if it is equal to 1.0, it corresponds to a surface-controlled process. This relation is derived from eq. 3.13;

$$i = av^b \qquad \textbf{eq. 3.13}$$

Where a and b are constant, i is the current density, and ν is the scan rate in CVs.[133], [181] Figure 3.110a shows the plot of log(j) in the oxidation peak of Ni^{2+} to Ni^{3+} vs

log(v) for the NiCoPP-30:30-300 electrode and the slope is 0.66. The graph in Figure 3.110b shows the change in b with increasing Co content in the electrode. The percentages of diffusion and surface-controlled processes are given in the graph for each data point for each electrode. The slope of log(j) vs. log(v) is close to 0.5 for the nickel-rich electrodes, and it increases linearly with the addition of Co(II) content to a value of 1.0. In between the pure compositions, the samples display both diffusion and surface-controlled processes together, where the diffusion-controlled process shows the battery-type process, whereas the surface-controlled one is a capacitive type. [182]

The right column of Figure 3.109 shows a typical GCD graph of capacitive behavior with a redox couple (results as a plateau in the graph). The GCD measurements start from fast to slow charging-discharging cycles at 7, 6, 5, 4, 3, 2, and 1 mA/cm^2 current densities and are tabulated in Table 3.9. Moreover, the percent coulombic efficiency of each electrode of GR-NiCoPP-n:t-300 is plotted to compare the electrodes with changing the mole ratio of the metal species, see Figure 3.111. The coulombic efficiency is drastically increased (from around 80% to about 97%) when Ni metal is added to the Co system.

Table 3.9: Specific capacitance and capacity values of the electrodes calcined at indicated temperatures of the GR-NiCoPP-n:t-300 (n and t are shown on the top).

	NiCoPP-50:10		NiCoPP-40:20		NiCoPP-30:30		NiCoPP-20:40		NiCoPP-10:50	
Current Density (mA/cm^2)	Capacity (mA·s)	Specific capacitance (mF/cm^2)	Capacity (mA·s)	Specific capacitance (mF/cm^2)	Capacity (mA·s)	Specific capacitance (mF/cm^2)	Capacity (mA·s)	Specific capacitance (mF/cm^2)	Capacity (mA·s)	Specific capacitance (mF/cm^2)
1	148	279	170	321	89	168	82	155	48	91
2	142	268	166	313	81	153	78	147	46	87
3	135	255	161	304	74	140	72	136	43	81
4	124	234	154	291	68	128	66	125	40	75
5	114	215	147	277	62	117	61	115	38	72
6	107	202	139	262	57	108	57	108	36	68
7	101	191	131	247	52	98	52	98	34	64

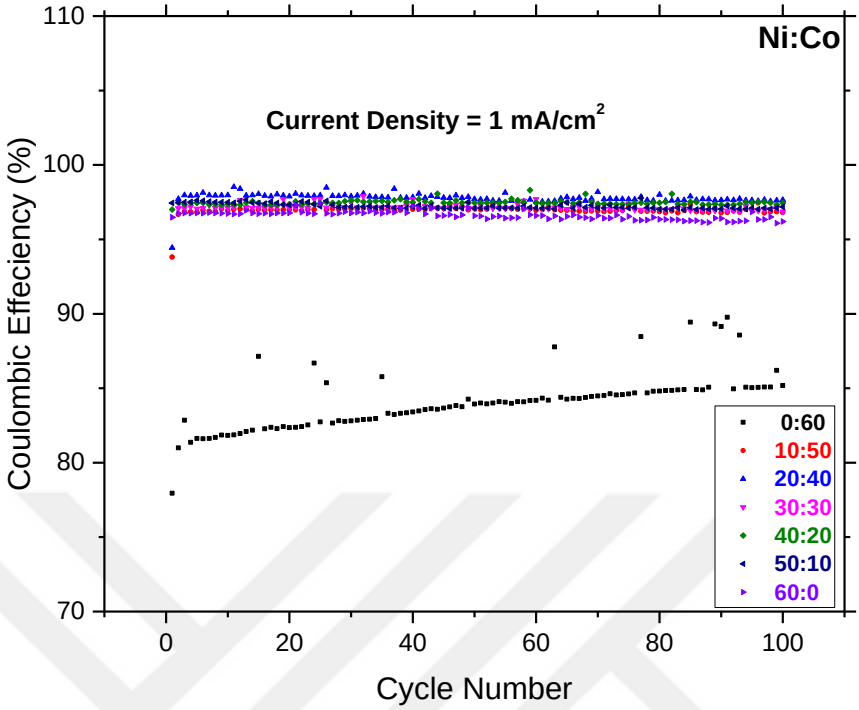

Figure 3.111: Graph of coulombic efficiencies of the GR-NiCoPP-n:t-300 electrodes (n and t are indicated on the graph) versus cycle number.

The capacity values at 1 mA/cm^2 current density of NiCoPP-n:t-300 electrodes are compared to pure NiPP-60-300 and CoPP-60-300 electrodes, see Figure 3.112. The addition of Ni(II) to the Co(II) system improves the capacity values of the electrodes. It increases the capacity values until the 40:20 mole ratio of Ni:Co and then almost linearly decreases until the pure CoPP values. The NiCoPP-40:20-300 sample (namely $Ni_{0.67}Co_{0.33}(OH)_2$) displays the highest capacity, and the process is 50 % diffusion- and 50 % surface-controlled, see Figure 3.110b. The surface-controlled process further increases with increasing Co content with decreasing capacity.

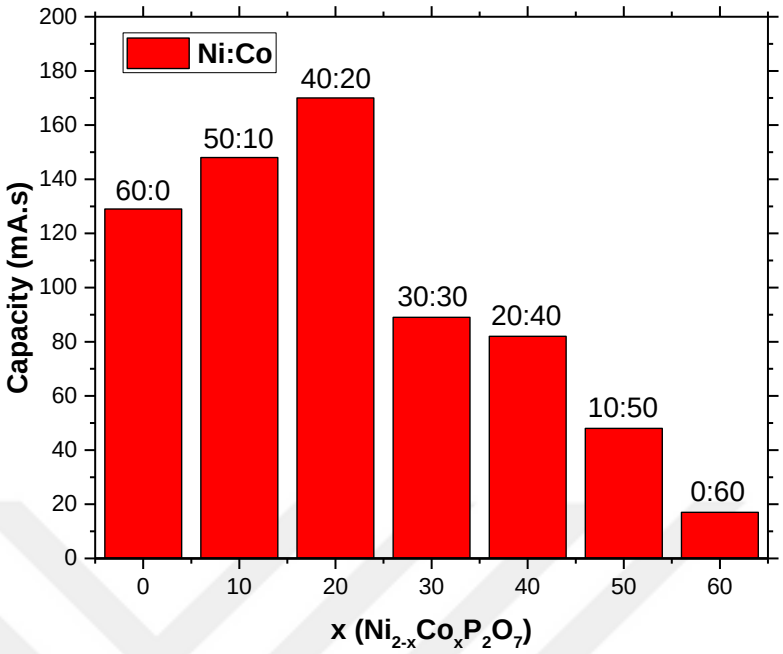

Figure 3.112: Graph of capacity values versus mole ratio of cobalt in the NiCoPP-300 electrodes.

Mixing two metals, especially Ni and Co, produces more capacitive electrodes. Determining whether the electrodes comprise a physical solid mixture of two end members or a homogeneous solid-solution becomes essential. The wide-angle XRD patterns of crystalline NiCoPP samples (at 700 ^{o}C) in each composition are collected to clarify the mixing mechanism. Both pure phases of NiPP and CoPP are dominantly forming the alpha phase of their pyrophosphates. When the two metals are fabricated in different compositions, the diffraction lines appear between pure NiPP and CoPP diffraction, see Figures 3.113a and b (zoomed patterns in the most intense diffraction lines at around 29^{o}, 2θ). It means the binary systems form uniformly mixed solid-solutions. Figures 3.113c and d show that 2 theta and d-spacing values at the most intense diffraction are mostly (except 40:20 and 50:10 mole ratios for Ni:Co) linearly dependent on the amount of Ni in the systems.

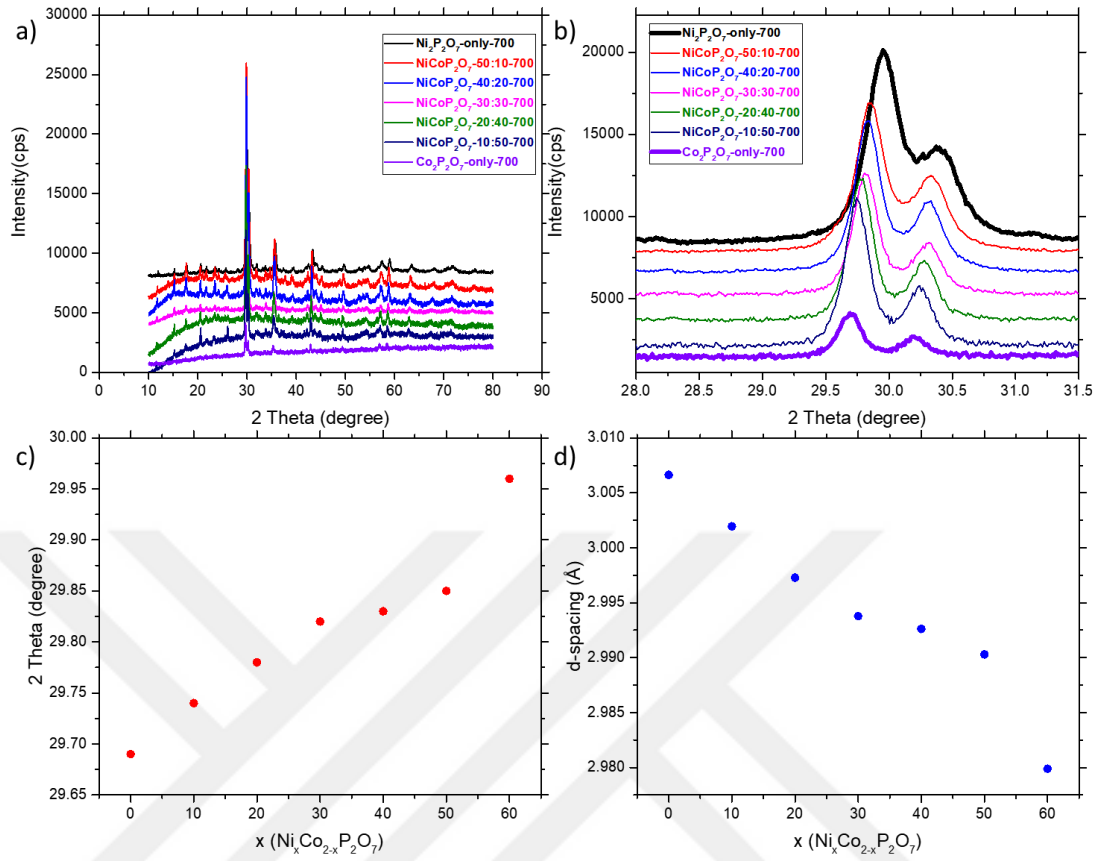

Figure 3.113: a) and b) Wide-angle XRD patterns of the NiCoPP-n:t-700 samples (n and t are indicated in the graphs), c) 2 theta values, and d) d-spacings of the most intense diffraction versus Ni content in the NiCoPP-n:t-700.

Before the transformation, Ni and Co species in their binary mixture constitute a homogeneous solid-solution. However, to clarify obtaining a higher capacitance value with the binary system than the pure phases, the mixing type of these species after transformation should be considered as well. For this purpose, different compositions of the Ni and Co binary mixtures are aged in 3M KOH for 1 h to collect their XRD patterns and ATR-FTIR spectra, see Figure 3.114. The XRD patterns show that increasing the Co amount in the binary system makes the diffraction lines sharper, corresponding to large β-$Co(OH)_2$ particles. Only pure NiPP-60 and NiCoPP-50:10 samples have only broad diffraction lines indexed to the small β-$Ni(OH)_2$ particles. In other compositions, the large particles of β-$Co(OH)_2$ dominate the mixture since the β-$Ni(OH)_2$ material has tiny particles. The β-$Ni(OH)_2$ particles are visible up to the NiPP-30:30 sample with very weak and broad lines, but in Co-rich samples, even those

weak diffractions are not detected. The solid-solution behavior, observed in the NiCoPP-n:t-700 samples, is not observed in the mixed metal hydroxides; instead, the physical mixture behavior is observed. The ATR-FTIR spectra, see Figure 3.114b, display a sharp peak at around 3600 cm^{-1}, characteristic of hydroxide species. The intensity of the hydroxide peak is increasing with the Co amount in the binary system. In contrast, the broad water peak, observed at 3600-3000 cm^{-1} and originating from the adsorbed water in the samples, loses intensity. The amount of adsorbed water is more in the NiCoPP-50:10 and NiCoPP-40:20 samples, which is an indication of having smaller particles. The electrodes of those ratios also display higher capacity and specific capacitance values. Moreover, the absorbed carbonate species shown at 1500-1250 cm^{-1} (which could not be removed even by several washings) are decreasing with the increasing Co amount in the system.

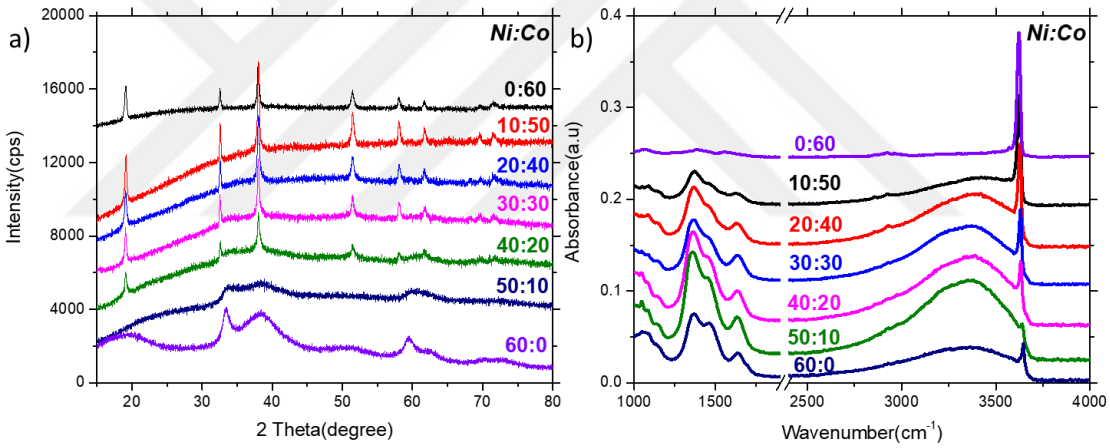

Figure 3.114: a) Wide-angle XRD patterns and b) ATR-FTIR spectra of *m*- NiCoPP-n:t-300 after aging in 3 M KOH solution for 1 h.

The colors of the Ni:Co binary mixture after aging in 3M KOH solution also indicate that they are physical mixtures. Remember that the purple-blue color of the CoPP sample is turning pale pink, which is the β-$Co(OH)_2$. With the addition of Ni to the system, the color becomes greenish, which is the color of β-$Ni(OH)_2$, see Figure 3.115. The transformation time is shortened with the addition of Co (see later), where the pure cobalt pyrophosphate transformation is very fast (30 sec), and with the color change, it is easy to understand the complete transformation.

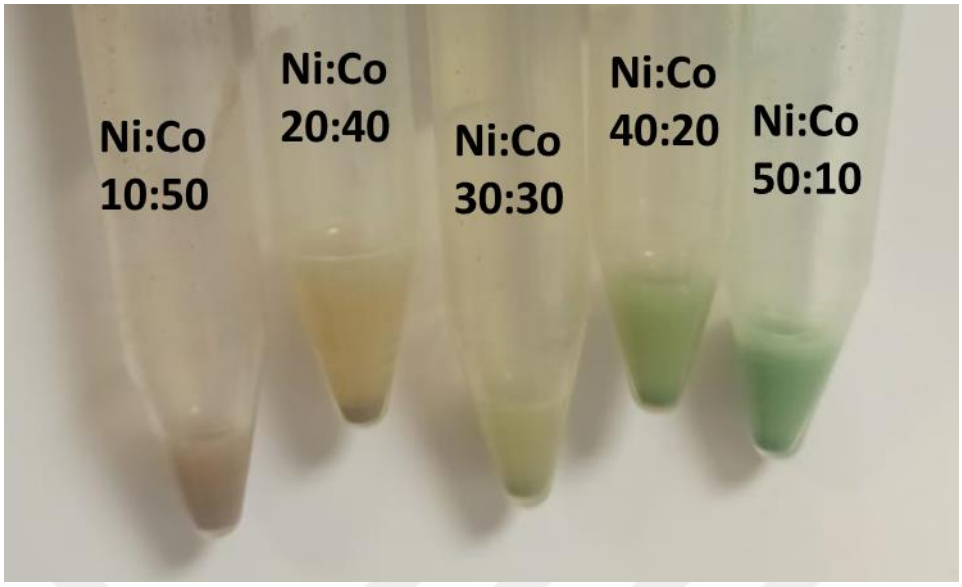

Figure 3.115: Photographs of NiCoPP-n:t-300 powders after aging in 3M KOH solution for 1 h (n:t is 10:50, 20:40, 30:30, 40:20, and 50:10 for Ni:Co from left to right).

The SEM images of each composition are also collected after aging the powders of NiCoPP-n:t-300 in 3M KOH solution in a centrifuge tube (with a closed cap) for 1 h to investigate the mixing type, see Figures 3.116 and 3.117. The Co-rich sample with the ratio of 10:50 for Ni:Co displays a plate-like structure with a perfect hexagonal shape (given in Figures 3.117a and b) like observed in the pure $Co(OH)_2$ sample, remember Figure 3.61. The size of those particles varies between 50-400 nm with a thickness of 30-50 nm, and those particles cover all samples. Increasing the Ni content in the system makes the spherical particles (which originated from the $Ni(OH)_2$ particles, remember Figure 3.35) near the hexagonal plates. While transforming to the hydroxide, the needle/flake-like particles form with conserved the spherical sphere of NiPP. Up to 50% percent composition, the hexagonal plates are prominent to the structure all over the sample. For the Ni-rich compositions, the spherical particles start to be dominant. Since the magnification of the SEM technique is not as good as TEM, it is hard to focus on the needle/flake-like particles on the spheres. However, from the sample with a 50:10 mole ratio for Ni:Co, those needles are also distinguishable in the image, see Figure 3.117c.

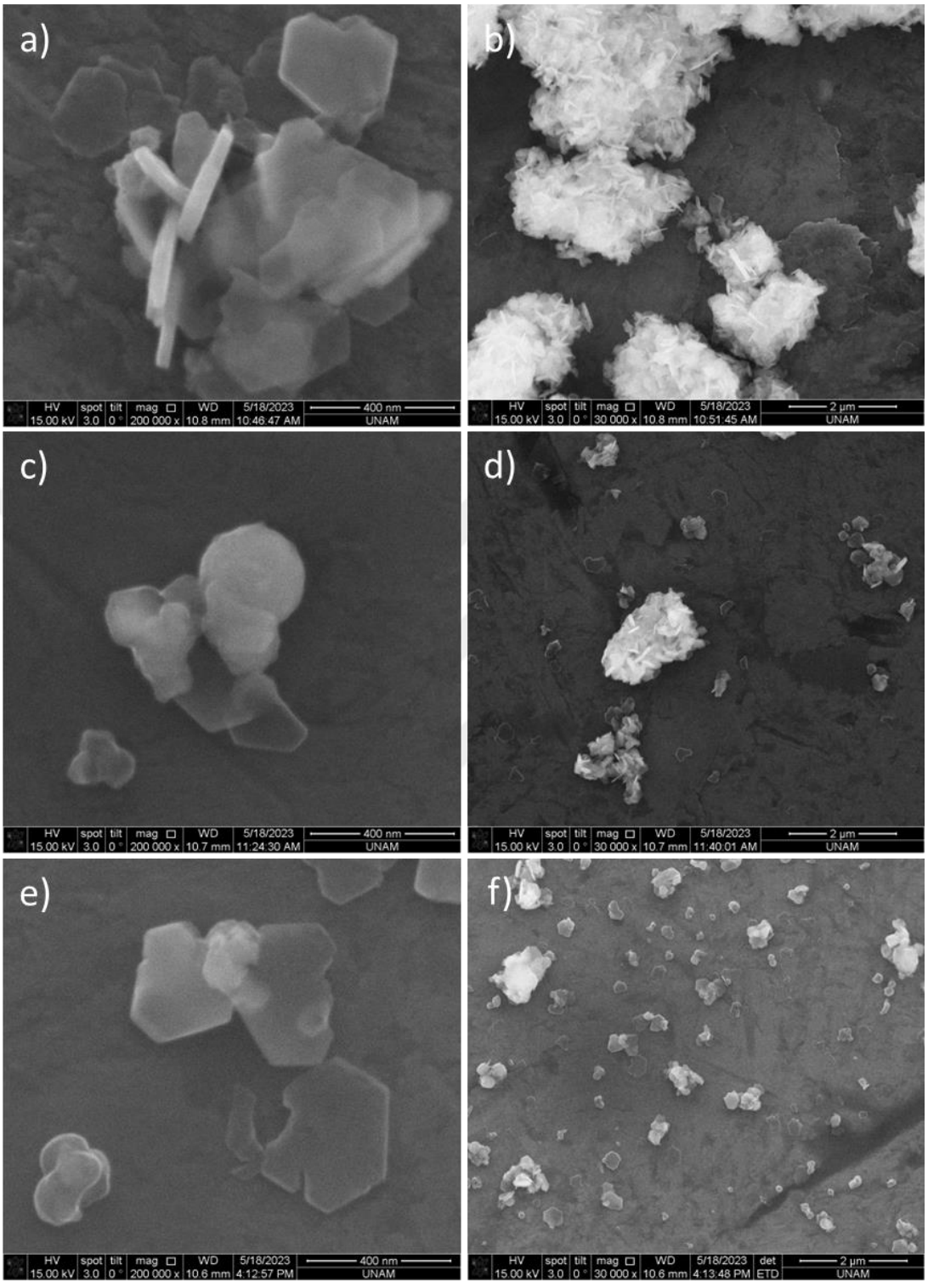

Figure 3.116: SEM images of a) and b) NiCo-10:50-300, c) and d) NiCo-20:40-300, e) and f) NiCo-30:30-300 samples after aging in 3 M KOH solution for 1 h (the scale bars are 400 nm and 2 μm for left and right images, respectively).

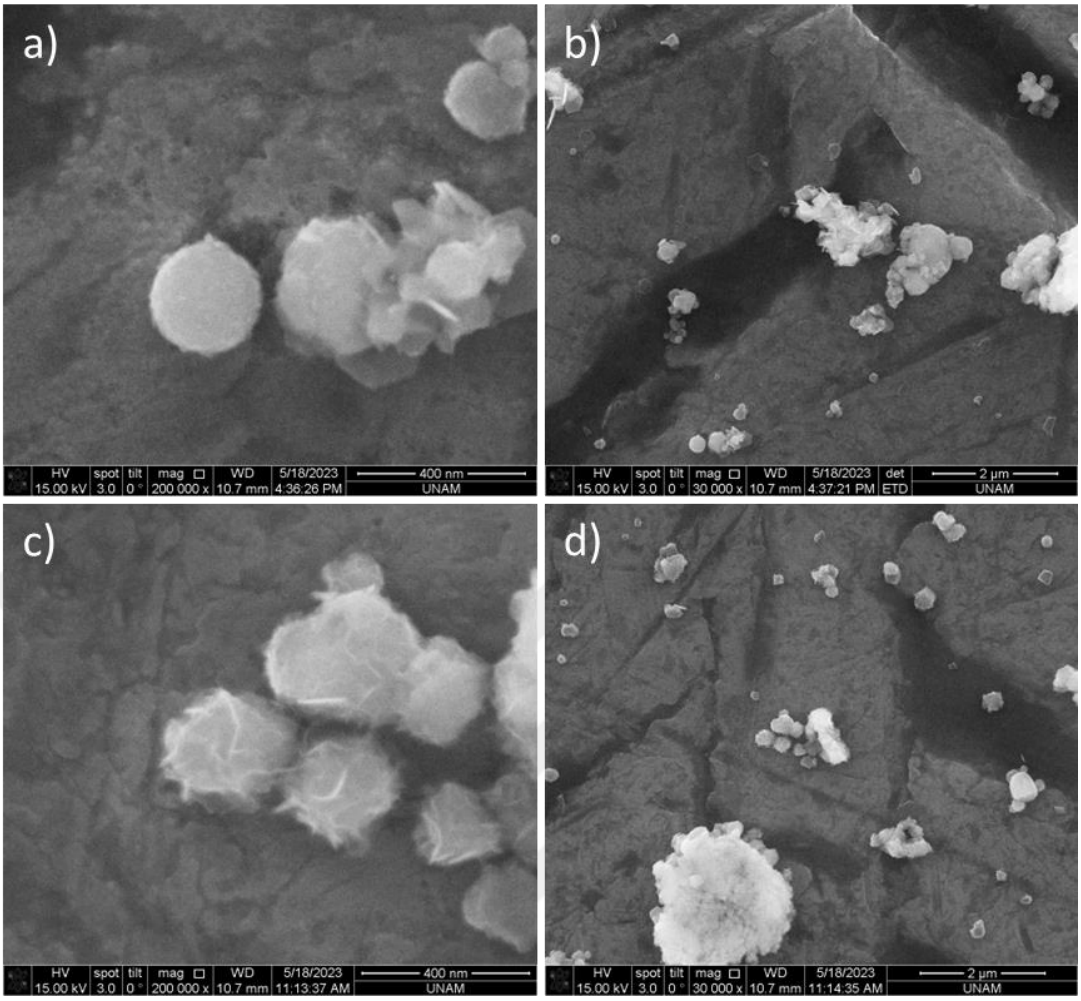

Figure 3.117: SEM images of a) and b) NiCo-40:20-300, c) and d) NiCo-50:10-300, samples after aging in 3 M KOH solution for 1 h, (the scale bars are 400 nm and 2 μm for left and right images, respectively).

Since the transformation times of pyrophosphate to hydroxides change with the various mole ratios of Ni:Co content, it is better to investigate the change in the K_{sp} values. The same design used in the NiPP-30-300 and NiPP-30-700 samples is established to calculate the K_{sp} values of the NiCoPP-n:t-300 samples. Since the oxidation and reduction peak currents are relatively low for the electrodes prepared from CoPP materials, nickel-containing materials having measurable current densities are tested for this purpose. It is started from the neutral electrolyte (2.4 M KOH + 0.6 M PPA) having no characteristic of any faradaic peaks, and then 1 ml of 3M KOH solution is added to the electrolyte every 10 CV cycles, see Figure 3.118.

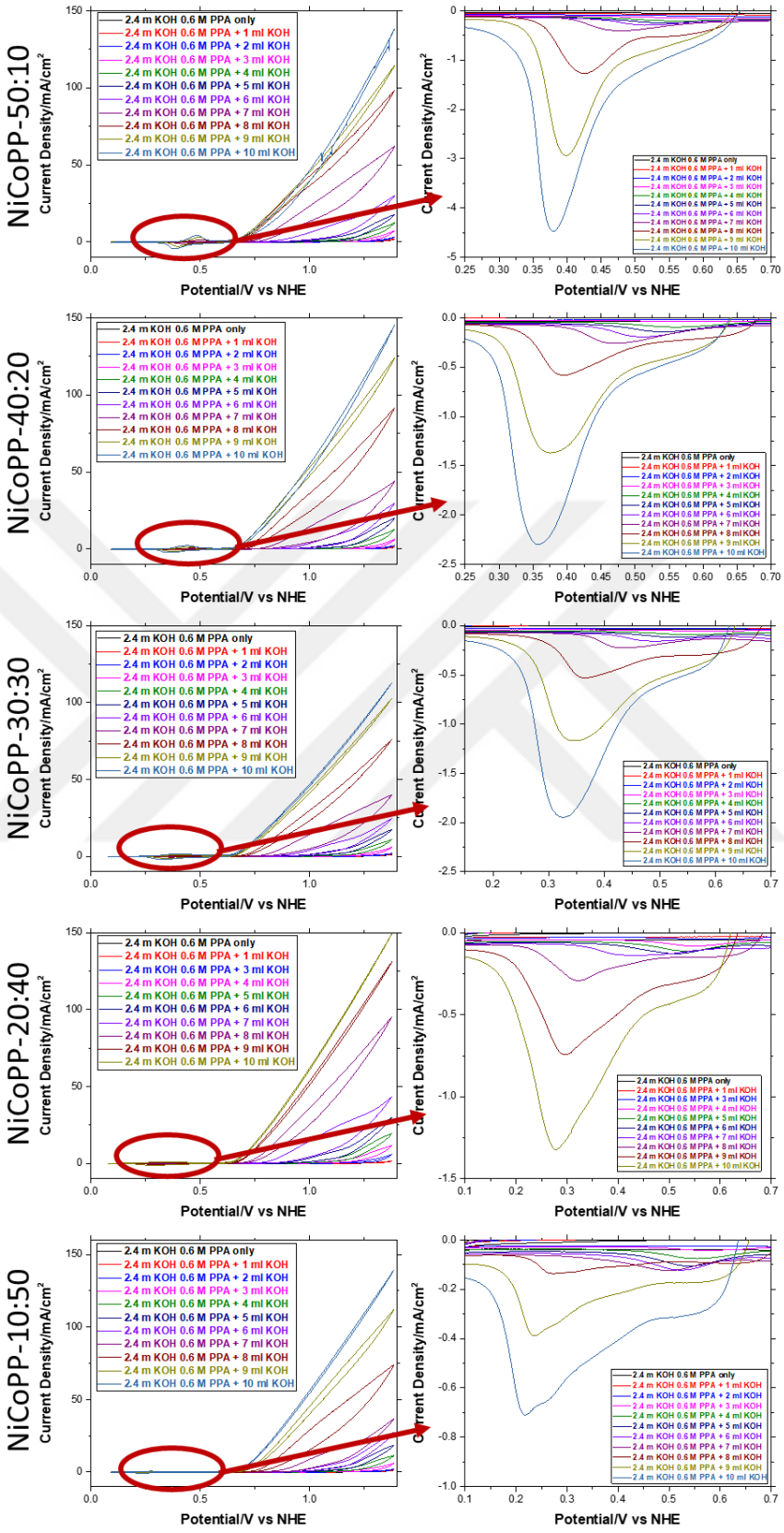

Figure 3.118: CV curves of GR-NiCoPP-n:t-300 samples with a scan rate of 50 mV/s for a potential window 0-1.3 V vs. Ag/AgCl in a neutral electrolyte by adding KOH solution.

The current densities of reduction peaks of samples from Figure 3.118 are plotted versus the volume of KOH added, and with the extrapolation, it is found that the first hydroxide transformation occurs when 1.98, 2.17, 2.37, 2.57, and 2.76 ml of 3M KOH is added for the NiCoPP-n:t-300 electrodes, where n:t is 10:50, 20:40, 30:30, 40:20, and 50:10, respectively. The mole fraction of nickel (x) in the $Ni_xCo_{1-x}(OH)_2$ sample versus the volume of KOH added provides a linear relationship which helps to find out the minimum amount of KOH solution to convert CoPP to $Co(OH)_2$ with extrapolation, see Figure 3.119. Similarly, with the K_{sp} values of pyrophosphates, there are no proved K_{sp} values for the mixed hydroxides in the literature. Therefore, with the assumption of having solid-solutions for the mixed metal hydroxides, the K_{sp} values of mixed metal hydroxides are estimated, see Table 3.10. The concentrations of [OH^-], [$P_2O_7^{4-}$], and [$Ni^{2+} + Co^{2+}$] are calculated according to the first transformation points and listed in the same graph. With the addition of Co content, the K_{sp} value of the material is increasing. This is consistent with the faster transformation of pure CoPP to $Co(OH)_2$. The Co-containing pyrophosphates are more soluble than the Ni-rich compositions.

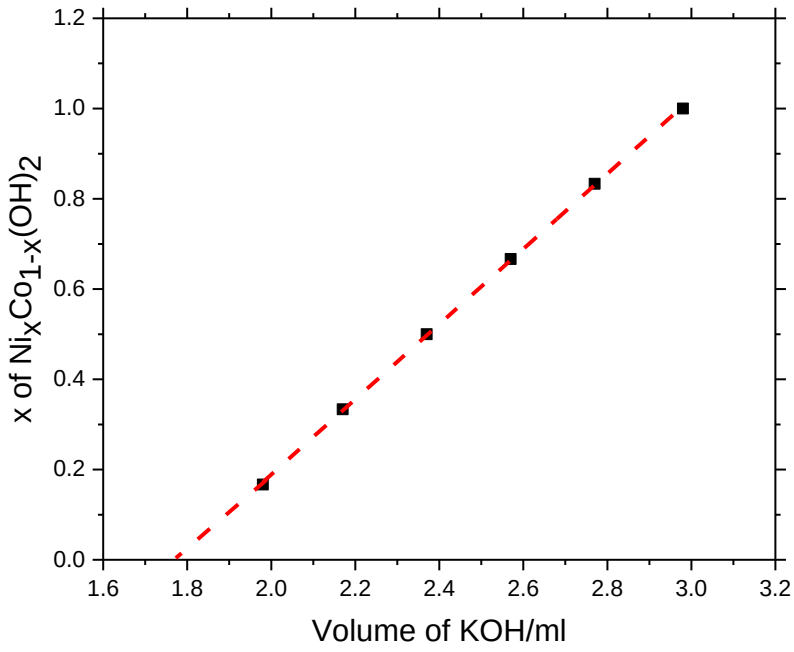

Figure 3.119: Nickel mole fraction versus volume of KOH plot derived from the extrapolation of KOH addition graph.

Table 3.10: The volume of KOH added to start the transformation of MPP to $M(OH)_2$, concentrations of ($[OH^-]$, $[P_2O_7^{4-}]$, and $[Ni^{2+} + Co^{2+}]$ and Ksp values of $Ni_xCo_{1-x}(OH)_2$ and $Ni_xCo_{2-x}P_2O_7$.

Composition (Ni:Co)	Volume of KOH added (ml)	$[OH^-]$ (M)	$[P_2O_7^{4-}]$ (M)	$[Ni^{2+}]+[Co^{2+}]$ (M)	Ksp of $Ni_xCo_{1-x}(OH)_2$ (M^3)	Ksp of $Ni_xCo_{2-x}P_2O_7$ (M^3)
0:60	1.76	0.166	0.567	$2.15x10^{-13}$	$5.92x10^{-15}$	$2.62x10^{-26}$
10:50	1.98	0.187	0.563	$1.41x10^{-13}$	$5.03x10^{-15}$	$1.16x10^{-26}$
20:40	2.17	0.202	0.560	$1.01x10^{-13}$	$4.14x10^{-15}$	$5.76x10^{-27}$
30:30	2.37	0.220	0.556	$6.71x10^{-14}$	$3.25x10^{-15}$	$2.51x10^{-27}$
40:20	2.57	0.237	0.553	$4.20x10^{-14}$	$2.36x10^{-15}$	$9.76x10^{-28}$
50:10	2.76	0.253	0.549	$2.62x10^{-14}$	$1.47x10^{-15}$	$3.76x10^{-28}$
60:0	2.98	0.271	0.546	$7.95x10^{-15}$	$5.84x10^{-16}$	$3.45x10^{-29}$

Since adding Ni(II) to the Co(II) system improves the capacitance and specific capacitance values, it is also tried to add Ni species to the Mn system to obtain the NiMnPP-n:t samples with various n:t ratios. Figure 3.120 shows that CV curves of the GR-NiMnPP-n:t-300 (n and t are changed by the increments 10, keeping n+t equal to 60) electrodes collected with the 3-electrode system in 3M KOH electrolyte. With increasing the Ni content in the binary system, the oxidation and reduction peaks of the Ni(II) species dominate in the CV curves. As mentioned, in the MnPP electrodes, there is a decomposition problem of manganese species during cycling when it reaches water oxidation potentials. With the addition of Ni(II) to the Mn(II) system, this problem is almost solved without the decomposition of MnO_4^- ions. It may have a small amount of decomposition in the Mn-rich samples, but with the naked eye, it is not detected. No decomposition is observed in the nickel-rich electrodes, meaning that adding Ni(II) in a manganese system makes the electrodes more stable and robust in water oxidation reactions.

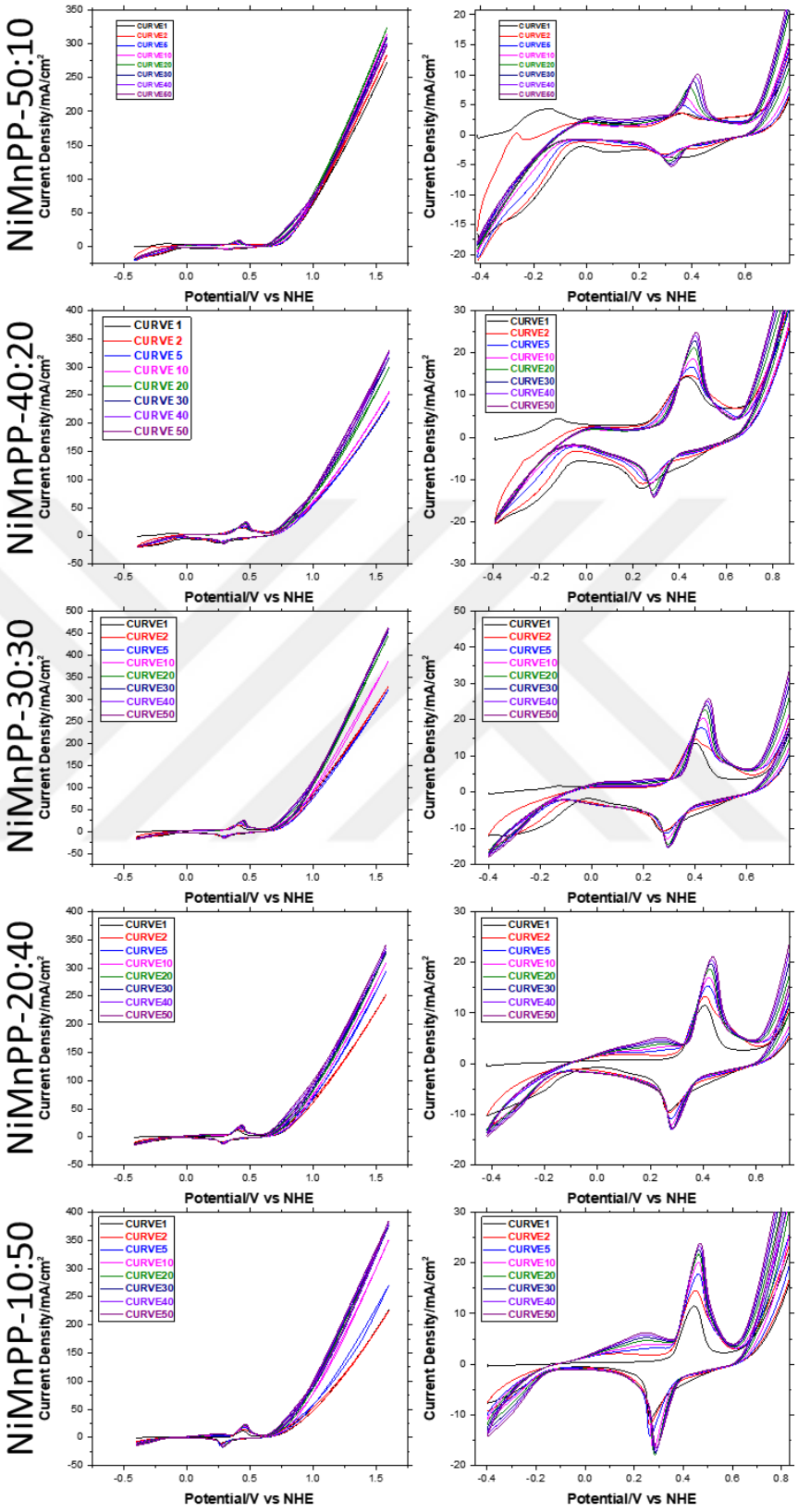

Figure 3.120: 50 CV cycles of the GR-NiMnPP-n:t-300 (n and t values are shown on the left) electrodes with a scan rate of 50 mV/s (the right column shows the zoomed plots in the oxidation-reduction region).

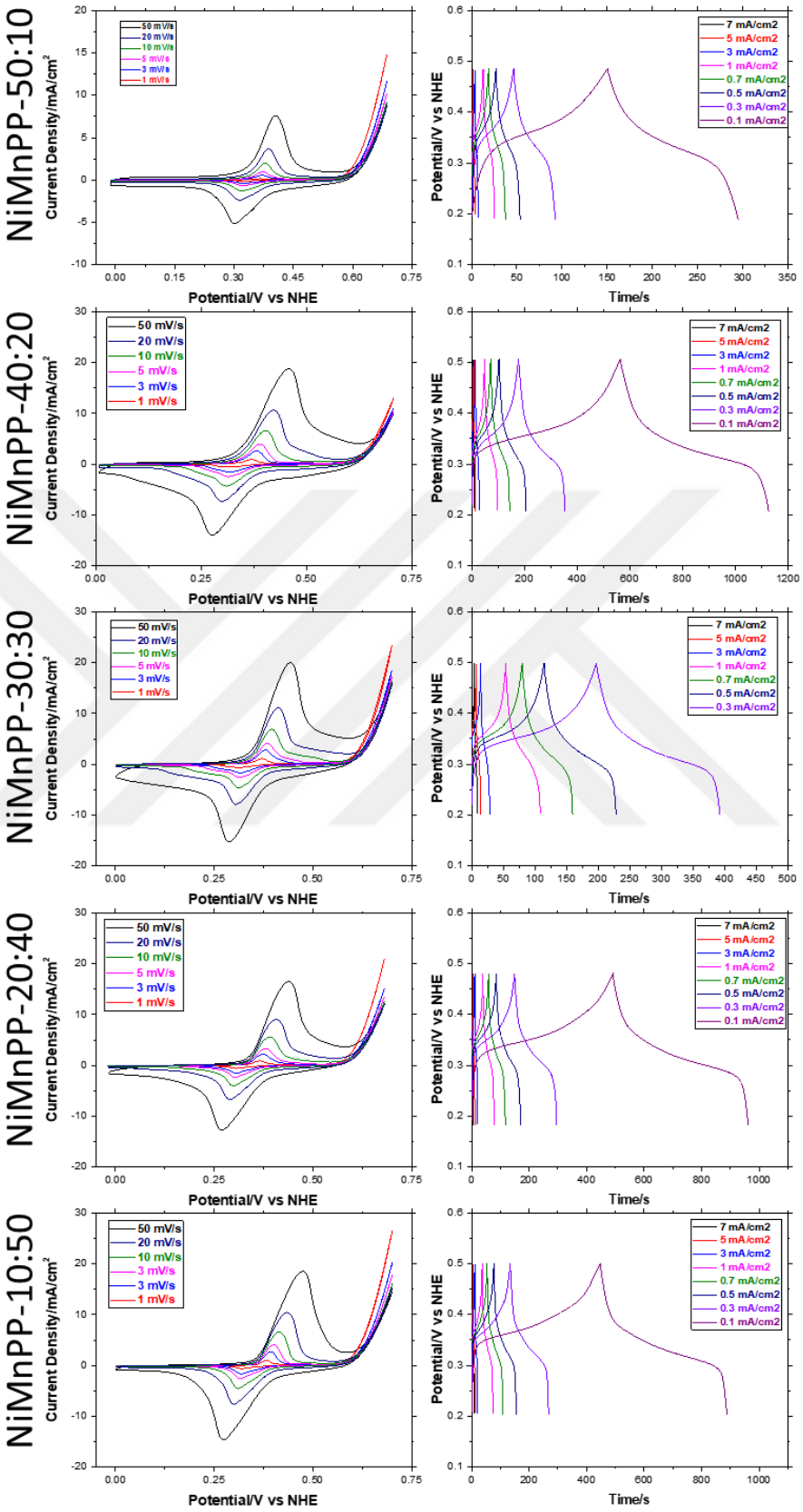

Figure 3.121: (Left column) Scan rate-dependent CV curves and (right column) GCD graphs of GR-NiMnPP-n:t-300 electrodes (n and t are indicated on the left).

The same electrodes are used to collect the CVs in a 3M KOH electrolyte solution continued to be used in the scan rate-dependent measurements and GCD cycling since the electrodes are stable in terms of decomposition. Continuing with the same electrode is important to ensure the complete transformation of pyrophosphates to the hydroxides, as discussed before. Figure 3.121 shows the scan rate-dependent CVs (left column) and GCD measurements (right column) of NiMnPP-n:t-300 electrodes. Likely in the 50 CV cycles, with the addition of the Ni(II), the oxidation and reduction peaks of Ni(II) species become dominant in the binary system. The GCD measurements start from fast to slow charging-discharging cycles at 7, 5, 3, 1, 0.7, 0.5, 0.3, and 0.1 mA/cm^2 current densities and are tabulated in Table 3.11.

The percent coulombic efficiency of each electrode in the GR-NiMnPP-n:t-300 series is calculated to compare the electrodes with varying mole ratios of the metal species, see Figure 3.122. The coulombic efficiency of the electrodes falls within the range of 90-98%. Notably, there is an increase in efficiency with the addition of nickel compared to the pure manganese system.

Table 3.11: Specific capacitance and capacity values of the electrodes calcined at indicated temperatures of the GR-NiMnPP-n:t-300 (n and t are shown on the top).

	NiMnPP-50:10		NiMnPP-40:20		NiMnPP-30:30		NiMnPP-20:40		NiMnPP-10:50	
Current Density (mA/cm^2)	Capacity ($mA{\cdot}s$)	Specific capacitance (mF/cm^2)	Capacity ($mA{\cdot}s$)	Specific capacitance (mF/cm^2)	Capacity ($mA{\cdot}s$)	Specific capacitance (mF/cm^2)	Capacity ($mA{\cdot}s$)	Specific capacitance (mF/cm^2)	Capacity ($mA{\cdot}s$)	Specific capacitance (mF/cm^2)
0.1	14.14	28.28	53.68	107.36	58.97	117.94	44.32	88.64	41.54	83.08
0.3	13.68	27.36	52.20	104.40	57.35	114.70	43.24	86.48	39.28	78.56
0.5	13.27	26.54	51.01	102.02	56.20	112.40	41.98	83.96	38.63	77.26
0.7	12.97	25.94	50.08	100.16	55.22	110.44	40.61	81.22	37.48	74.96
1	12.55	25.10	48.85	97.70	53.86	107.72	38.81	77.62	36.58	73.16
3	10.54	21.08	43.60	87.20	43.85	87.70	31.65	63.30	32.24	64.48
5	8.81	17.62	39.02	78.04	35.60	71.20	27.10	54.20	29.32	58.64
7	7.58	15.16	34.89	69.78	30.33	60.66	23.89	47.78	26.87	53.74

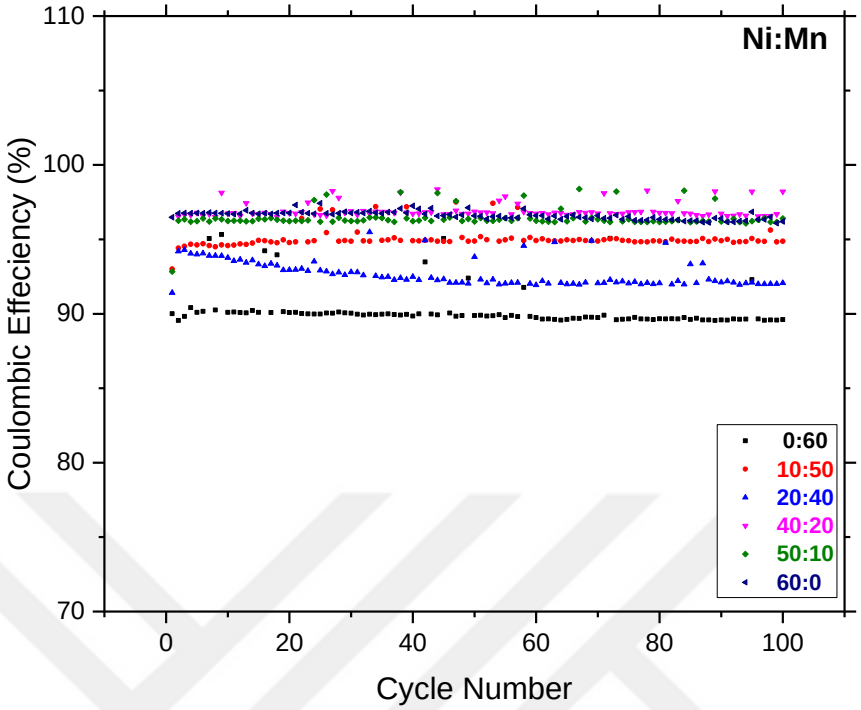

Figure 3.122: Graph of coulombic efficiencies of the GR-NiMnPP-n:t-300 electrodes (n and t are indicated on the graph) versus cycle number.

The capacity values at 0.1 mA/cm^2 current density of NiMnPP-n:t-300 electrodes are compared to pure NiPP-60-300 and MnPP-60-300 electrodes, see Figure 3.123. The higher capacity and specific capacitance values obtained in the NiCo binary system are not observed for the NiMn system. The pure Ni electrodes have almost 2-3 times higher capacity values than NiMn systems. Compared to the pure MnPP-60-300 electrode, the addition of Ni(II) to the system brings an improvement in terms of capacity values. However, the increase is not as drastic as in the NiCo system. Note also that the addition of Ni(II) to the Mn system helps to improve the stability of the electrodes during the cycling at the water oxidation potentials.

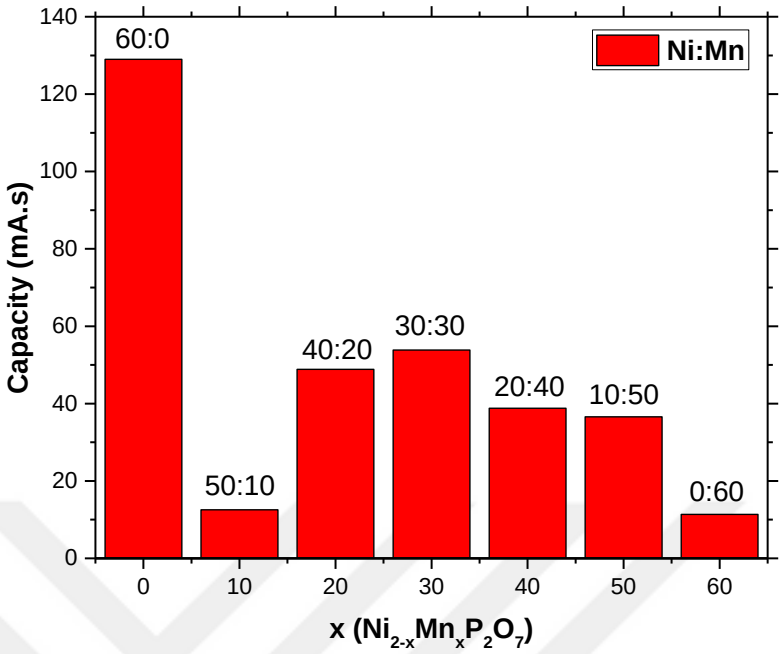

Figure 3.123: Graph of capacity values versus mole ratio of cobalt in the NiCoPP-300 electrodes.

Chapter 4

4.Conclusion

The homogeneous solutions with a broad concentration range of transition metal nitrates (namely, $[Ni(H_2O)_6](NO_3)_2$, $[Co(H_2O)_6](NO_3)_2$, and $[Mn(H_2O)_4](NO_3)_2$), pyrophosphoric acid or phosphoric acid, and P123 can be coated over glass substrate to form ordered mesophases. The mesophases obtained from PPA as a phosphate precursor form more ordered and oriented structures.

Three compositions (30, 60, and 90 as low, intermediate, and high) are selected for the Ni(II) system to investigate the solutions and their gelation further. Aging the gel-phases at room temperature produces ordered mesostructured semi-solid materials, denoted as $M_2H_xP_2O_7(NO_3)_x{\cdot}nH_2O$, through a polymerization reaction between transition metal ions and PPA. The polymerization initiates in the solution phase and continues during gelation and solidification of the mesophase. The values of x and n for the semi-solid mesostructured $M_2H_xP_2O_7(NO_3)_x{\cdot}nH_2O$ can be spectroscopically determined from their normalized ATR-FTIR spectra. The nitrate degradation from the media during the gelation and solidification process is related to water loss. The values of x and n depend on the initial composition and were determined to be 0.7 and 3.7 in the 30-mole ratio, 0.6 and 1.5 in the 60-mole ratio, and 0.3 and 1.4 in the 90-mole ratio. The compositions of the mesostructured semi-solid phase of Co(II) and Mn(II) systems are $Co_2H_{0.6}P_2O_7(NO_3)_{0.6}{\cdot}4.8H_2O$ and $Mn_2H_{0.4}P_2O_7(NO_3)_{0.4}{\cdot}3.6H_2O$. Further heating of the mesostructured semi-solid phase leads to the loss of more nitrate

and complete water removal, but complete water removal stops the nitrate degradation. However, cycling the sample between exposure to humidity and heating almost completely removes the nitrates from the sample, reducing them to 0.04 per nickel or lower. The nitrate degradation is strongly dependent on the presence of nearby water species.

The mesostructured semi-solid $M_2H_xP_2O_7(NO_3)_x \cdot nH_2O$ produces mesoporous spherical MPP particles upon calcination at 300 ^oC. The highest surface areas are 60, 111, and 41 m^2/g for the NiPP, CoPP, and MnPP, respectively, at a calcination temperature of 300 ^oC. The CoPP and MnPP crystallize at around 600 ^oC into their alpha and beta phases, respectively. The crystalline samples become bulk-like at 600 ^oC without a measurable surface area. However, the NiPP particles crystallize at around 700 ^oC with a mixed composition of mainly alpha and minimal delta NiPP phases while retaining their mesoporous structure.

The homogeneous solutions can be spin-coated over an FTO substrate or dip-coating onto a graphite rod and calcined at various temperatures to fabricate FTO-MPP or GR-MPP electrodes. However, the FTO-coated electrodes are not stable during the electrochemical process; the samples on the FTO tend to detach and fall into the electrolyte solution. In contrast, the GR-coated electrodes are robust and remain stable on the graphite surface even during long-time electrochemical measurements.

However, during the electrochemical measurements in 3M KOH electrolyte solution, the electrodes undergo a transformation from MPP to $M(OH)_2$. It is important to note that this transformation is not an electrochemical process; instead, it is a chemical process. The conversion of NiPP to $Ni(OH)_2$ occurs slowly, resulting in the formation of ultra-thin β-$Ni(OH)_2$ nanoflakes. In contrast, the transformation process for the CoPP and MnPP is very rapid. In the case of NiPP, the fast nucleation step follows a slow growth, whereas the nucleation is slow, and growth is fast in the CoPP and MnPP. Fast growth results in large plate-like particles for the beta cobalt and manganese hydroxides. The tiny (1.5 nm thick and 7 nm wide) needle/flake-like particles of β-$Ni(OH)_2$ are formed after the transformation of NiPP by preserving the spherical morphology that displays high capacity (varies between 102 and 177 $mA \cdot s/cm^2$) and specific capacitance (ranges between 340 and 590 mF/cm^2) at all temperatures. The crystalline electrodes are more robust against transformation. The

process is slow and further slows down for the crystalline NiPP samples. To highlight the difference in transformation between amorphous and crystalline phases, the K_{sp} values for both phases of NiPP are calculated using the oxidation and reduction peaks of $Ni(OH)_2$, which only appear only in the basic electrolyte. These values are $3.45x10^{-29}$ and $1.42x10^{-29}$ M^3 for amorphous and crystalline phases, respectively, determining the transformation rate. In contrast, the CoPP and MnPP electrodes exhibit almost identical CVs and GCD curves within their respective sets, regardless of the annealing temperatures. The capacity and specific capacitance values are almost 10 times lower than those of the Ni(II) systems.

The redox process of Ni(II) species is diffusion-controlled. The $Ni(OH)_2$ (Ni^{2+}) species oxidize to NiOOH (Ni^{3+}) in the first oxidation peak and may further oxidize to NiO_2 (Ni^{4+}) during the water oxidation process. However, the redox process of Co(II) species is surface-controlled.

In contrast, the MnPP electrodes behave differently from the NiPP and CoPP electrodes. There is an issue with the decomposition of the MnPP electrode during the CV measurements at high positive potentials. Permanganate (MnO_4^-) ions leach out from the electrode surface during the measurements and decompose to manganate (MnO_4^{2-}) ions, which further decompose to MnO_2 (brown solids) at the bottom of the electrochemical cell. However, the capacity measurements can be performed using the electrodes at lower potentials without reaching the water oxidation potentials.

The mixed metal (binary metals like MnCo and NiCo) systems can also be prepared and investigated to demonstrate the synergistic effect of having two metals on the mesophase formation and electrochemical analysis. The mesophases and mesostructured semi-solid phases display similar behaviors to their pure MPP phases. The mesostructured semi-solid produces mesoporous amorphous spherical MnCoPP and NiCoPP particles with surface areas of 70 and 68 m^2/g, respectively. The MnCoPP and NiCoPP samples crystallize into their beta and alpha phases at around 600 ^oC, respectively. The electrodes of MnCoPP and NiCoPP can be fabricated on both FTO substrates by spin-coating and GR by dip-coating of the initial solutions, followed by calcination. However, the FTO-coated electrodes are unstable (they washed out from the FTO surface). The GR-MnCoPP and GR-NiCoPP electrodes remain stable and robust at all annealing temperatures. The capacity and specific capacitance values are

almost identical to their pure phases. However, the addition of Co(II) to the Mn(II) systems makes the electrodes more stable with respect to the decomposition of permanganate ions during the measurements. Adding Ni(II) to the Co(II) system enhances the capacity and specific capacitance values compared to their pure pyrophosphate phases. The GR-NiCoPP-40:20-300 (more correctly $Ni_{0.67}Co_{0.33}(OH)_2$) electrode exhibits the highest capacity (170 mA·s/cm^2) and specific capacitance (309 mF/cm^2); they are 30 % higher than the GR-NiPP values. The mixing of Co and Ni makes a solid-solution of $Ni_xCo_{2-x}P_2O_7$. However, the transformation process produces individual $Ni(OH)_2$ and $Co(OH)_2$ particles. Lastly, adding Ni(II) to the Mn(II) system does not improve its capacitive properties; both contribute to reducing the decomposition of manganese species and maintaining their stability during measurements.

Chapter 5

5.Future Recommendations

Up to now, only water has been used as a solvent during the preparation of solutions for the synthesis of mesoporous metal pyrophosphates (MPP). A more volatile media was also tested to investigate the effect of the solvent on the synthesis of the MPPs using different types of alcohol. The difference between water and alcohol media starts while they are in the solution phases and ends up with having predominantly film-like morphology in the mesoporous MPPs. Using water as a solvent produces a homogeneous clear solution, which can stay clear for a very long time. On the contrary, the same ingredients result in a cloudy solution in the volatile medium for both phosphoric and pyrophosphoric acid systems, see Figure 5.1. The solution behaviors differ in different alcohols. In tert-butanol, trifluoroethanol, and 2-propanol, the cloudiness forms immediately (not shown); however, it takes about 10 mins to become a heterogeneous solution in ethanol and methanol. This change could be related to the acidities of alcohols that increase in the following order: tertiary, secondary, and primary alcohols and affect the precipitation reaction. [157]

All the ingredients are easily soluble in the ethanol solution, and the solution remains clear for 10 minutes. For the mesophase, the clear and cloudy solutions are analyzed separately to see the effect of the reaction in the solution phase. Both clear and cloudy solutions are spin-coated on a glass slide to obtain their gel phase and analyzed using small-angle XRD measurements. The gel-like precipitate is collected

by centrifugation and then spread over a glass substrate as smoothly as possible to collect its XRD pattern. The films obtained from the clear solution have no diffractions in the small-angle XRD pattern, but the main diffraction line may be below 1°, 2θ, see Figure 5.2a. The film obtained from the cloudy solution has a very weak broad diffraction line between 1 and 5°, 2θ, that may be due to the second line (200) having the main diffraction line (100) below 1°, 2θ, similar to the film obtained from the clear solution, see Figure 5.2c. The gel-like precipitate also shows the same trend (Figure 5.2b). However, the supernatant has a more orientated mesophase compared to the clear and cloudy solutions, with an obvious diffraction line at around 1.75°, 2θ, see Figure 5.2d. This diffraction line is shifting from 1.75 to 1.52°, 2θ while aging at RT, showing an expansion of the unit cell of the mesophase. The trend in the XRD patterns is similar for the mesophases prepared from methanol solutions (not shown). However, for the other alcohols (2-propanal, tert-butanol, and trifluoroethanol), there are some solubility problems that need to be studied more.

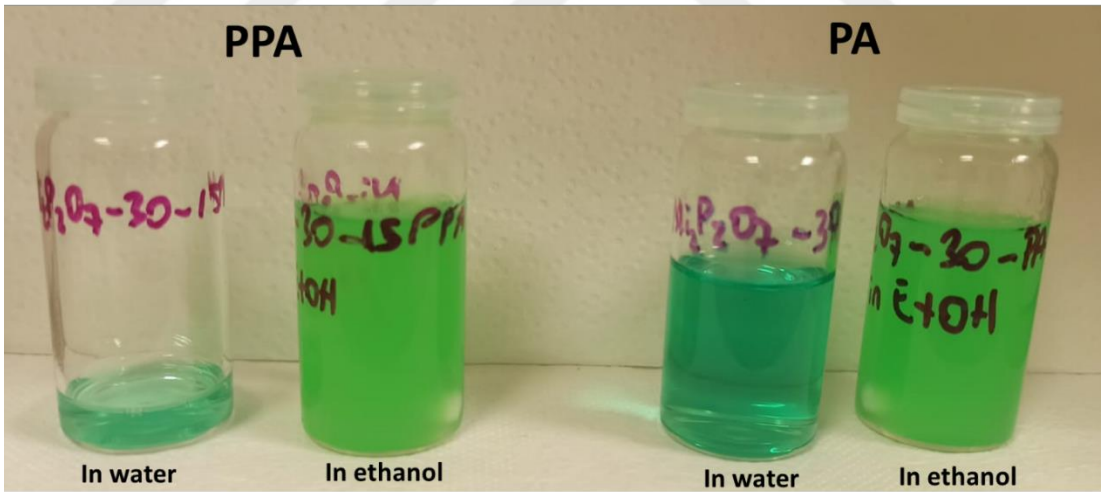

Figure 5.1: The photographs of NiPP-30 solutions prepared by PA and PPA in water and ethanol.

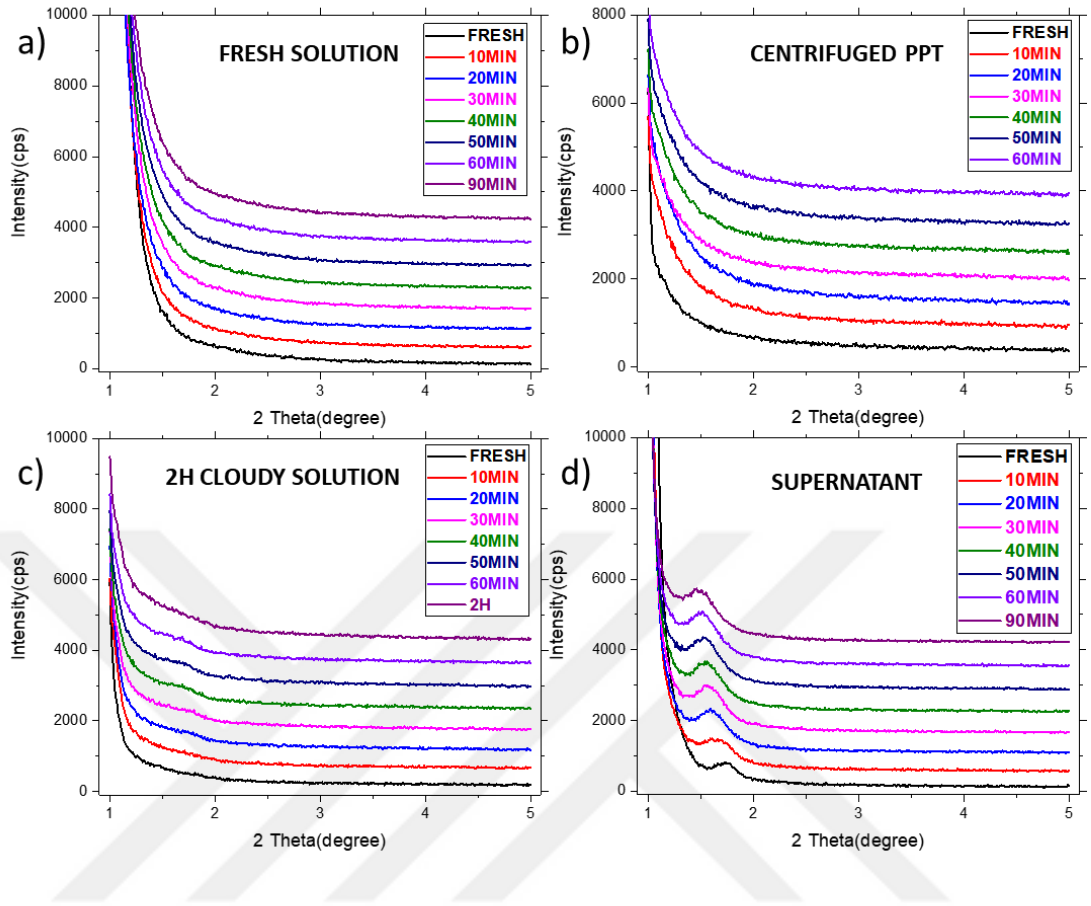

Figure 5.2: Small-angle XRD patterns of NiPP in ethanol, a) as prepared, c) cloudy, b) after centrifugation precipitate, and d) supernatant.

The difference between the gel-like precipitate and the supernatant obtained after centrifugation is also used to collect ATR-FTIR spectra from ethanol and methanol cloudy solutions. Figure 5.3 shows the differences between gel-like precipitate and supernatant parts aged on the ATR diamond for 3 h under ambient conditions. The peaks at around 3600-3000 and 1640 cm^{-1} originate from the stretching and bending modes of water species. The intensities of peaks at around 3000 - 2750 cm^{-1} are due to the surfactant (C-H stretching), which is displayed in both gel-like precipitate and supernatant parts for both ethanol and methanol solutions. Since they are not normalized spectra, it is hard to compare the amounts of surfactant. The 1500-1250 cm^{-1} region consists of nitrate and surfactant (bending mode of C-H). In 3 h aging, most of the nitrate species are removed from the media with the polymerization reaction observed and discussed in the water solutions. The removal of the nitrate species is more in the methanol compared to the ethanol solutions. Note also that the

nitrate amounts are more in the supernatant parts in ethanol and methanol cases. The peaks at around 1200-800 cm^{-1} result from the phosphate species, and there is a distinct structural difference for the phosphate species between the precipitate and supernatant parts. Moreover, the peak at around 750 cm^{-1} originated from the P-O-P symmetric stretching and is only visible with the gel-like precipitation. Clearly, the supernatant has more surfactant and nitrate upon gelation, prepared from both ethanol and methanol solutions. However, the precipitates also have surfactant with a highly reduced nitrate. Notice also that the higher intensity on the low energy side of the C-H stretching peaks originates from free surfactant, which is apparent in the gel of the supernatants.

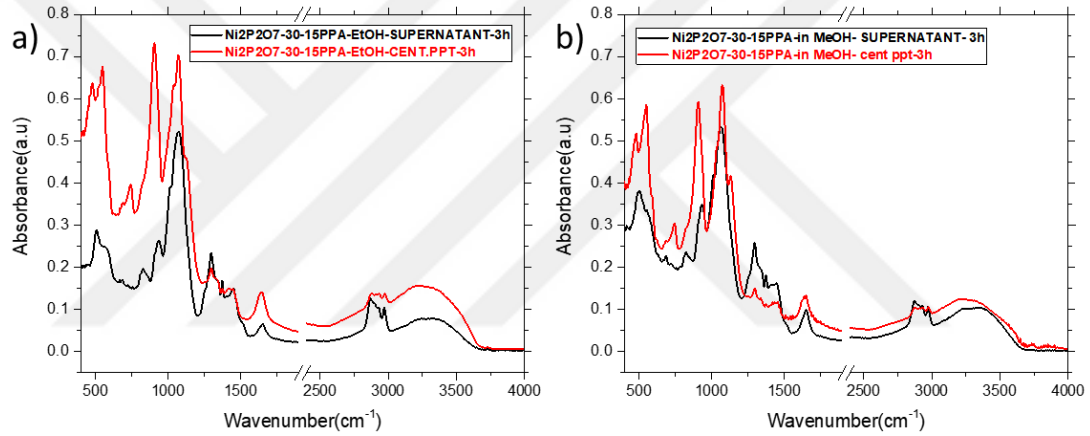

Figure 5.3: ATR-FTIR spectra of gel-like precipitates and supernatant of NiPP-30 prepared in a) ethanol and b) methanol after aging 3 h at RT.

The spin-coated clear and cloudy solutions and gel-like precipitate prepared in ethanol and methanol solutions are calcined at 300 ^{o}C to produce mesoporous NiPP-30. The SEM images of those samples are collected to observe the morphologies of the NiPP-30 sample. Figures 5.4 and 5.5 show that the film morphology is obtained with the samples prepared from ethanol solutions, fresh (clear) solution, cloudy solution, and gel-like precipitate, and from the methanol solutions with the clear and cloudy solutions. A different morphology (flake-like) is observed from the gel-like precipitate of methanol solution after calcination, see Figures 5.5e and f.

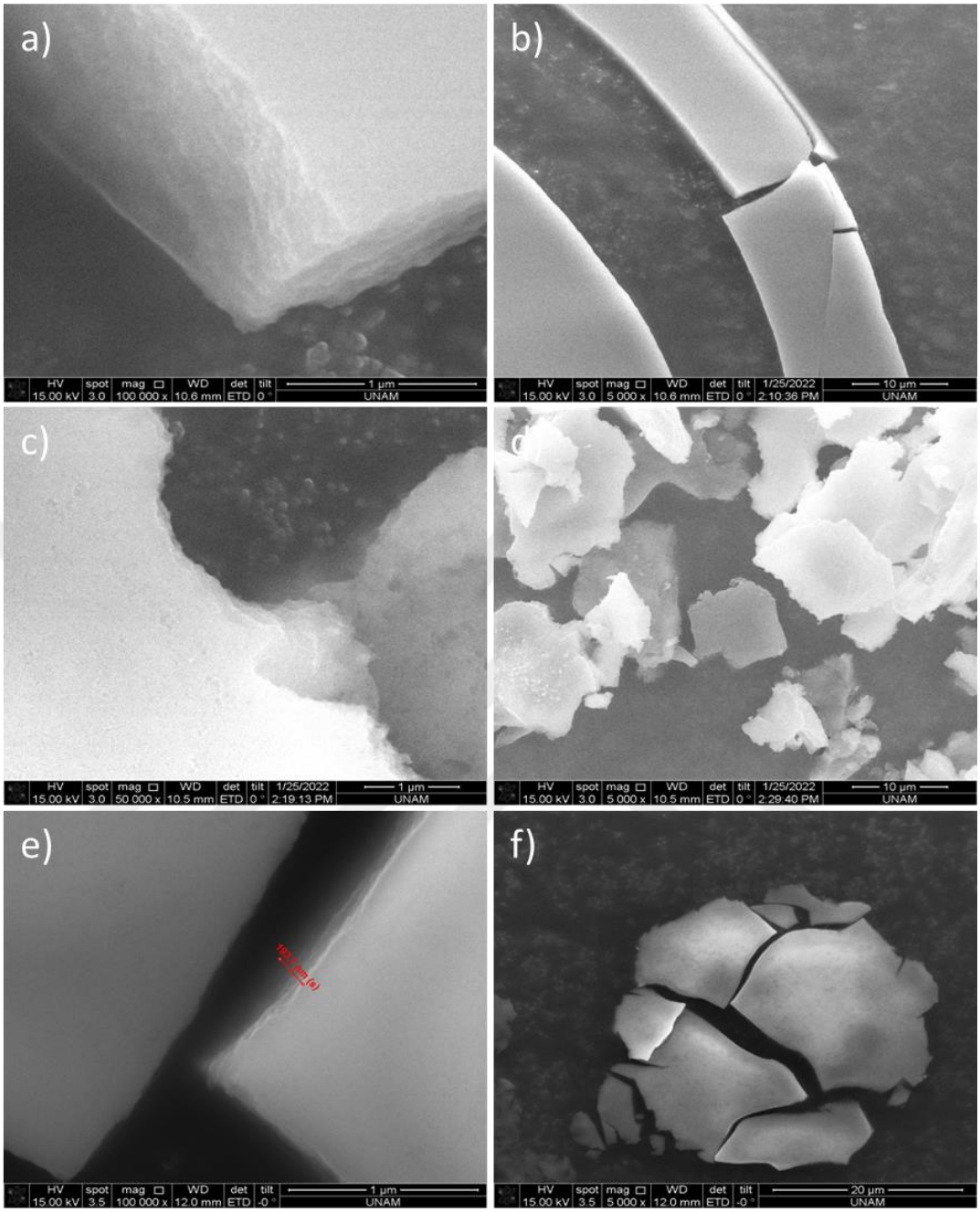

Figure 5.4: SEM images of the NiPP-30 samples, prepared in ethanol a) and b) from clear solution, c) and d) from cloudy solution, and e) and f) from gel-like precipitates calcined at 300 ºC, the scale bars are 1 μm, 10 μm, 1 μm, 10 μm, 1 μm, and 20 μm, respectively.

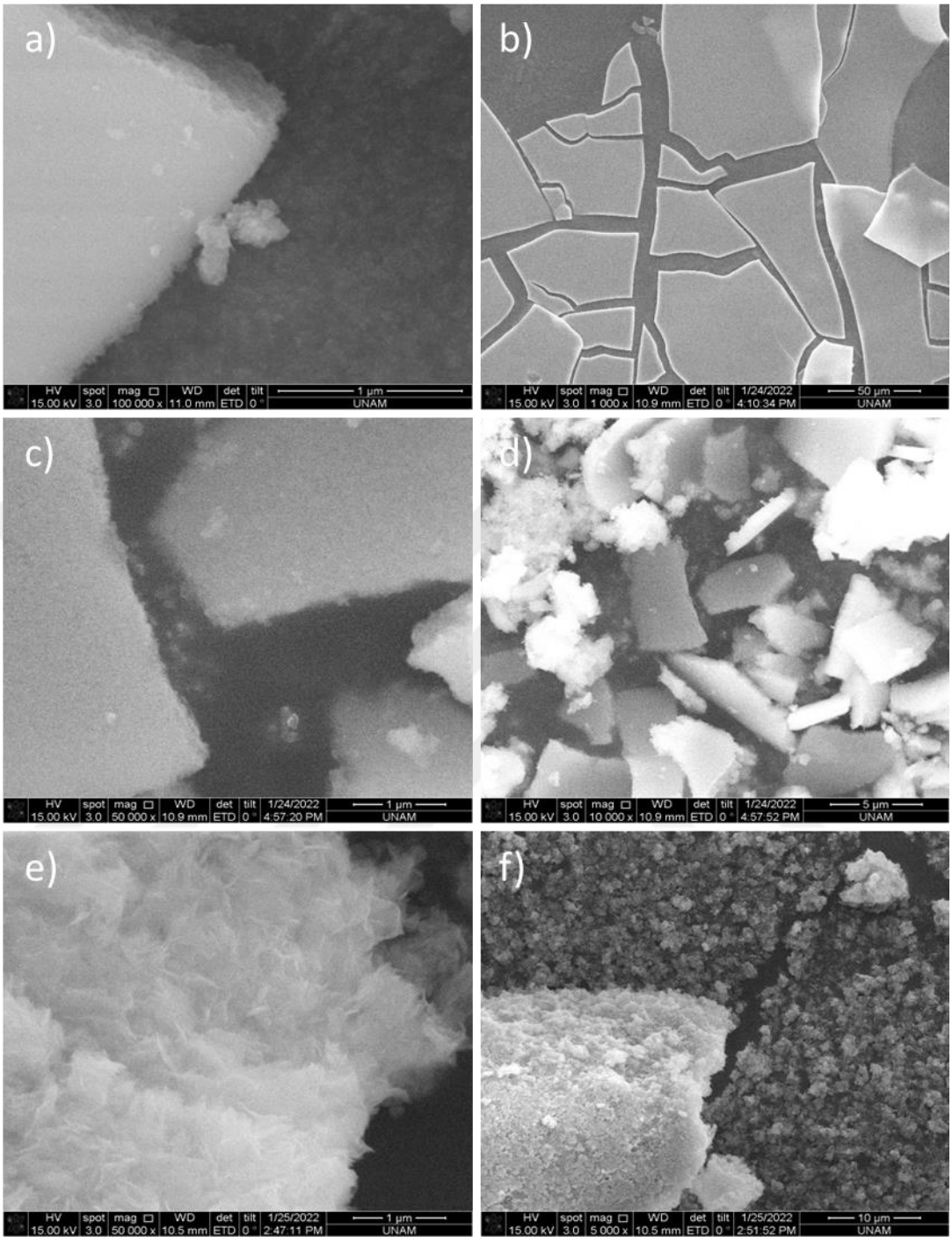

Figure 5.5: SEM images of the NiPP-30 samples, prepared in methanol a) and b) from clear solution, c) and d) from cloudy solution, and e) and f) from gel-like precipitates calcined at 300 ^{o}C, the scale bars are 1 μm, 50 μm, 1 μm, 5 μm, 1 μm, and 10 μm, respectively

The effect of the solvent is also tested on the synthesis of CoPP materials. After mixing all ingredients in ethanol, the cloudy solution forms faster for the CoPP case. The gel-like precipitate is collected by centrifugation prior to measurements. The spin-coated supernatant and gel-like precipitate are calcined at 300 °C, and TEM images of those samples are gathered to investigate the morphological change. They both display film morphology similar to the NiPP case, see Figure 5.6.

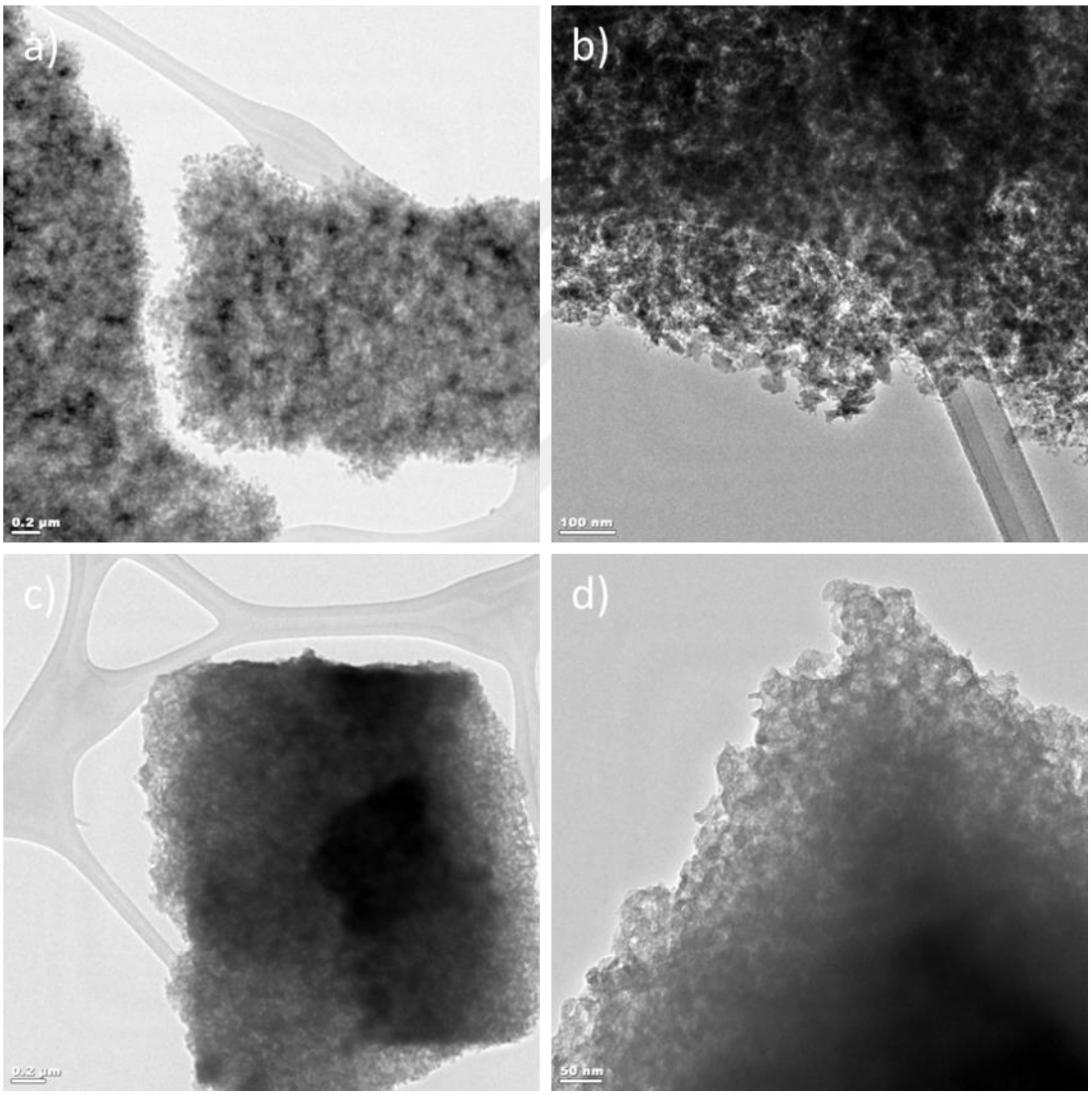

Figure 5.6: TEM images of the CoPP-30 samples, prepared in ethanol a) and b) from the supernatant, and c) and d) from gel-like precipitates calcined at 300 °C, the scale bars are 200, 100, 200, and 50 nm, respectively.

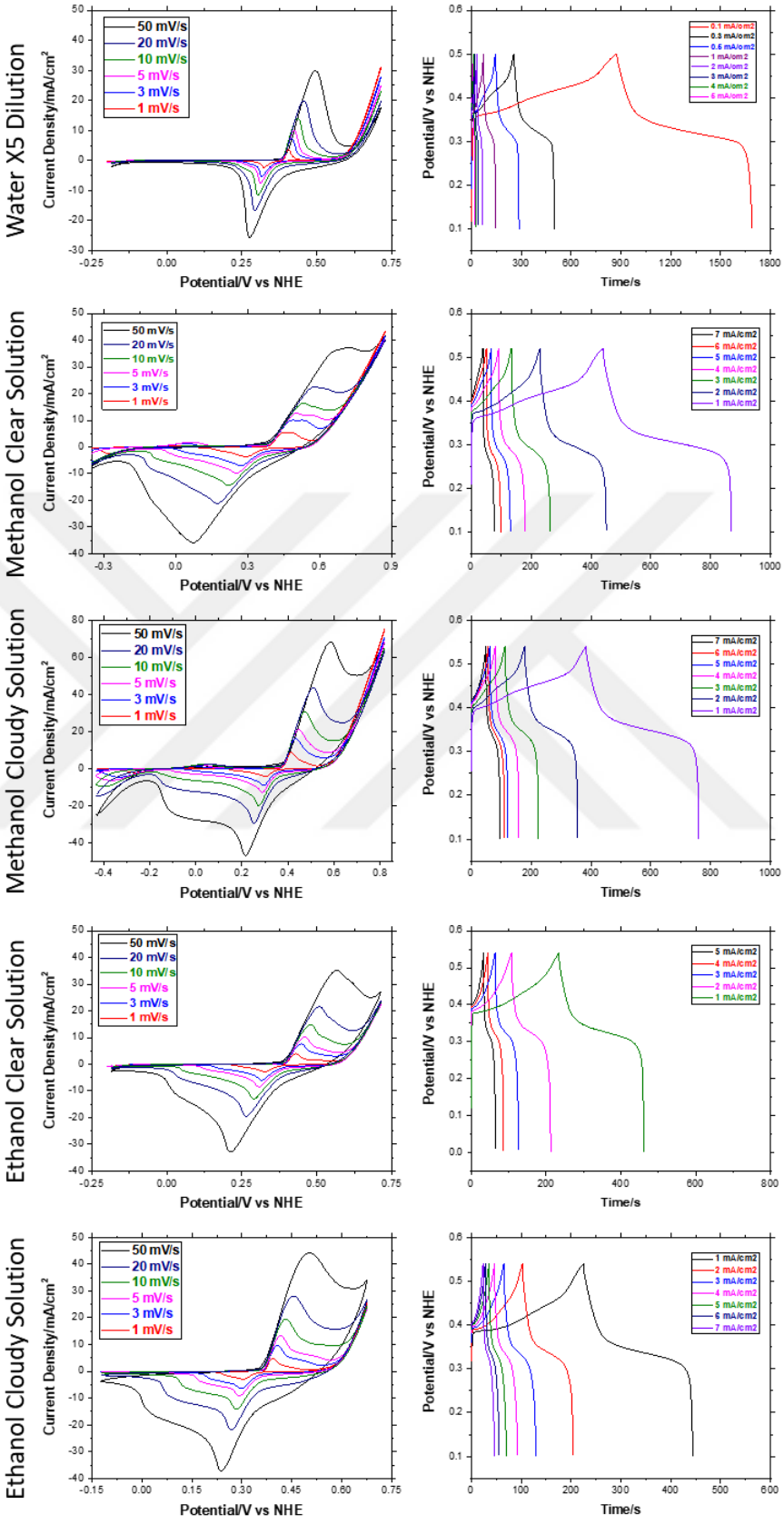

Figure 5.7: (Left column) Scan rate-dependent CV curves and (right column) GCD graphs of GR-NiPP-300 electrodes (Solvents are indicated on the left).

The electrochemical performances are also tested for the mesoporous nickel pyrophosphate samples prepared in volatile media and compared with those prepared in water. Remember that, for the water case, it is necessary to dilute the mother liquor prior to coating on the graphite rods (GR). The samples prepared in ethanol and methanol give thinner films on the GR after coating; therefore, the measurements are performed without dilution. The same procedure is followed during the electrochemical measurements; firstly, 50 cycles of CVs are collected (not shown), then, with the same electrode scan rate-dependent CVs are recorded to find out the proper range for the charge-discharge cycles, and finally, GCD curves are run with the 3-electrode system in 3M KOH solution, see Figure 5.7. Remember that the electrodes in alkali media are not stable; they undergo a transformation reaction. The same reaction takes place for the samples prepared in alcohol media, as evidenced by almost the same redox behavior in the CVs. Some minor changes can be originated from morphological differences. Note also that the scan rate-dependent analysis provides an information about the catalytically active sides or the mechanism of the redox reaction (for example, diffusion-controlled). The behavior observed in the NiPP sample from the water media is identical to that from the alcohol media (not shown).

The specific capacitance values are reported in Table 5.1. According to calculated specific capacitance values, the samples prepared in alcohol media have higher capacitance values than the samples prepared in a water environment. First, it can be thought that it is related to the dilution of water solution, but the current densities of oxidation peaks at the same scan rate CVs are very similar to each other (about 40 mA/cm^2 for 50 mV/s), see Figure 5.7. Among the alcohols, the sample synthesized from a clear methanol solution shows the highest capacitance values.

Table 5.1: Specific capacitance and capacity values of the electrodes calcined at indicated temperatures of the GR-NiPP-300 (Solvents are shown on the top).

	Water X5 Dilution		Methanol Clear		Methanol Cloudy		Ethanol Clear		Ethanol Cloudy	
Current Density (mA/cm^2)	Capacity (mA.s)	Specific capacitance (mF/cm^2)	Capacity (mA.s)	Specific capacitance (mF/cm^2)	Capacity (mA.s)	Specific capacitance (mF/cm^2)	Capacity (mA.s)	Specific capacitance (mF/cm^2)	Capacity (mA.s)	Specific capacitance (mF/cm^2)
1	102	368	478	1138	375	853	226	418	218	496
2	93	362	441	1049	351	797	209	388	201	458
3	85	358	392	933	333	757	184	342	192	436
4	80	368	357	849	314	715	170	314	183	416
5	76	377	323	770	304	690	155	288	174	396

Bibliography

[1] L. B. McCusker, F. Liebau, and G. Englehardt, “Nomenclature of Structural and Compositional Characteristics of Ordered Microporous and Mesoporous Materials with Inorganic Hosts (IUPAC Recommendations 2001): Physical Chemistry Division Commision on Colloid and Surface Chemistry Including Catalysis,” *Microporous Mesoporous Mater.*, vol. 58, no. 1, pp. 3–13, 2003, doi: 10.1016/S1387-1811(02)00545-0.

[2] L. B. McCusker, F. Liebau, and G. Engelhardt, “Commossion on Colloid and Surface Chemistry Including Catalysis Nomenclature of Structural and Compositional Characteristics of Ordered Microporous and Mesoporous Materials with Inorganic Hosts,” *Pure Appl. Chem.*, vol. 73, no. 2, pp. 381–394, 2001.

[3] W. Li and D. Zhao, “An Overview of the Synthesis of Ordered Mesoporous Materials,” *Chem. Commun.*, vol. 49, no. 10, pp. 943–946, 2013, doi: 10.1039/c2cc36964h.

[4] K. C. Yanagisawa Tsuneo, Shimizu Toshio, Kuroda Kazuyuki, “The Preparation of Alkyltriinethylaininonium–Kaneinite Complexes and Their Conversion to Microporous Materials,” *Chem. Soc. Japan*, vol. 63, no. 4, pp. 988–992, 1990.

[5] W. J. R. C. T. Kresge, M. E. Leonowicz and J. C. V. & J. S. Beckt, “Ordered Mesoporous Molecular Sieves Synthesized by a Liquid Crystal Template Mechanism,” *Nature*, vol. 359, pp. 710–712, 1992.

[6] J. S. Beck *et al.*, “A New Family of Mesoporous Molecular Sieves Prepared with Liquid Crystal Templates,” *J. Am. Chem. Soc.*, vol. 114, no. 27, pp. 10834–10843, 1992, doi: 10.1021/ja00053a020.

[7] A. Monnier *et al.*, “Cooperative Formation of Inorganic-Organic Interfaces in the Synthesis of Silicate Mesostructures,” *Science (80-.).*, vol. 261, no. 5126, pp. 1299–1303, 1993, doi: 10.1126/science.261.5126.1299.

[8] P. Behrens, “Mesoporous Inorganic Solids,” *Adv. Mater.*, vol. 5, no. 2, pp. 127–132, 1993, doi: 10.1002/adma.19930050212.

[9] Q. Huo *et al.*, “Generalized Synthesis of Periodic Surfactant/Inorganic Composite Materials,” *Nature*, vol. 368, no. 6469, pp. 317–321, 1994, doi: 10.1038/368317a0.

[10] S. Inagaki, Y. Fukushima, and K. Kuroda, “Synthesis of Highly Ordered Mesoporous Materials from a Layered Polysilicate,” *J. Chem. Soc. Chem. Commun.*, pp. 680–682, 1993, doi: 10.1039/C39930000680.

[11] P. T. Tanev and T. J. Pinnavaia, “Mesoporous Silica Molecular Sieves Prepared by Ionic and Neutral Surfactant Templating: A Comparison of Physical Properties,” *Chem. Mater.*, vol. 8, no. 8, pp. 2068–2079, 1996, doi: 10.1021/cm950549a.

[12] J. C. G. & C. G. G. George S. Attard, “Liquid-Crystalline Phases as Templates for the Synthesis of Mesoporous Silica,” *Nature*, vol. 378, pp. 366–368, 1995.

[13] H. Yang, N. Coombs, I. Sokolov, and G. A. Ozin, “Free-Standing and Oriented Mesoporous Silica Films Grown at the Air-Water Interface,” *Nature*, vol. 381, no. 6583. pp. 589–592, 1996, doi: 10.1038/381589a0.

[14] Ö. Dag, A. Verma, G. A. Ozin, and C. T. Kresge, “Salted Mesostructures: Salt-Liquid Crystal Templating of Lithium Triflate-Oligo(Ethylene Oxide) Surfactant-Mesoporous Silica Nanocomposite Films and Monoliths,” *J. Mater. Chem.*, vol. 9, pp. 1475–1482, 1999, doi: 10.1039/a900955h.

[15] T. Asefa, M. J. MacLachlan, N. Coombs, and G. A. Ozin, “Periodic mesoporous organosilicas with organic groups inside the channel walls,” *Nature*, vol. 402, pp. 867–871, 1999, doi: 10.1038/47229.

[16] J. Y. J. D.M. Antonelli, “Synthesis of Hexagonally Packed Mesoporous TiO, by a Modified Sol-Gel Method,” *Angw. Chem. lnr. Ed. Engl.*, vol. 34, no. 18, pp. 2014–2017, 1995.

[17] I. Karakaya, F. Karadas, B. Ulgut, and Ö. Dag, “Modification of Mesoporous $LiMn_2O_4$ and $LiMn_{2-x}Co_xO_4$ by SILAR Method for Highly Efficient Water

Oxidation Electrocatalysis," *Adv. Mater. Technol.*, vol. 5, no. 8, p. 2000353, 2020, doi: 10.1002/admt.202000353.

[18] A. Amirzhanova, N. Akmanşen, I. Karakaya, and Ö. Dag, "Mesoporous $MnCo_2O_4$, $NiCo_2O_4$, and $ZnCo_2O_4$Thin-Film Electrodes as Electrocatalysts for the Oxygen Evolution Reaction in Alkaline Solutions," *ACS Appl. Energy Mater.*, vol. 4, no. 3, pp. 2769–2785, 2021, doi: 10.1021/acsaem.1c00064.

[19] D. M. Antonelli and M. Trudeau, "Phase Changes and Electronic Properties in Toroidal Mesoporous Molybdenum Oxides," *Angew. Chemie - Int. Ed.*, vol. 38, pp. 1471–1475, 1999, doi: 10.1002/(SICI)1521-3773(19990517)38:10<1471::AID-ANIE1471>3.0.CO;2-R.

[20] J. K. A. Dapaah, Y. Uemichi, A. Ayame, H. Matsuhashi, and M. Sugioka, "Activity Enhancement of Mesoporous Silica (FSM-16) by Modification with Iron (II) Sulphate for the Isomerization of 1-Butene," *Appl. Catal. A Gen.*, vol. 187, no. 1, pp. 107–113, 1999, doi: 10.1016/S0926-860X(99)00205-7.

[21] B. Tian *et al.*, "Self-Adjusted Synthesis of Ordered Stable Mesoporous Minerals by Acid-Base Pairs," *Nat. Mater.*, vol. 2, pp. 159–163, 2003, doi: 10.1038/nmat838.

[22] I. Uzunok *et al.*, "Lyotropic Liquid Crystalline Mesophases Made of Salt-Acid-Surfactant Systems for the Synthesis of Novel Mesoporous Lithium Metal Phosphates," *Chempluschem*, vol. 84, no. 10, pp. 1544–1553, 2019, doi: 10.1002/cplu.201900435.

[23] E. Tunkara and Ö. Dag, "Salt-Acid-Surfactant Lyotropic Liquid Crystalline Mesophases: Synthesis of Highly Transparent Mesoporous Calcium Hydroxyapatite Thin Films," *Eur. J. Inorg. Chem.*, vol. 2016, no. 13–14, pp. 2114–2121, 2016, doi: 10.1002/ejic.201501116.

[24] A. S. Nugraha *et al.*, "Symmetry-Breaking Plasmonic Mesoporous Gold Nanoparticles with Large Pores," *Chem. Mater.*, vol. 34, no. 16, pp. 7256–7270, 2022, doi: 10.1021/acs.chemmater.2c01125.

[25] A. Amirzhanova *et al.*, "Synthesis and Water Oxidation Electrocatalytic and Electrochromic Behaviours of Mesoporous Nickel Oxide Thin Film

Electrodes," *J. Mater. Chem. A*, vol. 7, no. 38, pp. 22012–22020, 2019, doi: 10.1039/c9ta07693j.

[26] I. Ulu, B. Ulgut, and Ö. Dag, "Fabrication of Mesoporous Nickel Pyrophosphate Electrodes and Their Transformation to Nickel Hydroxide with High Capacitance in Alkali Media," *Submitted.*, 2023.

[27] P. V Braun, P. Osenar, and S. I. Stupp, "Semiconducting Superlattices Templated by Molecular Assemblies," *Nature*, vol. 380, pp. 325–328, 1996.

[28] Y. Türker, C. Karakaya, and Ö. Dag, "Fabrication of Mesoporous Metal Chalcogenide Nanoflake Silica Thin Films and Spongy Mesoporous CdS and CdSe," *Chem. - A Eur. J.*, vol. 18, no. 12, pp. 3695–3705, 2012, doi: 10.1002/chem.201102643.

[29] R. Ryoo, S. H. Joo, and S. Jun, "Synthesis of Highly Ordered Carbon Molecular Sieves via Template-Mediated Structural Transformation," *J. Phys. Chem. B*, vol. 103, no. 37, pp. 7743–7746, 1999, doi: 10.1021/jp991673a.

[30] H. Wang *et al.*, "Shape- and Size-Controlled Synthesis in Hard Templates: Sophisticated Chemical Reduction for Mesoporous Monocrystalline Platinum Nanoparticles," *J. Am. Chem. Soc.*, vol. 133, no. 37, pp. 14526–14529, 2011, doi: 10.1021/ja2058617.

[31] A. Stein, F. Li, and N. R. Denny, "Morphological Control in Colloidal Crystal Templating of Inverse Opals, Hierarchical Structures and Shaped Particles," *Chem. Mater.*, vol. 20, no. 3, pp. 649–666, 2008, doi: 10.1021/cm702107n.

[32] W. C. Li, A. H. Lu, C. Weidenthaler, and F. Schüth, "Hard-Templating Pathway to Create Mesoporous Magnesium Oxide," *Chem. Mater.*, vol. 16, no. 26, pp. 5676–5681, 2004, doi: 10.1021/cm048759n.

[33] H. Kim and J. Cho, "Hard Templating Synthesis of Mesoporous and Nanowire SnO_2 Lithium Battery Anode Materials," *J. Mater. Chem.*, vol. 18, no. 7, pp. 771–775, 2008, doi: 10.1039/b714904b.

[34] Z. Zhang, F. Zuo, and P. Feng, "Hard Template Synthesis of Crystalline Mesoporous Anatase TiO_2 for Photocatalytic Hydrogen Evolution," *J. Mater.*

Chem., vol. 20, no. 11, pp. 2206–2212, 2010, doi: 10.1039/b921157h.

[35] C. R. Martin, "Nanomaterials : A Membrane-Based Synthetic Approach," *Science (80-.).*, vol. 266, 1994.

[36] T. Waitz, M. Tiemann, P. J. Klar, J. Sann, J. Stehr, and B. K. Meyer, "Crystalline ZnO with an Enhanced Surface Area Obtained by Nanocasting," *Appl. Phys. Lett.*, vol. 90, no. 12, 2007, doi: 10.1063/1.2713872.

[37] J. Roggenbuck, H. Schäfer, T. Tsoncheva, C. Minchev, J. Hanss, and M. Tiemann, "Mesoporous CeO_2: Synthesis by Nanocasting, Characterisation and Catalytic Properties," *Microporous Mesoporous Mater.*, vol. 101, no. 3, pp. 335–341, 2007, doi: 10.1016/j.micromeso.2006.11.029.

[38] J. Roggenbuck, G. Koch, and M. Tiemann, "Synthesis of Mesoporous Magnesium Oxide by CMK-3 Carbon Structure Replication," *Chem. Mater.*, vol. 18, no. 17, pp. 4151–4156, 2006, doi: 10.1021/cm060740s.

[39] K. Zhu, B. Yue, W. Zhou, and H. He, "Preparation of Three-Dimensional Chromium Oxide Porous Single Crystals Templated by SBA-15," *Chem. Commun.*, no. 1, pp. 98–99, 2003, doi: 10.1039/b210065g.

[40] Y. J. Han, J. M. Kim, and G. D. Stucky, "Preparation of Noble Metal Nanowires using Hexagonal Mesoporous Silica SBA-15," *Chem. Mater.*, vol. 12, no. 8, pp. 2068–2069, 2000, doi: 10.1021/cm0010553.

[41] B. Tian *et al.*, "General Synthesis of Ordered Crystallized Metal Oxide Nanoarrays Replicated by Microwave-Digested Mesoporous Silica," *Adv. Mater.*, vol. 15, no. 16, pp. 1370–1374, 2003, doi: 10.1002/adma.200305211.

[42] F. Jiao, K. M. Shaju, and P. G. Bruce, "Synthesis of Nanowire and Mesoporous Low-Temperature $LiCoO_2$ by a Post-Templating Reaction," *Angew. Chemie*, vol. 117, no. 40, pp. 6708–6711, 2005, doi: 10.1002/ange.200501663.

[43] J. Jang and J. Bae, "Fabrication of Mesoporous Polymer using Soft Template Method," *Chem. Commun.*, vol. 1, no. 9, pp. 1200–1202, 2005, doi: 10.1039/b416518g.

[44] C. Avci *et al.*, "Molten Salt Assisted Self Assembly (MASA): Synthesis of

Mesoporous Metal Titanate ($CoTiO_3$, $MnTiO_3$, and $Li_4Ti_5O_{12}$) Thin Films and Monoliths," *Chem. Mater.*, vol. 26, no. 20, pp. 6050–6057, 2014, doi: 10.1021/cm503020y.

[45] J. Jang and J. Bae, "Fabrication of Mesoporous Polymer Using Soft Template Method," *Chem. Commun.*, vol. 1, no. 9, pp. 1200–1202, 2005, doi: 10.1039/b416518g.

[46] D. M. Antonelli, A. Nakahira, J. Y. Ying, C. Laoteppitaks, A. Ambrosini, and K. R. Poeppelmeier, "Ligand-Assisted Liquid Crystal Templating in Mesoporous Niobium Oxide Molecular Sieves," *Chemtracts*, vol. 12, no. 2, pp. 118–120, 1999.

[47] M. S. Wong, D. M. Antonelli, and J. Y. Ying, "Synthesis and Characterization of Phosphated Mesoporous Zirconium Oxide," *Acta Metall.*, vol. 9, no. 8, pp. 165–168, 1997.

[48] P. Liu, I. L. Moudrakovski, J. Liu, and A. Sayari, "Mesostructured Vanadium Oxide Containing Dodecylamine," *Chem. Mater.*, vol. 9, no. 11, pp. 2513–2520, 1997, doi: 10.1021/cm970067u.

[49] C. J. Brinker, Y. Lu, A. Sellinger, and H. Fan, "Evaporation-Induced Self-Assembly: Nanostructures Made Easy," *Adv. Mater.*, vol. 11, no. 7, pp. 579–585, May 1999, doi: 10.1002/(SICI)1521-4095(199905)11:7<579::AID-ADMA579>3.0.CO;2-R.

[50] Y. Lu *et al.*, "Continuous Formation of Supported Cubic and Hexagonal Mesoporous Films by Sol-Gel Dip-Coating," *Nature*, vol. 389, pp. 364–368, 1997, doi: 10.1038/38699.

[51] D. Grosso *et al.*, "Fundamentals of Mesostructuring through Evaporation-Induced Self-Assembly," *Adv. Funct. Mater.*, vol. 14, no. 4, pp. 309–322, 2004, doi: 10.1002/adfm.200305036.

[52] Y. Yamauchi and K. Kuroda, "Rational Design of Mesoporous Metals and Related Nanomaterials by a Soft-Template Approach," *Chem. - An Asian J.*, vol. 3, no. 4, pp. 664–676, 2008, doi: 10.1002/asia.200700350.

[53] R. Nisticò, D. Scalarone, and G. Magnacca, “Sol-Gel Chemistry, Templating and Spin-Coating Deposition: A Combined Approach to Control in a Simple Way the Porosity of Inorganic Thin Films/Coatings,” *Microporous Mesoporous Mater.*, vol. 248, pp. 18–29, 2017, doi: 10.1016/j.micromeso.2017.04.017.

[54] C. Karakaya, Y. Türker, C. Albayrak, and Ö. Dag, “Assembly of Molten Transition Metal Salt-Surfactant in a Confined Space for the Synthesis of Mesoporous Metal Oxide-Rich Metal Oxide-Silica Thin Films,” *Chem. Mater.*, vol. 23, no. 12, pp. 3062–3071, 2011, doi: 10.1021/cm200932k.

[55] F. M. Balcı, Ö. U. Kudu, E. Yılmaz, and Ö. Dag, “Synthesis of Mesoporous Lithium Titanate Thin Films and Monoliths as an Anode Material for High-Rate Lithium-Ion Batteries,” *Chem. - A Eur. J.*, vol. 22, pp. 18873–18880, 2016, doi: 10.1002/chem.201604253.

[56] C. Avcı, A. Aydın, Z. Tuna, Z. Yavuz, Y. Yamauchi, and N. Suzuki, “Molten Salt Assisted Self Assembly (MASA): Synthesis of Mesoporous Metal Titanate ($CoTiO_3$, $MnTiO_3$, and $Li_4Ti_5O_{12}$) Thin Films and Monoliths,” *Chem. Mater.*, vol. 26, p. 6050−6057, 2014.

[57] C. Karakaya, Y. Türker, and Ö. Dag, “Molten-Salt-Assisted Self-Assembly (MASA)-Synthesis of Mesoporous Metal Titanate-Titania, Metal Sulfi de-Titania, and Metal Selenide-Titania Thin Films,” *Adv. Funct. Mater.*, vol. 23, pp. 4002–4010, 2013, doi: 10.1002/adfm.201202716.

[58] G. Saat, F. M. Balci, E. P. Alsaç, F. Karadas, and Ö. Dag, “Molten Salt Assisted Self-Assembly: Synthesis of Mesoporous $LiCoO_2$ and $LiMn_2O_4$ Thin Films and Investigation of Electrocatalytic Water Oxidation Performance of Lithium Cobaltate,” *Small*, vol. 14, no. 1, pp. 1–11, 2018, doi: 10.1002/smll.201701913.

[59] F. M. Balci *et al.*, “Synthesis of Mesoporous $LiMn_2O_4$ and $LiMn_{2-x}Co_xO_4$ Thin Films using the MASA Approach as Efficient Water Oxidation Electrocatalysts,” *J. Mater. Chem. A*, vol. 6, pp. 13925–13933, 2018, doi: 10.1039/c8ta04138e.

[60] J. Prost and P. G. Gennes, *The Physics of Liquid Crystals*. 1993.

[61] G. Vertogen and W. H. de Jeu, *Thermotropic Liquid Crystals, Fundamental*.

1988.

[62] N. K. Raman, M. T. Anderson, and C. J. Brinker, “Template-Based Approaches to the Preparation of Amorphous, Nanoporous Silicas,” *Chem. Mater.*, vol. 8, no. 8, pp. 1682–1701, 1996, doi: 10.1021/cm960138+.

[63] K. Holmberg, B. Jönsson, B. Kronberg, and B. Lindman, *Surfactants and Polymers in Aqueous Solution*. John Wiley & Sons, 2002.

[64] M. S. Bakshi, “Micelle Formation by Anionic and Cationic Surfactants in Binary Aqueous Solvents,” *J. Chem. Soc. Faraday Trans.*, vol. 89, no. 24, pp. 4323–4326, 1993.

[65] W. J. Benton and C. A. Miller, “Topological Features of Oily Streak Defects and Parabolic Focal Conics in Dilute Lamellar Lyotropic Liquid Crystalline Phases.,” *Prog. Colloid Polym. Sci.*, vol. 68, pp. 71–81, 1983, doi: 10.1007/bfb0114142.

[66] D. Demus, J. Goodby, G. W. Gray, H.-W. Spiess, and V. Vill, *Handbook of Liquid Crystals, Volume 2B: Low Molecular Weight Liquid Crystals II*. WILEY-VCH, 1998.

[67] H. G. J. Moseley, “The High-Frequency Spectra of the Elements,” in *The London, Edinburgh and Dublin Philosophical Magazine and Journal of Science*, 6th ed., London-Edinburgh: Taylor & Francis, 1913, pp. 1024–1034.

[68] F. Reinitzer, “Beitr ge zur Kenntniss des Gholesterins,” *Monatshefte für Chemie*, vol. 9, no. 1, pp. 421–441, 1888.

[69] P. Alexandridis, U. Olsson, and B. Lindman, “A Record Nine Different Phases (Four Cubic, Two Hexagonal, and One Lamellar Lyotropic Liquid Crystalline and Two Micellar Solutions) in a Ternary Isothermal System of an Amphiphilic Block Copolymer and Selective Solvents (Water and Oil),” *Langmuir*, vol. 14, pp. 2627–2638, 1998, doi: 10.1021/la971117c.

[70] Ö. Çelik and Ö. Dag, “A New Lyotropic Liquid-Crystalline System: Oligo (Ethylene Oxide) Surfactants with Transition Metal Complexes,” *Angew. Chem. Int. Ed.*, vol. 40, no. 20, pp. 3799–3803, 2001.

[71] Ö. Dag, S. Alayoğlu, and I. Uysal, “Effects of Ions on the Liquid Crystalline Mesophase of Transition-Metal Salt: Surfactant (C_nEO_m),” *J. Phys. Chem. B*, vol. 108, no. 24, pp. 8439–8446, 2004, doi: 10.1021/jp049716x.

[72] A. Faik Demirörs, B. E. Eser, and Ö. Dag, “Liquid Crystalline Mesophases of Pluronics (L64, P65, and P123) and Transition Metal Nitrate Salts ($[M(H_2O)_6](NO_3)_2$),” *Langmuir*, vol. 21, no. 9, pp. 4156–4162, 2005, doi: 10.1021/la047136l.

[73] A. S. Poyraz, C. Albayrak, and Ö. Dag, “The Effect of Cationic Surfactant and Some Organic/Inorganic Additives on the Morphology of Mesostructured Silica Templated by Pluronics,” *Microporous Mesoporous Mater.*, vol. 115, no. 3, pp. 548–555, 2008, doi: 10.1016/j.micromeso.2008.02.033.

[74] C. Albayrak, N. Özkan, and Ö. Dag, “Origin of Lyotropic Liquid Crystalline Mesophase Formation and Liquid Crystalline to Mesostructured Solid Transformation in the Metal Nitrate Salt-Surfactant Systems,” *Langmuir*, vol. 27, no. 3, pp. 870–873, 2011, doi: 10.1021/la1035932.

[75] C. Albayrak, A. Cihaner, and Ö. Dag, “A New, Highly Conductive, Lithium Salt/Nonionic Surfactant, Lyotropic Liquid-Crystalline Mesophase and Its Application,” *Chem. - A Eur. J.*, vol. 18, pp. 4190–4194, 2012, doi: 10.1002/chem.201290051.

[76] C. Albayrak, G. Barim, and Ö. Dag, “Effect of Hygroscopicity of the Metal Salt on the Formation and Air Stability of Lyotropic Liquid Crystalline Mesophases in Hydrated Salt-Surfactant Systems,” *J. Colloid Interface Sci.*, vol. 433, pp. 26–33, 2014, doi: 10.1016/j.jcis.2014.07.008.

[77] E. B. Olutaş, F. M. Balcl, and Ö. Dag, “Strong Acid-Nonionic Surfactant Lyotropic Liquid-Crystalline Mesophases as Media for the Synthesis of Carbon Quantum Dots and Highly Proton Conducting Mesostructured Silica Thin Films and Monoliths,” *Langmuir*, vol. 31, no. 37, pp. 10265–10271, 2015, doi: 10.1021/acs.langmuir.5b02225.

[78] E. Tunkara, C. Albayrak, E. O. Polat, C. Kocabas, and Ö. Dag, “Highly Proton Conductive Phosphoric Acid-Nonionic Surfactant Lyotropic Liquid Crystalline

Mesophases and Application in Graphene Optical Modulators," *ACS Nano*, vol. 8, no. 10, pp. 11007–11012, 2014, doi: 10.1021/nn505199q.

[79] A. K. Padhi, K. S. Nanjundaswamy, and J. B. Goodenough, "Phospho-olivines as Positive-Electrode Materials for Rechargeable Lithium Batteries," *J. Electrochem. Soc.*, vol. 144, no. 4, pp. 1188–1194, 1997.

[80] F. Omenya *et al.*, "Why Substitution Enhances the Reactivity of $LiFePO_4$?," *Chem. Mater.*, vol. 25, pp. 85–89, 2013, doi: 10.1021/cm303259j.

[81] D. Yang *et al.*, "Synthesis of Two-Dimensional Transition-Metal Phosphates with Highly Ordered Mesoporous Structures for Lithium-Ion Battery Applications," *Angew. Chemie - Int. Ed.*, vol. 53, pp. 9352–9355, 2014, doi: 10.1002/anie.201404615.

[82] B. P. Bastakoti *et al.*, "Synthesis of Mesoporous Transition-Metal Phosphates by Polymeric Micelle Assembly," *Chem. - A Eur. J.*, vol. 22, pp. 7463–7467, 2016, doi: 10.1002/chem.201600435.

[83] L. Croguennec and M. R. Palacin, "Recent Achievements on Inorganic Electrode Materials for Lithium-Ion Batteries," *J. Am. Chem. Soc.*, vol. 137, no. 9, pp. 3140–3156, 2015, doi: 10.1021/ja507828x.

[84] C. Masquelier and L. Croguennec, "Polyanionic (Phosphates, Silicates, Sulfates) Frameworks as Electrode Materials for Rechargeable Li (or Na) Batteries," *Chem. Rev.*, vol. 113, pp. 6552–6591, 2013, doi: 10.1021/cr3001862.

[85] C. Sun, S. Rajasekhara, J. B. Goodenough, and F. Zhou, "Monodisperse Porous $LiFePO_4$ Microspheres for a High Power Li-Ion Battery Cathode," *J. Am. Chem. Soc.*, vol. 133, pp. 2132–2135, 2011, doi: 10.1021/ja1110464.

[86] D. B. Ravnsbæk *et al.*, "Extended Solid Solutions and Coherent Transformations in Nanoscale Olivine Cathodes," *Nano Lett.*, vol. 14, no. 3, pp. 1484–1491, 2014, doi: 10.1021/nl404679t.

[87] Y. Zhou *et al.*, "Chemical Precipitation Synthesis of Porous $Ni_2P_2O_7$ Nanowires for Supercapacitor," *J. Alloys Compd.*, vol. 790, pp. 36–41, 2019, doi:

10.1016/j.jallcom.2019.03.192.

[88] C. Chen, N. Zhang, Y. He, B. Liang, R. Ma, and X. Liu, “Controllable Fabrication of Amorphous Co-Ni Pyrophosphates for Tuning Electrochemical Performance in Supercapacitors,” *ACS Appl. Mater. Interfaces*, vol. 8, no. 35, pp. 23114–23121, 2016, doi: 10.1021/acsami.6b07640.

[89] Z. Khan, B. Senthilkumar, S. Lim, R. Shanker, Y. Kim, and H. Ko, “Redox-Additive-Enhanced High Capacitance Supercapacitors Based on $Co_2P_2O_7$ Nanosheets,” *Adv. Mater. Interfaces*, vol. 4, no. 12, pp. 1–7, 2017, doi: 10.1002/admi.201700059.

[90] B. Senthilkumar, Z. Khan, S. Park, K. Kim, H. Ko, and Y. Kim, “Highly Porous Graphitic Carbon and $Ni_2P_2O_7$ for a High Performance Aqueous Hybrid Supercapacitor,” *J. Mater. Chem. A*, vol. 3, no. 43, pp. 21553–21561, 2015, doi: 10.1039/c5ta04737d.

[91] C. Wei *et al.*, “Hierarchically Porous Bowknot-Like Sodium Doped $Ni_2P_2O_7$-$Co_2P_2O_7$ with Improved Supercapacitor Performances,” *Appl. Surf. Sci.*, vol. 465, no. September 2018, pp. 763–771, 2019, doi: 10.1016/j.apsusc.2018.09.223.

[92] K. V. Sankar, Y. Seo, S. C. Lee, and S. Chan Jun, “Redox Additive-Improved Electrochemically and Structurally Robust Binder-Free Nickel Pyrophosphate Nanorods as Superior Cathode for Hybrid Supercapacitors,” *ACS Appl. Mater. Interfaces*, vol. 10, no. 9, pp. 8045–8056, 2018, doi: 10.1021/acsami.7b19357.

[93] P. Matheswaran, P. Karuppiah, S. M. Chen, and P. Thangavelu, “A Binder-Free $Ni_2P_2O_7/Co_2P_2O_7$ Nanograss Array as an Efficient Cathode for Supercapacitors,” *New J. Chem.*, vol. 44, no. 30, pp. 13131–13140, 2020, doi: 10.1039/d0nj00890g.

[94] J. Zhang *et al.*, “In Situ Fabrication of a Rose-Shaped $Co_2P_2O_7$/C Nanohybrid via a Coordination Polymer Template for Supercapacitor Application,” *New J. Chem.*, vol. 44, no. 29, pp. 12514–12521, 2020, doi: 10.1039/d0nj02414g.

[95] C. Wei, C. Cheng, S. Wang, Y. Xu, J. Wang, and H. Pang, “Sodium-Doped Mesoporous $Ni_2P_2O_7$ Hexagonal Tablets for High-Performance Flexible All-

Solid-State Hybrid Supercapacitors," *Chem. - An Asian J.*, vol. 10, pp. 1731 – 1737, 2015, doi: 10.1002/asia.201500335.

[96] H. Pang *et al.*, "Cobalt Pyrophosphate Nano/Microstructures as Promising Electrode Materials of Supercapacitor," *J. Solid State Electrochem.*, vol. 17, pp. 1383–1391, 2013, doi: 10.1007/s10008-013-2007-5.

[97] H. Pang, Z. Yan, W. Wang, Y. Wei, X. Li, and J. Li, "Template-free Controlled Fabrication of $NH_4MnPO_4 \cdot H_2O$ and $Mn_2P_2O_7$ Micro-Nanostructures and Study of Their Electrochemical Properties," *Int. J. Electrochem. Sci.*, vol. 7, pp. 12340–12353, 2012.

[98] G. Li, H. Azuma, and M. Tohda, "$LiMnPO_4$ as the Cathode for Lithium Batteries," *Electrochem. Solid-State Lett.*, vol. 5, no. 6, pp. 135–138, 2002, doi: 10.1149/1.1475195.

[99] C. Delacourt, P. Poizot, M. Morcrette, J. M. Tarascon, and C. Masquelier, "One-Step Low-Temperature Route for the Preparation of Electrochemically Active $LiMnPO_4$ Powders," *Chem. Mater.*, vol. 16, pp. 93–96, 2004, doi: 10.1021/cm030347b.

[100] D. Dai, M. H. Whangbo, H. J. Koo, X. Rocquefelte, S. Jobic, and A. Villesuzanne, "Analysis of the Spin Exchange Interactions and the Ordered Magnetic Structures of Lithium Transition Metal Phosphates $LiMPO_4$ (M = Mn, Fe, Co, Ni) with the Olivine Structure," *Inorg. Chem.*, vol. 44, no. 7, pp. 2407–2413, 2005, doi: 10.1021/ic048431w.

[101] M. Pramanik, Y. Tsujimoto, V. Malgras, S. X. Dou, J. H. Kim, and Y. Yamauchi, "Mesoporous Iron Phosphonate Electrodes with Crystalline Frameworks for Lithium-Ion Batteries," *Chem. Mater.*, vol. 27, pp. 1082–1089, 2015, doi: 10.1021/cm5044045.

[102] J. Qian, M. Zhou, Y. Cao, X. Ai, and H. Yang, "Template-Free Hydrothermal Synthesis of Nanoembossed Mesoporous $LiFePO_4$ Microspheres for High-Performance Lithium-Ion Batteries," *J. Phys. Chem. C*, vol. 114, no. 8, pp. 3477–3482, 2010, doi: 10.1021/jp912102k.

[103] P. Mei *et al.*, "Two-Dimensional Mesoporous Vanadium Phosphate Nanosheets

through Liquid Crystal Templating Method toward Supercapacitor Application," *Nano Energy*, vol. 52, pp. 336–344, 2018, doi: 10.1016/j.nanoen.2018.07.052.

[104] T. Y. Ma and S. Z. Qiao, "Acid-Base Bifunctional Periodic Mesoporous Metal Phosphonates for Synergistically and Heterogeneously Catalyzing CO_2 Conversion," *ACS Catal.*, vol. 4, no. 11, pp. 3847–3855, 2014, doi: 10.1021/cs501124d.

[105] X. Wang *et al.*, "$NH_4CoPO_4 \cdot H_2O$ Microflowers and Porous $Co_2P_2O_7$ Microflowers: Effective Electrochemical Supercapacitor Behavior in Different Alkaline Electrolytes," *Int. J. Electrochem. Sci.*, vol. 8, no. 3, pp. 3768–3785, 2013.

[106] H. Pang, Y. Z. Zhang, Z. Run, W. Y. Lai, and W. Huang, "Amorphous Nickel Pyrophosphate Microstructures for High-Performance Flexible Solid-State Electrochemical Energy Storage Devices," *Nano Energy*, vol. 17, pp. 339–347, 2015, doi: 10.1016/j.nanoen.2015.07.030.

[107] N. Zhang *et al.*, "$Ni_2P_2O_7$ Nanoarrays with Decorated C_3N_4 Nanosheets as Efficient Electrode for Supercapacitors," *ACS Appl. Energy Mater.*, vol. 1, no. 5, pp. 2016–2023, 2018, doi: 10.1021/acsaem.8b00114.

[108] A. Padhy, A. K. Samantara, and J. N. Behera, "Cobalt Pyrophosphate ($Co_2P_2O_7$) Derived from an Open-Framework Cobalt Phosphite: a Durable Electroactive Material for Electrochemical Energy Conversion and Storage Application," *Sustain. Energy Fuels*, vol. 5, no. 14, pp. 3729–3736, 2021, doi: 10.1039/d1se00714a.

[109] M. Priyadharshini *et al.*, "Surfactant-Dependent Self Organisation of Nickel Pyrophosphate for Electrochemical Supercapacitors," *J. Mater. Sci. Mater. Electron.*, vol. 33, no. 12, pp. 9269–9276, 2022, doi: 10.1007/s10854-021-07261-y.

[110] S. S. Patil and P. S. Patil, "Transition Metal Pyrophosphate ($M_xP_2O_7$): A New Arrival in Hybrid Supercapacitors," *Chem. Eng. J.*, vol. 455, p. 140639, 2023, doi: 10.1016/j.cej.2022.140639.

[111] N. A. Blanc, Q. Williams, B. El, and B. Rachid, “A Vibrational Study of Phase Transitions in $Fe_2P_2O_7$ and $Cr_2P_2O_7$ under High-Pressures,” *J. Am. Ceram. Soc.*, vol. 101, pp. 5257–5268, 2018, doi: 10.1111/jace.15756.

[112] H. Li *et al.*, “Interfacial Engineering and a Low-Crystalline Strategy for High-Performance Supercapacitor Negative Electrodes: $Fe_2P_2O_7$ Nanoplates Anchored on N/P Co-doped Graphene Nanotubes,” *ACS Appl. Mater. Interfaces*, vol. 14, pp. 3363–3373, 2022, doi: 10.1021/acsami.1c17356.

[113] H. Zhou, S. Upreti, N. A. Chernova, G. Hautier, G. Ceder, and M. S. Whittingham, “Iron and Manganese Pyrophosphates as Cathodes for Lithium-Ion Batteries,” no. 6, pp. 293–300, 2011, doi: 10.1021/cm102922q.

[114] A. Agarwal and B. R. Sankapal, “Ultrathin $Cu_2P_2O_7$ Nanoflakes on Stainless Steel Substrate for Flexible Symmetric All-Solid-State Supercapacitors,” *Chem. Eng. J.*, vol. 422, no. April, p. 130131, 2021, doi: 10.1016/j.cej.2021.130131.

[115] A. Karaphun, P. Chirawatkul, S. Maensiri, and E. Swatsitang, “Influence of Calcination Temperature on the Structural, Morphological, optical, Magnetic and Electrochemical Properties of $Cu_2P_2O_7$ Nanocrystals,” *J. Sol-Gel Sci. Technol.*, pp. 407–421, 2018, doi: 10.1007/s10971-018-4819-3.

[116] V. Aravindan, M. V Reddy, S. Madhavi, S. G. Mhaisalkar, G. V. S. Rao, and B. V. R. Chowdari, “Hybrid Supercapacitor with Nano-TiP_2O_7 as Intercalation Electrode,” *J. Power Sources*, vol. 196, no. 20, pp. 8850–8854, 2011, doi: 10.1016/j.jpowsour.2011.05.074.

[117] Z. Shi, Q. Wang, W. Ye, Y. Li, and Y. Yang, “Synthesis and Characterization of Mesoporous Titanium Pyrophosphate as Lithium Intercalation Electrode Materials,” vol. 88, pp. 232–237, 2006, doi: 10.1016/j.micromeso.2005.09.013.

[118] A. Karaphun, S. Sawadsitang, T. Duangchuen, P. Chirawatkul, and T. Putjuso, “Influence of Calcination Temperature on Structural , Morphological , and Electrochemical Properties of $Zn_2P_2O_7$ nanostructure,” *Surfaces and Interfaces*, vol. 23, no. November 2020, p. 100961, 2021, doi: 10.1016/j.surfin.2021.100961.

[119] P. Miller, John R., Simon, “Electrochemical Capacitors for Energy

Management," *Science (80-.).*, vol. 5889, no. 321, pp. 651–652, 2008.

[120] J. P. Cheng, J. Zhang, and F. Liu, "Recent Development of Metal Hydroxides as Electrode Material of Electrochemical Capacitors," *RSC Adv.*, vol. 4, no. 73, pp. 38893–38917, 2014, doi: 10.1039/c4ra06738j.

[121] D. S. Hall, D. J. Lockwood, C. Bock, and B. R. MacDougall, "Nickel Hydroxides and Related Materials: A Review of Their Structures, Synthesis and Properties," *Proc. R. Soc. A Math. Phys. Eng. Sci.*, vol. 471, no. 2174, 2015, doi: 10.1098/rspa.2014.0792.

[122] Z. Liu, R. Ma, M. Osada, K. Takada, and T. Sasaki, "Selective and Controlled Synthesis of α- and β-Cobalt Hydroxides in Highly Developed Hexagonal Platelets," *J. Am. Chem. Soc.*, vol. 127, no. 40, pp. 13869–13874, 2005, doi: 10.1021/ja0523338.

[123] R. S. Mcewen, "Crystallographic Studies on Nickel Hydroxide and the Higher Nickel Oxides," *J. Phys. Chem.*, vol. 75, no. 12, pp. 1782–1789, 1971.

[124] A. A. S. Rovetta, M. P. Browne, A. Harvey, I. J. Godwin, J. N. Coleman, and M. E. G. Lyons, "Cobalt Hydroxide Nanoflakes and Their Application as Supercapacitors and Oxygen Evolution Catalysts," *Nanotechnology*, vol. 28, no. 37, 2017, doi: 10.1088/1361-6528/aa7f1b.

[125] J. Yan *et al.*, "Advanced Asymmetric Supercapacitors Based on $Ni(OH)_2$/Graphene and Porous Graphene Electrodes with High Energy Density," *Adv. Funct. Mater.*, vol. 22, no. 12, pp. 2632–2641, 2012, doi: 10.1002/adfm.201102839.

[126] S. Tang, S. Vongehr, Y. Wang, L. Chen, and X. Meng, "Ethanol-Assisted Hydrothermal Synthesis and Electrochemical Properties of Coral-Like β-$Co(OH)_2$ Nanostructures," *J. Solid State Chem.*, vol. 183, no. 9, pp. 2166–2173, 2010, doi: 10.1016/j.jssc.2010.07.030.

[127] T. Xue and J. M. Lee, "Capacitive Behavior of Mesoporous $Co(OH)_2$ Nanowires," *J. Power Sources*, vol. 245, pp. 194–202, 2014, doi: 10.1016/j.jpowsour.2013.06.135.

[128] F. Cao, G. X. Pan, P. S. Tang, and H. F. Chen, “Hydrothermal-Synthesized $Co(OH)_2$ Nanocone Arrays for Supercapacitor Application,” *J. Power Sources*, vol. 216, pp. 395–399, 2012, doi: 10.1016/j.jpowsour.2012.05.073.

[129] X. Yi, H. Sun, N. Robertson, and C. Kirk, “Nanoflower $Ni(OH)_2$ Grown in situ on Ni Foam for High-Performance Supercapacitor Electrode Materials,” *Sustain. Energy Fuels*, vol. 5, no. 20, pp. 5236–5246, 2021, doi: 10.1039/d1se01036k.

[130] S. Natarajan, M. Ulaganathan, and V. Aravindan, “Building Next-Generation Supercapacitors with Battery Type $Ni(OH)_2$,” *J. Mater. Chem. A*, vol. 9, no. 28, pp. 15542–15585, 2021, doi: 10.1039/d1ta03262c.

[131] H. Kim, W. Lee, W. Choi, S. Yun, E. Lee, and W. S. Yoon, “Crystal Water-Assisted Additional Capacity for Nickel Hydroxide Anode Materials,” *Adv. Funct. Mater.*, vol. 32, no. 17, pp. 1–11, 2022, doi: 10.1002/adfm.202110828.

[132] D. Shao, Q. Wang, X. Yao, Y. Zhou, and X. Y. Yu, “Phase-Engineering of Nickel Hydroxide in the $Ni/Ni(OH)_2$ Interface for Efficient Hydrogen Evolution and Hydrazine-Assisted Water Splitting in Seawater,” *J. Mater. Chem. A*, vol. 10, no. 41, pp. 21848–21855, 2022, doi: 10.1039/d2ta06481b.

[133] A. J. Bard and L. R. Faulkner, *Electrochemical Methods: Fundamentals and Applications*, 2nd ed. John Wiley & Sons: New York, 1980.

[134] N. Elgrishi, K. J. Rountree, B. D. McCarthy, E. S. Rountree, T. T. Eisenhart, and J. L. Dempsey, “A Practical Beginner’s Guide to Cyclic Voltammetry,” *J. Chem. Educ.*, vol. 95, pp. 197–206, 2018, doi: 10.1021/acs.jchemed.7b00361.

[135] P. T. Kissinger and W. R. Heineman, “Cyclic Voltammetry,” *J. Chem. Educ.*, vol. 60, no. 9, pp. 702–706, 1983, doi: 10.1021/ed060p702.

[136] P. Zanello, *Inorganic electrochemistry: Theory, practice and applications.* 2003.

[137] W. C. Heerens, “Application of Capacitance Techniques in Sensor Design,” *J. Phys. E.*, vol. 19, pp. 897–906, 1986, doi: 10.1088/0022-3735/19/11/002.

[138] E. E. Kalu, T. T. Nwoga, V. Srinivasan, and J. W. Weidner, “Cyclic

Voltammetric Studies of the Effects of Time and Temperature on the Capacitance of Electrochemically Deposited Nickel Hydroxide," *J. Power Sources*, vol. 92, pp. 163–167, 2001, doi: 10.1016/S0378-7753(00)00520-6.

[139] H. Wang and L. Pilon, "Physical Interpretation of Cyclic Voltammetry for Measuring Electric Double Layer Capacitances," *Electrochim. Acta*, vol. 64, pp. 130–139, 2012, doi: 10.1016/j.electacta.2011.12.118.

[140] Y. Su *et al.*, "Controllable Fabrication of Functional Microparticle Materials from Microfluidic Droplet Templates," *Huagong Xuebao/CIESC J.*, vol. 8, p. 23114−23121, 2021, doi: 10.11949/0438-1157.20201099.

[141] B. Dunn, H. Kamath, and J. M. Tarascon, "Electrical Energy Storage for the Grid: A battery of Choices," *Science (80-.).*, vol. 334, p. 928−935, 2011, doi: 10.1126/science.1212741.

[142] L. Liu, Z. Niu, L. Zhang, W. Zhou, X. Chen, and S. Xie, "Nanostructured Graphene Composite Papers for Highly Flexible and Foldable Supercapacitors," *Adv. Mater.*, vol. 26, p. 4855, 2014, doi: 10.1002/adma.201401513.

[143] Y. Huang *et al.*, "Magnetic-Assisted, Self-Healable, Yarn-Based Supercapacitor," *ACS Nano*, vol. 9, p. 6242−6251, 2015, doi: 10.1021/acsnano.5b01602.

[144] C. Yuan, J. Li, L. Hou, X. Zhang, L. Shen, and X. W. Lou, "Ultrathin Mesoporous $NiCo_2O_4$ Nanosheets Supported on Ni Foam as Advanced Electrodes for Supercapacitors," *Adv. Funct. Mater.*, vol. 22, p. 4592, 2012, doi: 10.1002/adfm.201200994.

[145] P. Sabatier and J. B. Senderens, "New Synthesis of Methane," *Comptes Rendus l'Académie des Sci. Paris*, 1902.

[146] R. K. B. Gover, N. D. Withers, S. Allen, R. L. Withers, and J. S. O. Evans, "Structure and Phase Transitions of SnP_2O_7," *J. Solid State Chem.*, vol. 166, no. 1, pp. 42–48, 2002, doi: 10.1006/jssc.2002.9554.

[147] M. Winter and R. J. Brodd, "What are Batteries, Fuel Cells, and

Supercapacitors?," *Chem. Rev.*, vol. 104, p. 4245, 2004, doi: 10.1021/cr020730k.

[148] P. Simon and Y. Gogotsi, "Materials for Electrochemical Capacitors," *Nat. Mater.*, vol. 7, p. 845, 2008, doi: 10.1038/nmat2297.

[149] Y. Jin, Y. Shen, and T. Hibino, "Proton Conduction in Metal Pyrophosphates (MP_2O_7) at Intermediate Temperatures," *J. Mater. Chem.*, vol. 20, pp. 6214–6217, 2010, doi: 10.1039/b924188d.

[150] T. Hibino, K. Kobayashi, M. Nagao, and S. Kawasaki, "High-Temperature Supercapacitor with a Proton-Conducting Metal Pyrophosphate Electrolyte," *Sci. Rep.*, vol. 5, p. 1,7, 2015, doi: 10.1038/srep07903.

[151] X. Ji *et al.*, "Different Charge-Storage Mechanisms in Disulfide Vanadium and Vanadium Carbide Monolayer," *J. Mater. Chem. A*, vol. 3, p. 9909, 2015, doi: 10.1039/c5ta01003a.

[152] Y. Wang, Y. Song, and Y. Xia, "Electrochemical Capacitors: Mechanism, Materials, Systems, Characterization and Applications," *Chem. Soc. Rev.*, vol. 45, p. 5925, 2016, doi: 10.1039/c5cs00580a.

[153] D. Galizzioli, F. Tantardini, and S. Trasatti, "Ruthenium Dioxide: A New Electrode Material. I. Behaviour in Acid Solutions of Inert Electrolytes," *J. Appl. Electrochem.*, vol. 4, p. 57, 1974, doi: 10.1007/BF00615906.

[154] A. S. Aricò, P. Bruce, B. Scrosati, J. M. Tarascon, and W. Van Schalkwijk, "Nanostructured materials for advanced energy conversion and storage devices," *Nat. Mater.*, vol. 4, p. 366, 2005, doi: 10.1038/nmat1368.

[155] T. Brezesinski, J. Wang, S. H. Tolbert, and B. Dunn, "Ordered mesoporous α-MoO_3 with Iso-Oriented Nanocrystalline Walls for Thin-Film Pseudocapacitors," *Nat. Mater.*, vol. 9, pp. 146–151, 2010, doi: 10.1038/nmat2612.

[156] N. Elgrishi, K. J. Rountree, B. D. McCarthy, E. S. Rountree, T. T. Eisenhart, and J. L. Dempsey, "A Practical Beginner's Guide to Cyclic Voltammetry," *J. Chem. Educ.*, vol. 95, no. 2, pp. 197–206, 2018, doi:

10.1021/acs.jchemed.7b00361.

[157] T. W. G. Solomons, C. B. Fryhle, and S. A. Snyder, *Organic Chemistry*. 2016.

[158] Querry Mr, Curnutte B, and Williams D, "Refractive Index of Water in The Infrared," *J. Opt. Soc. Amer.*, vol. 59, no. 10, pp. 1299–1305, 1969.

[159] E. Y. Topuzlu, B. Ulgut, and Ö. Dag, "Role of Water in the Lyotropic Liquid Crystalline Lithium Iodide-Iodine-Water-$C_{12}E_{10}$Mesophase as a Gel Electrolyte in a Dye-Sensitized Solar Cell," *Langmuir*, vol. 37, no. 27, pp. 8305–8313, 2021, doi: 10.1021/acs.langmuir.1c01094.

[160] A. G. Meguerdichian *et al.*, "Synthesis and Electrocatalytic Activity of Ammonium Nickel Phosphate, $[NH_4]NiPO_4 \cdot 6H_2O$, and β-Nickel Pyrophosphate, β-$Ni_2P_2O_7$: Catalysts for Electrocatalytic Decomposition of Urea," *Inorg. Chem.*, vol. 57, no. 4, pp. 1815–1823, 2018, doi: 10.1021/acs.inorgchem.7b02658.

[161] A. Hezel and S. D. Ross, "The Vibrational Spectra of Some Divalent Metal Pyrophosphates," *Spectrochim. Acta Part A Mol. Spectrosc.*, vol. 23, no. 5, pp. 1583–1589, 1967, doi: 10.1016/0584-8539(67)80381-7.

[162] N. Khay, A. Ennaciri, and M. Harcharras, "Vibrational Spectra of Double Diphosphates $RbLnP_2O_7$ (Ln = Dy, Ho, Y, Er, Tm, Yb)," *Vib. Spectrosc.*, vol. 27, no. 2, pp. 119–126, 2001, doi: 10.1016/S0924-2031(01)00123-0.

[163] M. Thommes, "Physical Adsorption Characterization of Nanoporous Materials," *Chemie-Ingenieur-Technik*, vol. 82, no. 7, pp. 1059–1073, 2010, doi: 10.1002/cite.201000064.

[164] M. Thommes *et al.*, "Physisorption of Gases, with Special Reference to the Evaluation of Surface Area and Pore Size Distribution (IUPAC Technical Report)," *Pure Appl. Chem.*, vol. 87, no. 9–10, pp. 1051–1069, 2015, doi: 10.1515/pac-2014-1117.

[165] A. P. Grosvenor, M. C. Biesinger, R. S. C. Smart, and N. S. McIntyre, "New Interpretations of XPS Spectra of Nickel Metal and Oxides," *Surf. Sci.*, vol. 600, no. 9, pp. 1771–1779, 2006, doi: 10.1016/j.susc.2006.01.041.

[166] J. C. Dupin, D. Gonbeau, P. Vinatier, and A. Levasseur, “Systematic XPS Studies of Metal Oxides, Hydroxides and Peroxides,” *Phys. Chem. Chem. Phys.*, vol. 2, no. 6, pp. 1319–1324, 2000, doi: 10.1039/a908800h.

[167] W. W. Rudolph, D. Fischer, and G. Irmer, “Vibrational Spectroscopic Studies and Density Functional Theory Calculations of Speciation in the CO_2-Water System,” *Appl. Spectrosc.*, vol. 60, no. 2, pp. 130–144, 2006, doi: 10.1366/000370206776023421.

[168] John Rumble, *CRC Handbook of Chemistry and Physics*, 99th ed. CRC Press, 2018.

[169] F. Capitelli, M. Harcharras, H. Assaaoudi, A. Ennaciri, A. G. G. Moliterni, and V. Bertolasi, “Crystal Structure of New Hexahydrate Dicobalt Pyrophosphate Comparison with $Co_2P_2O_7.2H_2O$, α- ,β- and γ-$Co_2P_2O_7$,” *Zeitschrift für Krist. - Cryst. Mater.*, vol. 218, pp. 345–350, 2003.

[170] Y. Chang *et al.*, “Coralloid $Co_2P_2O_7$ Nanocrystals Encapsulated by Thin Carbon Shells for Enhanced Electrochemical Water Oxidation,” *ACS Appl. Mater. Interfaces*, vol. 8, no. 34, pp. 22534–22544, 2016, doi: 10.1021/acsami.6b07209.

[171] L. Tian, J. L. Zhu, L. Chen, B. An, Q. Q. Liu, and K. L. Huang, “Synthesis and Characterization of α-Cobalt Hydroxide Nanobelts,” *J. Nanoparticle Res.*, vol. 13, no. 8, pp. 3483–3488, 2011, doi: 10.1007/s11051-011-0269-3.

[172] D. M. L. Goodgame, M. Goodgame, and F. A. Cotton, “The Electronic Structures of Tetrahedral Cobalt(II) Complexes,” *J. Am. Chem. Soc*, vol. 83, no. 2, pp. 4690–4699, 1961.

[173] C. Calvo, “The Crystal Structure and Phase Transition of β-$Zn_2P_20_7$,” *Can. J. Chem.*, vol. 43, no. 17, 1964.

[174] S. Schneider and R. L. Collin, “Crystal Structure of Manganese Pyrophosphate Dihydrate, $Mn_2P_20_7$ -$2H_20$,” *Inorg. Chem.*, vol. 12, no. 9, pp. 2136–2139, 1973.

[175] D. G. Lee, C. R. Moylan, T. Hayashi, and J. I. Brauman, “Photochemistry of Aqueous Permanganate Ion,” *J. Am. Chem. Soc.*, vol. 109, no. 10, pp. 3003–

3010, 1987, doi: 10.1021/ja00244a023.

[176] H.-C. Hu, H.-S. Hu, B. Zhao, P. Cui, P. Cheng, and J. Li, “Metal-Organic Frameworks (MOFs) of a Cubic Metal Cluster with Multicentered Mn^{I}-Mn^{I} Bonds,” *Angew. Chemie*, vol. 127, no. 40, pp. 11847–11851, 2015, doi: 10.1002/ange.201504758.

[177] M. C. Biesinger, B. P. Payne, A. P. Grosvenor, L. W. M. Lau, A. R. Gerson, and R. S. C. Smart, “Resolving Surface Chemical States in XPS Analysis of First Row Transition Metals, Oxides and Hydroxides: Cr, Mn, Fe, Co and Ni,” *Appl. Surf. Sci.*, vol. 257, no. 7, pp. 2717–2730, 2011, doi: 10.1016/j.apsusc.2010.10.051.

[178] C. S. Fadley, D. A. Shirley, A. J. Freeman, P. S. Bagus, and J. V. Mallow, “Multiplet Splitting of Core-Electron Binding Energies in Transition-Metal Ions,” *Phys. Rev. Lett.*, vol. 23, no. 24, pp. 1397–1401, 1969, doi: 10.1103/PhysRevLett.23.1397.

[179] M. Toupin, T. Brousse, and D. Bélanger, “Charge Storage Mechanism of MnO_2 Electrode used in Aqueous Electrochemical Capacitor,” *Chem. Mater.*, vol. 16, no. 16, pp. 3184–3190, 2004, doi: 10.1021/cm049649j.

[180] E. S. Ilton, J. E. Post, P. J. Heaney, F. T. Ling, and S. N. Kerisit, “XPS Determination of Mn Oxidation States in Mn(hydr)oxides,” *Appl. Surf. Sci.*, vol. 366, pp. 475–485, 2016, doi: 10.1016/j.apsusc.2015.12.159.

[181] H. Lindström *et al.*, “Li^{+} Ion Insertion in TiO_2 (Anatase). 1. Chronoamperometry on CVD Films and Nanoporous Films,” *J. Phys. Chem. B*, vol. 101, no. 39, pp. 7710–7716, 1997, doi: 10.1021/jp970489r.

[182] P. Simon, Y. Gogotsi, and B. Dunn, “Where Do Batteries End and Supercapacitors Begin?,” *Science (80-.).*, vol. 343, pp. 1210–1211, 2014.